University of Thessaly

School of Engineering

Department of Mechanical Engineering

PhD Thesis

Bayesian Optimal Experimental Design Tools

by

Tulay Ercan

A thesis submitted
in partial fulfillment of the
requirements for the degree of
Doctor of Philosophy

July, 2022

This project has received funding from the European Union's Horizon 2020 research and innovation programme under the Marie Skłodowska-Curie grant agreement No 764547.

Approved by the members of the seven-member examination committee:

First Examiner (Supervisor)	Dr. Costas Papadimitriou Professor, Department of Mechanical Engineering, University of Thessaly
Second Examiner	Dr. Eleni Chatzi Associate Professor, Department of Civil, Environmental and Geomatic Engineering, ETH Zurich
Third Examiner	Dr. Keith Worden Professor, Department of Mechanical Engineering, The University of Sheffield
Fourth Examiner	Dr. Dimitrios Giagopoulos Associate Professor, Department of Mechanical Engineering, Aristotle University of Thessaloniki
Fifth Examiner	Dr. Sotirios Natsiavas Professor, Department of Mechanical Engineering, Aristotle University of Thessaloniki
Sixth Examiner	Dr. Lambros Katafygiotis Professor, Department of Civil and Environmental Engineering, The Hong Kong University of Science and Technology
Seventh Examiner	Dr. Konstantinos Ampountolas Associate Professor, Department of Mechanical Engineering, University of Thessaly

Acknowledgements

First of all, I would like to thank my advisor, Prof. Costas Papadimitriou for guiding me through this work until completion. This thesis would not have been possible without his help and guidance. I am grateful for his patience and support.

I would like to thank my cross-institutional supervisors Prof. Eleni Chatzi, Prof. Keith Worden and Dr. Rob Barthorpe (former) for their contributions and constructive comments during my PhD. I want to express my gratitude to my committee members Prof. Lambros Katafygiotis, Prof. Sotirios Natsiavas and Prof. Dimitrios Giagopoulos and Dr. Konstantinos Ampountolas for their inputs. Additionally, thanks to Dr. Omid Sedehi who has significantly contributed to my study as an external collaborator from HKUST.

I would like to acknowledge DyVirt Project under the Marie Skłodowska-Curie ITN (Grant No. 764547) that supported this work. In addition to the financial opportunities, the project provided a professional network consisting of many experienced scientists and engineers. Specifically, thanks to Ulf T. Tygesen and members of his team for their help during my secondment in Ramboll, Denmark and Dr. Tina Dardeno of University of Sheffield for her assistance during my virtual secondment. I am thankful to all researchers who were part of the project, Prof. David Wagg, all DyVirt project managers and administrators for their contribution to this great experience.

During my years in University of Thessaly, I have met a lot of great people. Many thanks to Nicoletta Sachinidou of Mechanical Engineering Department for her help in the past four years. I thank my colleagues George Trousas, Matina Moraiti and visitors from HKUST Victor Flores Terrazas and Antonina Kosikova for discussions, encouragements, and enjoyable moments that we had. Ones again, thanks to Victor for his help with FE models. Special thanks to Xinyu Jia for not only being a good colleague but also being a very good friend and helping me whenever I needed.

Finally, all my friends and my parents have encouraged me in difficult times of these years. They have also impressed me with their own life struggling. I would like to thank my best friend Turkan and Panagiotis for their invaluable support, Tuce, Tuana and Alp for reminding me the joys of life.

Tulay Ercan

Bayesian Optimal Experimental Design Tools

Tulay Ercan
Department of Mechanical Engineering, University of Thessaly, 2022

Supervisor: Prof. Costas Papadimitriou

Abstract

In structural dynamics, optimal experimental design (OED) aims to maximize the information gained from data by optimizing the location, type and number of sensors and actuators as well as the excitation characteristics. In this thesis, a Bayesian OED framework is presented for (a) virtual sensing and (b) parameter estimation, to support the decision-making processes regarding structural health, safety, and performance. The OED framework utilizes information theoretic-based measures to build a utility function robust to measurement, modeling and input uncertainties. The information contained in the data collected from a sensor configuration is defined as the Kullback-Leibler divergence between the prior and posterior distribution of the model parameters or the predicted response quantities of interest, estimated using Bayesian learning techniques. The multidimensional integrals over the prior distribution of the model parameters, the modeling uncertainties and input variabilities, arising in the formulation, are estimated by using asymptotic approximations, as well as Monte Carlo and/or sparse grid techniques.

The optimization of the utility function in terms of the type and location of sensors is performed using genetic algorithms and heuristic forward and backward sequential sensor placement (SSP) algorithms. The computational effort and accuracy of the optimization algorithms is investigated and a new SSP algorithm is proposed that exploits the computational efficiency of the less accurate forward SSP algorithm and the accuracy of the computationally expensive backward SSP algorithm.

The optimal sensor placement (OSP) framework for virtual sensing is developed based on modal expansion and Kalman-based input-state estimation techniques. The framework is applicable to response and/or input time history reconstruction over the structure given output-only vibration measurements. The Gaussian nature of the response estimates for linear models of structures is exploited to derive useful and informative analytical expressions for the util-

ity function in terms of the covariance of the error of the reconstructed response and/or input quantities of interest. The advantages and limitations of each technique for response and input reconstruction as well as their potential for fusing different types of vibration sensors are investigated. The effect of the measurement and model/prediction errors and their uncertainties, as well as the input uncertainties on the optimal sensor configuration is thoroughly studied, highlighting the importance of accounting for robustness to errors and other uncertainties.

A Bayesian OED framework for reliable parameter estimation of linear and nonlinear models of structures using input-output response time history measurements is also developed, accounting for the modelling and input uncertainties. Optimal sensor locations are selected as the ones that maximize the information gained from the data for evaluating the system parameters. Asymptotic approximations, valid for large number of data, simplify part of the multidimensional integrals arising in the utility formulation in terms of a scalar measure of the sensitivities of model responses at the measured locations with respect to the model parameters to be inferred from the data. Such approximations provide valuable insight into the information provided from the data and the information built into the prior distribution quantifying the uncertainties in the model parameters. Robustness of OSP to nuisance parameters related to modeling and input uncertainties is investigated. In particular, the framework addresses the problem where the excitation is measured from installed sensors but its time history remains unknown at the experimental design phase. Stochastic models used to simulate the random variability of the excitation time histories and characteristics are incorporated into the framework to optimally design sensor configurations, robust to unknown input variability. The applicability and effectiveness of the method is demonstrated for structures with restoring forces exhibiting hysteretic nonlinearities. The high computational cost and excessive storage requirements for robust OSP designs are pointed out and remedies to resolve such issues are proposed. Structural differences at the utility function between the design of optimal sensor configuration and the design of optimal actuator and excitation characteristics are addressed.

The effectiveness of the OED framework for virtual sensing is finally demonstrated with artificial and real measurements using full-scale components of engineering structures, including a wind turbine blade and a helicopter blade tested at a laboratory environment.

Contents

List of Figures

List of Tables

Chapter 1. Introduction

1.1 Research Background and Motivation

Design of experiments is a critical task in order to obtain high quality data for a thorough understanding of physical systems and improve future predictions throughout their numerical models. In practical applications, some constraints exist and considerably affect the quality of the obtained data. The possible sensor locations may reach millions of points when deciding the most suitable experimental setup, the positioning of sensors to measure input and output in critical locations might be difficult, or even impossible. Another limitation is the type and number of sensors due to their cost. Therefore, a judicious design is needed to obtain the most efficient data to achieve the purpose of the experiment, taking into account these constraints.

1.1.1 The purpose of the experiment

Optimal experimental design (OED) has a broad area of application in science and engineering in the design process or during operation; in the material, component, substructure, or system level. In addition to areas such as psychology [1], biology [2, 3], epidemiology [4, 5], the OED finds application in structural dynamics for data gathering related to safety, predictive and preventive maintenance actions of critical infrastructures. The importance of building digital twins of critical and complex systems such as renewable energy structures [6–8] is increasing recently as a result of their economic and environmental impact. The use of techniques to improve experimental data that help to build better computational models that represent realistic operational conditions becomes significant, as well. The purpose of experiments includes building trusted, data-informed virtual models (digital twins), selecting the best model among the competing models of the systems, and virtual sensing of important output quantity of interests (QoIs).

In dynamic simulations of civil, mechanical and aerospace systems, virtual sensing is used to estimate unmeasured QoIs from available measurements. This is particularly important for fatigue assessment when direct strain measurements are not available at hot spot locations.

Predicting responses at unmeasured locations or estimating loads using a set of available measurements such as accelerations, displacements, or strains, it is possible to foresee the remaining lifetime of structural components [9, 10]. Among others, model based solutions including modal expansion to reconstruct the responses [11–15] and filtering techniques to reconstruct the responses and inputs [16–20] are extensively used in the literature and industrial applications. However, the design of the sensor configuration to reduce the error in the predictions remains an issue to investigate. Although a number of OSP methods have been developed for the reconstruction of responses to support the reliability of future predictions [21–24], little has been done to address the problem of optimally designing a sensing system under unknown input using output only vibration measurements [25, 26].

Experimental data can provide useful information for deciding how detailed or complex model is needed to explain observations, update model parameters, and even detect damages in terms of location and severity by monitoring the damage sensitive features. Usually, numerical models that explain the observations contain modelling errors, and it is important to consider these errors in the predictions. Furthermore, measurements are sensitive to noise and uncertainties associated with the experimental and environmental conditions. Thus, Bayesian methods have been found to be beneficial in quantifying uncertainty for model updating problems [27, 28]. Many OSP techniques have been developed in the past for reliable parameter estimation of linear systems [29–33], for model selection [34], and for damage identification [35–37].

OED problems considering input characteristics [38] and system nonlinearities [39] have been addressed in the literature. In particular, the selection of the input characteristics in the experiment are investigated for the purpose of activating and identifying the nonlinear features. However, there is a lot of room for improvement for the OED methods for estimating the parameters of nonlinear models and considering complex loading conditions. Especially the structures operating in highly dynamic environment, exposed to random loads such as wind, wave, and earthquake requires comprehensive understanding of the physics and require consideration of the uncertainties of the exciting loads.

OED can be formulated as an optimization problem to minimize (or maximize) a user-defined objective function related to the specific target of the experiment and the characteristics of a system, where the design variables are defined as discrete or continuous variables. In the context of structural dynamics, the objective function has been defined in various forms [40].

Modal identification based techniques such as effective independence (EI) [41], and kinetic energy [42, 43] and information based approaches are commonly used for structural dynamics and structural health monitoring (SHM) applications. Information-theoretic measures such as Kullback-Leibler divergence (KL-div) [44, 45], mutual information [46, 47], the information entropy [30, 32, 34, 48, 49], the joint entropy [50, 51] of the anticipated uncertainty of the model parameters, or quantities derived from them, provide useful criteria for building objective functions taking into account all possible values of data, operational and experimental variabilities.

1.1.2 Bayesian optimal experimental design

Bayesian methods allow us to refine our prior knowledge (which is not affected by the experimental procedure and is often available before the data are gathered) of the predicted quantity with the experimental data through a prediction model. In OED, it allows us to consider all possible values of data that are not available before the experiment and uncertainties in the model and measurements. Lindley presented a comprehensive introduction to the Bayesian treatment of decision theory and optimal experimental design [45]. Since its introduction, it has been applied using various utility functions [52]. Fisher information matrix (FIM) based approaches (based on the determinant or trace of FIM) have been used to form the objective function of the OED in the past [41, 53, 54]. Flynn and Todd [55] presented a Bayesian OSP framework based on a metric related to the probability of damage detection. Undoubtedly, the definition of the most suitable utility function is critical to reach the target of the experimental design. Studies on comparison of the utility functions used in Bayesian OED can be found in the literature [56].

An information entropy based approach for OSP is introduced by Papadimitriou et al. [48] by extending the Bayesian model updating framework presented by Beck and Katafygiotis [27]. Information entropy is used to form the objective function that suits the purpose of the experiment, which is reliable parameter estimation. It is shown that information entropy allows one to trace the information gain from additional sensors, and thus is beneficial for cost-effective OSP by minimizing the number of sensors. For large number of data, asymptotic approximations of the information entropy are introduced [29, 48]. When an exact solution of posterior can not be obtained easily, it is shown that asymptotic techniques are computationally efficient compared to sampling techniques [44] and are convenient with sufficient accuracy

[57, 58]. Solutions to the problem of information redundancy obtained with closely spaced sensors are presented by introducing a correlation to the prediction error covariance matrix [57].

Several optimization models have also been developed for multi objective decision-making problems. In [59], OSP is formulated as a multi-objective problem for model selection using the Pareto front concept. Yuen and Kuok [30] present a sequential algorithm for the multi-type sensor placement problem. More recently, OSP has been concerned from the perspective of decision-making using the value of information [60–62]. Mehrjoo et al. [63] considered sensor installation cost in the design of the optimal sensor configuration for parameter estimation and virtual sensing. Colombo et al. [64] presented a multi-objective OSP that minimizes the cost.

Some research has studied the effect of excitation characteristics, since the design of the optimal sensor configuration depends on the location, intensity, and frequency content of the inputs. Yuen and Katafygiotis considered the issue of unknown excitations [33] in OSP for parameter identification. The design of optimal input characteristics for nonlinear models is investigated in [39].

Developments on Bayesian OED paved the way for progress in robust OED studies to make the experimental set-up insensitive to modelling and input uncertainties. Bayesian OSP is implemented by considering the influence of measurement noise [65] and prediction error [66], uncertainties in the prior and nuisance parameters [67]. For the purpose of response prediction, OSP techniques have been presented by considering uncertain [38] loads. Additionally, some studies developed robust OED techniques considering the sensor failure [68].

Despite the theoretical developments on OED, the computational cost to perform the optimization is still a challenge. Various algorithms are available to solve optimization problem. Reviews of computational challenges in Bayesian OED exist in the literature [40, 69, 70]. Among others, heuristic search methods and genetic algorithms (GA) provide computationally effective near optimal solutions.

1.2 Research Objectives

The main objective of the research presented in this thesis is to develop novel Bayesian optimal experimental design methods in order to define the most informative and effective test campaigns to improve and validate models and perform reliable model-based predictions. Fur-

thermore, it aims developing OED strategies to be robust to uncertainties arising from experimental conditions, and environmental and manufacturing variabilities. In Fig. 1.1 the overall OED concept with methods of analysis, type of analysis, design varaibles and applications is shown.

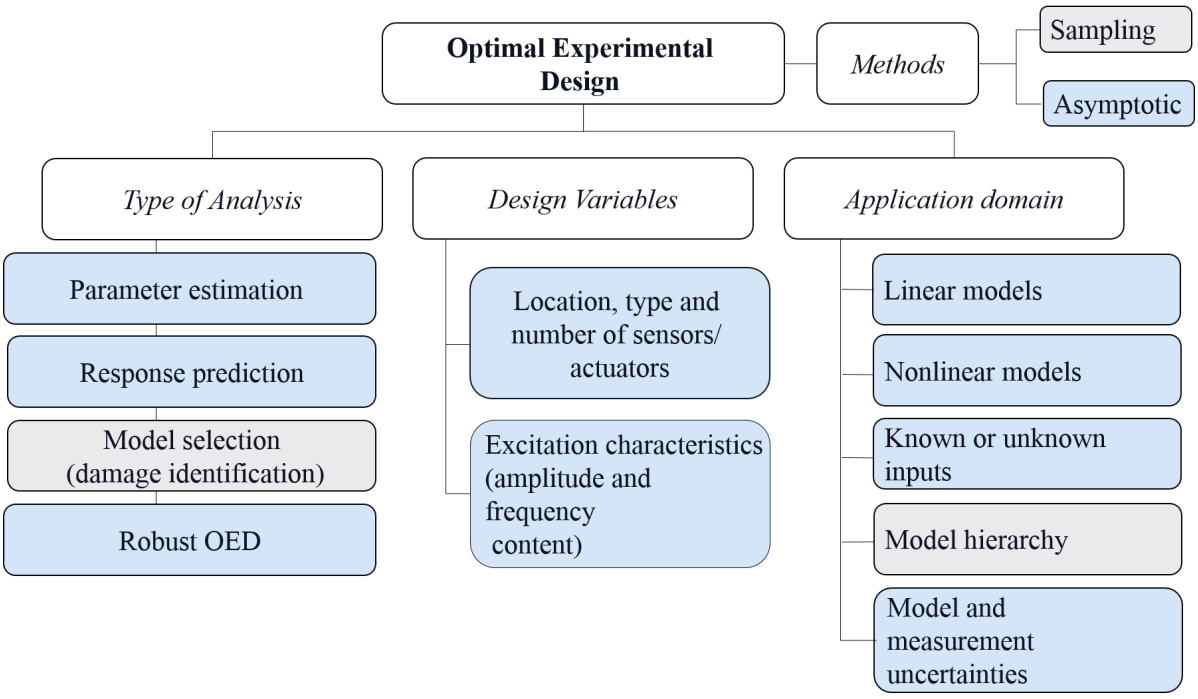

Fig. 1.1. A schematic representation of the optimal experimental design framework. The subjects that are explored in this thesis are shown in blue.

Major accomplishments of the thesis are as follows.

- Development of a comprehensive Bayesian OED framework with software tools to maximize the quality of experimental data used to improve models and model-based predictions.
- Extension of the framework for robustness to the uncertainties arising from experimental conditions, environmental, and manufacturing variabilities considering the measurement and model errors, input and prior distribution uncertainties.
- Provide a framework that can be used for nonlinear models of systems, considering the different kind of inputs and their uncertainties.
- Addressing the challenges in computational effort of optimization due to the complexity of the computational models by integrating heuristic tools, GA, and parallel computing

strategies.

- Demonstration and validation of the developed methods using virtual examples and laboratory experiments on components of full-scale industrial structures.

1.3 Contributions and Organization of the Thesis

The current work presents an efficient theoretical OED framework to support decision-making related to the selection of the type, location, and number of sensors that provide the most informative data for parameter estimation of models structures and also for reliable response predictions. It addresses the problem of reconstructing responses for the case of linear models of structures and output-only vibration measurements. Also it addresses the problem of parameter estimation of nonlinear models of structures. The developed methods enable the maximization of information in the data and allow narrowing the uncertainties in the predictions and/or the parameter estimates. Modeling and input uncertainties are taken into consideration, leading to a cost-effective and robust OED. Optimization of the dynamic characteristics of the actuating forces, such as location of actuator(s) and excitation characteristics (amplitude and frequency content), which is specifically important for parameter estimation of nonlinear models of structures are also covered in this study.

Efforts made on the framework have led to a journal [71] and peer-reviewed conference papers [72–74]. Additionally, a paper has been submitted for review and possible publication [75].

Chapter 1 introduces the background and motivation of Bayesian OED, highlighting the contributions and clarifying the organization of the present work. The novel theoretical developments in this thesis are presented in Chapter 2 to 4, while in Chapter 5 part of these developments are applied on components of energy related and industrial structures. A detailed chapter-by-chapter overview is given below.

Chapter 2. Optimal Sensor Placement for Reliable Virtual Sensing Using Modal Expansion and Information Theory

(https://doi.org/10.3390/s21103400, Published in Sensors)

Chapter 2 presents a novel Bayesian OED framework for response reconstruction/virtual sens-

ing for linear models of structures using output-only vibration measurements by combining the modal expansion technique for response predictions and information theory for measuring the information in the data. Informative mathematical expressions for the utility function are derived using the Gaussian nature of the response QoI and its linear relationship with the modal coordinates. The utility function to be optimized is shown to be independent of the data, which allows performing the OSP in the experimental design phase. A plate FE model is used to demonstrate the methodology by designing the optimal location of the strain or displacement sensors. The effect of model, prediction, and measurement errors and their uncertainties, as well as the prior uncertainties in the modal coordinates, on the information gained from the data and selection of the optimal sensor configuration are discussed. The importance of robustness to modeling errors and other uncertainties is pointed out. The effect of the Finite element (FE) mesh size and the spatial correlation in model error on the information gain and the optimal sensor configuration is investigated. Heuristic forward and backward sequential sensor placement (SSP) strategies are combined to obtain a more reliable estimate of near-optimal sensor locations. The effectiveness of the proposed OSP methodology is shown for reliable strain response reconstruction that are important for providing data-driven safety and performance estimates of systems, and predicting fatigue damage accumulation.

Chapter 3. Information Theoretic-Based Optimal Sensor Placement for Virtual Sensing using Augmented Kalman Filtering

(https://doi.org/10.5281/zenodo.6508382, Submitted for review and possible publication to Mechanical Systems and Signal Processing (MSSP))

Chapter 3 extends the Bayesian OED framework presented in Chapter 2, with the use of the filtering methods for virtual sensing. In contrast to modal expansion techniques used in Chapter 2, filtering techniques allows to fuse different types of sensors (e.g. acceleration, displacement and strain sensors) and extends the OED for response and input reconstruction. Following the framework in Chapter 2, a novel OSP framework is presented for reliable response and input prediction based on the augmented Kalman filtering (AKF) technique for input-state-response estimation and information theory for measuring the information in the data. The utility function that quantifies the expected information gained from the data is built using the KL-div measure of the information gain provided from a sensor configuration, AKF equations and the Gaussian nature of the response QoI. The utility function is taken as the expected infor-

mation gain over all possible data that would arise under all possible input realizations. The optimal sensor configuration is obtained by maximizing the utility function. To solve the optimization problem, heuristic forward and backward SSP strategies are combined in a way to overcome the large computational expense that may arise due to the large size of optimization domain, without sacrificing accuracy. GA are used as an alternative to the heuristic SSP algorithms. The effectiveness of the framework is presented by using a FE model of a plate and designing the optimal sensor configuration for reliable input and response reconstruction by fusing different types of sensors. The importance of rationally selecting the measurement and model/prediction errors and their uncertainties, as well as the input uncertainties, is highlighted.

Chapter 4. Bayesian Optimal Experimental Design for Parameter Estimation Under Modeling and Loading/Input Uncertainty

Chapter 4 introduces the Bayesian OED for parameter estimation of nonlinear models of structures using input-output vibration measurements and considering modeling and input uncertainties. The utility function is built from the appropriate measures of information in the data. The information gain from a sensor configuration is quantified using KL-div between the prior and posterior distributions of the model parameters. For a large number of data, asymptotic approximations are proposed for estimating part of the multidimensional integrals arising in the utility formulation in terms of the sensitivities of model responses at the measured locations with respect to the model parameters to be estimated. The uncertainties in nuisance (non-inferred or non-updatable) parameters are also considered by estimating the expected utility value over all possible values of the nuisance parameters. In particular, the formulation handles the case where the input loads on the structure, assumed to be measured during the inference process, are actually unknown at the experimental design phase. An example is the inference of the model parameters of civil infrastructure during earthquake excitation. The seismic loads are often measured using properly installed sensors. However, at the OED phase they are unknown and are modelled by available stochastic processes. The OSP is then performed by maximizing the expected utility function over all possible realizations of the stochastic input. The effectiveness of the method is demonstrated for a system involving restoring force nonlinearities represented by the Bouc-Wen model. The OED is also extended to consider as design variables the location of actuators and/or the characteristics of the excitation (amplitude vari-

ation and frequency content). Different types of inputs including white noise, filtered white noise and harmonic inputs are used and the influence of their uncertainties to OED is explored. The computational burden and excessive storage requirements are pointed out. Based on the results of the analysis, remedies are provided for reducing the high computational cost and the storage requirements.

Chapter 5. Optimal Sensor Placement for Virtual Sensing: Applications to Wind Turbine and Helicopter Blade

Chapter 5 demonstrates the OED applications for reliable response predictions (acceleration, displacement, and strain) under unknown excitation using output-only vibration measurements on components of two energy-related and industrial examples: a wind turbine blade and a helicopter blade. It demonstrates and validates the optimal sensor placement tools proposed in Chapters 2 and 3 for the two laboratory examples using synthetic and available experimental data under the existence of modelling errors and uncertainties in loads and environmental or operating conditions.

Chapter 6 summarizes the conclusions of this dissertation, providing also future research directions.

1.4 References

[1] J. I. Myung and M. A. Pitt. Optimal experimental design for model discrimination. *Psychological review*, 116(3):499, 2009.

[2] E. Balsa-Canto, A. A. Alonso, and J. R. Banga. Computational procedures for optimal experimental design in biological systems. *IET systems biology*, 2(4):163–172, 2008.

[3] X. Wang, N. Rai, B. Merchel Piovesan Pereira, A. Eetemadi, and I. Tagkopoulos. Accelerated knowledge discovery from omics data by optimal experimental design. *Nature communications*, 11(1):1–9, 2020.

[4] A. R. Cook, G. J. Gibson, and C. A. Gilligan. Optimal observation times in experimental epidemic processes. *Biometrics*, 64(3):860–868, 2008.

[5] M. Chatzimanolakis, P. Weber, G. Arampatzis, D. Wälchli, I. Kičić, P. Karnakov, C. Pa-

padimitriou, and P. Koumoutsakos. Optimal allocation of limited test resources for the quantification of covid-19 infections. *Swiss Medical Weekly*, 150:w20445, 2020.

[6] D. J. Willis, C. Niezrecki, D. Kuchma, E. Hines, S. R. Arwade, R. J. Barthelmie, M DiPaola, P. J. Drane, C. J. Hansen, M. Inalpolat, et al. Wind energy research: State-of-the-art and future research directions. *Renewable Energy*, 125:133–154, 2018.

[7] D. J. Augustyn. *Towards offshore wind digital twins: Application to jacket substructures*. PhD thesis, 2022.

[8] M. Song, S. Christensen, B. Moaveni, A. Brandt, and E. Hines. Joint parameter-input estimation for virtual sensing on an offshore platform using output-only measurements. *Mechanical Systems and Signal Processing*, 170:108814, 2022.

[9] C. Papadimitriou, C. P. Fritzen, P. Kraemer, and E. Ntotsios. Fatigue predictions in entire body of metallic structures from a limited number of vibration sensors using Kalman filtering. *Structural Control and Health Monitoring*, 18(5):554–573, 2011.

[10] K. Maes, A. Iliopoulos, W. Weijtjens, C. Devriendt, and G. Lombaert. Dynamic strain estimation for fatigue assessment of an offshore monopile wind turbine using filtering and modal expansion algorithms. *Mechanical Systems and Signal Processing*, 76:592–611, 2016.

[11] H. P. Hjelm, R. Brincker, J. Graugaard-Jensen, and K. Munch. Determination of stress histories in structures by natural input modal analysis. In *Proceedings of the 23rd International Modal Analysis Conference,IMAC*, pages 838–844, 2005.

[12] A. Iliopoulos, R. Shirzadeh, W. Weijtjens, P. Guillaume, D. Van Hemelrijck, and C. Devriendt. A modal decomposition and expansion approach for prediction of dynamic responses on a monopile offshore wind turbine using a limited number of vibration sensors. *Mechanical Systems and Signal Processing*, 68:84–104, 2016. ISSN 10961216.

[13] P. Pingle and P. Avitabile. Full-field dynamic stress/strain from limited sets of measured data. *Sound and Vibration*, 2(8):187–200, 2011.

[14] P. Avitabile, E. Harvey, and J. Ruddock. Comparison of full field strain distributions to

predicted strain distributions from limited sets of measured data for SHM applications. *Key Engineering Materials*, 569-570:1140–1147, 2013.

[15] J. Kullaa. Bayesian virtual sensing in structural dynamics. *Mechanical Systems and Signal Processing*, 115:497–513, 1 2019.

[16] E. Lourens, E. Reynders, G. De Roeck, G. Degrande, and G. Lombaert. An augmented kalman filter for force identification in structural dynamics. *Mechanical systems and signal processing*, 27:446–460, 2012.

[17] S. E. Azam, E. Chatzi, and C. Papadimitriou. A dual kalman filter approach for state estimation via output-only acceleration measurements. *Mechanical systems and signal processing*, 60:866–886, 2015.

[18] F. Naets, J. Cuadrado, and W. Desmet. Stable force identification in structural dynamics using kalman filtering and dummy-measurements. *Mechanical Systems and Signal Processing*, 50:235–248, 2015.

[19] V. K. Dertimanis, E. N. Chatzi, S. E. Azam, and C. Papadimitriou. Input-state-parameter estimation of structural systems from limited output information. *Mechanical Systems and Signal Processing*, 126:711–746, 2019.

[20] M. Impraimakis and A. W. Smyth. An unscented kalman filter method for real time input-parameter-state estimation. *Mechanical Systems and Signal Processing*, 162:108026, 2022.

[21] C. Papadimitriou and C. Argyris. Bayesian optimal experimental design for parameter estimation and response predictions in complex dynamical systems. In *Procedia Engineering*, volume 199, pages 972–977. Elsevier Ltd, 2017.

[22] E. M. Hernandez. Efficient sensor placement for state estimation in structural dynamics. *Mechanical Systems and Signal Processing*, 85:789–800, 2017.

[23] Z. Peng, K. Dong, and H. Yin. A modal-based Kalman filter approach and OSP method for structural response reconstruction. *Shock and Vibration*, 2019, 2019.

[24] S. Vettori, E. Di Lorenzo, R. Cumbo, U. Musella, T. Tamarozzi, B. Peeters, and E. Chatzi. Kalman-based virtual sensing for improvement of service response replication in environmental tests. In *Model Validation and Uncertainty Quantification, Volume 3*, pages 93–106. Springer, 2020.

[25] R. Cumbo, L. Mazzanti, T. Tamarozzi, P. Jiranek, W. Desmet, and F. Naets. Advanced optimal sensor placement for kalman-based multiple-input estimation. *Mechanical Systems and Signal Processing*, 160:107830, 2021.

[26] T. Tamarozzi, E. Risaliti, W. Rottiers, K Janssens, and W Desmet. Noise, ill-conditioning and sensor placement analysis for force estimation through virtual sensing. In *International Conference on Noise and Vibration Engineering (ISMA2016)*, pages 1741 – 1756, Leuven, 2016.

[27] J. L. Beck and L. S. Katafygiotis. Updating models and their uncertainties. i: Bayesian statistical framework. *Journal of Engineering Mechanics*, 124(4):455–461, 1998.

[28] K. V. Yuen and S. C. Kuok. Bayesian methods for updating dynamic models. *Applied Mechanics Reviews*, 64(1), 2011.

[29] C. Papadimitriou. Optimal sensor placement methodology for parametric identification of structural systems. *Journal of Sound and Vibration*, 278(4-5):923–947, 2004.

[30] K. V. Yuen and S. C. Kuok. Efficient Bayesian sensor placement algorithm for structural identification: a general approach for multi-type sensory systems. *Earthquake Engineering & Structural Dynamics*, 44(5):757–774, 2015.

[31] Y. Robert-Nicoud, B. Raphael, and I. F. Smith. Configuration of measurement systems using Shannon's entropy function. *Computers and Structures*, 83(8-9):599–612, 2005.

[32] H. Ebrahimian, R. Astroza, J. P. Conte, and R. R. Bitmead. Information-theoretic approach for identifiability assessment of nonlinear structural finite-element models. *Journal of Engineering Mechanics*, 145(7):04019039, 2019.

[33] K. V. Yuen, L. S. Katafygiotis, C. Papadimitriou, and N. C. Mickleborough. Optimal sensor placement methodology for identification with unmeasured excitation. *Journal of*

Dynamic Systems, Measurement and Control, Transactions of the ASME, 123(4):677–686, 2001.

[34] N. J. Bertola, S. G. Pai, and I. F. Smith. A methodology to design measurement systems when multiple model classes are plausible. *Journal of Civil Structural Health Monitoring*, 11(2):1–22, 2021. ISSN 2190-5479.

[35] S. Q. Ye and Y. Q. Ni. Information entropy based algorithm of sensor placement optimization for structural damage detection. *Smart Structures and Systems*, 10(4_5):443–458, 2012. ISSN 17381991. doi: 10.12989/sss.2012.10.4_5.443.

[36] T. Yin, H. F. Lam, and H. M. Chow. A Bayesian probabilistic approach for crack characterization in plate structures. *Computer-Aided Civil and Infrastructure Engineering*, 25 (5):375–386, 2010.

[37] G. Capellari, E. Chatzi, S. Mariani, and S. E. Azam. Optimal design of sensor networks for damage detection. *Procedia engineering*, 199:1864–1869, 2017.

[38] C. Papadimitriou, Y. Haralampidis, and K. Sobczyk. Optimal experimental design in stochastic structural dynamics. *Probabilistic Engineering Mechanics*, 20(1):67–78, 2005.

[39] P. Metallidis, G. Verros, S. Natsiavas, and C. Papadimitriou. Fault detection and optimal sensor location in vehicle suspensions. *Journal of Vibration and Control*, 9(3-4):337–359, 2003.

[40] R. J. Barthorpe and K. Worden. Emerging trends in optimal structural health monitoring system design: From sensor placement to system evaluation. *Journal of Sensor and Actuator Networks*, 9(3):31, 2020.

[41] D. C. Kammer. Sensor placement for on-orbit modal identification and correlation of large space structures. *Journal of Guidance, Control, and Dynamics*, 14(2):251–259, 1991.

[42] D. S. Li, H. N. Li, and C. P. Fritzen. The connection between effective independence and modal kinetic energy methods for sensor placement. *Journal of sound and vibration*, 305 (4-5):945–955, 2007.

[43] T. H. Yi, H. N. Li, and M. Gu. Optimal sensor placement for structural health monitoring based on multiple optimization strategies. *The Structural Design of Tall and Special Buildings*, 20(7):881–900, 2011.

[44] X. Huan and Y. M. Marzouk. Simulation-based optimal Bayesian experimental design for nonlinear systems. *Journal of Computational Physics*, 232(1):288–317, 1 2013.

[45] D. V. Lindley. On a measure of the information provided by an experiment. *The Annals of Mathematical Statistics*, 27(4):986–1005, 1956.

[46] P. Bhattacharyya and J. Beck. Exploiting convexification for Bayesian optimal sensor placement by maximization of mutual information. *Structural Control and Health Monitoring*, 27(10):1–18, 2020.

[47] C. Argyris. *Bayesian uncertainty quantification and optimal experimental design in data driven simulations of engineering systems*. PhD thesis, University of Thessaly, 2010.

[48] C. Papadimitriou, J. L. Beck, and S. K. Au. Entropy-based optimal sensor location for structural model updating. *JVC/Journal of Vibration and Control*, 6(5):781–800, 2000.

[49] C. Stephan. Sensor placement for modal identification. *Mechanical Systems and Signal Processing*, 27(1):461–470, 2012.

[50] N. J. Bertola, M. Papadopoulou, D. Vernay, and I. F. Smith. Optimal multi-type sensor placement for structural identification by static-load testing. *Sensors*, 17:2904, 2017.

[51] M. Papadopoulou, B. Raphael, I. F. Smith, and C. Sekhar. Hierarchical sensor placement using joint entropy and the effect of modeling error. *Entropy*, 16(9):5078–5101, 2014.

[52] K. Chaloner and I. Verdinelli. Bayesian experimental design: A review. *Statistical Science*, 10(3):273–304, 1995.

[53] F. E. Udwadia. Methodology for optimum sensor locations for parameter identification in dynamic systems. *Journal of Engineering Mechanics*, 120(2):368–390, 1994.

[54] E. Heredia-Zavoni and L. Esteva. Optimal instrumentation of uncertain structural systems subject to earthquake ground motions. *Earthquake engineering & structural dynamics*, 27(4):343–362, 1998.

[55] E. B. Flynn and M. D. Todd. A bayesian approach to optimal sensor placement for structural health monitoring with application to active sensing. *Mechanical Systems and Signal Processing*, 24(4):891–903, 2010.

[56] F. Igea, M. N. Chatzis, and A. Cicirello. On the investigation of utility functions on optimal sensor locations. In *Conference on Uncertainty Quantification in Computational Sciences and Engineering*, volume 28, page 30, 2021.

[57] C. Papadimitriou, E. M. Lourens, G. Lombaert, G. De Roeck, and K. Liu. Prediction of fatigue damage accumulation in metallic structures by the estimation of strains from operational vibrations. In *Life-Cycle and Sustainability of Civil Infrastructure Systems - Proceedings of the 3rd International Symposium on Life-Cycle Civil Engineering, IALCCE*, pages 304–310, 2012.

[58] D. I. Papadimitriou and C. Papadimitriou. Optimal Sensor Placement for the Estimation of Turbulence Model Parameters in CFD. *International Journal for Uncertainty Quantification*, 5(6):545–568, 2015.

[59] C. Papadimitriou. Pareto optimal sensor locations for structural identification. *Computer Methods in Applied Mechanics and Engineering*, 194(12-16):1655–1673, 4 2005.

[60] C. Malings and M. Pozzi. Value of information for spatially distributed systems: Application to sensor placement. *Reliability Engineering and System Safety*, 154:219–233, 2016.

[61] C. Malings and M. Pozzi. Submodularity issues in value-of-information-based sensor placement. *Reliability Engineering and System Safety*, 183:93–103, 2019.

[62] S. Cantero-Chinchilla, J. Chiachío, M. Chiachío, D. Chronopoulos, and A. Jones. Optimal sensor configuration for ultrasonic guided-wave inspection based on value of information. *Mechanical Systems and Signal Processing*, 135:106377, 2020.

[63] A. Mehrjoo, M. Song, B. Moaveni, C. Papadimitriou, and E. Hines. Optimal sensor placement for parameter estimation and virtual sensing of strains on an offshore wind turbine considering sensor installation cost. *Mechanical Systems and Signal Processing*, 169:108787, 2022.

[64] L. Colombo, M. D. Todd, C. Sbarufatti, and M. Giglio. On statistical multi-objective optimization of sensor networks and optimal detector derivation for structural health monitoring. *Mechanical Systems and Signal Processing*, 167:108528, 2022.

[65] G. Capellari, E. Chatzi, and S. Mariani. An optimal sensor placement method for shm based on bayesian experimental design and polynomial chaos expansion. In *European Congress on Computational Methods in Applied Sciences and Engineering*, pages 6272–6282. National Technical University of Athens (NTUA), 2016.

[66] C. Argyris, S. Chowdhury, V. Zabel, and C. Papadimitriou. Bayesian optimal sensor placement for crack identification in structures using strain measurements. *Structural Control and Health Monitoring*, 25(5):2137, 5 2018.

[67] C. Argyris and C. Papadimitriou. Bayesian optimal experimental design using asymptotic approximations. In *Proceedings of the 35th International Modal Analysis Conference, IMAC*, volume 3, pages 273–275, 2017.

[68] K. V. Yuen, X. H. Hao, and S. C. Kuok. Robust sensor placement for structural identification. *Structural Control and Health Monitoring*, 29(1):e2861, 2022.

[69] T. H. Yi and H. N. Li. Methodology developments in sensor placement for health monitoring of civil infrastructures. *International Journal of Distributed Sensor Networks*, 8(8): 612726, 2012.

[70] E. G. Ryan, C. C. Drovandi, J. M. McGree, and A. N. Pettitt. A review of modern computational algorithms for bayesian optimal design. *International Statistical Review*, 84(1):128–154, 2016.

[71] T. Ercan and C. Papadimitriou. Optimal Sensor Placement for Reliable Virtual Sensing Using Modal Expansion and Information Theory. *Sensors*, 21(10):3400, 2021. doi: doi.org/10.3390/s21103400.

[72] T. Ercan, P. Koumoutsakos, and C. Papadimitriou. Robust Bayesian optimal sensor placement for model parameter estimation and response predictions. In *Proceedings of the International Conference on Structural Dynamics, EURODYN*, volume 2, pages 3904–3910, 2020.

[73] T. Ercan, O. Sedehi, C. Papadimitriou, and L. S. Katafygiotis. Robust optimal sensor placement for response reconstruction using output only vibration measurements. In *Proceedings of the 29th European Safety and Reliability Conference, ESREL*, pages 1270–1276. Research Publishing Services, 2019.

[74] T. Ercan and C. Papadimitriou. Optimal Experimental Design Methodology for Parameter Estimation of Nonlinear Models. In *Proceedings of 10th International Conference on Structural Health Monitoring of Intelligent Infrastructure, SHMII 10*, pages 689–693. Universidade do Porto, 2021.

[75] T. Ercan, O. Sedehi, L. S. Katafygiotis, and C. Papadimitriou. Information theoretic-based optimal sensor placement for virtual sensing using augmented kalman filtering, Submitted to MSSP, 2022.

Chapter 2. Optimal Sensor Placement for Reliable Virtual Sensing Using Modal Expansion and Information Theory

Original paper: T. Ercan and C. Papadimitriou. Optimal Sensor Placement for Reliable Virtual Sensing Using Modal Expansion and Information Theory, Sensors (2021).
https://doi.org/10.3390/s21103400

ABSTRACT

A framework for optimal sensor placement (OSP) for virtual sensing using the modal expansion technique and taking into account uncertainties is presented based on information and utility theory. The framework is developed to handle virtual sensing under output-only vibration measurements. The OSP maximizes a utility function that quantifies the expected information gained from the data for reducing the uncertainty of quantities of interest (QoI) predicted at the virtual sensing locations. The utility function is extended to make the OSP design robust to uncertainties in structural model and modeling error parameters, resulting in a multidimensional integral of the expected information gain over all possible values of the uncertain parameters and weighted by their assigned probability distributions. Approximate methods are used to compute the multidimensional integral and solve the optimization problem that arises. The Gaussian nature of the response QoI is exploited to derive useful and informative analytical expressions for the utility function. A thorough study of the effect of model, prediction and measurement errors and their uncertainties, as well as the prior uncertainties in the modal coordinates on the selection of the optimal sensor configuration is presented, highlighting the importance of accounting for robustness to errors and other uncertainties.

2.1 Introduction

Virtual sensing is used to complement the physical sensing when the direct observations are not available in field and laboratory experiments. Virtual sensing is accomplished by combining the information in output-only vibration measurements with the information contained in a model (usually a finite element model) of the system to predict response time histories

of various quantities of interest (QoI). The subject of virtual sensing, also known as response reconstruction, has received a lot of attention recently due to its importance in monitoring critical performance and safety-related quantities such as accelerations, displacements, structural shapes, interstory drifts, strains/stresses and fatigue damage accumulation in structures that operate in a dynamic environment.

Filtering techniques for input, state and parameter estimation as well as modal expansion techniques for response reconstruction are the two type of methods extensively used in the literature for virtual sensing and response reconstruction. The optimal sensor placement techniques developed in this work are based on modal expansion techniques for virtual sensing. The modal expansion technique represents the system response QoI (acceleration, displacement, strain, etc.) as a modal superposition involving the modeshapes of the structure (e.g., displacement or strain modeshapes) and a fixed number of modal coordinates. This allows the prediction (virtual sensing) of any response QoI by estimating the temporal variability of the modal coordinates from measured response time histories and borrowing the information from a finite element model for representing the rest of the quantities involved in the modal expansion. The modal expansion method has been used in structural dynamics for reconstructing stress/strain fields using limited number of acceleration measurements [1] or displacement/strain measurements [2–4]. It is pointed out that estimating the strains/stresses is important for fatigue damage identification. The potential of providing fatigue damage accumulation predictions in the entire body of metallic structures based on virtual strain/stress sensing has been demonstrated for the first time in [5, 6] by combining output-only vibration measurements, finite element models and filtering techniques with stochastic and deterministic fatigue theories. Such predictions are based on the actual operating conditions of structures and thus provide realistic fatigue estimates consistent with existing fatigue theories.

Following these works, the modal expansion and filtering techniques were applied for strain/stress virtual sensing [3, 7–15] and fatigue estimation [16–21] for a number of structures using limited number of displacement/strain physical sensors. In particular, modal expansion techniques have been used in mechanical and aerospace systems for shape and/or strain reconstruction using sparse displacement and/or strain measurements [22–29] or fusing acceleration and strain measurements [30]. The aforementioned studies cover a number of applications, including components of mechanical structures [1, 2], components of civil structures such as railway bridges [20], wind turbine jacket substructures [11], truss structures [12], wind turbine

towers [7–10, 16, 25], wind turbine blades [27, 28], offshore structures [11], components of industrial structures [17, 21], roller coaster [18], rotating [26] and underwater structures [13], as well as biologicaly inspired wing structures for robotic applications [29]. Recently, it is suggested to use virtual sensing in isolated linear components of linear and nonlinear models of structures [31–34] considering the forces at the interface between the analyzed linear component and the rest of the structure as unknown forces. In a limited number of past studies the effect of the number and location of sensors, as well as the measurement error, on the accuracy of the response reconstruction was investigated and its importance was pointed out [2, 22–24, 35].

Bayesian methods were applied for modal identification and virtual sensing using modal expansion techniques to better account for the model and measurement errors in the modal coordinates estimation [36] and response predictions [37–39] and also used for damage detection [40–42]. Such methods have the advantage of predicting also the uncertainty in the modal coordinates and/or predictions. In particular, the uncertainty formulation is useful for optimizing the location and number of sensors by minimizing the uncertainty in the estimates of the modal coordinates [36] and response predictions or virtual sensing [38, 43, 44].

OSP techniques have been developed in the past for the purpose of extracting the most informative data from a given number of sensors. A recent article [45] reviews methods and optimization algorithms for optimizing the location of sensor in a structure. Selecting the most informative sensor configuration is often performed using information theory based approaches. Measures of information that have been used in the past for structural dynamics problems include the Fisher information matrix (FIM) [46–51], the information entropy [52–64], the joint entropy [65, 66], the expected Kullback–Liebler divergence (KL-div) index [67–69] and mutual information [70, 71], and the value of information [72–74]. FIM-based OSP techniques address problems of parameter estimation of physics-based models for linear structural systems [46–48], modal estimation [51], as well as identification of distributed parameter systems [49, 50]. The OSP techniques based on information and joint entropy address problems of parameter estimation of linear systems subjected to known [54–56, 63, 64] and unknown [53] excitation, model updating [52, 61], modal identification [59], model selection [58], structural health monitoring and damage detection [60, 62]. In particular, techniques to avoid sensor clustering by taking into account the redundant information contained in the measurements have been discussed in [57, 59]. OSP approaches based on expected KL-div

and utility theory also address problems of parameter estimation of linear [70, 75–77] and nonlinear [78] structural systems, modal estimation [71, 79] and structural health monitoring [80, 81]. Finally, OSP issues related to multi-type sensor placement have also been addressed [56, 65]. The aforementioned methods, however, have focused on OSP problems for parameter estimation of physics-based or mathematical models. Using information theory formulations, the OSP problem for response reconstruction has been studied recently considering that the input forces are known [38, 44]. OSP for response reconstruction under unknown input forces modeled by stochastic processes has been attempted in [82] using the kriging technique. An OSP formulation to handle the case of output-only vibration measurements has also been presented recently by combining filtering techniques with information theory [43].

In this work, considering output-only vibration measurements, a novel OSP framework is presented for accurate response reconstruction and virtual sensing in linear systems based on modal expansion techniques and information theory. The information gained by a sensor configuration is measured by the KL-div [83] between the posterior and prior probability distribution of the response QoI to be virtually sensed or reconstructed, by combining available modal expansion techniques and data. The KL-div is averaged over all possible QoI to be sensed. This is obtained using the Lindley's utility function [68, 84] quantifying the average information in the data over all possible measurements generated by the prediction error model. The measure is extended to include uncertainties in the model parameters, as well as in the model/prediction and measurement errors which are assigned in the modeling process for the Bayesian estimation of the posterior distribution of the modal coordinates. The optimal sensor configuration is obtained by maximizing the utility function. For the case of uncertainties in model parameters, the utility function involves a multidimensional integral over the uncertain parameter space which can be computed using sparse grid or Monte Carlo techniques. Due to the linearity of the response QoI and the modal coordinates, exact analytical expressions are developed for the utility function in terms of the variance of the responses of the QoI to be sensed. The structure of the analytical expressions developed are used to derive useful formulas that show the effect of measurements and model/prediction errors on the expected information gained from the data, as well as derive the dependence of the information gain as a function of the number of sensors.

This study is organized as follows: in Section 2.2, the modal expansion is outlined for formulating the uncertainty in the predictions of response QoI. In Section 2.3, the optimal

sensor placement methodology for predicting response time histories of desirable QoI (virtual sensing) with the least uncertainty is presented based on utility and information theory. In Section 2.4, models for the model/prediction and measurement errors required in the formulation are introduced. Section 2.5 discusses implementation issues and the importance of taking into account the uncertainties in the input characteristics for optimizing the sensor placement. An application on a square plate structure is used in Section 2.6 to demonstrate the capabilities and effectiveness of the OSP methodology for reliable virtual sensing. Conclusions are drawn in Section 2.8.

2.2 Bayesian Virtual Sensing Using the Modal Expansion Method

Consider a structural model used to predict the temporal variability of the response vector $\underline{z}(t;\underline{\varphi}) \in R^{n_z}$ (e.g., accelerations, displacements, strain or stresses) at n_z locations given the values of a structural model parameter set $\underline{\varphi}$ (e.g., stiffness, mass and damping related parameters) and the excitation vector $\underline{u}\,(t) \in R^{n_u}$. Let $D = \left\{\underline{y}(t) \in R^{N_0}\right\}$ be the vector of response time history data collected by placing N_0 sensors in the structure. These data depend on the sensor configuration vector $\underline{\delta} \in R^{N_0}$ indicating the location and measurement direction of sensors placed in a structure. The data may consist of either acceleration, displacement and strain measurements. In what follows, a linear model of the structure is assumed. Additionally, it is assumed that the excitation time histories $\underline{u}\,(t)$ are not available.

2.2.1 Modal Expansion for Virtual Sensing

Given output-only data $\underline{y}\,(t)$, the modal expansion technique is used to predict responses at measured and unmeasured output QoI $\underline{z}(t;\underline{\varphi})$ using modal coordinates and mode shape vectors. Based on the modal expansion technique, the measured displacement or strain response time histories at N_0 degrees of freedom (DOFs) are given with respect to the modal coordinates by the mode superposition equation

$$\underline{y}(t) = L(\underline{\delta})\Phi(\underline{\varphi})\underline{\xi}(t) + \underline{e}(t) \tag{2.1}$$

where $\underline{\xi}(t) \in R^m$ is the vector of m modal coordinates satisfying the modal equations, $L(\underline{\delta}) \in R^{N_0 \times n}$ is the observation matrix that maps the displacements at all n model DOF

to the measured displacement or strain quantities indicated by the sensor location vector $\underline{\delta}$, $\Phi(\underline{\varphi}) \in R^{n\times m}$ is the displacement mode shape matrix corresponding to the n model DOF and m contributing modes, and $\underline{e}\,(t)$ is a multi-variable zero-mean Gaussian noise term with covariance matrix Q_e that accounts for measurement and model errors. The modal can be written as

$$\ddot{\underline{\xi}}(t) + Z(\underline{\varphi})\dot{\underline{\xi}}(t) + \Lambda(\underline{\varphi})\underline{\xi}(t) = \Phi^T(\underline{\varphi})M\underline{u}(t) \tag{2.2}$$

where Λ is the diagonal matrix of the squares ω_r^2 of the modal frequencies ω_r, Z is the diagonal matrix with the r-th diagonal element equal to $2\omega_r\zeta_r$, ζ_r is the modal damping ratio, and $M \in R^{n\times n_u}$ is a matrix of zeros and ones associating the independent excitations in the vector $\underline{u}(t)$ to the DOF of the structural model. Displacement, strain and/or stress predictions at output locations or DOF are given by the prediction equation

$$\underline{z}(t) = \Psi(\underline{\varphi})\underline{\xi}(t) + \underline{\varepsilon}(t) \tag{2.3}$$

where $\Psi(\underline{\varphi}) \in R^{n_z\times m}$ are the corresponding displacement, strain and/or stress mode shapes that relates the modal coordinates to displacement, strain and/or stress QoI, and $\underline{\varepsilon}\,(t)$ is a zero-mean prediction error with covariance matrix Q_ε accounting for model error. The mode shape matrices $\Phi(\underline{\varphi})$ and $\Psi(\underline{\varphi})$ are available by analyzing the model (e.g., finite element model) of the structure.

It should be noted that formulation using Eq. 2.1 and Eq. 2.3 can also be used when the available measurements and predictions consist of accelerations. In this case the modal vector $\underline{\xi}\,(t)$ in Eq. 2.1 and Eq. 2.3 refers to the second derivatives of the modal coordinates with respect to time.

2.2.2 Bayesian Virtual Sensing

Bayesian inference is next used to estimate the modal vector parameter $\underline{\xi}(t) \equiv \underline{\xi}(t;\underline{\delta},\underline{\varphi})$ and its uncertainties based on the data collected from a sensor configuration $\underline{\delta}$ and then propagate these uncertainties to predictions of output QoI $\underline{z}(t) \equiv \underline{z}(t;\underline{\delta},\underline{\varphi})$. The posterior probability distribution function (PDF) $p\left(\underline{\xi}(t)|\underline{y}(t),\underline{\delta},\underline{\varphi}\right)$ quantifying the uncertainty in the modal coordinates $\underline{\xi}(t)$ at time t, given the data $\underline{y}(t)$, the sensor configuration $\underline{\delta}$ and the model parameters

$\underline{\varphi}$, takes the form

$$p\left(\underline{\xi}(t)|\underline{y}(t),\underline{\delta},\underline{\varphi}\right) \propto p\left(\underline{y}(t)|\underline{\xi}(t),\underline{\delta},\underline{\varphi}\right)\ p\left(\underline{\xi}(t)|\underline{\varphi}\right) \tag{2.4}$$

where, using the assumption that $\underline{e}(t)$ in Eq. 2.1 follows a Gaussian distribution $N(\underline{e}(t)|\underline{0},Q_e)$ with mean $\underline{0}$ and covariance Q_e, the likelihood takes the form

$$p\left(\underline{y}(t)|\underline{\xi}(t),\underline{\delta},\underline{\varphi}\right) = N\left(\underline{y}(t)|L(\underline{\delta})\Phi(\underline{\varphi})\underline{\xi}(t),Q_e\right) \tag{2.5}$$

The prior PDF $p(\underline{\xi}(t)|\underline{\varphi})$ is postulated to be a zero-mean Gaussian $p\left(\underline{\xi}\left(t\right)|\underline{\varphi}\right) = N\left(\underline{\xi}\left(t\right)|\underline{0},S\right)$ with covariance matrix S. Substituting Eq. 2.5 into Eq. 2.4 it is straightforward to show that the output modal coordinates follow a multi-variable normal distribution [37, 43]

$$p\left(\underline{\xi}(t)|\underline{y}(t),\underline{\delta},\underline{\varphi}\right) = N\left(\underline{\xi}(t)|\hat{\underline{\xi}}(t;\underline{\delta},\underline{\varphi}),\Sigma_{\xi|D}(\underline{\delta},\underline{\varphi})\right) \tag{2.6}$$

with mean

$$\hat{\underline{\xi}}(t;\underline{\delta},\underline{\varphi}) = \left[\Phi^T(\underline{\varphi})L^T(\underline{\delta})Q_e^{-1}(\underline{\delta},\underline{\varphi})L(\underline{\delta})\Phi(\underline{\varphi}) + S^{-1}\right]^{-1}\Phi^T(\underline{\varphi})L^T(\underline{\delta})Q_e^{-1}(\underline{\delta},\underline{\varphi})\underline{y}(t) \tag{2.7}$$

and covariance matrix

$$\Sigma_{\xi|D}(\underline{\delta},\underline{\varphi}) = \left[\Phi^T(\underline{\varphi})L^T(\underline{\delta})Q_e^{-1}(\underline{\delta},\underline{\varphi})L(\underline{\delta})\Phi(\underline{\varphi}) + S^{-1}\right]^{-1} \tag{2.8}$$

Using Eq. 2.3 and Eq. 2.6 to propagate uncertainty to output QoI $\underline{z}(t)$, it can be readily obtained that $\underline{z}(t)$ also follows a multivariable normal distribution

$$p\left(\underline{z}(t)|\underline{y}(t),\underline{\delta},\underline{\varphi}\right) = N\left(\underline{z}(t)|\hat{\underline{z}}(t;\underline{\delta},\underline{\varphi}),\Sigma_{z|D}(\underline{\delta},\underline{\varphi})\right) \tag{2.9}$$

with mean

$$\hat{\underline{z}}(t;\underline{\delta},\underline{\varphi}) = \Psi(\underline{\varphi})\ \hat{\underline{\xi}}(t;\underline{\delta},\underline{\varphi}) \tag{2.10}$$

that depends on the data, and covariance matrix $\Sigma_{z|D}(\underline{\delta}, \underline{\varphi})$ given by

$$\Sigma_{z|D}(\underline{\delta}, \underline{\varphi}) = \Psi(\underline{\varphi}) \left[\Phi^T(\underline{\varphi}) L^T(\underline{\delta}) Q_e^{-1}(\underline{\delta}, \underline{\varphi}) L(\underline{\delta}) \Phi(\underline{\varphi}) + S^{-1}\right]^{-1} \Psi^T(\underline{\varphi}) + Q_\varepsilon \tag{2.11}$$

In particular, the variance of the i-th element $z_i(t; \underline{\delta}, \underline{\varphi})$ of the response vector $\underline{z}(t; \underline{\delta}, \underline{\varphi})$ is given by the i-th diagonal element $\Sigma_{z_i|D}(\underline{\delta}, \underline{\varphi})$ of the covariance matrix $\Sigma_{z|D}(\underline{\delta}, \underline{\varphi})$ as follows

$$\Sigma_{z_i|D}(\underline{\delta}, \underline{\varphi}) = \psi_i^T(\underline{\varphi}) \left[\Phi^T(\underline{\varphi}) L^T(\underline{\delta}) Q_e^{-1}(\underline{\delta}, \underline{\varphi}) L(\underline{\delta}) \Phi(\underline{\varphi}) + S^{-1}\right]^{-1} \psi_i(\underline{\varphi}) + Q_{\varepsilon_i} \tag{2.12}$$

where $\psi_i(\underline{\varphi})$ denotes the i-th column of the matrix $\Psi^T(\underline{\varphi})$, and Q_{ε_i} is the i-th diagonal element of the matrix Q_ε.

For a Gaussian prior PDF $N(\underline{\xi}(t)|\underline{0}, \Sigma_\xi)$ of the modal coordinate vector $\underline{\xi}(t)$, the prediction of the QoI $\underline{z}$ prior to the data can be readily obtained from Eq. 2.3 to be Gaussian with mean zero and covariance matrix $\Sigma_z(\underline{\varphi}) = \Psi(\underline{\varphi}) \Sigma_\xi(\underline{\varphi}) \Psi^T(\underline{\varphi}) + Q_\epsilon$, where $\Sigma_\xi(\underline{\varphi}) = S$ is the covariance matrix corresponding to the assigned prior distribution. In particular, the variance of the i-th element $z_i(t; \underline{\varphi})$ prior to the data is given by

$$\Sigma_{z_i}(\underline{\varphi}) = \psi_i^T(\underline{\varphi}) S \psi_i(\underline{\varphi}) + Q_{\varepsilon_i} \tag{2.13}$$

The posterior and prior variances $\Sigma_{z_i|D}(\underline{\delta}, \underline{\varphi})$ in Eq. 2.12 and $\Sigma_{z_i}(\underline{\varphi})$ in Eq. 2.13, described in terms of the parameters $\underline{\varphi}$ and the sensor locations $\underline{\delta}$, are the main quantities involved in the next section to solve the optimal sensor location problem for virtual sensing and response reconstruction. It is clear that these variances are independent of the measurements/data $\underline{y}(t)$ and depend only on the structural model parameters $\underline{\varphi}$, the model and measurement error covariances Q_e and Q_ε, as well as the covariance matrix S of the prior probability distribution of the modal coordinates $\underline{\xi}(t)$. For practical convenience and without loss of generality, stationarity conditions are assumed, where the covariance matrices Q_e, Q_ϵ and S are independent of time t. As a results the posterior and prior variances defined in Eq. 2.12 and Eq. 2.13 do not depend on time t. The parameters that define the model/prediction and measurement error covariances can be included in the parameter set $\underline{\varphi}$. A probability distribution $p(\underline{\varphi})$ can be postulated to quantify the uncertainties in the values of model and input characteristics involved in $\underline{\varphi}$.

Note that the matrix $\Phi^T(\underline{\varphi}) L^T(\underline{\delta}) Q_e^{-1}(\underline{\delta}, \underline{\varphi}) L(\underline{\delta}) \Phi(\underline{\varphi})$ in Eq. 2.12 is nonsingular only if the number of sensors is greater or equal to the number of modes. Thus, for $S = 0$, the

condition $N_0 \geq m$ should be met in order for the system to be identifiable [36]. The prior covariance matrix S is particularly important when the condition $N_0 \geq m$ is not met. This matrix contributes subjective information from the prior that allows the inversion of the matrix appearing in the first term of Eq. 2.11 for values of $N_0 < m$.

2.3 Optimal Sensor Placement Formulation

2.3.1 Expected Utility Using Information Gain

Information theory is next combined with utility theory to measure the usefulness of a sensor configuration for reliable virtual sensing that is robust to modeling and measurement uncertainties. The objective is to select the sensor locations that maximize the information contained in the data for predicting with the least uncertainty the output response QoI at desirable locations. A measure of the information gain for estimating a response QoI z_i, given a set of data $\underline{y}$ and the model parameters $\underline{\varphi}$, is the KL-div [83] between the prior and posterior probability distribution of the output QoI z_i, defined for an experimental design $\underline{\delta}$ as

$$\tilde{D}_i(\underline{\delta}, \underline{y}, \underline{\varphi}) = \int_{Z_i} p(z_i|\underline{y}, \underline{\delta}, \underline{\varphi}) \ln \frac{p(z_i|\underline{y}, \underline{\delta}, \underline{\varphi})}{p(z_i|\underline{\varphi})} dz_i \tag{2.14}$$

For several output QoI included in the vector $\underline{z}$, the measure can be extended to the weighted average of the information gain for all possible output QoI, given as

$$\tilde{D}(\underline{\delta}, \underline{y}, \underline{\varphi}) = \sum_{i=1}^{N_z} w_i \tilde{D}_i(\underline{\delta}, \underline{y}, \underline{\varphi}) \tag{2.15}$$

with $\sum_{i=1}^{N_z} w_i = 1$, $w_i \geq 0$, where the values of the weight w_i are selected to quantify the importance of the i-th QoI z_i in the design of the sensor configuration.

In the initial design phase the data are not available. Instead they can be generated by the prediction error model Eq. 2.1 for given values of the model parameters $\underline{\varphi}$ and the probability distribution of the prediction error term $\underline{e}(t)$. Following Lindley's work [68], utility theory is used to measure the usefulness of the experiment with the utility function selected to be the expected value of the information gain in Eq. 2.15 over all possible values of the experimental data. Extending the utility function to include the uncertainty in the model parameters $\underline{\varphi}$ as

well, one introduces the expected utility function

$$U(\underline{\delta}) = \int_{\tilde{\Phi}} \int_{Y} \tilde{D}(\underline{\delta}, \underline{\varphi}, \underline{y})\, p(\underline{y}, \underline{\varphi}|\underline{\delta})\, d\underline{y}\, d\underline{\varphi} = \sum_{i=1}^{N_z} w_i U_i(\underline{\delta}) \tag{2.16}$$

that quantifies the usefulness of learning from the data for predicting the output QoI included in the vector $\underline{z}$, in the presence of model and measurement uncertainties, where

$$U_i(\underline{\delta}) = \int_{\tilde{\Phi}} \int_{Y} \tilde{D}_i(\underline{\delta}, \underline{\varphi}, \underline{y})\, p(\underline{y}, \underline{\varphi}|\underline{\delta})\, d\underline{y}\, d\underline{\varphi} \tag{2.17}$$

is the expected utility function that accounts for a component z_i of the response QoI $\underline{z}$, $p(\underline{y}, \underline{\varphi}|\underline{\delta}) = p(\underline{y}|\underline{\varphi}, \underline{\delta})\, p(\underline{\varphi})$, $p(\underline{y}|\underline{\varphi}, \underline{\delta})$ is the uncertainty in the outcome $\underline{y}$ given the model parameters $\underline{\varphi}$, and $p(\underline{\varphi})$ is the uncertainty in the model parameters. The utility function defined in Eq. 2.16 and Eq. 2.17 is an average of the information gain over all the possible data outcomes.

It is shown in Appendix A that the expected utility function $U_i(\underline{\delta})$ can be formulated in terms of the change in the expected information entropy before and after the data are collected, given by

$$U_i(\underline{\delta}) = \int_{\Phi} H_{z_i}(\underline{\varphi})\, p(\underline{\varphi})\, d\underline{\varphi} - \int_{\tilde{\Phi}} \int_{Y} H_{z_i|D}(\underline{\delta}, \underline{y}, \underline{\varphi})\, p(\underline{y}|\underline{\varphi}, \underline{\delta})\, d\underline{y}\, p(\underline{\varphi})\, d\underline{\varphi} \tag{2.18}$$

where $H_{z_i}(\underline{\varphi})$ is the prior information entropy in $z_i(t)$ given the model parameter set $\underline{\varphi}$, and $H_{z_i|D}(\underline{\delta}, \underline{y}, \underline{\varphi})$ is the posterior information entropy in $z_i(t)$ given the data $\underline{y}$ and the model parameter set $\underline{\varphi}$. For Gaussian probability distribution of the response $z_i(t)$, the posterior information entropy given the values of the data set and the model parameter set $\underline{\varphi}$ is given in terms of the i-th diagonal component of the covariance matrix $\Sigma_{z|D}(\underline{\delta}, \underline{\varphi})$ of the error in the estimate of $\underline{z}$ as follows

$$H_{z_i|D}(\underline{\delta}, \underline{y}, \underline{\varphi}) \equiv H_{z_i|D}(\underline{\delta}, \underline{\varphi}) = \frac{1}{2}[\ln(2\pi) + 1] + \frac{1}{2} \ln \det \Sigma_{z_i|D}(\underline{\delta}, \underline{\varphi}) \tag{2.19}$$

Thus it depends on the sensor locations and the values of the parameters set $\underline{\varphi}$, while it is independent of the data. For the prior information entropy $H_{z_i}(\underline{\varphi})$ an expression similar to Eq. 2.19 holds with the posterior $\Sigma_{z_i|D}(\underline{\delta}, \underline{\varphi})$ replaced by the prior $\Sigma_{z_i}(\underline{\varphi})$.

Taking into account that the prior information entropy $H_{z_i}(\underline{\varphi})$ in Eq. 2.18 is constant, independent of the sensor configuration $\underline{\delta}$, and that the posterior information entropy $H_{z|D}(\underline{\delta}, \underline{y}, \underline{\varphi})$

does not depend on the data, the expected utility function U_i finally takes the form

$$U_i(\underline{\delta}) = -\Delta\bar{H}_i(\underline{\delta}) = -\left[\bar{H}_{z_i|D}(\underline{\delta}) - \bar{H}_{z_i}\right] = -\frac{1}{2}\int_{\tilde{\Phi}} \ln \frac{\Sigma_{z_i|D}(\underline{\delta},\underline{\varphi})}{\Sigma_{z_i}(\underline{\varphi})}\, p(\underline{\varphi})\, d\underline{\varphi} \tag{2.20}$$

where

$$\bar{H}_{z_i|D}(\underline{\delta}) = \int_{\tilde{\Phi}} H_{z_i|D}(\underline{\delta},\underline{\varphi})\, p(\underline{\varphi})\, d\underline{\varphi} \tag{2.21}$$

and

$$\bar{H}_{z_i} = \int_{\tilde{\Phi}} H_{z_i}(\underline{\varphi})\, p(\underline{\varphi})\, d\underline{\varphi} \tag{2.22}$$

are respectively the expected posterior and prior information entropies over all possible values of the model parameters $\underline{\varphi}$, weighted by the PDF $p(\underline{\varphi})$ of the model parameters.

Substituting Eq. 2.20 into Eq. 2.16, the expected utility function that accounts for all response entries in the vector $\underline{z}$ takes the form

$$U(\underline{\delta}) = -\Delta\bar{H}(\underline{\delta}) = -\sum_{i=1}^{n_z} w_i \Delta\bar{H}_i(\underline{\delta}) = -\frac{1}{2}\sum_{i=1}^{n_z} w_i \int_{\Phi} \ln r(\underline{\delta},\underline{\varphi})\, p(\underline{\varphi})\, d\underline{\varphi} \tag{2.23}$$

where $r(\underline{\delta},\underline{\varphi})$ is defined as the ratio

$$r(\underline{\delta},\underline{\varphi}) = \frac{\Sigma_{z_i|D}(\underline{\delta},\underline{\varphi})}{\Sigma_{z_i}(\underline{\varphi})} \tag{2.24}$$

Using equal weight values $w_i = 1/n_z$, the utility function takes the form

$$U(\underline{\delta}) = -\frac{1}{2n_z}\int_{\tilde{\Phi}} \ln \frac{\prod_{i=1}^{n_z}\left[\Sigma_{z_i|D}(\underline{\delta},\underline{\varphi})\right]}{\prod_{i=1}^{n_z}\left[\Sigma_{z_i}(\underline{\varphi})\right]}\, p(\underline{\varphi})\, d\underline{\varphi} \tag{2.25}$$

The integral in Eq. 4.10 or Eq. 2.25 is a probability integral over the space of uncertain parameters $\underline{\varphi}$. This integral represents the robust information entropy change before and after the data are available, weighted over all possible values of the model parameters quantified by the PDF $p(\underline{\varphi})$. The multidimensional integral can be evaluated using Monte Carlo techniques or sparse grid methods [85, 86]. It is verified in Appendix B that the ratio $r(\underline{\delta},\underline{\varphi})$ in Eq. 2.24 cannot exceed the value of 1 and so the information entropy change is always non-positive or,

equivalently the utility function is non-negative as expected, meaning that there can be only information gain when placing a given number of sensors in the structure.

2.3.2 Optimal Sensor Placement

The optimal sensor configuration $\underline{\delta}_{opt}$ is obtained by maximizing the utility $U(\underline{\delta})$ or, equivalently, minimizing the change in information entropy $\Delta\bar{H}_{z|D}(\underline{\delta})$, with respect to the design variables $\underline{\delta}$, that is

$$\underline{\delta}_{opt} = \underset{\underline{\delta}}{\text{argmax}}\ U(\underline{\delta}) = \underset{\underline{\delta}}{\text{argmin}} \Delta\bar{H}_{z|D}(\underline{\delta}) \tag{2.26}$$

The optimal number of sensors in the sensor configuration can be estimated by monitoring the gain in information as additional sensors are placed in the structure. Usually, after sufficiently number of sensors are placed in the structure, the information gain using additional sensors is relatively small and the process of adding sensors in the structure is terminated.

The optimization in Eq. 2.26 may result in multiple local/global solutions [57]. The optimization problem can be solved using continuous design variables $\underline{\delta}$ accounting for the location of the sensors over the physical domain of the structure or discrete design variables $\underline{\delta}$ accounting for the discrete locations (e.g., DOF at nodes for placing displacement/acceleration sensors or Gauss integration points for placing strains sensors in a finite element mesh). Global optimization algorithms [87, 88] as well as stochastic optimization algorithms, such as CMA-ES [89] and genetic algorithms [45, 90–93] can be employed in order to avoid premature convergence to a local optimum. Alternative heuristic forward and backward sequential sensor placement (FSSP/BSSP) algorithms [54, 57] are effective in solving the optimization problem. The heuristic algorithms bypass the problem of multiple local/global optima manifested in optimal experimental designs, providing near optima solutions in a fraction of the computational effort required in stochastic optimization algorithms or exhaustive search methods [52]. For a total of N_{all} possible sensors positions and N_0 sensors to be placed in the structure, for N_0 relatively small compared to N_{all} the FSSP algorithm requires approximately $N_F = N_0 N_{all}$ function evaluations, while the BSSP algorithm requires approximately $N_B = N_{all}(N_{all}+1)/2$ function evaluations [54]. Although the computational effort for the BSSP is approximately $N_B/N_F \approx 0.5N_{all}/N_0$ times larger than the computational effort of FSSP and thus FSSP should be preferred for $N_0 << N_{all}$, the estimate from BSSP may in some cases be better than

the FSSP estimate and thus the combined estimate should be used in the optimization. More details are presented in the applications Section 2.6.

2.4 Model Prediction Error Formulation

Following the analysis in Section 2.2.1, the prediction error $\underline{e} = \underline{e}_{meas} + \underline{e}_{model}$ in Eq. 2.1 is partly due to a term, $\underline{e}_{meas}$, accounting for the measurement error and partly due to a term, $\underline{e}_{model}$, accounting for the model error. Assuming that measurement and model errors are independent and zero-mean Gaussian vectors with covariance matrices $Q_{e,meas}$ and $Q_{e,model}$, the covariance of the total prediction error is

$$Q_e = Q_{e,meas} + Q_{e,model} \tag{2.27}$$

To proceed with the optimal sensor placement design one has to select the values of the covariance matrices $Q_{e,meas}$ and $Q_{e,model}$. The selection depends on the nature of the problem analyzed. The following selections follow the suggestions presented in [94]. For the measurement error term it is reasonable to assume independence of the values of the errors from the intensity of the response so that $Q_{e,meas} = s^2 I$, where I is the identity matrix, and the level s depends on the sensor accuracy and characteristics. A reasonable choice of the model error variance $Q^{(ii)}_{e,model}$ at the i-th DOF is to have it proportional to the square of the intensity of the QoI at DOF i, given by $Q^{(ii)}_y$. That is, we select $Q^{(ii)}_{e,model} = \sigma_e^2 Q^{(ii)}_y$, where σ_e denotes the level of model error in relation to the intensity of the QoI. In this way, the level of model error is independent on the intensity of the response. In addition, a certain degree of correlation is expected for the model errors between two neighborhood locations, arising from the underlining model dynamics [57]. This correlation can be taken into account by selecting a non-diagonal covariance matrix $Q_{e,model}$. The correlation $Q^{(ij)}_{e,model}$ between the predictions errors $e_{i,model}$ and $e_{j,model}$ at DOFs i and j, respectively, can be assumed to be

$$Q^{(ij)}_{e,model} = \sqrt{Q^{(ii)}_{e,model} Q^{(jj)}_{e,model}}\, \rho(d_{ij}) \tag{2.28}$$

so that it accounts for the spatial distance d_{ij} between the DOFs i and j, where $\rho(d_{ij})$ is a correlation function satisfying $\rho(0) = 1$. However, in the experimental design phase where data

are not available, the actual errors and correlations should be postulated in order to proceed with the design of the optimal sensor locations. Several correlation functions can be explored. For demonstration purposes in this study, the following exponentially decaying correlation function is assumed:

$$\rho(d_{ij}) = exp\left(-\frac{d_{ij}}{\lambda}\right) \tag{2.29}$$

where λ is a measure of the spatial correlation length. However, the formulation in this work is general and does not depend on the choice of the correlation model.

Using the aforementioned selections, the covariance matrix Q_e in Eq. 2.27, required in Eq. 2.12, simplifies to

$$Q_e = s^2 I + \sigma_e^2 \tilde{Q}_y^{1/2} R \tilde{Q}_y^{1/2} \tag{2.30}$$

where the notation $\tilde{Q}$ denotes a diagonal matrix that contains in i-th diagonal entry the quantity $Q_y^{(ii)}$, $\tilde{Q}^{1/2}$ represents a diagonal matrix with elements the square roots of the elements in $\tilde{Q}$, and R is the correlation matrix with the (i, j) element R_{ij} equal to $\rho(d_{ij})$.

A similar formulation can be used for the variance Q_{ϵ_i} involved in Eq. 2.12 of the error $\underline{\varepsilon}_i$ for the predicted QoI z_i. In this case only the model error exists and the i-th diagonal element of the covariance matrix can be selected to be

$$Q_{\varepsilon_i} = \sigma_\varepsilon^2 Q_{z_i} \tag{2.31}$$

were Q_{z_i} is the square of the intensity of the predicted QoI $z_i(t)$, and σ_ε is the level of model error in relation to the intensity of the predicted QoI.

The formulation for the errors and the mathematical structure of the ratio $r(\underline{\theta}, \underline{\varphi})$ in Eq. 2.24 can be used to show a number of useful properties for the utility function and thus for the information gain. Specifically, in Appendix B.1 it is shown that as the measurement and model/prediction errors increase for a given sensor configuration, the ratio $r(\underline{\theta}, \underline{\varphi})$ increases and so the utility function decreases. This indicates that the higher the errors, the less the information gain from the sensor configuration. Finally, another important property shown in Appendix B.2 is that adding a sensor in an existing sensor configuration increases the information gain, which is similar to the results presented in [54] for parameter estimation. This

should be expected since as a sensor is added in an existing sensor configuration, there can be null or extra information provided by this sensor. As a result, the maximum and minimum value of the utility function is an increasing function of the number of sensors. Lastly, the spatially correlated structure of the model error, introduced in Eq. 2.29, has the important effect of avoiding clustering of sensors as it was theoretically shown in [57] for OSP for parameter estimation.

2.5 Implementation

It should be noted that the estimate in Eq. 2.10 of the response QoI $\underline{z}$ and the error in the estimate, quantified by the covariance matrix $\Sigma_z(\underline{\delta}, \underline{\varphi})$ in Eq. 2.12, depends on the measurement/model and prediction error covariance matrices Q_e and Q_ϵ, as well as the covariance matrix S of the prior Normal distribution assumed for the modal coordinates $\underline{\xi}(t)$. The effect of the values of these covariance matrices on the optimal sensor placement for response predictions is investigated in this work.

The selection of the the covariance matrix S of the prior normal distribution should take into account the relative contribution of the different modal coordinates on the response of the system. Such contribution depends highly on the excitation characteristics. Eq. 2.30 and Eq. 2.31 also suggest that the values of the covariance matrices Q_e and Q_ε of the model prediction errors should be carefully selected based on the intensity of the measured and predicted responses which are not known at the OSP design phase. To proceed with rational selections, the intensities of measured and predicted QoI have to be considered which depend on the characteristics of the excitation. Thus, the characteristics of the excitation have to be considered in the analysis in order to decide on the values of the covariance matrices S, Q_e and Q_ϵ upon which the OSP design will be based. Failing to consider the intensity of the modal coordinates and the responses in the selection of the prior and error covariance matrices may lead to OSP designs that are based on non-rational choices of these error covariance matrices.

Due to the uncertainty in the excitation characteristics the values to be assigned for the model/prediction and measurement errors involve large uncertainty. We proceed with a thorough investigation of the effect of the model/prediction and measurement errors as well as the effect of the uncertainty in the prior distribution on the information gain and the optimal sensor location. Finally, the robust design proposed in this work will take into account these

uncertainties in the design of the optimal sensor configuration.

To demonstrate concepts, we assume a zero-mean stationary white noise excitation. We also assume, without loss of generality, that the location of the excitation is known. Unknown locations or multiple excitation components can as well be treated in the formulation. However, such an analysis is beyond the scope of the present work. Using a linear model (e.g., a finite element model) of the structure, one can readily obtain the covariance Q_ξ of the modal quantities, as well as the covariance of the response QoI (displacements, velocities, strains and stresses) Q_y and Q_z. These matrices can be used in Eq. 2.30 and Eq. 2.31 to make the proper assignment for Q_e and Q_ε through the proper selection of the prediction error parameters σ_e, σ_ε and s. Furthermore, accepting that the excitation is white noise, it is also reasonable to assume that the covariance of the prior distribution for $\underline{\xi}(t)$ is selected to be proportional to the covariance Q_ξ of the modal quantities $\underline{\xi}(t)$, i.e.,

$$S = \alpha^2 Q_\xi \tag{2.32}$$

where α quantifies the extent of the uncertainty in the prior distribution. This assignment will correctly take into account the participation of each mode in the vibration analysis of the structure.

The analysis for estimating the covariance matrix Q_ξ of the modal coordinates and the covariance matrices Q_y and Q_z of various response QoI is presented next based on the finite element model of the structure and a discrete state space representation of the modal equations in Eq. 2.2. Introducing the state space vector $\underline{x}_k^T = [\ \underline{\xi}_k^T \quad \dot{\underline{\xi}}_k^T\ ]^T$ at time instant $t = k\Delta t$, where $\underline{\xi}_k = \underline{\xi}(k\Delta t)$ and Δt is the sampling time of a signal, the modal in Eq. 2.2 can be written in the discrete state space form

$$\underline{x}_{k+1} = A\underline{x}_k + B\underline{u}_k \tag{2.33}$$

where, using zero-order hold, the state space matrices are given as $A = exp(A_c\Delta t)$ and $B = (A - I)A_c^{-1}B_c$ with

$$A_c = \begin{bmatrix} 0 & I \\ -\Lambda & -Z \end{bmatrix}, \quad B_c = \begin{bmatrix} 0 \\ \Phi^T M \end{bmatrix} \tag{2.34}$$

An output vector QoI $\underline{h}_k$ at time $t = k\Delta t$, either it corresponds to measured quantities $\underline{y}$ or predicted quantities $\underline{z}$, can be written in the form

$$\underline{h}_k = C\underline{x}_k + D\underline{u}_k \tag{2.35}$$

where the matrices C and D relate the response QoI to the state vector and input load vector, respectively. For displacement, strain or stress responses at all DOF of the structure, the matrices $C = G\Phi[\ I \quad 0\ ]$ and $D = 0$, where the matrix G relates the displacement DOF with the output QoI (displacements, strains and stresses). For acceleration responses the matrices $C = G\Phi[\ -\Lambda \quad -Z\ ]$ and $D = G\Phi\Phi^T M$. Here it is assumed that Φ is mass normalized. In particular, to estimate $\underline{\ddot{\xi}}_k$ one uses Eq. 2.35 with $C = [\ -\Lambda \quad -Z\ ]$ and $D = \Phi^T M$.

Assuming a scalar stationary zero-mean Gaussian white noise excitation with variance σ_{wn}^2, the covariance Q_x of the state vector under stationary conditions is given by $Q_x = \sigma_{wn}^2 \bar{Q}_x$, where $\bar{Q}_x$ can be obtained by solving the discrete Liapunov equation

$$A\bar{Q}_x A^T - \bar{Q}_x + BB^T = 0 \tag{2.36}$$

Using Eq. 2.35, the covariance of the output response QoI in the vector $\underline{h}(t)$ is given by

$$Q_h = \sigma_{wn}^2 (C\bar{Q}_x C^T + DD^T) \tag{2.37}$$

and is proportional to the variance σ_{wn}^2 of the discrete white noise excitation. Setting $\underline{h} = \underline{y}$, or $\underline{h} = \underline{z}$, or $\underline{h} = \underline{\xi}$, the covariance matrices Q_y, or Q_z, or Q_ξ are obtained, required in the error covariance matrices Q_e and Q_{ε_i} in Eq. 2.30 and Eq. 2.31 and the prior distribution S in Eq. 2.32.

2.6 Applications

The methodology is demonstrated for a square plate structure modeled by thin-shell finite elements (FEs). The plate is fixed at the left edge. The model is meshed with eight-node shell elements containing six DOFs per node (Fig. 2.1). To investigate the effect of mesh size on the optimal sensor placement, two models are considered corresponding to different mesh types: a coarse and a fine mesh. The coarse mesh model consist of 420 elements, 441 nodes, while

the fine mesh model consists of 3660 elements and 3721 nodes. Linear elastic behavior is assumed. The lowest eight natural frequencies of the models for the coarse and fine mesh are presented in Table 2.1.

Table 2.1: Modal frequencies of the plate modeled with coarse and fine mesh.

Natural Frequency (Hz)	Mode 1	Mode 2	Mode 3	Mode 4	Mode 5	Mode 6	Mode 7	Mode 8
Coarse mesh	0.956	2.344	5.897	7.520	8.563	14.989	17.176	17.895
Fine mesh	0.956	2.344	5.868	7.497	8.532	14.934	16.909	17.696
% difference	0.00	0.00	0.49	0.31	0.36	0.37	1.55	1.11

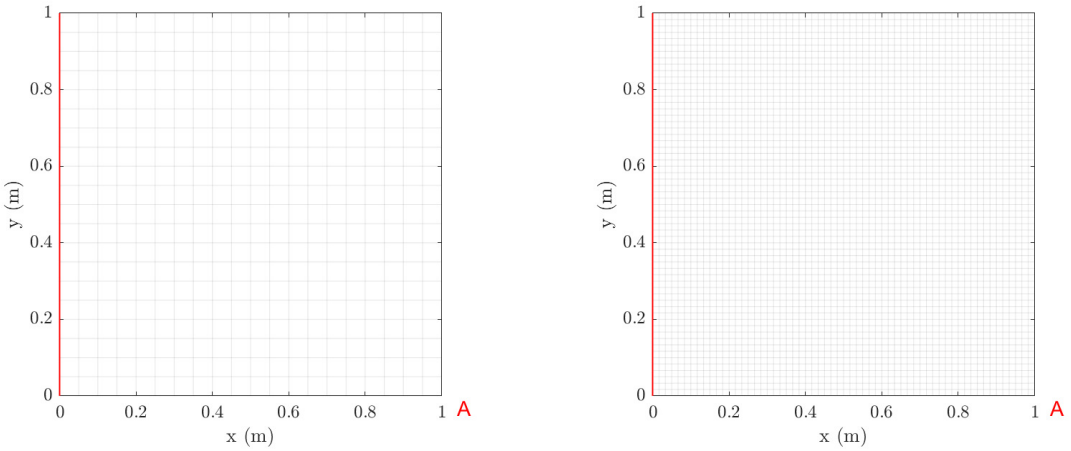

(a) **(b)**

Fig. 2.1. Square thin plate with left edge fixed (shown in red line); (a) coarse mesh, (b) fine mesh.

2.6.1 Strain Predictions Using Strain Observations

Normal strain measurements and predictions are considered along the x direction at the mid-points of all finite elements of the plate surface comprising the mesh. OSP of strain sensors is performed for predicting the strains at all finite elements of the mesh (Fig. 2.1). Contribution of the lower eight modes to the dynamic behavior of the plate is assumed in designing the optimal location of sensors.

2.6.1.1 Model/Prediction Errors, Measurement Error and Prior Distribution

Reasonable choices of the error parameters s, σ_e and σ_ε involved in the covariance matrices Q_e and Q_ε in Eq. 2.30 and Eq. 2.31 of the model/prediction and measurement error models are next considered. For this, it is assumed that the plate is subjected to a concentrated load

applied at the right bottom corner A, as shown in Fig. 2.1. A broad band excitation is considered, modeled by a discrete Gaussian white noise sequence with standard deviation σ_{wn}. To select the standard deviation s of the measurement error, the intensities of the normal strain responses along the x direction predicted for white noise input are computed and shown in Fig. 2.2(a) and (b) for the coarse and fine mesh, respectively. The intensity of a response QoI z_i is quantified by the standard deviation $Q_{z_i}^{1/2}$ computed by solving the Liapunov Eq. 2.36 and using Eq. 4.38. The results in Fig. 2.2 are normalized with respect to the intensity σ_{wn} of the white noise input. Approximately 98% of the computed intensities of the strains in all plate elements are greater than $\epsilon_{min} \equiv Q_{z,min}^{1/2} = 10^{-6}$, while the maximum strain intensity value is approximately $\epsilon_{max} \equiv Q_{z,max}^{1/2} = 2x10^{-5} = 20\epsilon_{min}$. To investigate the effect of measurement error, the parameter s of the error covariance matrix in Eq. 2.30 is selected as shown in Table 2.2 to have four different values corresponding to very small, small, moderate and large measurement error, respectively. The σ_e of the model error and σ_ε of the prediction error involved in Eq. 2.30 and Eq. 2.31 are selected to be $\sigma_e = \sigma_\varepsilon = 0.01$ and 0.001 corresponding to small and very small model/prediction errors, respectively. The case of uncorrelated prediction error is considered ($\lambda = 0$ in Eq. 2.29).

The intensities of the modal coordinates $\underline{\xi}(t)$ predicted for white noise input are shown in Fig. 2.2(c). It is clear that the intensities of the modal coordinates vary considerably from mode to mode. This reinforces the fact that the covariance of the prior distribution of the modal coordinates should carefully be chosen using Eq. 2.32 to take into account the different intensities of each mode. These modal intensities highly depend on the spatial and temporal excitation characteristics (number and location of excitation, frequency characteristics, etc.). The value of α in Eq. 2.32 is selected to be $\alpha = 10^2$ and $\alpha = 1$ corresponding respectively to large and small uncertainties in the prior distribution of the modal coordinates $\underline{\xi}$.

Table 2.2: Different measurement errors s assumed. $\epsilon_{\min} = Q_{z,min}^{1/2} \approx 10^{-6}$ is the minimum value of the element strain that cover 98% of the plate surface. $\epsilon_{\max} = Q_{z,max}^{1/2} \approx 2 \times 10^{-5}$ is the maximum value of the strain in the plate surface.

Measurement Error	s	$s/\varepsilon_{\min}$	$s/\varepsilon_{\max}$
Very small	10^{-9}	10^{-3}	5×10^{-5}
Small	10^{-8}	10^{-2}	5×10^{-4}
Moderate	10^{-7}	10^{-1}	5×10^{-3}
Large	10^{-6}	10^{0}	5×10^{-2}

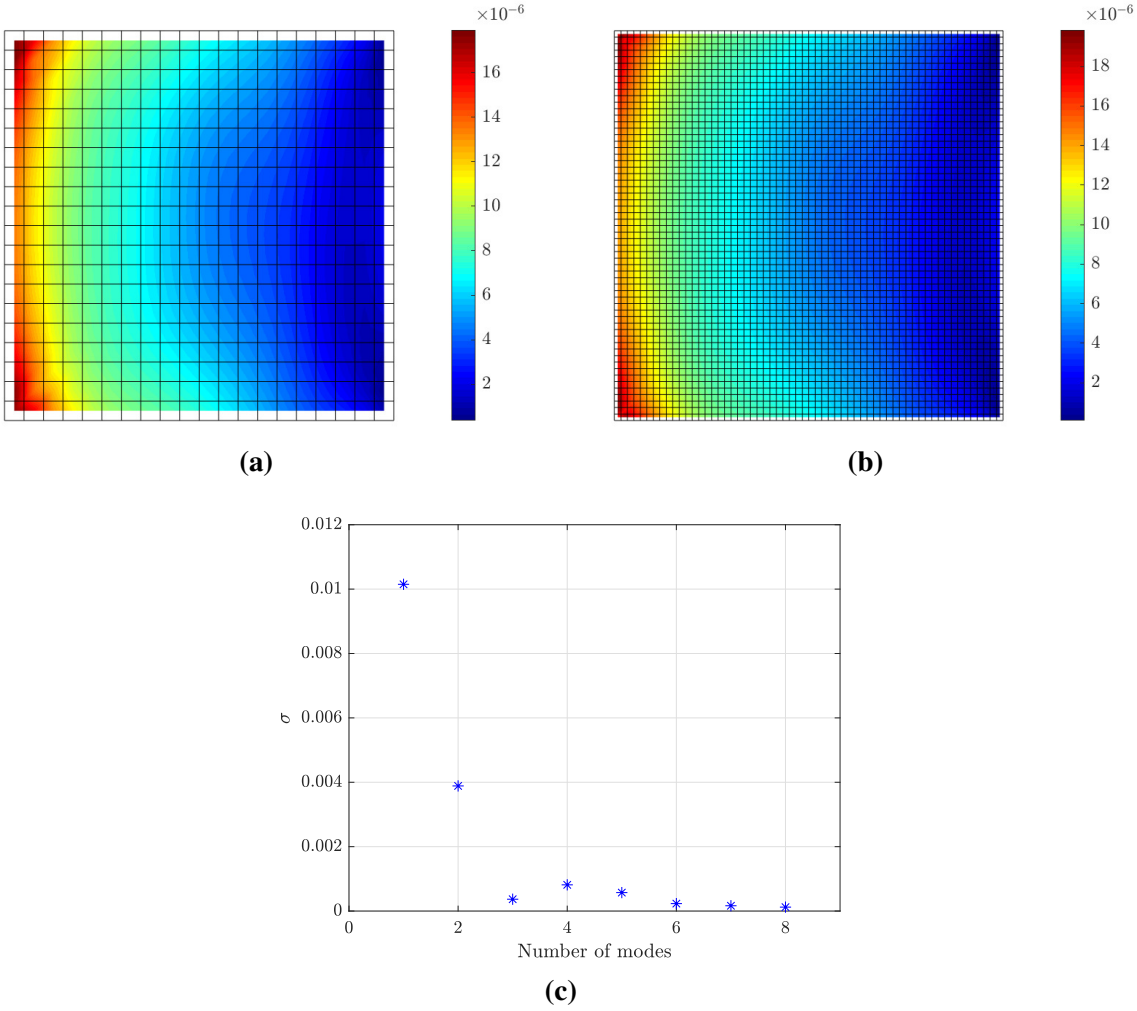

Fig. 2.2. Intensities of normal strains computed along the x direction at the middle of the finite elements of the mesh (a) for coarse mesh, (b) for fine mesh. (c) Intensities of the modal coordinates $Q_{\xi}^{1/2}$ as a function of the number of modes.

FSSP and BSSP Algorithms

The results for the utility values obtained using the FSSP and BSSP algorithms for $\sigma_e = \sigma_\varepsilon = 0.01$ (small model/prediction errors), $s = 10^{-7}$ (moderate measurement error) and $\alpha = 10^2$ (large prior uncertainty in modal coordinates) are compared in Fig. 2.3 for coarse (Fig. 2.3(a)) and fine meshes (Fig. 2.3(b)). The estimates from the two algorithms differ due to the fact that both algorithms are heuristic and provide approximate values. In this specific case and for the coarse mesh, the BSSP algorithm provides better solutions for the maximum and minimum utility for more than eight sensors, while the FSSP algorithm provides better solution than the BSSP algorithm for one to seven sensors. This observation is not consistent for the fine mesh where FSSP algorithms provides better estimates for the minimum utility for all number of sensors, while the BSSP provides a better estimate for the maximum utility for seven sensors. Similar behavior for the accuracy of the results provided from the FSSP and

BSSP algorithms is observed for other error cases as well.

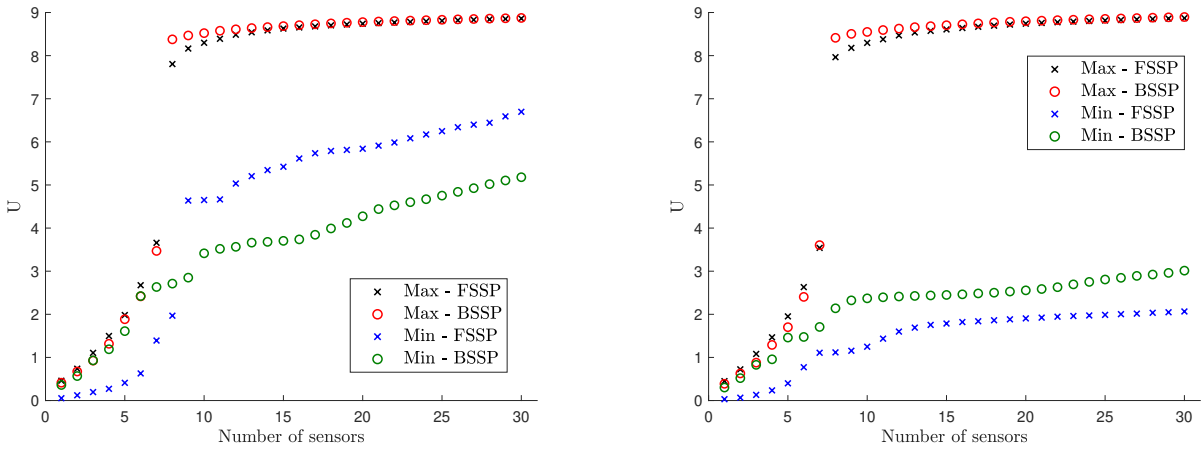

Fig. 2.3. Comparison of the maximum and minimum utility values as a function of the number of sensors obtained from FSSP and BSSP algorithms for (a) coarse mesh and (b) fine mesh.

To increase the reliability of the estimates arising from the two heuristic algorithms, the final solution is taken from the combination of the FSSP and BSSP solutions. Specifically, for each sensor configuration containing a fixed number of sensors, the final maximum utility value is taken to be $U_{max} = max(U_{F,max}, U_{B,max})$, where $U_{F,max}$ and $U_{B,max}$ are the maximum values estimated from the FSSP and BSSP algorithms, respectively. Additionally, the optimal sensor placement is selected among the FSSP and BSSP optimal sensor placement that corresponds to the value of U_{max}. A similar procedure is used for the minimum utility value, i.e., $U_{min} = max(U_{F,min}, U_{B,min})$. The combined FSSP/BSSP result will be referred from here on as the sequential sensor placement (SSP) estimate.

The use of BSSP to obtain results has the effect of raising substantially the computational cost in relation to FSSP. Specifically, comparing the number of function evaluations N_F and N_B for the FSSP and BSSP algorithms one has that for $N_0 = 30$ sensors that $N_B/N_F = 0.5N_{all}/N_0 \approx 6$ for the coarse mesh and $N_B/N_F \approx 60$ for the fine mesh. The number of functions evaluations for BSSP for the fine mesh is two order of magnitude larger than the one required for FSSP. Additionally, for the spatially correlated prediction error case, the FSSP and BSSP require the repeated solutions of algebraic linear system of equations of size (see Eq. 2.12) as high as N_0 and N_{all}, respectively, raising substantially the computational effort for BSSP in relation to FSSP for the common case for which the number of possible sensor locations N_{all} is usually much higher than number of sensors N_0 ($N_{all} >> N_0$) in a sensor

configuration.

2.6.1.2 Information Gain versus Number of Sensors

The SSP results for the maximum and minimum utility values as a function of the number of sensors for the optimal and worst sensor configurations for up to 30 sensors are shown in Fig. 2.4 for different measurement and model/prediction errors for both coarse (Fig. 2.4(a) and (c)) and fine (Fig. 2.4(b) and (d)) meshes. Large prior uncertainty in the modal coordinates is assumed ($\alpha = 10^2$). Comparing the maximum utility values in Fig. 2.4(a) and (c) for the coarse mesh with the corresponding maximum utility values in Fig. 2.4(b) and (d) for the fine mesh, it can be seen that the results are almost indistinguishable. Thus, the mesh size does not affect the maximum value of the expected information gain, as it should be expected since the dynamic characteristics from both meshes do not differ significantly as shown in Table 2.1. However, the mesh size affects the minimum value of the information gain, providing substantially lower values of the utility for the fine mesh. This is due to the fact that a fine mesh contains significantly more finite elements and thus more strain sensor locations with non-informative strains than the coarse mesh does. It should be noted that the difference between maximum and minimum expected information entropy values for a fixed number of sensors gives the maximum information gain that can be achieved by employing the optimal sensor placement methodology.

To interpret the results in Fig. 2.4, it should be kept in mind that for eight contributing modes one needs at least eight sensors in order for the information matrix in Eq. 2.12 to be invertible and the problem to be identifiable without the use of the subjective information from the prior PDF of the modal coordinates. For less than eight sensors the information matrix in Eq. 2.12 is not invertible without prior information. The prior covariance matrix S of the modal coordinates provides the missing information required to make the problem identifiable. From the results in Fig. 2.4(a), it is observed that the expected information gain steadily increases as one adds from one to seven sensors due to the increase of the information from the data, and rises sharply from seven to eight sensors due to the fact that eight sensors placed at their optimal positions provide the necessary information without the need of the small complementary information from the prior.

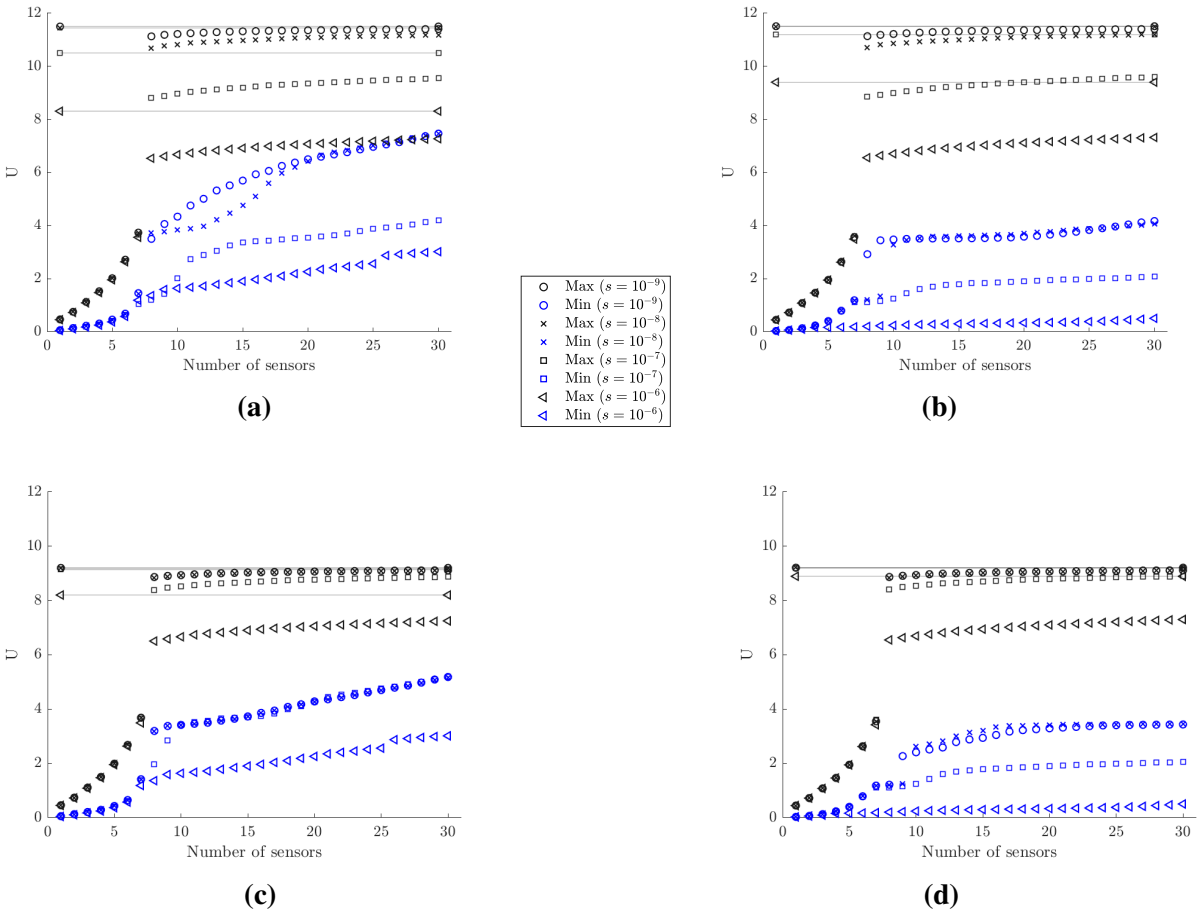

Fig. 2.4. SSP results for maximum and minimum utility values for model/prediction error $\sigma_e = \sigma_\varepsilon = 0.001$ (a,b) and $\sigma_e = \sigma_\varepsilon = 0.01$ (c,d) obtained for the coarse (a,c) and fine (b,d) meshes. Results are presented for different measurement errors s as shown in the legend and for $\alpha = 10^2$. The horizontal lines are the maximum utility values that can be achieved by using strain sensors at all finite elements of the coarse and fine meshes.

Normalized utility values obtained by dividing the maximum and minimum utility values in Fig. 2.4 by the utility values obtained by placing the maximum number of strain sensors at all finite elements of the mesh (420 for coarse mesh and 3660 for fine mesh) are presented in Fig. 2.5 for each measurement and model/prediction error case. By tracking the maximum normalized information gain values as a function of the number of sensors, it is possible to decide on the number of sensors to be kept in an optimal sensor configuration. One should stop adding sensors in the structure when the information gained by additional sensors is not significant compared to the information gained by the existing sensors, or when the information gained by a number of sensors is a sufficiently large percentage of the maximum information that can be achieved by placing sensors at all possible locations (e.g., all finite elements of the mesh in the plate problem).

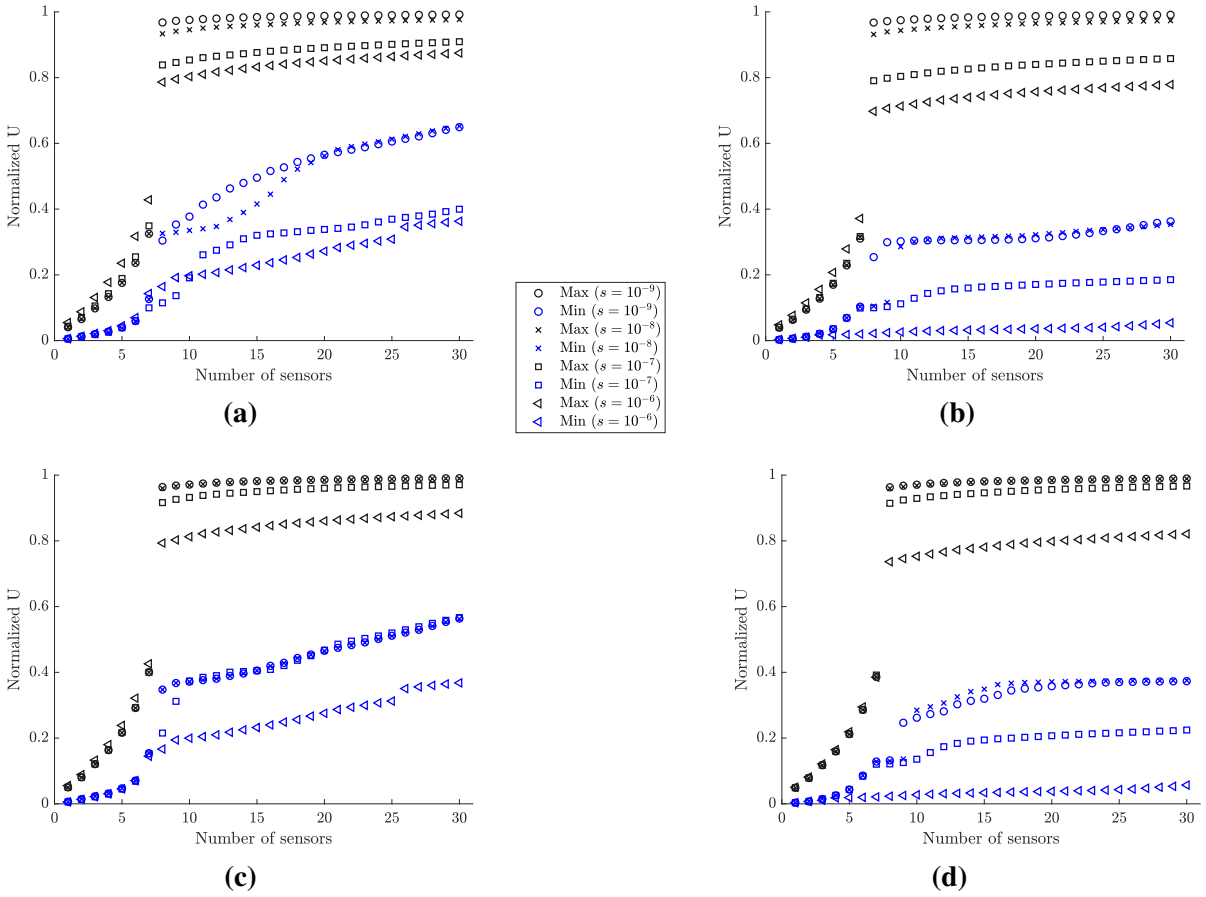

Fig. 2.5. Normalized utility values for model/prediction error $\sigma_e = \sigma_\epsilon = 0.001$ (a,b) and $\sigma_e = \sigma_\epsilon = 0.01$ (c,d) obtained for the coarse (a,c) and fine (b,d) meshes. Results are presented for different measurement errors s as shown in the legend and for $\alpha = 10^2$.

2.6.1.3 Information Gain versus Measurement Error

As seen in Fig. 2.5(a) and (b), for very small model error ($\sigma_e = \sigma_\epsilon = 0.001$) and for very small ($s = 10^{-9}$) to small ($s = 10^{-8}$) measurement error, eight sensors placed at their optimal positions account for approximately 97% to 93% of the maximum information that can be gained by adding strain sensors at all possible locations. For moderate ($s = 10^{-7}$) and large ($s = 10^{-6}$) measurement error, eight optimally located sensors provide an information gain of the order of 84% and 79% for the coarse mesh and 79% and 70% for the fine mesh compared to the maximum information gain that can be achieved for the coarse and fine mesh, respectively. These lower values are due to the fact that information extracted from sensors is affected by the model and measurement errors. The higher the error, the less the information extracted from the sensors. Additionally, comparing the normalized information gain values for the fine and coarse meshes, smaller normalized information gain values are reported for the fine mesh due to the fact that in these large error case the 3660 strain sensors provide more information

than the 440 strain sensors placed at all finite element of the fine and coarse mesh, respectively. Thus the normalizing quantity for the fine mesh is highest for the fine mesh and as a result the normalized information gain values for the fine mesh appear smaller than the corresponding ones for the coarse mesh.

For the small measurement error cases ($s = 10^{-9}$ and $s = 10^{-8}$), eight sensors placed at their optimal positions provide most of the information for accurate response prediction (Fig. 2.5). Given that eight sensors have been placed on the structure, there is very small gain in information (less than 7%) if the plate is fully populated with sensors. This is mainly due to the fact that quality of the measurements is very good and/or the model error is small, so the number of sensors needed is at most the number of sensors required for making the problem identifiable. For large measurement errors in Fig. 2.5, the quality of information deteriorates significantly due to measurements and/or model error and so the minimum number of eight sensors required for identifiability appears less informative than the case of small measurement error. More than eight sensors increase further the utility values, providing significant additional information to counterbalance the deteriorated quality of the measurements.

Considering the cost of instrumentation, the process of placing more sensors optimally in the structure in order to gain a higher percentage of the total information should be considered with care and in some cases might not be justifiable (like in the case of small measurement and model error for the plate problem). Nevertheless, the final choice of the number of sensors to be placed in the structure depends on the cost of instrumentation which may also affect the location of sensors, especially for the cases where instrumentation cost depends on the location of sensors. For example, not easily accessible areas in a structure, such as underwater locations in off-shore platforms or wind turbines, might substantially increase the cost of adding sensors in relation to the cost of instrumenting easily accessible areas. However, considering cost issues in designing the sensor configuration falls outside the objectives of this work and the reader is referred to value of information formulations (e.g., [72, 73]).

Fig. 2.6 and Fig. 2.7 plots the information gain as a function of the measurement error s for 8, 30 and N_{all} sensors, for both the coarse and the fine mesh, where N_{all} is the number of finite elements in the coarse or fine mesh. For fixed number of sensors, the information gain decreases as the measurement error increases. This is due to the fact that the quality of information contained in measurements decreases due to higher noise to signal ratio, and thus the information gain is lower as the measurement error increases. The decrease is more

pronounced for very small modeling error ($\sigma_e = \sigma_\epsilon = 0.001$) since most of the error in this case, modeled in the covariance matrix Q_e in Eq. 2.27, arises from the measurement error. For higher model error ($\sigma_e = \sigma_\epsilon = 0.01$) shown in Fig. 2.6(c) and (d), the information gain values are less sensitive to the measurement error values of $s = 10^{-9}$ (very small), $s = 10^{-8}$ (small) and $s = 10^{-7}$ (moderate), while there is a more pronounced drop in information gain for large measurement error ($s = 10^{-6}$). This insensitivity of the information gain to smaller values of the measurement error is due to the fact that the larger value of model error dominates the very small to moderate measurement errors as seen by the mathematical model for Q_e in Eq. 2.30. The quality of information in the data will be further deteriorated only for sufficiently large values of measurement error (here $s = 10^{-6}$).

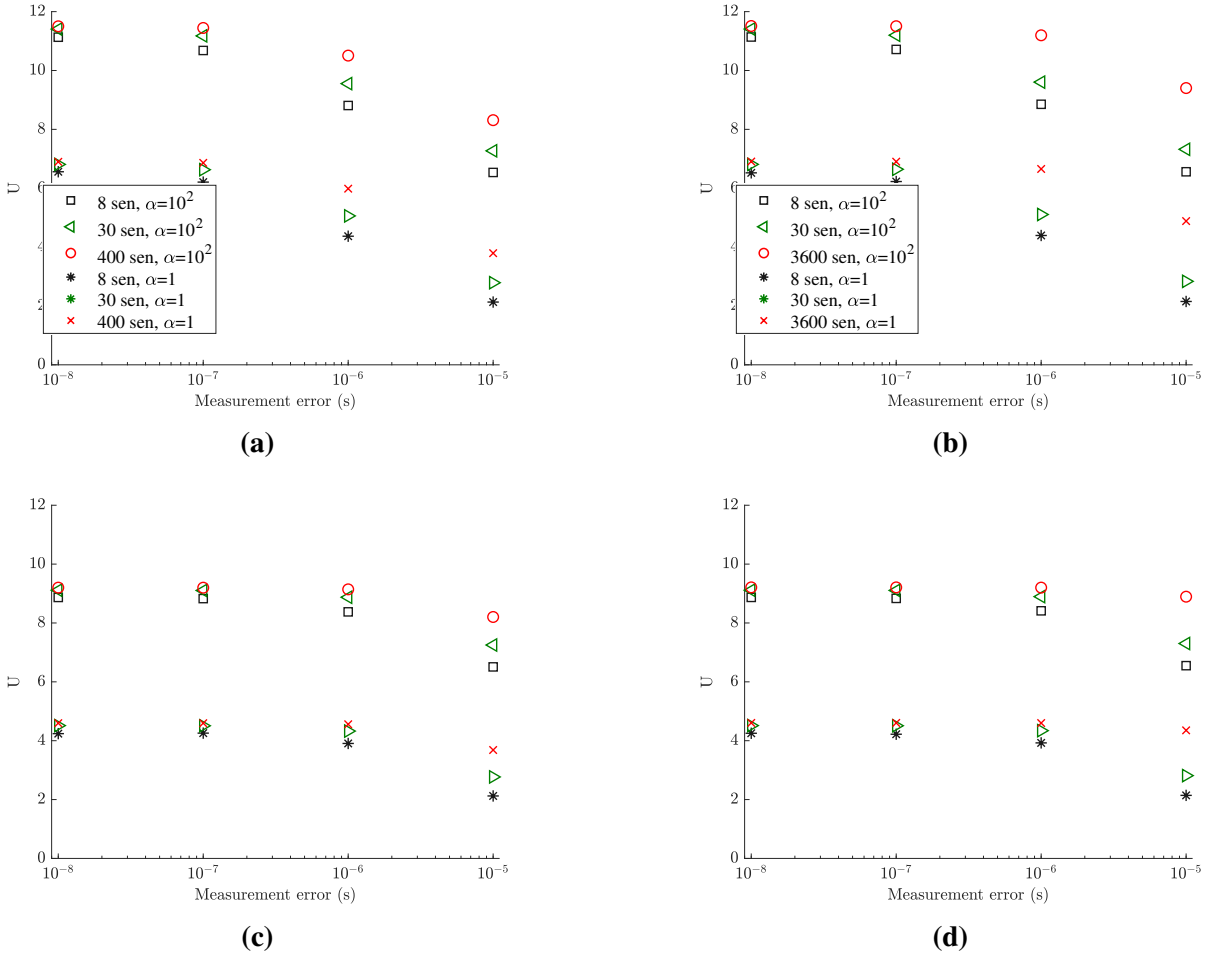

Fig. 2.6. Information gain values versus measurement error for 8, 30 sensors and N_{all} sensors ($N_{all} = 440$ and 3660 respectively for the coarse and fine mesh), for $\alpha = 10^2$ and $\alpha = 1$; (a,b) $\sigma_e = \sigma_\epsilon = 0.001$, (c,d) $\sigma_e = \sigma_\epsilon = 0.01$, (a,c) coarse mesh, (b,d) fine mesh.

Comparing the results in Fig. 2.6 for values of $\alpha = 1$ and $\alpha = 10^2$ corresponding to small and large prior uncertainty in the modal coordinates, it is clearly seen that the information

gain for small prior uncertainty is less than the information gain for large prior uncertainty since significant part of the information is provided from the more informative (due to narrower bounds) prior distribution of the modal coordinates $\underline{\xi}(t)$, making the data effectively less informative. Comparing the results in Fig. 2.7, the decrease in the percentage information gain, normalized with respect to the maximum information that can be achieved by fully populating the plate with strain sensors, is more pronounced as the measurement error increases. For example, 30 sensors placed at their optimal position using $\alpha = 1$ (narrower prior bounds) accounts for approximately 70% of the information that can be gained from strain sensor placement as opposed to approximately 90% of the percentage information gain that can be achieved with $\alpha = 10^2$ (large prior uncertainty bounds). This is expected since in the case of $\alpha = 1$ the prior contains significant information in relation to the information provided from the data.

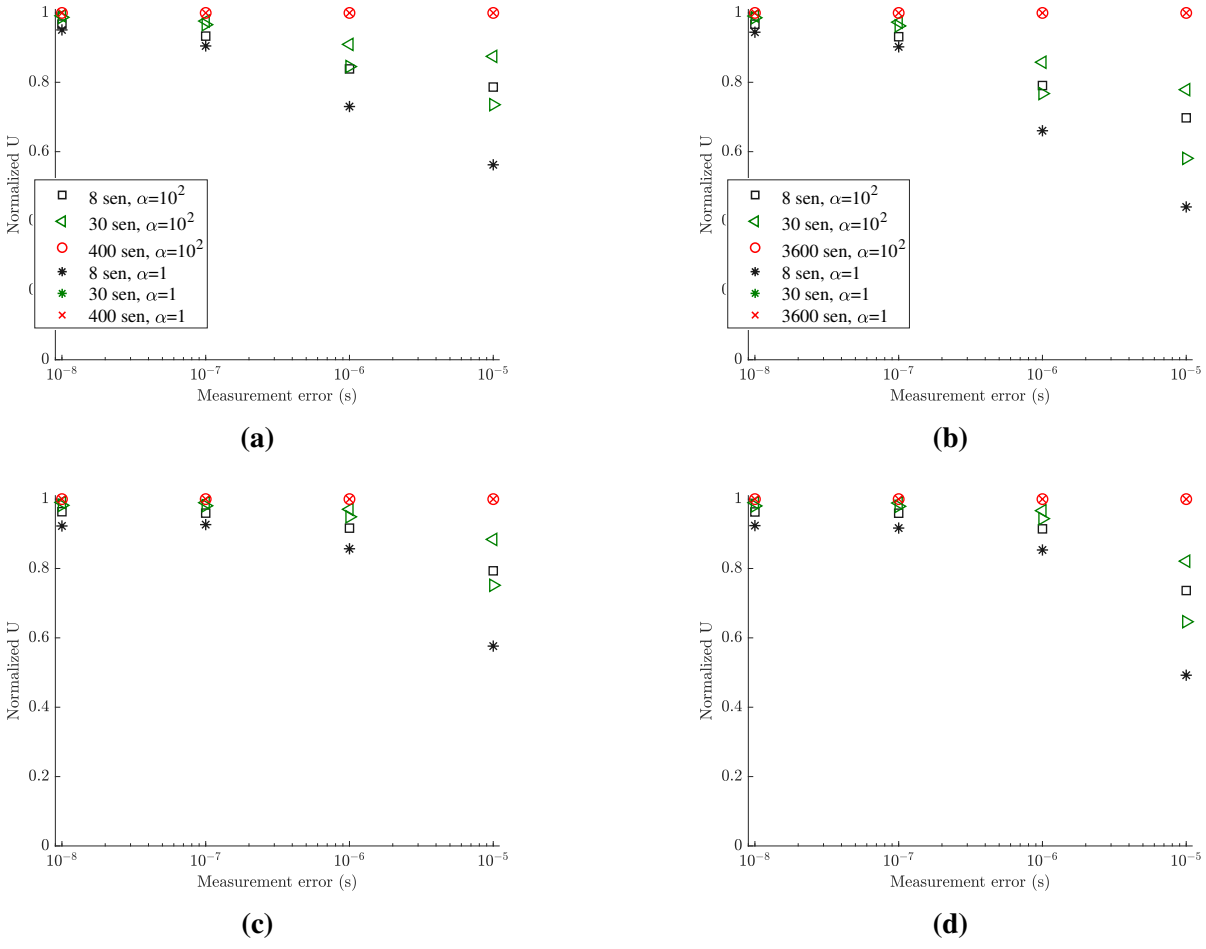

Fig. 2.7. Normalized information entropy versus measurement error for 8, 30 and N_{all} sensors ($N_{all} = 440$ and 3660 respectively for the coarse and fine mesh), for $\alpha = 10^2$ and $\alpha = 1$; (a,b) $\sigma_e = \sigma_\epsilon = 0.001$, (c,d) $\sigma_e = \sigma_\epsilon = 0.01$, (a,c) coarse mesh, (b,d) fine mesh.

2.6.2 Optimal Locations of Strain Sensors

Optimal strain sensor positions for 8 and 30 sensors are shown in Fig. 2.8 and Fig. 2.9 for model/prediction errors $\sigma_e = \sigma_\epsilon = 0.001$ and 0.01, respectively. The optimal sensor locations are compared for different values of the measurement errors. Comparing Fig. 2.8(a) and (b) for eight sensors and Fig. 2.8(c) and (d) for 30 sensors, it can be seen that the results for the coarse and the fine mesh are very similar for a given measurement error. For very small measurement error, sensors are placed towards the right edge of the plate where strains are small compared to the strains at the left side and middle area of the plate. The reason is that the OSP methodology for predicting strain responses in all finite elements of the plate has a tendency to spread the sensors to cover the whole surface of the plate as long as the quality of information is very good over the plate surface. In the very small measurement error case, the errors are much smaller than the intensity of the strains and so signal to noise ratio is high and most strain locations in the plate are informative. For large measurement errors, placing sensors in the right edge is avoided since the signal to noise ratio decreases and the quality of information from sensors placed towards the right edge is substantially deteriorated. For higher model/prediction error values of $\sigma_e = \sigma_\epsilon = 0.01$ (see Fig. 2.9) there is a tendency that the sensor moves from left to the right, towards strains with smaller intensities. This is due to the fact that higher model/prediction error dominates the overall error, with the size of measurement error playing a lesser role in the optimal sensor placement design. In this case, since the model error is assigned in each position as a fraction of the intensity of the strains measured in the respective positions, all positions on the surface plate do provide similar information with the noise (here model error) to signal ratio to be the same, thus the sensors towards the left edge are equally counted in the optimal sensor placement methodology.

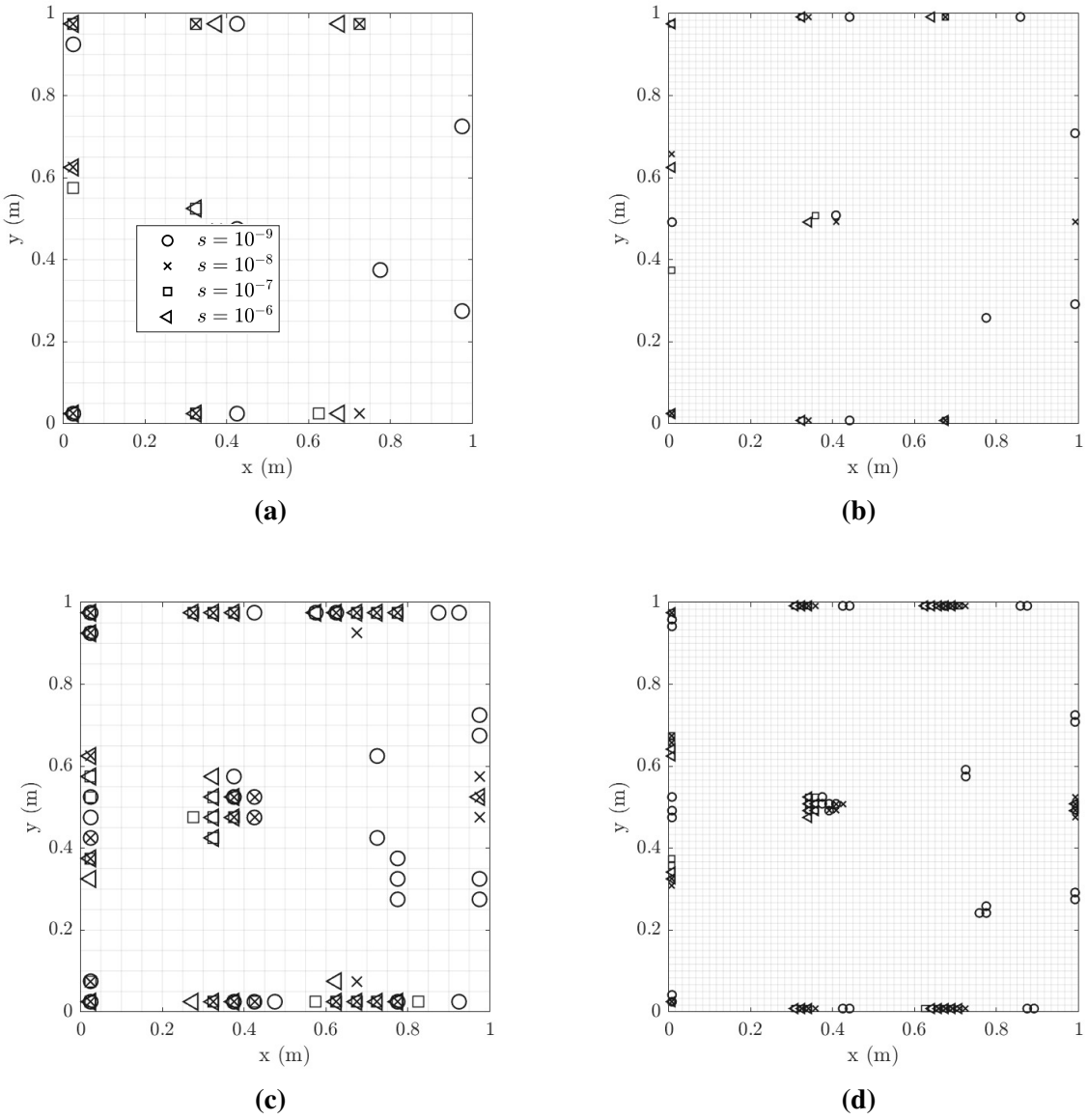

Fig. 2.8. Best sensor positions obtained with model/prediction error $\sigma_e = \sigma_\epsilon = 0.001$ for 8 sensor for (a) coarse and (b) fine mesh, and for 30 sensor for (c) coarse and (d) fine mesh.

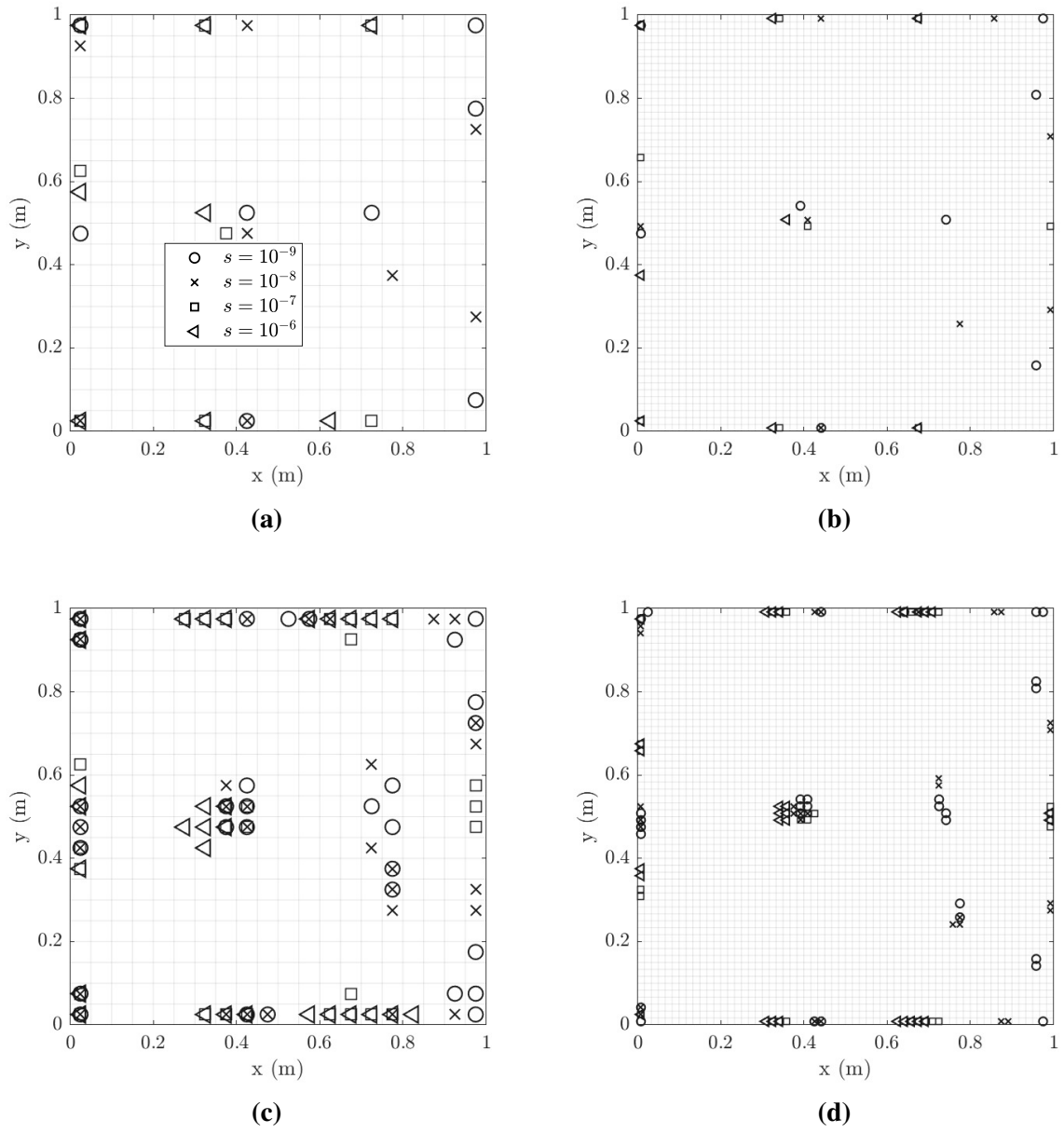

Fig. 2.9. Best sensor positions obtained with model/prediction error $\sigma_e = \sigma_\epsilon = 0.01$ for 8 sensor for (a) coarse and (b) fine mesh, and for 30 sensor for (c) coarse and (d) fine mesh.

2.6.3 Effect of Spatial Correlation of Model Error

It is observed in Fig. 2.8(c) and (d) and Fig. 2.9(c) and (d) that the 30 sensors placed optimally in the structure are clustered in specific regions on the plate surface. The size of each clustering region is proportional to the size of the finite element used for coarse and fine mesh. So clustering in similar for both coarse and fine mesh sizes. To avoid sensor clustering one has to use the spatial correlation function in Eq. 2.29 [57] for the prediction error.

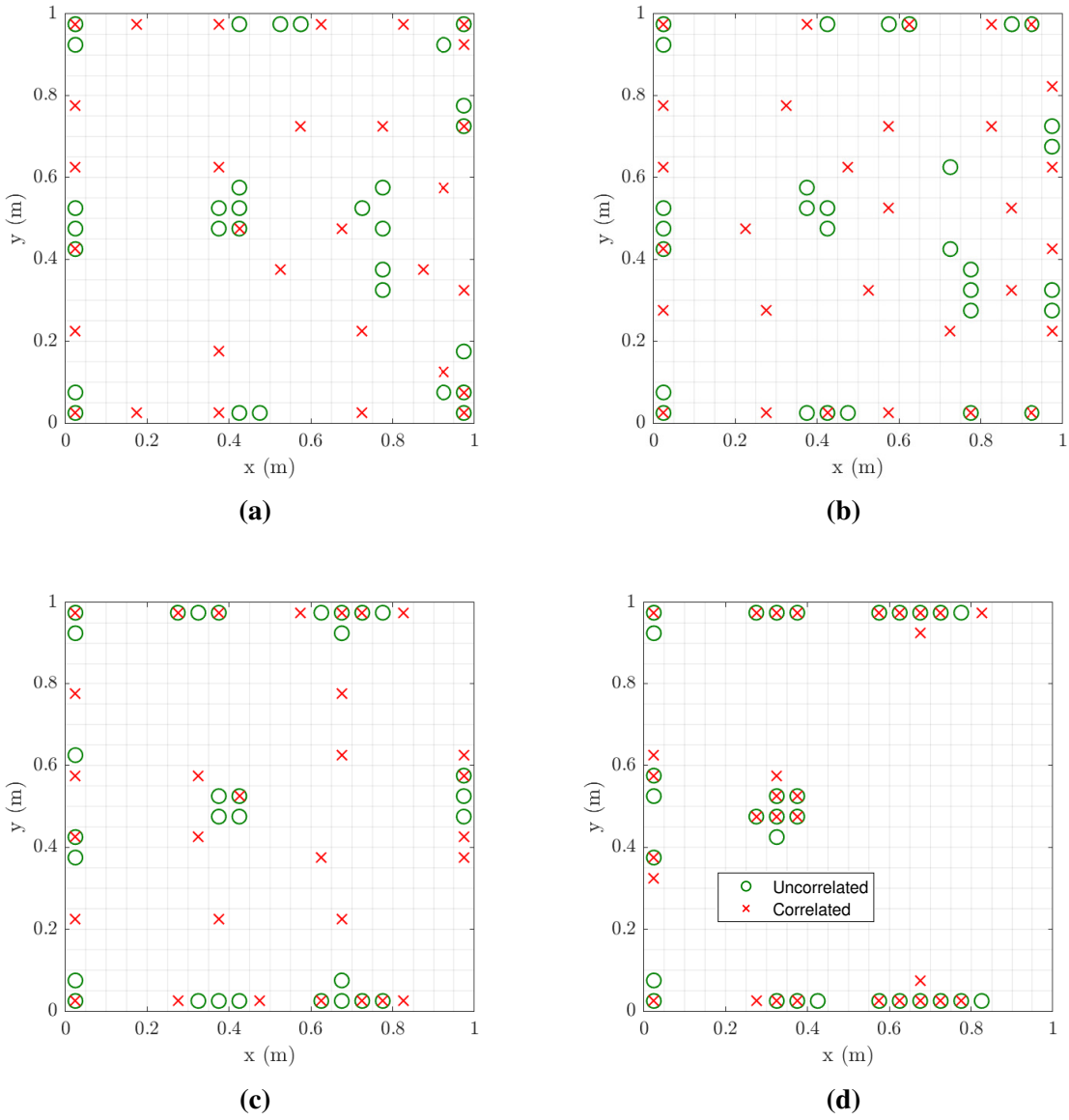

Fig. 2.10. Comparison of optimal sensor placement for 30 sensors for the spatially uncorrelated ($\lambda = 0$) and correlated ($\lambda = 0.1$) cases; $\sigma_e = \sigma_\epsilon = 0.01$, $\alpha = 10^2$ and measurement error (a) very small ($s = 10^{-9}$), (b) small ($s = 10^{-8}$), (c) moderate ($s = 10^{-7}$), (d) large ($s = 10^{-6}$).

The effect of correlation in the model error is next investigated as a function of the size of measurement and model error. Fig. 2.10 compares the optimal sensor locations for 30 sensors for spatially uncorrelated ($\rho = 0$) and correlated ($\rho = 0.1$) prediction error models for different values of the measurement error and for model/prediction error equal to $\sigma_e = \sigma_\varepsilon = 0.01$. The results clearly indicate that for the correlated case clustering is avoided and the 30 sensors are more uniformly distributed over the surface of the plate for relatively small to moderate measurement error. This is due to the fact that the model error dominates the prediction error

for relatively small measurement error and thus the measurement error has a small effect on the design of optimal sensor locations. However, for large measurement error, clustering persists (Fig. 2.10(d)) since the measurement error is the dominant source of error compared to the model error. Thus model error and as a result the effect of spatial correlation structure of the model error is insignificant and does not affect the design of the sensors for large ($s = 10^{-6}$) values of the measurement error. So the clustering problem reappears and the model error correlation structure has no effect on the optimal sensor placement.

2.6.4 Effectiveness of Optimal Sensor Configuration for Response Predictions

The effectiveness of the best sensor configuration is next investigated using simulated measurements. For this, simulated strain response time histories are generated from the model of the plate subjected to white noise input at location A (Fig. 2.1) and using up to eight contributing modes. The simulations are generated using a sampling period $\Delta t = 0.01$ seconds and the standard deviation $\sigma_{wn} = 1$ of a Gaussian white noise sequence. To simulate measurement error (noise from sensors), zero mean Gaussian white noise with standard deviation 1% of the simulated response at each time instant is added to generate the noise contaminated measurements. Alternatively, to simulate model error, the measured data are simulated using a model with mass values for all finite elements randomly perturbed by adding to the nominal mass values zero-mean Gaussian distributed values with standard deviation equal to 5% of the nominal mass values.

The relative errors between the strain responses predicted by the modal expansion technique given a fixed number of sensors and the simulated measurements are used to demonstrate the effectiveness of the optimal sensor configuration in the presence of measurement or model error. The relative strain error at each location is defined as the ratio of the root mean square error ϵ between the predicted and measured responses over the root mean square value (intensity) of the measured strain response time history, given by

$$\epsilon_{i,rel} = \frac{\sqrt{\frac{1}{N}\sum_{k=1}^{N}\left[\hat{z}_i\left(k\right) - z_i\left(k\right)\right]^2}}{\sqrt{\frac{1}{N}\sum_{k=1}^{N}\left[z_i\left(k\right)\right]^2}} \tag{2.38}$$

where N is the number of data points in the time histories, $\hat{z}_i\left(k\right)$ is the predicted values from the nominal model based on the modal expansion Eq. 2.10, and $z_i\left(k\right)$ is the simulated

"measurements" at the i-th DOF, and k indicates the time index corresponding to time instant $t_k = k\Delta t$.

Fig. 2.11(a) and (b) presents the results for the relative errors of the optimal sensor configuration design for eight sensors corresponding to information gain value of $U = 8.38$ (92% of the maximum that could be achieved by fully populating the plate surface with strain sensors), and for two alternative sub-optimal sensor configurations for eight sensors (Fig. 2.11(c) and (d))) corresponding to lower information gain value of $U = 7.4$ (81%) and for higher number of 10 sensors (Fig. 2.11(e) and (f)) also corresponding to lower information gain value of $U = 7$ (80%). For the optimal sensor configuration cases the predictions are quite reliable with relative errors less than 2% and 0.8% over 90% of the surface of the plate for measurements simulated for noise and model error, respectively. The errors are higher over 10% of the surface close to the right edge where strain level are very low with high noise to signal ratio in the measured time histories. For both measurement errors (Fig. 2.11(a),(c) and (e)) and model/prediction error (Fig. 2.11(b),(d) and (f)), the predictions from the optimal sensor configuration (Fig. 2.11(a) and (b)) are consistently better than the predictions obtained from the sub-optimal sensor configurations since the relative errors based on the optimal sensor configuration are overall lower than the relative errors obtained from the sub-optimal sensor configurations over the surface of the plate. In particular, for the case of measurement error, the predictions based on a sensor configuration with higher number of 10 sub-optimal sensors (Fig. 2.11(e)) are significantly worse than the predictions from the optimal configuration containing less number of eight sensors (Fig. 2.11(a)), emphasizing the need of a cost-effective design of the sensor network in a structure. It is also clear that the errors in response predictions obtained at the measured locations is lower than errors in the predictions at other non-measured locations. Finally, it should be noted that there exist sensor configurations corresponding to information gain values closer to the minimum information gain (not shown in the figures) that provide relative errors higher than 100% which means that predictions can be completely unreliable from such non-optimal sensor configurations.

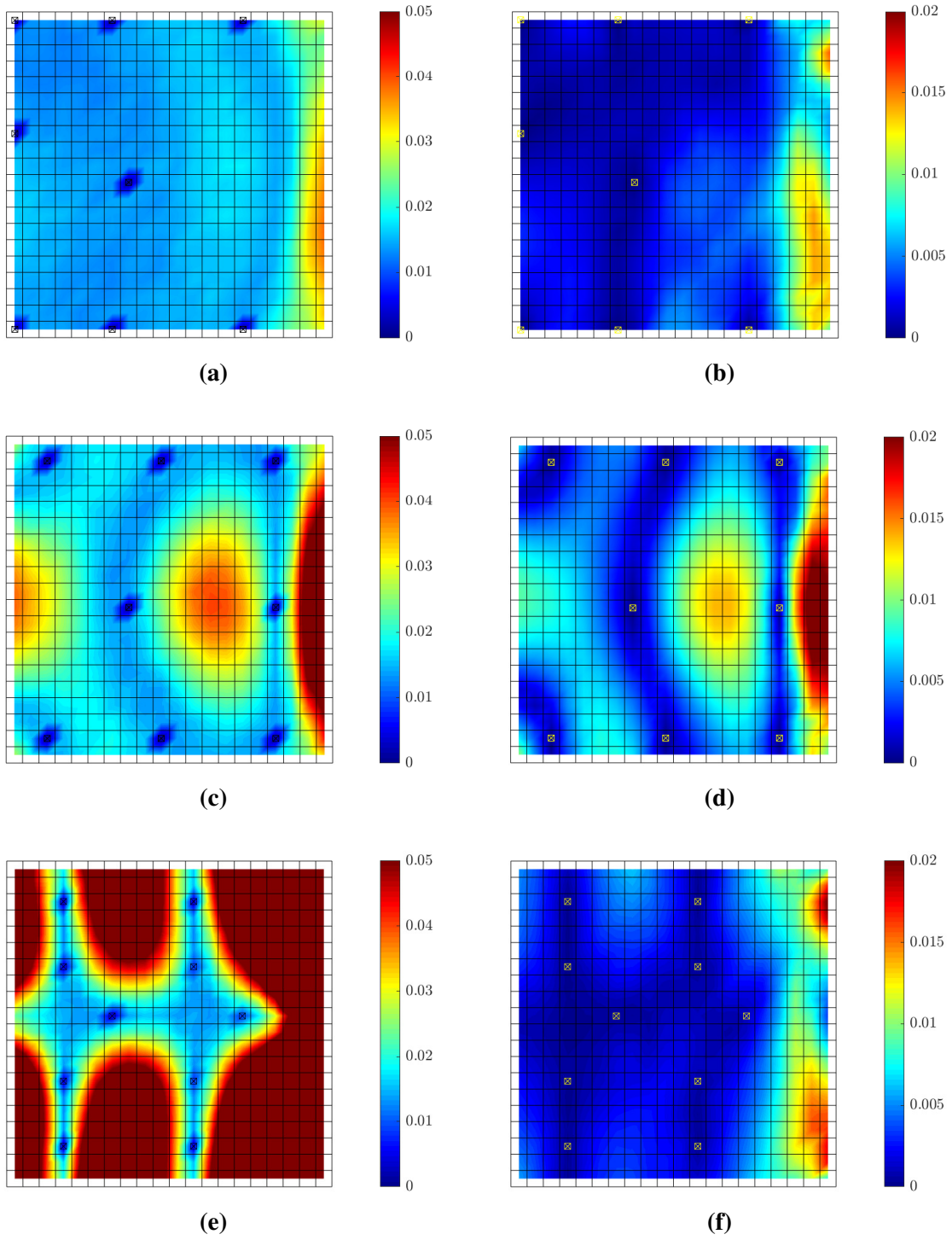

Fig. 2.11. Relative error in response predictions with 8 optimally located strain sensors corresponding to information gain $U = 8.38$ (92%) (a,b), with alternative sensor locations with 8 sensors corresponding to information gain $U = 7.4$ (81%) (c,d) and with 10 sensors corresponding to information gain $U = 7$ (77%) (e,f); (a,c,e) for measurement error, (b,d,f) for model error. The location of sensors are shown with the box-cross symbols in each subfigure. ($\sigma_e = \sigma_\epsilon = 0.01$, $s = 10^{-7}$ and $\alpha = 10^2$).

Fig. 2.12 presents relative error results for two optimal sensor configurations for seven

sensors designed using large prior uncertainty ($\alpha = 10^2$) in the modal coordinates and for two choices of the covariance matrix S of the prior distribution. The first case corresponds to covariance matrix of the prior proportional to the non-diagonal covariance matrix of the modal coordinates obtained for white noise input (see Eq. 2.32), while the second choice corresponds to diagonal isotropic covariance matrix with strength proportional to the variance of the first modal coordinate ($S = \alpha^2 Q_\xi(1,1)I$). In the first case the relative intensity of the modal coordinates is taken into account in the definition of the prior covariance matrix, while in the second case this relative intensity is ignored and all modal coordinates are equally considered in the definition of the covariance matrix S of the prior distribution. It can be seen that the error distribution over the plate surface differs for the two optimal designs. Moreover, the relative errors in the predictions obtained from the first optimal sensor configuration are lower than the errors obtained from the second optimal sensor configuration, signifying the importance in considering the intensity of each mode, affected by the excitation frequency content, in the choice of the prior.

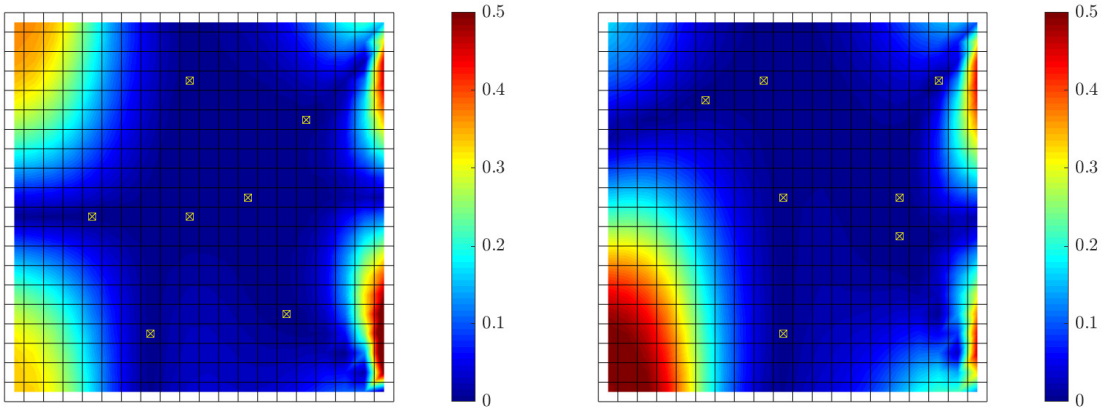

(a) **(b)**

Fig. 2.12. Relative error in response prediction with 7 best sensor positions (a) with $S = \alpha^2 Q_\xi$ and (b) with $S = \alpha^2 Q_\xi(1,1)I$. ($\sigma_e = \sigma_\epsilon = 0.01$, $s = 10^{-7}$ and $\alpha = 10^2$).

2.6.5 Robustness to Model/Prediction and Measurement Error Uncertainties

Robust optimal sensor placement results are next obtained by taking into account the uncertainties in the model/prediction error parameters σ_e and σ_ε and the measurement error parameter s. Specifically, the re-parameterization $\sigma_e = \sigma_\varepsilon = 10^{-\beta_\sigma}$ and $s = 10^{-\beta_s}$ is used and uniform uncertainty is assigned in the values of β_σ and β_s with bounds that cover the previously lower and upper values of these parameters. The distributions are selected to be

$\beta_\sigma \sim U(2,3)$, $\beta_s \sim U(6,9)$, where $U(a,b)$ denotes a uniform distribution with lower bound a and upper bound b. This case accounts for the realistic scenario of uncertain model/prediction and measurement errors assigned in the formulation, arising mostly from the uncertain excitation intensities and frequency content that have to be taken into account in the design of the optimal sensor configuration. The uncertain parameters β_σ and β_s are included in the nuisance parameter set φ and their uncertainty is taken into account in the generalized utility function introduced in Eq. 2.25. The sparse grid algorithm [86] of order 4 is used to evaluate the integrals in Eq. 2.25.

Results for the maximum robust information gain values are compared in Fig. 2.13(a) and (b) with the corresponding maximum information gain values obtained by fixing the uncertain error parameters values (σ_e, σ_ε and s) to the minimum values by selecting $\beta_\sigma = 3$ and $\beta_s = 9$, as well as maximum values by selecting $\beta_\sigma = 2$ and $\beta_s = 6$. The corresponding optimal sensor locations are compared in Fig. 2.13(c) and (d). It can be seen that the robust information gain estimates differ from the estimates obtained from the fixed minimum and maximum values of the model/prediction and measurement error parameters. As expected the results for the robust information gain values are found between the information gain values using the minimum or maximum values of the error parameters. The optimal sensor configuration proposed by the robust OSP methodology differs from the optimal sensor configuration obtained by the OSP methodology corresponding to minimum values of the error parameters. Specifically, for the very small model/prediction error case the sensors tend to be placed towards the right edge of the plate since, despite the smaller strain intensity in this area, the noise to signal ratio is very small and thus the measurements from this right edge are also informative. The robust OSP design seems to be closer to the OSP design corresponding to the maximum values of the error parameters. This is due to the high measurement and model/prediction errors that are taken into account in the assigned probability distribution of the error parameters. As a result, sensors designed according to the robust information gain are placed farther away from the right edge of the plate due to larger noise to signal ratio in the locations close to the right edge.

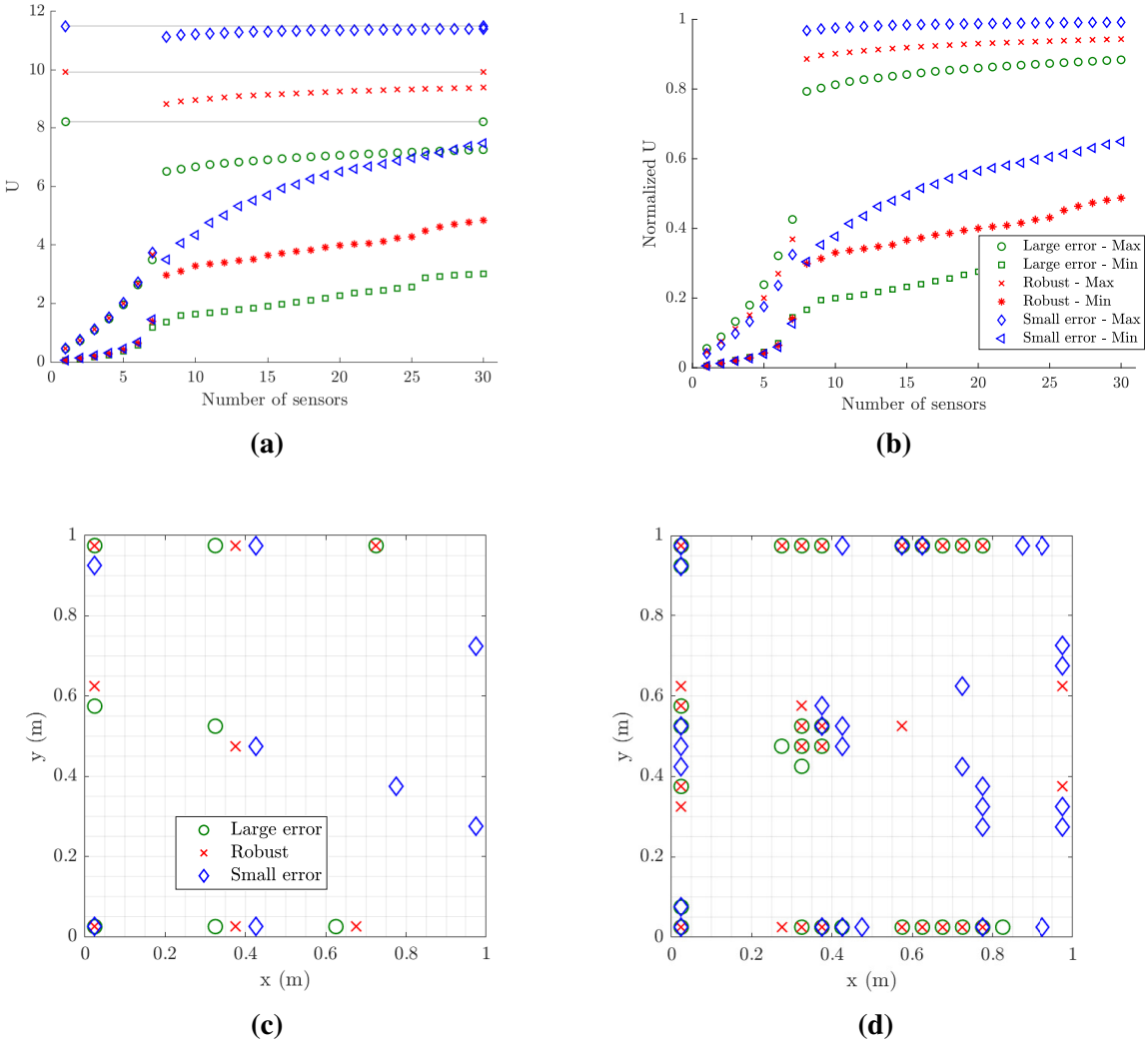

Fig. 2.13. Comparison of best SSP robust results with best SSP results obtained from large and small model/prediction and measurement error cases for the coarse mesh and strain sensors; (a) maximum utility values, (b) normalized utility values; Optimal sensor placement for (c) 8 sensors, and (d) 30 sensors.

2.7 Strain Predictions Using Displacement Observations

The methodology is next applied to the case where displacement sensors are used for predicting strains at the midpoints of all finite elements of the coarse mesh. Displacement sensors measure out-of-plane displacements at the nodes of the mesh, perpendicular to the plate surface. As before, the number of contributing modes are kept to eight. For choosing the measurement and model/prediction error parameters, the intensities of the displacement responses at all nodes of the finite element mesh to a white noise excitation at the right lower corner of the plate (point A in Fig. 2.1) are shown in Fig. 2.14. Based on the results in this figure the

measurement errors can now be selected as in Table 2.3.

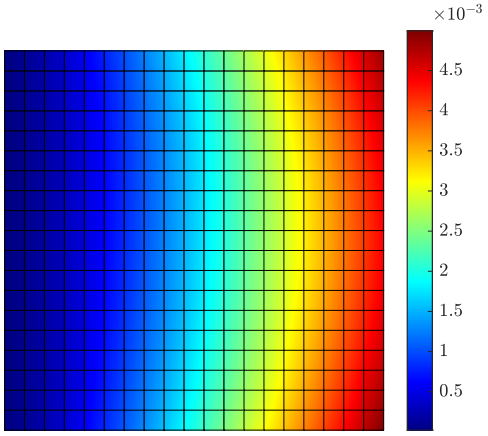

Fig. 2.14. Intensities of the displacement observation $Q_y^{1/2}$ as a function of the number of modes for the coarse mesh.

Table 2.3: Different measurement errors assumed. $d_{\min} = Q_{z,min}^{1/2} \approx 10^{-4}$ is the minimum value of the node displacements to discrete white noise input with σ_{wn} that cover 92% of the plate surface. $d_{\max} = Q_{z,max}^{1/2} \approx 5 \times 10^{-3}$ is the maximum value of the displacement to same white noise input.

Measurement Error	s	$s/d_{\min}$	$s/d_{\max}$
Very small	10^{-7}	10^{-3}	2×10^{-5}
Small	10^{-6}	10^{-2}	2×10^{-4}
Moderate	10^{-5}	10^{-3}	2×10^{-4}
Large	10^{-4}	10^{0}	2×10^{-2}

Uncertainties in the model/prediction error parameters σ_e and σ_ε and the measurement error parameter s are accounted for in the sensor placement design. As before, the re-parameterization $\sigma_e = \sigma_\varepsilon = 10^{-\beta_\sigma}$ and $s = 10^{-\beta_s}$ is used and uniform uncertainty is assigned in the values of β_σ and β_s with bounds to cover the lower and upper values of these parameters shown in Table 2.3. Thus, the distributions are selected to be $\beta_\sigma \sim U(2,3)$, $\beta_s \sim U(4,7)$.

Results for the maximum robust information gain values are compared in Fig. 2.15(a) and (b) with the corresponding maximum information gain values obtained for very small errors ($\beta_\sigma = 3$ and $\beta_s = 7$) as well as large errors ($\beta_\sigma = 2$ and $\beta_s = 4$). The corresponding optimal sensor locations are compared in Fig. 2.15(c) for eight sensors and Fig. 2.15(d) for 30 sensors. Comparing the results for the robust error case with the ones for small and large error cases, the results are found to be qualitatively similar to the ones obtained for strain sensor measurements in Fig. 2.13. Specifically, the robust sensor placement design differs significantly from the design based on small error case, while it is closer to the sensor placement design based

on the large error case. The optimal location of displacement sensors for the small error case tends to also cover the left fixed edge of the plate where displacements are relatively small compared to the middle and right locations of the plate since the noise to signal ratio from these displacement locations is small and thus the measured displacements, despite their relative small values, are informative. The optimal sensor placement for large error tends to move towards the left edge of the plate where the displacements are usually large and the noise to signal ratio is small. The locations close to the left edge (fixed support) of the plate are avoided in this case due to high noise to signal ratio for large measurement errors.

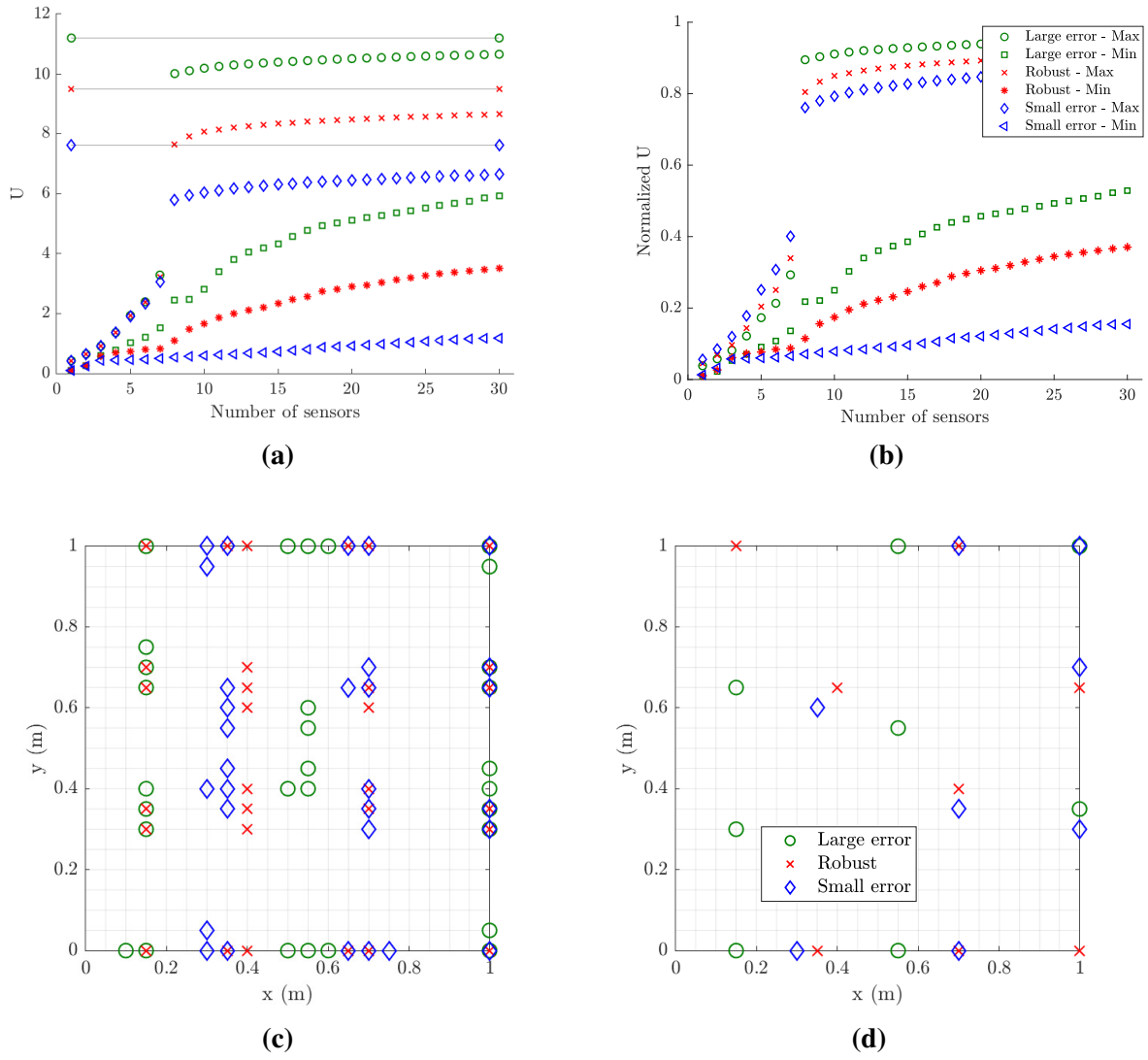

Fig. 2.15. Comparison of best SSP robust results with best SSP results obtained from large and small model/prediction and measurement error cases for the coarse mesh and displacement sensors; (a) maximum utility values, (b) normalized utility values; Optimal sensor placement for (c) eight sensors, and (d) 30 sensors.

Fig. 2.16(a) and (b) presents the results for the relative errors for the optimal displacement

sensor configuration for 8 sensors corresponding to information gain value of $U = 7.3$ (84%), and for two alternative sub-optimal sensor configurations for 8 sensors (Fig. 2.16(c) and (d)) corresponding to lower information gain value of $U = 6.8$ (78%) and for higher number of 10 sensors (Fig. 2.16(e) and (f)) also corresponding to lower information gain value of $U = 6.6$ (75%). Comparing the effectiveness of the optimal and the two sub-optimal sensor configurations, the results are qualitatively similar to the ones presented in Fig. 2.11(a) and (b) for the strain sensor case. The relative errors for the optimal sensor configurations are lower than the relative errors for the two sub-optimal sensor configurations for both 8 and 10 sensors and for both measurement (Fig. 2.16(a),(c) and (e)) and model (Fig. 2.16(b),(d) and (f)) errors, pointing out the superiority of the optimal sensor configuration for reliable response predictions.

Comparing Fig. 2.15(a) and (b) with Fig. 2.13(a) and (b), it is clear that the information gain values for strain sensors in Fig. 2.13(a) and (b) are higher than the information gain values for displacement sensors in Fig. 2.15(a) and (b). Thus, among the two type of strain and displacement sensors it is preferred to place in the structure strain sensors. This is also confirmed from the relative errors values for the optimal sensor configuration obtained for the displacement sensors in Fig. 2.16(a) and (b). These relative errors reach values as high as 13% and 1% for the simulated measurement error and the model/prediction error cases, respectively, which are higher than the corresponding values of 2% and 0.8% for strain sensors presented in Fig. 2.11(a) and (b). However, this result holds for the specific plate structure analysed and cannot be generalized for other applications. An investigation for the best combination of displacement and strain sensors has to be performed for each application. The methodology proposed in this work can be extended to fuse sensors by optimally placing simultaneously displacement and strain sensors for gaining the maximum information for response predictions with the smallest uncertainty.

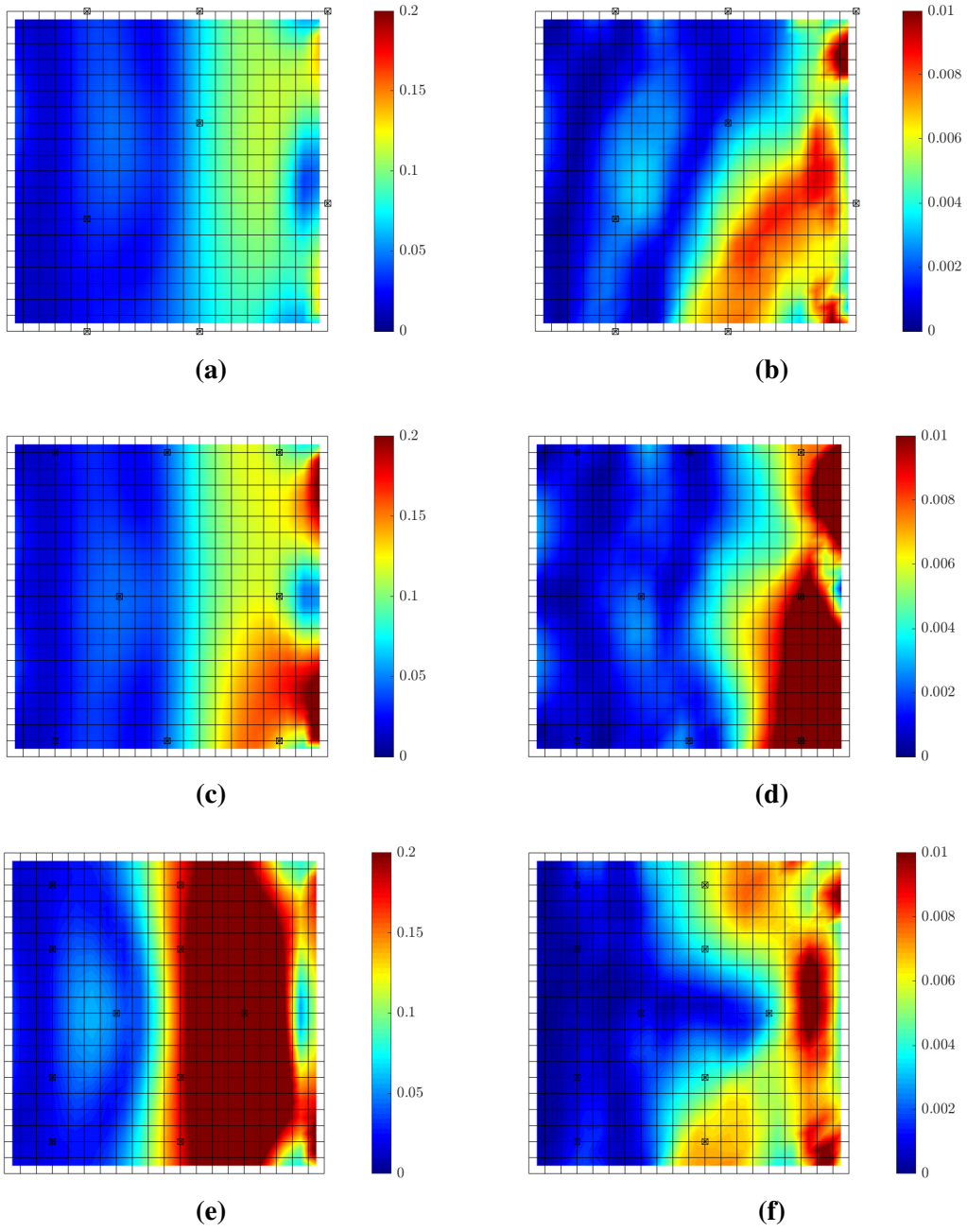

Fig. 2.16. Relative error in response prediction with eight optimally located displacement sensors corresponding to information gain $U = 7.3$ (84%) (a,b), with alternative sensor locations with eight sensors corresponding to information gain $U = 6.8$ (78%) (c,d) and with 10 sensors corresponding to information gain $U = 6.6$ (75%) (e,f); (a,c,e) for measurement error, (b,d,f) for model error. The location of sensors are shown with the box-cross symbols in each subfigure. ($\sigma_e = \sigma_\epsilon = 0.01$, $s = 10^{-5}$).

2.8 Conclusions

Using information and utility theory, the optimal sensor placement problem for reliable virtual sensing and response reconstruction is formulated based on the modal expansion technique as a problem of maximizing a multi-dimensional integral quantifying the information gain from the data. The framework addresses the challenging case of output-only vibration measurements and provides optimal sensor configurations that are robust to uncertainties in model parameters as well as in model/prediction and measurement errors. Such uncertainties are usually not known in the initial optimal experimental design phase and thus need to be postulated using prior distributions. Sparse grid or Monte Carlo techniques can be used to estimate the multi-dimensional integral that arises in the robust formulation. Computationally efficient heuristic forward and backward sequential sensor placement strategies are combined to estimate the near optimal sensor locations. Useful expressions are derived for the effect of measurement and model/prediction errors on the information gained by a sensor configuration. As these errors increase, it was shown analytically that the information gain decreases. In addition, it was analytically derived that the information increases as one adds sensors in the structure, as it would be intuitively expected.

The methodology was demonstrated by designing the optimal strain or displacement sensors over a plate model of a structure. A thorough investigation was conducted on the effect of measurement and model/prediction errors, the size of the prior uncertainty in the modal coordinates, the spatial correlation structure of the model error, the uncertainties in model/prediction and measurement errors on the optimal sensor placement and the variation of the highest and lowest utility (information gain) values as a function of the number of sensors. The issue of the effect of the excitation characteristics on the design of the optimal sensor configuration was also pointed out. Excitation characteristics (location, intensity and frequency content of excitations) affect response intensities and thus the selection of the level of measurement errors due to sensor accuracy and the model/prediction error levels due to different mechanisms activated/re-activated from different excitation levels and/or excitation frequencies. It was demonstrated that sensor accuracy (measurement error), related to noise to signal ratio, affected the optimal placement of sensors. The model/prediction error has also an effect on the optimal design. In particular, when model/prediction error dominates the measurement error, the accuracy of the sensors plays insignificant role in the design of the optimal sensor

configuration. The level of noise to signal ratio are not known a priori since the intensity and frequency content of the excitation and thus the level of measured response is not known. The size of model/prediction errors due to model inadequacy is also not known a priori. Thus a robust design is more rational to use in order to better account for uncertainty in measurements and model/prediction errors. Such robust design over wide uncertainty bounds of errors leads to optimal sensor placement designs that are closer to the ones obtained for high measurement and model/prediction errors, provided that measurement error dominates the model/prediction error. The effectiveness of the optimal designs was validated against sub-optimal ones by comparing errors in the predictions between the modal expansion method and simulated noise and/or model error contaminated measurements. It was also found that strain measurements are slightly more informative than displacement measurements for virtual strain sensing for the specific application. The proposed information-based method can be extended to select the optimal sensor configuration that contains both displacement and strain sensors.

The proposed OSP methodology is appropriate to use for reliably reconstructing responses that are important for providing data-driven safety and performance estimates of systems, as well as reconstructing stress response time histories that are needed for predicting fatigue damage accumulation.

Appendix A. Proof of Eq. 2.18

Substituting Eq. 2.14 into the inner integral of Eq. 2.17 and using the properties of the logarithm ($\ln(A/B) = \ln A - \ln B$), one has

$$\begin{aligned}\int_Y \tilde{D}_i(\underline{\delta},\underline{\varphi},\underline{y})\, p(\underline{y},\underline{\varphi}|\underline{\delta})\, d\underline{y} &= \int_Y\int_Z p(z_i|\underline{y},\underline{\delta},\underline{\varphi})\ \ln p(z_i|\underline{y},\underline{\delta},\underline{\varphi})\, d\underline{z}_i\ \ p(\underline{y}|\underline{\varphi},\underline{\delta})\, d\underline{y} \\ &\quad - \int_Z \left[\int_Y p(z_i|\underline{y},\underline{\delta},\underline{\varphi})\, p(\underline{y}|\underline{\varphi},\underline{\delta})\, d\underline{y}\right]\ \ln p(z_i|\underline{\varphi})\, d\underline{z}_i \qquad \text{(A.1)} \\ &= \int_Y\int_Z p(z_i|\underline{y},\underline{\delta},\underline{\varphi}) \ln p(z_i|\underline{y},\underline{\delta},\underline{\varphi})\, d\underline{z}_i\ \ p(\underline{y}|\underline{\varphi},\underline{\delta})\, d\underline{y} \\ &\quad - \int_Z p(z_i|\underline{\varphi},\underline{\delta})\ \ln p(z_i|\underline{\varphi})\, d\underline{z}_i \qquad \text{(A.2)}\end{aligned}$$

where the last equality is obtained by interchanging the order of integration of the double integral in the second term of Eq. A.1 and noting that

$$\int_Y p(z_i|\underline{y},\underline{\delta},\underline{\varphi})\, p(\underline{y}|\underline{\varphi},\underline{\delta})\, d\underline{y} = p(z_i|\underline{\delta},\underline{\varphi}) \qquad \text{(A.3)}$$

Introducing the prior information entropy

$$H_{z_i}\left(\underline{\varphi}\right) = -\int_Z p(z_i|\underline{\varphi},\underline{\delta})\ \ln p(z_i|\underline{\varphi})\ d\underline{z}_i \tag{A.4}$$

of $z_i(t)$ given the model parameter set $\underline{\varphi}$, and the posterior information entropy

$$H_{z_i|D}(\underline{y},\underline{\delta},\underline{\varphi}) = -\int_Z p(z_i|\underline{y},\underline{\delta},\underline{\varphi}) \ln p(z_i|\underline{y},\underline{\delta},\underline{\varphi})\ d\underline{z}_i \tag{A.5}$$

of $z_i(t)$ given the data $\underline{y}$ and the model parameter set $\underline{\varphi}$, the integral in Eq. A.2 simplifies to

$$\int_Y \tilde{D}_i(\underline{\delta},\underline{\varphi},\underline{y})\ p(\underline{y},\underline{\varphi}|\underline{\delta})d\underline{y} = -\int_Y H_{z_i|D}(\underline{y},\underline{\delta},\underline{\varphi})\ \ p(\underline{y}|\underline{\varphi},\underline{\delta})\ d\underline{y} + H_{z_i}\left(\underline{\varphi}\right) \tag{A.6}$$

Eq. 2.18 is readily obtained by substituting Eq. A.6 into Eq. 2.17.

Appendix B. Properties of Information Gain (Utility Function)

For notational convenience, in the following analysis the dependence of the quantities on the uncertain parameter set $\underline{\varphi}$ is dropped. From the mathematical structure of the covariance matrix $\Sigma_{z_i|D}(\underline{\delta})$ appearing in Eq. 2.12, one can readily observe that the quantity $\Sigma_{z_i|D}(\underline{\delta})$ is non-negative. Additionally, for four matrices $A_1 \in R^{n\times n}$, $B_1 \in R^{m\times m}$, $V \in R^{m\times n}$ and $U \in R^{m\times n}$, the following useful property for the inverse of the sum of two matrices holds

$$(U^T B_1 V + A_1)^{-1} = A_1^{-1} - A_1^{-1}U^T(B_1 + V A_1^{-1}U^T)^{-1}V A_1^{-1} \tag{B.1}$$

Setting $A_1 = S^{-1}$, $B_1 = Q_e^{-1}$, $U = V = L(\underline{\delta})\Phi$ and applying Eq. B.1, the covariance matrix $\Sigma_{z_i|D}(\underline{\delta})$ in Eq. 2.12 can be written in the alternative form

$$\Sigma_{z_i|D}(\underline{\delta}) = \underline{\psi}_i^T S\ \underline{\psi}_i - \underline{\psi}_i^T S\Phi^T L^T(\underline{\delta})\left[L(\underline{\delta})\Phi S\Phi^T L^T(\underline{\delta}) + Q_e\right]^{-1} L(\underline{\delta})\Phi S\underline{\psi}_i + Q_{\varepsilon_i} \tag{B.2}$$

The ratio between the posterior and prior covariance matrices in Eq. 2.24 can thus be simplified in the form

$$r_{z_i|D}\left(\underline{\delta}\right) = 1 - \frac{(L(\underline{\delta})\Phi S\underline{\psi}_i)^T\left[L(\underline{\delta})\Phi S\Phi^T L^T(\underline{\delta}) + Q_e\right]^{-1}(L(\underline{\delta})\Phi S\underline{\psi}_i)}{\underline{\psi}_i^T S\ \underline{\psi}_i + Q_{\varepsilon_i}} \tag{B.3}$$

Taking into account that the matrices S and $L(\underline{\delta})\Phi S\Phi^T L^T(\underline{\delta}) + Q_e$ are semi-positive defi-

nite and that $Q_{\varepsilon_i} > 0$, it can be concluded that the second term in Eq. B.3 is non-negative and thus the value of the ratio is always less than or equal to one, i.e., $r_{z_i|D}\left(\underline{\delta}\right) \leq 1$. As a result, the utility function, quantifying the information gain from the data for least uncertainty in the response prediction, is always greater than or equal to zero.

Appendix B.1. Effect of Modelling and Measurement Errors

Next we examine the effects of measurement and model errors quantified by the matrices Q_e and Q_ε. The higher the value of the prediction error variance Q_{ε_i}, the higher the value of the denominator $\underline{\psi}_i^T S\ \underline{\psi}_i + Q_{\varepsilon_i}$ in Eq. B.3 and the smaller the information gained by the sensor configuration. Let now $Q_e^{'}$ be an error covariance matrix similar to Eq. 2.30, corresponding to higher values of the measurement and model error, so that it admits the representation $Q_e^{'} = Q_e + \Delta Q_e$, where ΔQ_e is positive definite matrix. This representation is true for the case where the values of σ_e and/or σ_{em} in Eq. 2.30 are increased to represent higher measurement and/or modeling error. Substituting $Q_e^{'}$ in place of Q_e in Eq. B.3 and using the expansion Eq. B.1 for the inverse of $[L(\underline{\delta})\Phi S\Phi^T L^T(\underline{\delta}) + Q_e^{'}] = [L(\underline{\delta})\Phi S\Phi^T L^T(\underline{\delta}) + Q_e + \Delta Q_e]$ by setting $A = [L(\underline{\delta})\Phi S\Phi^T L^T(\underline{\delta}) + Q_e]$, $B = \Delta Q_e$ and $U = V = I$, the following expression for the new ratio $r_{z_i|D}^{'}\left(\underline{\delta}\right)$ corresponding to the error covariance matrix $Q_e^{'}$ arises

$$r_{z_i|D}^{'}\left(\underline{\delta}\right) = r_{z_i|D}\left(\underline{\delta}\right) + \frac{\underline{g}^T\left[\Delta Q_e + (L(\underline{\delta})\Phi S\Phi^T L^T(\underline{\delta}) + Q_e)^{-1}\right]^{-1}\underline{g}}{\underline{\psi}_i^T S\ \underline{\psi}_i + Q_{\varepsilon_i}} \tag{B.4}$$

where $\underline{g} = (L(\underline{\delta})\Phi S\Phi^T L^T(\underline{\delta}) + Q_e)^{-1}(L(\underline{\delta})\Phi S\underline{\psi}_i)$. The numerator in the second term in the right hand side of Eq. B.4 is positive due to the fact that both the matrices ΔQ_e and $(L(\underline{\delta})\Phi S\Phi^T L^T(\underline{\delta}) + Q_e)$ are positive definite matrices. Thus, the ratio $r_{z_i|D}^{'}\left(\underline{\delta}\right) > r_{z_i|D}\left(\underline{\delta}\right)$ which implies that the information gain decreases as the measurement and model/prediction errors increase. As the model or measurement errors σ_e, σ_ε and σ_{em} become very large (in the limit as errors approach infinity), the ratio $r_{z_i|D}(\underline{\delta})$ between the posterior and prior covariance matrices approach zero and the information gain is zero, independent of the number of sensors placed in the structure.

Appendix B.2. Utility Versus Number of Sensors

Consider a sensor configuration $\underline{\delta}$ and a new sensor configuration $\underline{\delta}_1$ which consists of the sensors in the configuration $\underline{\delta}$ and one additional sensor placed in the structure. We will show that the utility value for the sensor configuration $\underline{\delta}_1$, containing an extra sensor, cannot be

lower than the utility value of the sensor configuration $\underline{\delta}$, that is, $U_i(\underline{\delta}_1) \geq U_i(\underline{\delta})$. Let $L(\underline{\delta}_1)$ and $\tilde{Q}_e$ be the sensor locator matrix and the covariance error matrix in Eq. 2.24 for $r_{z_i|D}(\underline{\delta}_1)$ corresponding to the augmented sensor configuration $\underline{\delta}_1$. Then one has the partitions

$$L^T(\underline{\delta}_1) = \left[\begin{array}{cc} L^T(\underline{\delta}) & \underline{\ell}_1 \end{array} \right], \quad \tilde{Q}_{1,e} = \left[\begin{array}{cc} Q_e & \underline{q}_1 \\ \underline{q}_1^T & Q_0 \end{array} \right] \quad \text{and} \quad \tilde{Q}_{1,e}^{-1} = \left[\begin{array}{cc} \tilde{Q}_e^{-1} & \underline{p}_1 \\ \underline{p}_1^T & p_0^{-1} \end{array} \right] \tag{B.5}$$

where using the properties of the inverse of a partitioned matrix $\tilde{Q}_e$ one has

$$p_0 = Q_0 - \underline{q}_1^T Q_e^{-1} \underline{q}_1 \tag{B.6}$$

$$\tilde{Q}_e = Q_e - \underline{q}_1 Q_0^{-1} \underline{q}_1^T \tag{B.7}$$

$$\tilde{Q}_e^{-1} = Q_e^{-1} + \Delta\tilde{Q}_e \tag{B.8}$$

$$\Delta\tilde{Q}_e = Q_e^{-1} \underline{q}_1 [Q_0 - \underline{q}_1^T Q_e^{-1} \underline{q}_1]^{-1} \underline{q}_1^T Q_e^{-1} \tag{B.9}$$

and $\underline{p}_1$ depends on the partitions of $\tilde{Q}_{1,e}$. Eq. B.7 was derived using the identity in Eq. B.1. Using the third of Eq. B.5 and Eq. B.7, the quantity $L^T(\underline{\delta}_1) Q_{1,e}^{-1} L(\underline{\delta}_1)$ involved in the ratio $r_{z_i|D}(\underline{\delta}_1)$ simplifies to

$$L^T(\underline{\delta}_1) Q_{1,e}^{-1} L(\underline{\delta}_1) = \left[\begin{array}{cc} L^T(\underline{\delta}) & \underline{\ell}_1 \end{array} \right] \left[\begin{array}{cc} \tilde{Q}_e^{-1} & \underline{p}_1 \\ \underline{p}_1^T & p_0^{-1} \end{array} \right] \left[\begin{array}{c} L(\underline{\delta}_1) \\ \underline{\ell}_1^T \end{array} \right] \tag{B.10}$$

$$= \left[\begin{array}{cc} L^T(\underline{\delta}) & \underline{\ell}_1 \end{array} \right] \left[\begin{array}{cc} Q_e^{-1} & \underline{0} \\ \underline{0}^T & 0 \end{array} \right] \left[\begin{array}{c} L(\underline{\delta}) \\ \underline{\ell}_1^T \end{array} \right] + L^T(\underline{\delta}_1) \left[\begin{array}{cc} \Delta\tilde{Q}_e^{-1} & \underline{p}_1 \\ \underline{p}_1^T & p_0^{-1} \end{array} \right] L(\underline{\delta}_1) \tag{B.11}$$

$$= L^T(\underline{\delta}) Q_e^{-1} L(\underline{\delta}) + L^T(\underline{\delta}_1) \Delta\tilde{Q}_{1,e} L(\underline{\delta}_1) \tag{B.12}$$

where

$$\Delta\tilde{Q}_{1,e} = \left[\begin{array}{cc} \Delta\tilde{Q}_e^{-1} & \underline{p}_1 \\ \underline{p}_1^T & p_0^{-1} \end{array} \right] \tag{B.13}$$

Note that p_0 in Eq. B.6 is positive since it is the diagonal element of the inverse of a covariance matrix. Thus $\Delta\tilde{Q}_e$ in Eq. B.9 is a positive definite matrix and as a result $\Delta\tilde{Q}_{1,e}$ in Eq. B.13 is also a positive definite matrix.

Substituting in the numerator in Eq. 2.24 for the sensor configuration $\underline{\delta}_1$, setting $E = \Phi^T L^T(\underline{\delta}) Q_e^{-1} L(\underline{\delta}) \Phi + S^{-1}$ and using Eq. B.1 with $A = E$, $B = \Delta\tilde{Q}_{1,e}$ and $U = V = L(\underline{\delta}_1)\Phi$,

the ratio $r(\underline{\delta}_1)$ for the sensor configuration $\underline{\delta}_1$ takes the form

$$\begin{aligned} r_{z_i|D}(\underline{\delta}_1) &= \frac{\underline{\psi}_i^T[\Phi^T L^T(\underline{\delta}) Q_e^{-1} L(\underline{\delta})\Phi + \Phi^T L^T(\underline{\delta}_1)\Delta\tilde{Q}_{1,e} L(\underline{\delta}_1)\Phi + S^{-1}]^{-1}\underline{\psi}_i + Q_{\varepsilon_i}}{\underline{\psi}_i^T Q_e^{-1}\underline{\psi}_i + Q_{\varepsilon_i}} \\ &= \frac{\underline{\psi}_i^T[E + \Phi^T L^T(\underline{\delta}_1)\Delta\tilde{Q}_{1,e} L(\underline{\delta}_1)\Phi]^{-1}\underline{\psi}_i + Q_{\varepsilon_i}}{\underline{\psi}_i^T Q_e^{-1}\underline{\psi}_i + Q_{\varepsilon_i}} \\ &= \frac{\underline{\psi}_i^T E^{-1}\underline{\psi}_i - \underline{\psi}_i^T Z(\underline{\delta}_1)\underline{\psi}_i + Q_\varepsilon}{\underline{\psi}_i^T Q_e^{-1}\underline{\psi}_i + Q_{\varepsilon_i}} = \frac{\underline{\psi}_i^T E^{-1}\underline{\psi}_i + Q_{\varepsilon_i}}{\underline{\psi}_i^T Q_e^{-1}\underline{\psi}_i + Q_{\varepsilon_i}} - \frac{\underline{\psi}_i^T Z(\underline{\delta}_1)\underline{\psi}_i}{\underline{\psi}_i^T Q_e^{-1}\underline{\psi}_i + Q_{\varepsilon_i}} \\ &= r_{z_i|D}(\underline{\delta}) U_i(\underline{\delta}) - \frac{\underline{\psi}_i^T Z(\underline{\delta}_1)\underline{\psi}_i}{\underline{\psi}_i^T Q_e^{-1}\underline{\psi}_i + Q_{\varepsilon_i}} \end{aligned} \tag{B.14}$$

where

$$Z(\underline{\delta}_1) = E^{-1}\Phi^T L^T(\underline{\delta}_1)[\Delta\tilde{Q}_{1,e} + L(\underline{\delta}_1)\Phi E^{-1}\Phi^T L^T(\underline{\delta}_1)]^{-1} L(\underline{\delta}_1)\Phi E^{-1} \tag{B.15}$$

from which it follows that $r_{z_i|D}(\underline{\delta}_1) \leq r_{z_i|D}(\underline{\delta})$ since the matrices $\Delta\tilde{Q}_{1,e}$, Q_e, E and thus $Z(\underline{\delta}_1)$ are symmetric and semi-positive definite. As a result, $U_i(\underline{\delta}_1) \geq U_i(\underline{\delta})$ and thus the information gained by adding a sensor in an existing sensor configuration, which is consistent with intuition. Moreover, it is straightforward to conclude that the maximum information gain is an increasing function of the number of sensors.

2.9 References

[1] H. P. Hjelm, R. Brincker, J. Graugaard-Jensen, and K. Munch. Determination of stress histories in structures by natural input modal analysis. In *Proceedings of the 23rd International Modal Analysis Conference,IMAC*, pages 838–844, 2005.

[2] P. Pingle and P. Avitabile. Full-field dynamic stress/strain from limited sets of measured data. *Sound and Vibration*, 2(8):187–200, 2011.

[3] J. Baqersad, K. Bharadwaj, and P. Poozesh. Modal expansion using strain mode shapes. In *Shock & Vibration, Aircraft/Aerospace, Energy Harvesting, Acoustics & Optics,*, volume 9, pages 219–226. Springer New York LLC, 2017.

[4] P. Avitabile, E. Harvey, and J. Ruddock. Comparison of full field strain distributions to

predicted strain distributions from limited sets of measured data for SHM applications. *Key Engineering Materials*, 569-570:1140–1147, 2013.

[5] C. Papadimitriou, C. P. Fritzen, P. Kraemer, and E. Ntotsios. Fatigue predictions in entire body of metallic structures from a limited number of vibration sensors using Kalman filtering. *Structural Control and Health Monitoring*, 18(5):554–573, 2011.

[6] C. Papadimitriou, E. M. Lourens, G. Lombaert, G. De Roeck, and K. Liu. Prediction of fatigue damage accumulation in metallic structures by the estimation of strains from operational vibrations. In *Life-Cycle and Sustainability of Civil Infrastructure Systems - Proceedings of the 3rd International Symposium on Life-Cycle Civil Engineering, IALCCE*, pages 304–310, 2012.

[7] K. Maes, A. Iliopoulos, W. Weijtjens, C. Devriendt, and G. Lombaert. Dynamic strain estimation for fatigue assessment of an offshore monopile wind turbine using filtering and modal expansion algorithms. *Mechanical Systems and Signal Processing*, 76:592–611, 2016.

[8] A. Iliopoulos, R. Shirzadeh, W. Weijtjens, P. Guillaume, D. Van Hemelrijck, and C. Devriendt. A modal decomposition and expansion approach for prediction of dynamic responses on a monopile offshore wind turbine using a limited number of vibration sensors. *Mechanical Systems and Signal Processing*, 68:84–104, 2016. ISSN 10961216.

[9] M. S. Nabiyan, H. Ebrahimian, B. Moaveni, and F. Khoshnoudian. Structural identification for dynamic strain estimation in wind turbine towers. In *Proceedings of the 36th International Modal Analysis Conference,IMAC*, pages 239–245. Springer, 2019. doi: 10.1007/978-3-319-74421-6_32.

[10] M. S. Nabiyan, F. Khoshnoudian, B. Moaveni, and H. Ebrahimian. Mechanics-based model updating for identification and virtual sensing of an offshore wind turbine using sparse measurements. *Structural Control and Health Monitoring*, 28(2):e2647, 2021.

[11] M. Henkel, J. Häfele, W. Weijtjens, C. Devriendt, C. G. Gebhardt, and R. Rolfes. Strain estimation for offshore wind turbines with jacket substructures using dual-band modal expansion. *Marine Structures*, 71:102731, 2020.

[12] P. Ren and Z. Zhou. Strain estimation of truss structures based on augmented Kalman filtering and modal expansion. *Advances in Mechanical Engineering*, 9(11):1–10, 2017.

[13] Y. Chen, D. Joffre, and P. Avitabile. Underwater dynamic response at limited points expanded to full-field strain response. *Journal of Vibration and Acoustics, Transactions of the ASME*, 140(5):1–9, 2018.

[14] S. Vettori, E. Di Lorenzo, B. Peeters, and E. Chatzi. Kalman-based coupled response-input estimation during environmental tests on the box assembly with removable component structure. In *Proceedings of the 11th International Conference on Structural Dynamics,EURODYN*, pages 3878–3885. EASD Procedia, 2020.

[15] S. Vettori, E. Di Lorenzo, R. Cumbo, U. Musella, T. Tamarozzi, B. Peeters, and E. Chatzi. Kalman-based virtual sensing for improvement of service response replication in environmental tests. In *Model Validation and Uncertainty Quantification, Volume 3*, pages 93–106. Springer, 2020.

[16] A. Iliopoulos, W. Weijtjens, D. Van Hemelrijck, and C. Devriendt. Fatigue assessment of offshore wind turbines on monopile foundations using multi-band modal expansion. *Wind Energy*, 20(8):1463–1479, 8 2017.

[17] D. Giagopoulos, A. Arailopoulos, V. Dertimanis, C. Papadimitriou, E. Chatzi, and K. Grompanopoulos. Computational framework for online estimation of fatigue damage using vibration measurements from a limited number of sensors. In *Procedia Engineering*, volume 199, pages 1906–1911, 2017.

[18] S. P. Tchemodanova, K. Tatsis, V. Dertimanis, E. Chatzi, and M. Sanayei. Remaining fatigue life prediction of a roller coaster subjected to multiaxial nonproportional loading using limited measured strain locations. In *Structures Congress 2019: Bridges, Nonbuilding and Special Structures, and Nonstructural Components*, pages 112–121, 2019.

[19] M. Tarpø, B. Nabuco, C. Georgakis, and R. Brincker. Expansion of experimental mode shape from operational modal analysis and virtual sensing for fatigue analysis using the modal expansion method. *International Journal of Fatigue*, 130:105280, 2020.

[20] K. Maes and G. Lombaert. Fatigue monitoring of railway bridges by means of virtual sensing. In *Proceedings of the Belgian and Dutch National Groups of IABSE - Young Engineers Colloquium 2019,YEC2019*, pages 24–25, 2019.

[21] D. Giagopoulos, A. Arailopoulos, V. Dertimanis, C. Papadimitriou, E. Chatzi, and K. Grompanopoulos. Structural health monitoring and fatigue damage estimation using vibration measurements and finite element model updating. *Structural Health Monitoring*, 18(4):1189–1206, 2019.

[22] G. C. Foss and E. Haugse. Using modal test results to develop strain to displacement transformations. In *Proceedings of the 13th International Modal Analysis Conference,IMAC*, volume 2460, pages 112–118, 1995.

[23] S. Rapp, L. H. Kang, J. H. Han, U. C. Mueller, and H. Baier. Displacement field estimation for a two-dimensional structure using fiber Bragg grating sensors. *Smart Materials and Structures*, 18:025006, 2009.

[24] R. Glaser, V. Caccese, and M. Shahinpoor. Shape monitoring of a beam structure from measured strain or curvature. *Experimental Mechanics*, 52(6):591–606, 2012.

[25] H. J. Bang, S. W. Ko, M. S. Jang, and H. I. Kim. Shape estimation and health monitoring of wind turbine tower using a FBG sensor array. In *International Instrumentation and Measurement Technology Conference Proceedings,2012 IEEE I2MTC*, number 3, pages 496–500. IEEE, 2012. ISBN 978-1-4577-1772-7.

[26] Z. C. Wang, D. Geng, W. X. Ren, and H. T. Liu. Strain modes based dynamic displacement estimation of beam structures with strain sensors. *Smart Materials and Structures*, 23(12):125045, 2014.

[27] H. I. Kim, J. H. Han, and H. J. Bang. Real-time deformed shape estimation of a wind turbine blade using distributed fiber Bragg grating sensors. *Wind Energy*, 17(9):1455–1467, 2014.

[28] G. Fu, A. Untaroiu, and W. O'Brien. An approach to approximate the full strain field of turbofan blades during operation. In *Proceedings of the ASME Turbo Expo*, pages 1–9, 2018. ISBN 9780791851159.

[29] W. Johns, L. Davis, and M. Jankauski. Reconstructing full-field flapping wing dynamics from sparse measurements. *Bioinspiration and Biomimetics*, 16(1):016005, 2021.

[30] J. W. Park, S. H. Sim, and H. J. Jung. Displacement estimation using multimetric data fusion. *IEEE/ASME Transactions on Mechatronics*, 18(6):1675–1682, 2013.

[31] D. C. Papadioti. *Management of uncertainties in structural response and reliability simulations using measured data*. PhD thesis, University of Thessaly, 2015.

[32] D. Giagopoulos, A. Arailopoulos, S. E. Azam, C. Papadimitriou, E. Chatzi, and K. Grompanopoulos. Dynamic response estimation and fatigue prediction in a linear substructure of a complex mechanical assembly. In *Proceedings of 8th European Workshop on Structural Health Monitoring, EWSHM*, volume 2, pages 890–899, 2016.

[33] M. Tarpø, T. Friis, B. Nabuco, S. Amador, E. Katsanos, and R. Brincker. Operational modal analysis based stress estimation in friction systems. In *Conference Proceedings of the Society for Experimental Mechanics Series*, volume 1, pages 143–153. Springer, 2019.

[34] K. E. Tatsis, V. K. Dertimanis, C. Papadimitriou, E. Lourens, and E. N. Chatzi. A general substructure-based framework for input-state estimation using limited output measurements. *Mechanical Systems and Signal Processing*, 150:107223, 2021.

[35] X. H. Zhang, Y. L. Xu, S. Zhu, and S. Zhan. Dual-type sensor placement for multi-scale response reconstruction. *Mechatronics*, 24(4):376–384, 2014.

[36] C. Argyris, C. Papadimitriou, and Panagiotis Panetsos. Bayesian optimal sensor placement for modal identification of civil infrastructures. *Journal of Smart Cities*, 2(2):69–86, 2017.

[37] J. Kullaa. Bayesian virtual sensing for full-field dynamic response estimation. In *Procedia Engineering*, volume 199, pages 2126–2131. Elsevier Ltd, 2017.

[38] C. Papadimitriou and C. Argyris. Bayesian optimal experimental design for parameter estimation and response predictions in complex dynamical systems. In *Procedia Engineering*, volume 199, pages 972–977. Elsevier Ltd, 2017.

[39] J. Kullaa. Bayesian virtual sensing in structural dynamics. *Mechanical Systems and Signal Processing*, 115:497–513, 1 2019.

[40] J. Kullaa. Structural health monitoring using a large sensor network and Bayesian virtual sensors. In *Proceedings of the 1st International Conference on Advances in Signal Processing and Artificial Intelligence*, pages 20–22, Barcelona, Spain, 2019. IFSA Publishing.

[41] J. Kullaa. Robust damage detection using Bayesian virtual sensors. *Mechanical Systems and Signal Processing*, 135:106384, 2020.

[42] J. Kullaa. Robust damage detection in the time domain using Bayesian virtual sensing with noise reduction and environmental effect elimination capabilities. *Journal of Sound and Vibration*, 473:115232, 2020.

[43] T. Ercan, O. Sedehi, C. Papadimitriou, and L. S. Katafygiotis. Robust optimal sensor placement for response reconstruction using output only vibration measurements. In *Proceedings of the 29th European Safety and Reliability Conference, ESREL*, pages 1270–1276. Research Publishing Services, 2019.

[44] C. Argyris, C. Papadimitriou, G. Samaey, and G. Lombaert. A unified sampling-based framework for optimal sensor placement considering parameter and prediction inference. *Mechanical Systems and Signal Processing*, 161:107950, 2021.

[45] R. J. Barthorpe and K. Worden. Emerging trends in optimal structural health monitoring system design: From sensor placement to system evaluation. *Journal of Sensor and Actuator Networks*, 9(3):31, 2020.

[46] P. C. Shah and F. E. Udwadia. A methodology for optimal sensor locations for identification of dynamic systems. *Journal of Applied Mechanics*, 45(1):188–196, 3 1978.

[47] F. E. Udwadia. Methodology for optimum sensor locations for parameter identification in dynamic systems. *Journal of Engineering Mechanics*, 120(2):368–390, 1994.

[48] P. H. Kirkegaard and R. Brincker. On the optimal location of sensors for parametric identification of linear structural systems. *Mechanical Systems and Signal Processing*, 8 (6):639–647, 11 1994.

[49] D. Ucinski. Optimal sensor location for parameter estimation of distributed processes. *International Journal of Control*, 73(13):1235–1248, 2000.

[50] Z. H. Qureshi, T. S. Ng, and G. C. Goodwin. Optimum experimental design for identification of distributed parameter systems. *International Journal of Control*, 31(1):21–29, 1 1980.

[51] D. C. Kammer. Sensor placement for on-orbit modal identification and correlation of large space structures. *Journal of Guidance, Control, and Dynamics*, 14(2):251–259, 1991.

[52] C. Papadimitriou, J. L. Beck, and S. K. Au. Entropy-based optimal sensor location for structural model updating. *JVC/Journal of Vibration and Control*, 6(5):781–800, 2000.

[53] K. V. Yuen, L. S. Katafygiotis, C. Papadimitriou, and N. C. Mickleborough. Optimal sensor placement methodology for identification with unmeasured excitation. *Journal of Dynamic Systems, Measurement and Control, Transactions of the ASME*, 123(4):677–686, 2001.

[54] C. Papadimitriou. Optimal sensor placement methodology for parametric identification of structural systems. *Journal of Sound and Vibration*, 278(4-5):923–947, 2004.

[55] Y. Robert-Nicoud, B. Raphael, and I. F. Smith. Configuration of measurement systems using Shannon's entropy function. *Computers and Structures*, 83(8-9):599–612, 2005.

[56] K. V. Yuen and S. C. Kuok. Efficient Bayesian sensor placement algorithm for structural identification: a general approach for multi-type sensory systems. *Earthquake Engineering & Structural Dynamics*, 44(5):757–774, 2015.

[57] C. Papadimitriou and G. Lombaert. The effect of prediction error correlation on optimal sensor placement in structural dynamics. *Mechanical Systems and Signal Processing*, 28:105–127, 4 2012.

[58] N. J. Bertola, S. G. Pai, and I. F. Smith. A methodology to design measurement systems when multiple model classes are plausible. *Journal of Civil Structural Health Monitoring*, 11(2):1–22, 2021. ISSN 2190-5479.

[59] C. Stephan. Sensor placement for modal identification. *Mechanical Systems and Signal Processing*, 27(1):461–470, 2012.

[60] S. Q. Ye and Y. Q. Ni. Information entropy based algorithm of sensor placement optimization for structural damage detection. *Smart Structures and Systems*, 10(4_5):443–458, 2012. ISSN 17381991. doi: 10.12989/sss.2012.10.4_5.443.

[61] H. M. Chow, H. F. Lam, T. Yin, and S. K. Au. Optimal sensor configuration of a typical transmission tower for the purpose of structural model updating. *Structural Control and Health Monitoring*, 18(3):305–320, 4 2011.

[62] T. Yin, H. F. Lam, and H. M. Chow. A Bayesian probabilistic approach for crack characterization in plate structures. *Computer-Aided Civil and Infrastructure Engineering*, 25 (5):375–386, 2010.

[63] T. Yin, K. V. Yuen, H. F. Lam, and H. P. Zhu. Entropy-based optimal sensor placement for model identification of periodic structures endowed with bolted joints. *Computer-Aided Civil and Infrastructure Engineering*, 32(12):1007–1024, 12 2017.

[64] H. Ebrahimian, R. Astroza, J. P. Conte, and R. R. Bitmead. Information-theoretic approach for identifiability assessment of nonlinear structural finite-element models. *Journal of Engineering Mechanics*, 145(7):04019039, 2019.

[65] N. J. Bertola, M. Papadopoulou, D. Vernay, and I. F. Smith. Optimal multi-type sensor placement for structural identification by static-load testing. *Sensors*, 17:2904, 2017.

[66] M. Papadopoulou, B. Raphael, I. F. Smith, and C. Sekhar. Hierarchical sensor placement using joint entropy and the effect of modeling error. *Entropy*, 16(9):5078–5101, 2014.

[67] X. Huan and Y. M. Marzouk. Simulation-based optimal Bayesian experimental design for nonlinear systems. *Journal of Computational Physics*, 232(1):288–317, 1 2013.

[68] D. V. Lindley. On a measure of the information provided by an experiment. *The Annals of Mathematical Statistics*, 27(4):986–1005, 1956.

[69] K. Chaloner and I. Verdinelli. Bayesian experimental design: A review. *Statistical Science*, 10(3):273–304, 1995.

[70] P. Bhattacharyya and J. Beck. Exploiting convexification for Bayesian optimal sensor placement by maximization of mutual information. *Structural Control and Health Monitoring*, 27(10):1–18, 2020.

[71] C. Argyris. *Bayesian uncertainty quantification and optimal experimental design in data driven simulations of engineering systems*. PhD thesis, University of Thessaly, 2010.

[72] C. Malings and M. Pozzi. Value of information for spatially distributed systems: Application to sensor placement. *Reliability Engineering and System Safety*, 154:219–233, 2016.

[73] S. Cantero-Chinchilla, J. Chiachío, M. Chiachío, D. Chronopoulos, and A. Jones. Optimal sensor configuration for ultrasonic guided-wave inspection based on value of information. *Mechanical Systems and Signal Processing*, 135:106377, 2020.

[74] C. Malings and M. Pozzi. Submodularity issues in value-of-information-based sensor placement. *Reliability Engineering and System Safety*, 183:93–103, 2019.

[75] R. Pasquier, J. A. G., and I. F. Smith. Measurement system design for civil infrastructure using expected utility. *Advanced Engineering Informatics*, 32:40–51, 2017.

[76] B. Li and A. Der Kiureghian. Robust optimal sensor placement for operational modal analysis based on maximum expected utility. *Mechanical Systems and Signal Processing*, 75:155–175, 2016.

[77] C. Leyder, E. Chatzi, A. Frangi, and G. Lombaert. Comparison of optimal sensor placement algorithms via implementation on an innovative timber structure. In Klaas van Breugel Jaap Bakker, Dan M. Frangopol, editor, *Life-Cycle of Engineering Systems:Emphasis on Sustainable Civil Infrastructure*, pages 260–267. CRC Press, 11 2016.

[78] P. L. Green, E. J. Cross, and K. Worden. Bayesian system identification of dynamical systems using highly informative training data. *Mechanical Systems and Signal Processing*, 56:109–122, 2015.

[79] C. Leyder, V. Ntertimanis, E. Chatzi, and A. Frangi. Optimal sensor placement for the modal identification of an innovative timber structure. In *Proceedings of the 1st In-*

ternational Conference on Uncertainty Quantification in Computational Sciences and Engineering, UNCECOMP, pages 467–476, 2015.

[80] G. Capellari, E. Chatzi, and S. Mariani. Structural health monitoring sensor network optimization through Bayesian experimental design. *ASCE-ASME Journal of Risk and Uncertainty in Engineering Systems, Part A: Civil Engineering*, 4(2):04018016, 2018.

[81] G. Capellari, E. Chatzi, and S. Mariani. Cost–benefit optimization of structural health monitoring sensor networks. *Sensors*, 18(7):1–22, 2018.

[82] C. Papadimitriou, Y. Haralampidis, and K. Sobczyk. Optimal experimental design in stochastic structural dynamics. *Probabilistic Engineering Mechanics*, 20(1):67–78, 2005.

[83] S. Kullback and R. A. Leibler. On information and sufficiency. *The Annals of Mathematical Statistics*, 22(1):79–86, 1951.

[84] K. J. Ryan. Estimating Expected Information Gains for Experimental Designs with Application to the Random Fatigue-Limit Model. *Journal of Computational and Graphical Statistics*, 12(3):585–603, 2003.

[85] T. Gerstner and M. Griebel. Numerical integration using sparse grids. *Numerical Algorithms*, 18(3):209–232, 1998.

[86] F. Heiss and V. Winschel. Likelihood approximation by numerical integration on sparse grids. *Journal of Econometrics*, 144(1):62–80, 2008.

[87] B. Hofmeister, M. Bruns, and R. Rolfes. Finite element model updating using deterministic optimisation: A global pattern search approach. *Engineering Structures*, 195: 373–381, 2019. doi: 10.1016/j.engstruct.2019.05.047.

[88] M. Girardi, C. Padovani, D. Pellegrini, and L. Robol. A finite element model updating method based on global optimization. *Mechanical Systems and Signal Processing*, 152: 107372, 2021. doi: 10.1016/j.ymssp.2020.107372.

[89] N. Hansen, S. D. Müller, and P. Koumoutsakos. Reducing the time complexity of the derandomized evolution strategy with covariance matrix adaptation (CMA-ES). *Evolutionary Computation*, 11(1):1–18, 2003.

[90] K. Worden and W. J. Staszewski. Impact location and quantification on a composite panel using neural networks and a genetic algorithm. *Strain*, 36(2):61–68, 2000.

[91] M. M. Abdullah, A. Richardson, and J. Hanif. Placement of sensors/actuators on civil structures using genetic algorithms. *Earthquake Engineering and Structural Dynamics*, 30(8):1167–1184, 2001.

[92] L. Yao, W. A. Sethares, and D. C. Kammer. Sensor placement for on-orbit modal identification via a genetic algorithm. *AIAA Journal*, 31(10):1922–1928, 1993.

[93] F. Bianconi, G. P. Salachoris, F. Clementi, and S. Lenci. A genetic algorithm procedure for the automatic updating of fem based on ambient vibration tests. *Sensors*, 20(11): 3315, 2020. doi: 10.3390/s20113315.

[94] D. I. Papadimitriou and C. Papadimitriou. Optimal Sensor Placement for the Estimation of Turbulence Model Parameters in CFD. *International Journal for Uncertainty Quantification*, 5(6):545–568, 2015.

Chapter 3. Information Theoretic-Based Optimal Sensor Placement for Virtual Sensing using Augmented Kalman Filtering

Original paper: T. Ercan, O. Sedehi, L. S. Katafygiotis and C. Papadimitriou. Information Theoretic-Based Optimal Sensor Placement for Virtual Sensing using Augmented Kalman Filtering, Mechanical Systems and Signal Processing. Submitted. (2022).
https://doi.org/10.5281/zenodo.6508382

ABSTRACT

An optimal sensor placement (OSP) framework for virtual sensing using the augmented Kalman Filter (AKF) technique is presented based on information and utility theory. The framework is applicable to input and response reconstruction when output-only vibration measurements are available. Using information theory, a utility function is built to quantify the expected information gained from the data for reducing the uncertainty of unmeasured quantities of interest (QoI). Taking into account the AKF equations and exploiting the Gaussian nature of the response QoI arising from linear dynamic systems, useful and informative analytical expressions are derived for the utility function. Subsequently, the utility function is extended to make the OSP design robust to uncertainties in the structural model and modeling error parameters, resulting in a multidimensional integral of the expected information gain over all possible values of the uncertain parameters, weighted by their assigned probability distributions. The proposed OSP framework maximizes this utility function through heuristic sequential sensor placement (SSP) strategies (forward and backward SSP) and genetic algorithms (GA) to optimize the type and location of sensors. A new modified SSP strategy is proposed that exploits the computational efficiency of the less accurate forward SSP algorithm and the accuracy of the computationally expensive backward SSP algorithm. A thorough study of the effect of the measurement and model/prediction errors and their uncertainties, as well as the input uncertainties on the selection of the optimal sensor configuration is presented using a finite element model of a plate loaded by a single concentrated input force, highlighting the importance of accounting for robustness to errors and other uncertainties.

3.1 Introduction

In the context of structural identification, the calculation of dynamical responses is required for system identification, damage detection, reliability analysis, and fatigue monitoring. Although physical sensors serve to provide such information, their usage naturally visits budget constraints, as well as practical considerations like inaccessibility of positions and infeasibility of obtaining direct measurements. Consequently, the reconstruction of unknown quantities from a limited number of physical sensors, also referred to as "virtual sensing", has attracted extensive attention due to its pivotal role in monitoring performance/safety-related indices, e.g., accelerations, displacements, inter-story drifts, strains, and stresses. However, the success of virtual sensing in structural dynamics heavily depends on proper placement of a limited number of sensors, which is the subject of the present work.

Modal expansion [1–6] and filtering techniques [7–15] are conventional virtual sensing tools. Although the former technique can reconstruct unobserved history responses, it cannot calculate external loadings applied to the structure. Additionally, the modal expansion is not flexible enough for fusing different types of physical sensors as it only applies to estimating dynamical responses, e.g., strains, displacements, and accelerations, from the same kind of sensors. In contrast, filtering techniques, including Minimum-Variance Unbiased filters [8] and Bayesian filtering methods [16, 17], can handle both input reconstruction and multi-type sensor fusion.

Virtual sensing of strain/stress responses is necessary for fatigue damage identification. Papadimitriou et al. [18, 19] were the first to combine output-only vibration measurements, finite element models, and virtual sensing tools with stochastic and deterministic fatigue theories for characterizing fatigue damage accumulation in the entire body of metallic structures. Such predictions are based on the actual operating conditions of structures and thus provide realistic fatigue estimates consistent with existing fatigue theories. In recent years, modal expansion and filtering techniques were applied for strain/stress virtual sensing [3, 20–28] and fatigue estimation [29–34] for numerous structures using a limited number of displacement/strain sensors. Substructure decoupling of linear and nonlinear models of structures has been integrated into fatigue monitoring methods, which uses filtering techniques for identifying the forces at the interface between the analyzed linear substructure (or component) and the rest of the structure [35–38].

Optimal sensor placement techniques for structural dynamics applications have been proposed to extract the most informative data that will increase the accuracy of the estimates from a given number of sensors. A recent article [39] reviews the subject, summarizing methods and optimization algorithms for optimizing the location of sensors in structural dynamics applications. However, a limited number of OSP studies exist for virtual sensing based on output-only vibration measurements.

Based on filtering techniques introduced for the case of unknown loads, a number of OSP methods have been developed recently for state estimation and response reconstruction [28, 40, 41], as well as for load estimation [42, 43]. The methods are based on minimizing a scalar measure of the steady-state reconstruction error covariance of the response and/or input with respect to the location of sensors. In most of the approaches, the scalar measure is chosen to be the trace of the reconstruction error covariance matrix. The use of a scalar measure (usually the trace) of the steady-state covariance of the reconstruction error is borrowed from optimal sensor placement strategies proposed in structural dynamics applications for response reconstruction based on Kalman-type filter methods subjected to known loads [44–46]. The size of the reduction of the measure as a function of the number of sensors is used to select a reasonable number of sensors. More specifically, in [47] a multi-type OSP strategy is proposed based on Gillijns and De Moor filtering technique [48], demonstrating the OSP to be independent of the type and time evolution of the external excitation(s). The forward sequential sensor placement (FSSP) technique [49] was used as a heuristic algorithm to carry out the optimization problem in which acceleration and strain sensors were added sequentially at their optimal location that maximizes the estimation error of the reconstructed responses. In a very similar approach, Peng et al. [41] proposed the backward sequential placement (BSSP) algorithm [49], instead of the FSSP algorithm, to optimize the location of acceleration and strain sensors.

Focusing on optimal sensor placement for multiple load estimation, a method is proposed in [43] based on the condition number of a system observability metric using AKF for linear systems [7, 50] and using extended Kalman filter for nonlinear system [51]. Recognising that observability offers only the minimum requirements for a stable estimation, two alternative metrics for best load identification are proposed in [42], based on steady-state error covariance of the load estimation and sensor bandwidth through the transfer function between real and estimated inputs. The metric in the first method involves the trace of the steady-state error co-

variance of the load estimation. Satisfying conditions of observability and invertability, Maes et al. [52] proposed an optimal sensor layout for load estimation which leads to a minimum set of position and acceleration sensors equal to the number of loads to be identified.

Information theoretic-based methods have also been used in structural dynamics to optimize the sensor configuration [53–64]. In these methods a measure of the information gained from the sensor data, such as mutual information, relative entropy and Kullback-Leibler divergence (KL-div) computed from a Bayesian formulation is optimized with respect to the sensor locations. OSP techniques based on information-theoretic methods for virtual sensing has also proposed based on either modal expansion technique [65–67] or filtering techniques [68, 69].

In this work, considering the availability of output-only vibration measurements, a novel OSP framework is presented for accurate virtual sensing (response and/or load reconstruction) in linear systems based on the AKF technique and information theory. The information gained by a sensor configuration is measured by the KL-div [70] between the posterior and prior probability distribution of the response QoI to be virtually sensed or reconstructed at each time step, by combining available AKF techniques and sensor data. This is obtained using the Lindley's utility function [71, 72] quantifying the average information in the data over all possible measurements generated by the prediction error model. For more than one reconstructed QoI, the KL-div is averaged over all possible virtually sensed QoI. For linear models of systems, exact analytical expressions are developed for the utility function in terms of the variance of the responses of the virtually sensed QoI. The utility measure is extended to include uncertainties in the model parameters, as well as in the model/prediction and measurement errors, which during the experimental design phase are subjectively assigned in the modeling and filtering process. The optimal sensor configuration is finally obtained by maximizing the expected information gain over all possible values of the uncertain parameters. The resulting multidimensional integral are computed using sparse grid or Monte Carlo techniques. Heuristic algorithms and a GA are introduced to carry out the discrete optimization problem. The high computational burden associated with BSSP and the lack of sufficient accuracy of the FSSP are discussed, and remedies are proposed to attain an accurate and computationally efficient algorithm.

This study is organized as follows: In Section 3.2, the AKF technique is outlined for characterizing the uncertainty in the prediction of input and response QoI. In Section 3.3, the optimal sensor placement methodology is presented based on utility and information theory.

An application on a square plate structure is used in Section 3.4 to demonstrate the capabilities and effectiveness of the OSP methodology for reliable virtual sensing. Conclusions are drawn in Section 3.5.

3.2 Bayesian Virtual Sensing Using Augmented Kalman Filter

Consider a structural model used to predict the temporal variability of the response $\underline{z}(t;\underline{\varphi}) \in R^{n_z}$ (e.g., accelerations, displacements, strain or stresses) at n_z locations given the values of a structural model parameter set $\underline{\varphi}$ (e.g., stiffness, mass and damping related parameters) and the excitation vector $\underline{u}\,(t) \in R^{n_u}$. Let $D = \left\{\underline{y}(t) \in R^{N_0}\right\}$ be the vector of response time history data collected by placing N_0 sensors on the structure. These data depend on the sensor configuration vector $\underline{\delta} \in R^{N_0}$ indicating the location and measurement direction of sensors. The data may consist of acceleration, displacement, and strain measurements.

In what follows, a linear finite element model of the structure is assumed with n degrees of freedom (DOF). The governing equations of motion are developed either in the physical space or in the modal space using modal analysis and keeping up to m contributing modes.

3.2.1 State-Space Formulation

The governing equations of motion of the structure are formulated in state-space form by defining the state vector $\underline{x}(t) \in R^n$ of the displacement and velocity vector or, for the case of modal analysis, the state vector is defined as $\underline{x}(t) = (\underline{\xi}(t), \dot{\underline{\xi}}(t))^T$, with respect to the modal coordinate vector $\underline{\xi}(t) \in R^m$ and its first derivative. Converting the continuous state space equation into the discrete state space using the notation $\underline{x}_k = \underline{x}(k\Delta t)$, where k is the time index and Δt is the discretization time interval, the discrete state-space system becomes

$$\underline{x}_{k+1} = A\underline{x}_k + B\underline{u}_k + \underline{w}_k \tag{3.1}$$

where A and B are the system matrices and $\underline{w}_k$ the process noise assumed to be zero-mean Gaussian, i.e. $\underline{w}_k \sim N(\underline{0}, Q)$ with process noise covariance $Q \in R^{m\times m}$. The observation equation is given by

$$\underline{y}_k = G\underline{x}_k + J\underline{u}_k + \underline{v}_k \tag{3.2}$$

where the measurement error term follows a zero-mean Gaussian distribution, i.e. $\underline{v}_k \sim N(\underline{0}, R)$, with measurement error covariance $R \in R^{N_0 \times N_0}$. The prediction equation takes a similar form to the observation equation,

$$\underline{z}_k = \tilde{G}\underline{x}_k + \tilde{J}\underline{u}_k + \underline{\varepsilon}_k \tag{3.3}$$

where the prediction error term also follows a Gaussian distribution, i.e. $\underline{\varepsilon}_k \sim N(\underline{0}, R_\varepsilon)$, with prediction error covariance $R_\varepsilon \in R^{n_z \times n_z}$.

3.2.2 Review of AKF

In this work, it is assumed that the excitation time histories denoted by $\underline{u}\,(t)$ are not available. Lourens et al. [7] presented an AKF technique to identify the dynamic forces applied to the structure and also estimate the state of the system This is achieved by using a random walk model for the forces [50, 73]

$$\underline{u}_{k+1} = \underline{u}_k + \underline{\eta}_k \tag{3.4}$$

where $\underline{u}_k \equiv \underline{u}(k\Delta t)$ is the input force at $t_k = k\Delta t$, $\underline{\eta}_k \sim N(\underline{0}, S)$ is a zero-mean Gaussian prediction error with covariance matrix $S \in R^{n_u \times n_u}$. The unknown forces are added in the state vector, and then this augmented vector can be estimated using a standard KF. Specifically, introducing the augmented state vector $\underline{x}_k^a = [\underline{x}_k^T, \underline{u}_k^T]^T \in R^{2m+n_u}$ and using Eq. 3.1 and Eq. 3.4, the augmented state-space model and observation equations are formulated as follows:

$$\begin{aligned} \underline{x}_{k+1}^a &= A_a \underline{x}_k^a + \underline{\zeta}_k \\ \underline{y}_k &= G_a \underline{x}_k^a + \underline{v}_k \end{aligned} \tag{3.5}$$

where the augmented state space matrix $A_a \in R^{(2m+n_u)\times(2m+n_u)}$ and observation matrix $G_a \in R^{N_0 \times (2m+n_u)}$ are defined as

$$A_a = \begin{bmatrix} A & B \\ 0 & I \end{bmatrix}, \quad G_a = \begin{bmatrix} G & J \end{bmatrix} \tag{3.6}$$

while the augmented process noise covariance matrix $Q_a \in R^{(m+n_u)\times(m+n_u)}$ of the zero-mean

Gaussian white noise sequence $\underline{\zeta}_k \sim N(0, Q_a)$ is given as

$$Q_a = \begin{bmatrix} Q & 0 \\ 0 & S \end{bmatrix} \tag{3.7}$$

The augmented state vector can be estimated through the standard Kalman filter (KF), which provides the estimate $\underline{\hat{x}}^a_{k|k}$ and the error covariance matrix $P_{k|k} \in R^{(2m+n_u)\times(2m+n_u)}$ obtained using the following time and measurement update steps:
Time update:

$$\begin{aligned} \underline{\hat{x}}^a_{k|k-1} &= A_a \underline{\hat{x}}^a_{k-1|k-1} \\ P_{k|k-1} &= A_a P_{k-1|k-1} A_a^T + Q_a \end{aligned} \tag{3.8}$$

Measurement update:

$$\begin{aligned} L_k &= P_{k|k-1} G_a^T (G_a P_{k|k-1} G_a^T + R)^{-1} \\ \underline{\hat{x}}^a_{k|k} &= \underline{\hat{x}}^a_{k|k-1} + L_k(\underline{y}_k - G_a \underline{\hat{x}}^a_{k|k-1}) \\ P_{k|k} &= P_{k|k-1} - L_k G_a P_{k|k-1} \end{aligned} \tag{3.9}$$

It should be noted that these equations provide the mean and covariance of the underlying Gaussian distribution. Substituting the first of Eq. 3.9 into the third of Eq. 3.9, the error covariance matrix $P_{k|k}$ also takes the convenient form

$$P_{k|k} = P_{k|k-1} - P_{k|k-1} G_a^T (G_a P_{k|k-1} G_a^T + R)^{-1} G_a P_{k|k-1} \tag{3.10}$$

Using the augmented formulation, the prediction equation Eq. 3.3 takes the form

$$\underline{z}_k = \Psi \underline{x}^a_k + \underline{\varepsilon}_k \tag{3.11}$$

where $\Psi = \begin{bmatrix} \tilde{G} & \tilde{J} \end{bmatrix}$ with mean $\underline{\hat{z}}_k = \Psi \underline{\hat{x}}^a_k$ and error covariance matrix $P_{z,k|k} \equiv E[(\underline{z}_k - \underline{\hat{z}}_k)(\underline{z}_k - \underline{\hat{z}}_k)^T]$ given by

$$P_{z,k|k} = \Psi P_{k|k} \Psi^T + R_\varepsilon \tag{3.12}$$

For practical convenience and without loss of generality, stationarity conditions are next assumed, implying that the covariance matrices R, R_ε and S are independent of the time index k. Moreover, the parameter set $\underline{\varphi}$ is augmented to include the parameters defining the covariance matrices R, R_ε and S. Although it is not explicitly stated in the above formulation, the error covariance matrices $P_{k|k-1}$ and $P_{k|k}$ at the time update and the measurement update steps, respectively, depend on the parameter set $\underline{\varphi}$ and the sensor configuration $\underline{\delta}$. This dependence will be explicitly introduced in the formulation provided in the following section.

3.2.3 Steady-State Formulation of Prediction Error Covariance Matrices for Time and Measurement Update

In particular, the steady-state solution is obtained by setting $P_{k+1|k} = P_{k|k-1} = P_\infty \equiv P_\infty(\underline{\delta}, \underline{\varphi}) \in R^{(2m+n_u)\times(2m+n_u)}$, where the last notation is introduced to represent the dependence of P_∞ on the model parameter set $\underline{\varphi}$ and the sensor configuration $\underline{\delta}$. Substituting Eq. 3.10 into the first line equation of Eq. 3.9, the converged steady state error covariance P_∞ at the time update step is then obtained by solving the following discrete-time algebraic Riccati equation:

$$A_a P_\infty A_a^T - P_\infty - A_a P_\infty G_a^T (G_a P_\infty G_a^T + R)^{-1} G_a P_\infty A_a^T + Q_a = 0 \tag{3.13}$$

The steady-state solution for the error covariance matrix at the measurement update step is denoted by $P_{k|k} \equiv \Sigma_{x|D}(\underline{\delta}, \underline{\varphi})$. Setting $P_{k|k-1} = P_\infty$ and $P_{k|k} = \Sigma_{x|D}(\underline{\delta}, \underline{\varphi})$ in Eq. 3.10, one derives that $\Sigma_{x|D}(\underline{\delta}, \underline{\varphi})$ is given in terms of P_∞ as follows:

$$\Sigma_{x|D}(\underline{\delta}, \underline{\varphi}) = P_\infty - P_\infty G_a^T (G_a P_\infty G_a^T + R)^{-1} G_a P_\infty \tag{3.14}$$

Finally, the steady-state error covariance matrices $P_{z,k|k-1} \equiv \Sigma_z(\underline{\delta}, \underline{\varphi})$ and $P_{z,k|k} \equiv \Sigma_{z|D}(\underline{\delta}, \underline{\varphi})$ of the predicted QoI $\underline{z}$ at the time update and the measurement update steps, respectively, are derived from Eq. 3.14 to be in the form

$$\Sigma_z(\underline{\delta}, \underline{\varphi}) = \Psi P_\infty(\underline{\delta}, \underline{\varphi}) \Psi^T + R_\varepsilon \tag{3.15}$$

$$\Sigma_{z|D}(\underline{\delta}, \underline{\varphi}) = \Psi \Sigma_{x|D}(\underline{\delta}, \underline{\varphi}) \Psi^T + R_\varepsilon \tag{3.16}$$

Note that from the structure of the process, observation, and prediction equations, the response

prediction vector $\underline{z}$ follows a multivariable normal distribution

$$p(\underline{z}|(\underline{\delta},\underline{\varphi}) = N\left(\underline{z}|\underline{\hat{z}}(\underline{\delta},\underline{\varphi}),\Sigma(\underline{\delta},\underline{\varphi})\right) \tag{3.17}$$

with mean $\underline{\hat{z}}(\underline{\delta},\underline{\varphi})$ given by Eq. 3.11 that depends on the data, and covariance matrix $\Sigma(\underline{\delta},\underline{\varphi})$ given by Eq. 3.15 for the time update step and by Eq. 3.16 for the measurement update step that does not depend on the data. In particular, the variance of the i-th element $z_i(t;\underline{\delta},\underline{\varphi})$ of the response vector $\underline{z}(t;\underline{\delta},\underline{\varphi})$ is given by the i-th diagonal element of the covariance matrix, which simplify to

$$\Sigma_{z_i}(\underline{\delta},\underline{\varphi}) = \psi_i^T P_\infty(\underline{\delta},\underline{\varphi})\psi_i + R_{\varepsilon_{ii}} \tag{3.18}$$

$$\Sigma_{z_i|D}(\underline{\delta},\underline{\varphi}) = \psi_i^T \Sigma_{x|D}(\underline{\delta},\underline{\varphi})\psi_i + R_{\varepsilon_{ii}} \tag{3.19}$$

for the time update and the measurement update steps, respectively, where ψ_i is the i-th row of the matrix Ψ.

The prior variance $\Sigma_{z_i}(\underline{\delta},\underline{\varphi})$ in Eq. 3.18 and the posterior variance $\Sigma_{z_i|D}(\underline{\delta},\underline{\varphi})$ in Eq. 3.19, described in terms of the parameters $\underline{\varphi}$ and the sensor locations $\underline{\delta}$, are the main quantities involved in the next section to solve the optimal sensor location problem for response reconstruction. It is clear that these variances are independent of the measurements/data $\underline{y}(t)$ and depend only on the structural model parameters $\underline{\varphi}$, the process, measurement and prediction error covariances Q_a, R and R_ε.

3.3 Optimal Sensor Placement Formulation

3.3.1 Expected Utility Using Information Gain

The design objective is to select the sensor configuration (type, location, and number of sensors) that maximizes the information contained in the data for predicting with the least uncertainty in the output response QoI z_i at desirable DOF or locations i. This is achieved by combining the information theory with utility theory to evaluate the usefulness of a sensor configuration. A measure of the information gained from a sensor configuration $\underline{\delta}$ for estimating a response QoI z_i, given a set of data D and the model parameters $\underline{\varphi}$, is the KL-div [70] between the prior and posterior probability distribution of the output QoI z_i. Following Lindley's

work [71], utility theory is used to measure the usefulness of the sensor configuration, with the utility function selected to be the expected value of the information gain quantified by the expected KL-div over all possible values of the experimental data.

At each time step, the information is gained only in the measurement update step of the KF formulation. By solving the Riccati equation, the stationary prior variance $\Sigma_{z_i}(\underline{\delta}, \underline{\varphi})$ can be updated, giving the stationary posterior variance $\Sigma_{z_i|D}(\underline{\delta}, \underline{\varphi})$. Using the steady-state formulation and recognising that the probability distributions of the estimates at the time and measurement update steps are Gaussian with the variances of these distribution to be independent of the data, the information gained using the data from $k-1$ to k time instances is given by [66]

$$U_i(\delta, \underline{\varphi}) = -\Delta H_i(\underline{\delta}) = -\left[H_{z_i|D}(\delta, \underline{\varphi}) - H_{z_i}(\delta, \underline{\varphi})\right] \tag{3.20}$$

where $H_{z_i}(\delta, \varphi)$ and $H_{z_i|D}(\delta, \varphi)$ are the information entropies corresponding to the Gaussian distributions with variances given by Eq. 3.18 and Eq. 3.19 at the time update and measurement update steps of the KF formulation. Using the expressions for the information entropy of a Gaussian distribution scalar variable written with respect to the variance of the variable, the expected utility function U_i finally takes the form [66]

$$U_i(\underline{\delta}) = -\frac{1}{2} \ln \frac{\Sigma_{z_i|D}(\underline{\delta}, \underline{\varphi})}{\Sigma_{z_i}(\underline{\delta}, \underline{\varphi})} \tag{3.21}$$

Here, $U_i(\underline{\delta})$ represents the expected information gain over all possible values of the data, given the value of the model parameters $\underline{\varphi}$.

For several output QoI included in the vector $\underline{z}$, the information gain measure can be extended to the weighted average of the information gain for all possible output QoI, given as

$$\bar{U}(\underline{\delta}) = \sum_{i=1}^{N_z} w_i U_i(\underline{\delta}) \tag{3.22}$$

with $\sum_{i=1}^{N_z} w_i = 1$, $w_i \geq 0$, where the values of the weight w_i are selected to quantify the importance of the i-th QoI z_i in the design of the sensor configuration. Substituting Eq. 3.21 into Eq. 3.22, and extending the utility function to include the uncertainty in the model parameters $\underline{\varphi}$, the expected utility function that accounts for all response entries in the vector $\underline{z}$ takes the

form

$$U(\underline{\delta}) = \int_{\Phi} \bar{U}(\underline{\delta})\, p(\underline{\varphi})\, d\underline{\varphi} = -\frac{1}{2} \sum_{i=1}^{n_z} w_i \int_{\Phi} \ln \frac{\Sigma_{z_i|D}(\underline{\delta}, \underline{\varphi})}{\Sigma_{z_i}(\underline{\delta}, \underline{\varphi})}\, p(\underline{\varphi})\, d\underline{\varphi} \tag{3.23}$$

Using equal weight values $w_i = 1/n_z$, the utility function takes the form

$$U(\underline{\delta}) = -\frac{1}{2n_z} \int_{\tilde{\Phi}} \ln \prod_{i=1}^{n_z} \frac{\Sigma_{z_i|D}(\underline{\delta}, \underline{\varphi})}{\Sigma_{z_i}(\underline{\delta}, \underline{\varphi})}\, p(\underline{\varphi})\, d\underline{\varphi} \tag{3.24}$$

where $p(\underline{\varphi})$ is a probability distribution that is postulated to quantify the uncertainties in the values of model and input characteristics involved in $\underline{\varphi}$; $U(\underline{\delta})$ represents the expected information gain over all possible values of the model parameters $\underline{\varphi}$, weighted by the prior PDF $p(\underline{\varphi})$ of the model parameters. The multidimensional integral in Eq. 3.23 or Eq. 3.24 is a probability integral representing the robust information gain. The multidimensional integral can be evaluated using Monte Carlo techniques or sparse grid methods [74, 75].

3.3.2 Optimal Sensor Placement

The optimal sensor configuration $\underline{\delta}_{opt}$ is obtained by maximizing the utility $U(\underline{\delta})$ with respect to the design variables $\underline{\delta}$, i.e.

$$\underline{\delta}_{opt} = \arg \max_{\underline{\delta}} U(\underline{\delta}) \tag{3.25}$$

The optimal number of sensors in the sensor configuration can be estimated by monitoring the information gain as additional sensors are placed in the structure. Usually, once sufficient number of sensors is placed, the information gain using additional sensors is relatively small and the process of adding sensors in the structure is terminated. The optimization problem is solved using discrete design variables associated with either the DOF where acceleration/displacement sensors are placed or the Gauss integration points where strain sensors are placed. To implement the discrete optimization algorithms for two types of sensors simultaneously, say N_a acceleration sensors and N_s strain sensors, we order the possible sensor locations in a new set containing all $N_{all} = N_a + N_s$ sensor locations consisting of 1 to N_a acceleration sensors and $N_a + 1$ to $N_a + N_s$ strain sensors and the optimization is then performed over the new set of N_{all} sensors. The optimization is performed using the SSP and/or GA algorithms.

3.3.2.1 Heuristic SSP Algorithms

Heuristic algorithms [39, 49, 63] have been used to effectively solve the optimization problem and provide near optimal solutions. Herein, the forward and backward sequential sensor placement (FSSP/BSSP) algorithms [49, 76] and the combined FSSP/BSSP algorithm [66], termed SSP, are used to provide near optima solutions [53]. Let N_0 be the number of sensors to be placed in the structure at N_{all} possible sensors positions. As demonstrated in the past [53], FSSP and BSSP algorithms offer systematic and computationally very efficient approaches for computing sequentially a near optimal sensor configuration involving 1 to N_0 sensors. Specifically, for the FSSP algorithm, given the positions of $(i-1)$ sensors in the structure computed in the previous $(i-1)$ steps, the position of the next ith sensor is obtained as the one, out of the remaining $(N_{all}-i+1)$ possible sensor positions, that gives the highest increase in the information gain for i sensors, with the positions of the first $(i-1)$ sensors fixed at the optimal ones already obtained in the previous $(i-1)$ steps. This process starts for $i=1$ and is continued for up to N_0 sensors. BSSP algorithm starts with N_{all} sensors placed at all possible position of the structure and proceeds by removing sequentially one sensor at a time from the position that results in the smallest decrease in the information gain. Given that i sensor remain in the structure after removing $N_{all}-i+1$ sensors, the process of evaluating which sensor to remove from the remaining i positions involves evaluating i sensor configuration each one involving $i-1$ sensors. This procedure is repeated, starting from $i=N_{all}$ until it terminates for $i=2$. It should be noted that the FSSP provides the optimal sensor location for 1 up to N_0 sensors, while BSSP provides the optimal sensor configuration for 1 to N_{all} sensors.

The computational cost depends on the number of function evaluations and the floating-point operations involved in each function evaluation. Note that the floating-point operations for solving the Riccatti equation (Eq. 3.13) is expected to increase as the number of sensors in a sensor configuration increases.

BSSP evaluates sensors configurations starting with as many as N_{all} sensors and sequentially removing 1 sensor at each step until a sensor configuration with 1 sensor is reached. Conversely, FSSP evaluates sensor configurations starting with 1 sensor and sequentially adding a sensor until a sensor configuration with N_0 sensors is reached.

For $N_{all} > N_0$, i.e. for the case that the number of sensors to be placed in the structure is small compared to the number of possible sensor positions, usually the case in structural

dynamics applications, the use of BSSP to obtain results has the effect of raising substantially the computational cost as compared to FSSP. Thus, from the computational point of view, the FSSP algorithm should be the preferred algorithm in applications. However, the estimates from the two algorithms are expected to differ due to the fact that both algorithms are heuristic and provide approximate values.

To increase the reliability of the estimates arising from the two heuristic algorithms, the final solution is taken from the combination of the FSSP and BSSP solutions, referred as the SSP estimate. Specifically, for each sensor configuration containing a fixed number of sensors, the final maximum utility value is taken to be $U_{\max} = \max(U_{F,\max}, U_{B,\max})$, where $U_{F,\max}$ and $U_{B,\max}$ are the maximum values estimated from the FSSP and BSSP algorithms, respectively. Additionally, the optimal sensor placement is selected among the FSSP and BSSP optimal sensor placement that corresponds to the value of $U_{\max}$. A similar procedure is used for the minimum utility value, i.e., $U_{\min} = \max(U_{F,\min}, U_{B,\min})$.

When FSSP is used to compute the best sensor configuration, in order to meet the AKF stability conditions for n_p input loads, the first n_p sensors are required to be acceleration sensors placed at their optimal positions. Similarly, when the worst sensor configuration is computed, the first n_p sensors are selected to be acceleration sensors placed at their worst positions.

3.3.2.2 Genetic Algorithms (GA)

Genetic algorithms can also be used with discrete design variables to estimate the optimal sensor locations as well as the type of sensors to be combined. In this work, the GA routine in Matlab is used for optimizing the location of N_0 sensors, consisting of acceleration and/or strain sensors. In this case, there are N_0 discrete-valued design variables with the values of each one constrained to be a lower bound of 1 and an upper bound of N_{all}. In order to meet the AKF stability conditions, for the case where both acceleration and strain sensors are used simultaneously, the first N_p design variables out of the N_0 design variables are constrained to involve acceleration sensors only by allowing the values of the design variable to vary from 1 to N_a, excluding the values of $N_a + 1$ to N_{all} that correspond to strain sensors. The GA is carried out using a population size of $10 \times N_0$ and maximum generations of 10000. GA stops if the average relative change in the best fitness function value is less than a tolerance value selected as 10^{-8}.

3.3.3 State, Observation and Model Prediction Errors

The covariance R of the observation error is assumed to be diagonal with the (i, i) component $R^{(ii)}$ given in the form [66, 76, 77]

$$R^{(ii)} = s^2 + \sigma_e^2 Q_y^{(ii)} \tag{3.26}$$

where $Q_y^{(ii)}$ is the square of the intensity of the QoI y_i at DOF i. The first term accounts for the measurement error and its value is considered to be independent of the response intensity, with the level s of the measurement error to depend on the sensor accuracy and characteristics. The second term accounts for the model error with the error at DOF i selected to be proportional to the variance $Q_y^{(ii)}$ of the square of the intensity of the observed QoI y_i at DOF i. The parameter σ_e denote the levels of model error in relation to the intensity of the QoI. Spatial correlation between the errors in the two measured QoI has also been introduced [76] to avoid sensor clustering due to the redundant information provided by closely spaced sensors measuring the same QoI. More details about the choice of the observation error and the rationale behind it can be found in a number of previous works on the subject [66, 76, 77].

A similar formulation can be used for the variance R_{ε_i} involved in Eq. 3.16 of the error ε_i for the predicted QoI z_i. In this case, only the model error exists and the i-th diagonal element of the covariance matrix can be selected to be

$$R_{\varepsilon_i} = \sigma_\varepsilon^2 Q_{z_i} \tag{3.27}$$

where Q_{z_i} is the square of the intensity of the predicted QoI $z_i(t)$, and σ_ε is the level of model error adjusted in relation to the intensity of the predicted QoI.

The process noise covariance matrix Q is defined based on the magnitude of the state vector

$$Q = \sigma_x^2 diag(Q_x) \tag{3.28}$$

where the standard deviation σ_x controls the order of magnitude of error, while the input force vector error covariance matrix S is defined based on the magnitude of the input intensity

$$S = \alpha^2 diag(Q_u) \tag{3.29}$$

which signifies that the random walk fluctuations of the input is a fraction α of the input intensity.

3.4 Applications

A square plate structure (Fig. 3.1) modeled by thin-shell finite elements (FEs) is used to demonstrate the methodology. The plate is fixed at the left edge. The model is meshed with eight-node shell elements containing six DOF per node. The mesh consists of 420 elements and 441 nodes. Linear elastic behavior is considered. For demonstration purposes, it is assumed that only the lowest eight modes contribute to the response. The lowest eight natural frequencies of the model are presented in Table 3.1. The modal damping ratios for all contributing modes are taken to be equal to 2%. The optimal location of acceleration and/or strain sensors is obtained for the purpose of predicting strains in the structure.

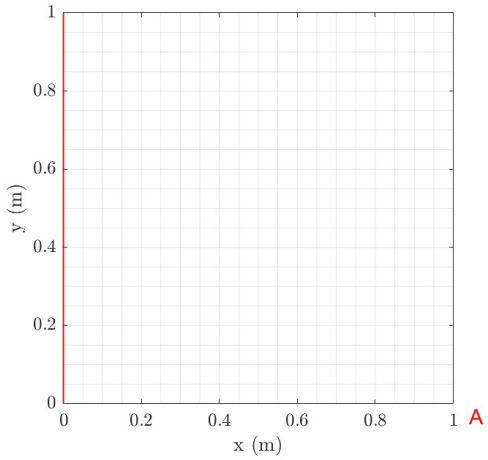

Fig. 3.1. Square thin plate with left edge fixed (shown in red line), meshed with 8-node square elements.

Table 3.1: Contributing modal frequencies of the plate.

Mode	Mode 1	Mode 2	Mode 3	Mode 4	Mode 5	Mode 6	Mode 7	Mode 8
Natural Frequency (Hz)	0.956	2.34	5.90	7.52	8.56	14.99	17.18	17.90

3.4.1 Selection of Process/Plant, Measurement, Model/Prediction and Load Error Parameters

It is assumed that the plate is subjected to a concentrated load applied at the right bottom corner A shown in Fig. 3.1. The effect of the values of the process/plant, measurement and prediction error covariance matrices Q, R and R_ε on the optimal sensor placement for reliable response reconstruction is investigated in this work. For this, to study the effect of small, moderate and large errors, it is required to carefully select the quantities appearing in the definition of Q, R and R_ε in Eq. 3.28, Eq. 3.26 and Eq. 3.27, respectively. Specifically, the quantities Q_x, $Q_y^{(ii)}$ and Q_{z_i} are selected based on a nominal broadband excitation applied at point A, modeled by a Gaussian white noise sequence with standard deviation σ_{wn}. Estimates of the intensities (root mean square) of the accelerations at the DOF perpendicular to the xy plane (plate surface) and the normal strains along the x direction on the upper plate surface are then readily obtained. Specifically, for a scalar discrete stationary zero-mean Gaussian white noise excitation $\underline{u}(t)$ with variance σ_{wn}^2, the covariance matrix Q_z of the response QoI $\underline{z}$ defined in Eq. 3.3 with $\varepsilon_k = 0$ is given by

$$Q_z = \sigma_{wn}^2(\tilde{G}\bar{Q}_x\tilde{G}^T + \tilde{J}S\tilde{J}^T) \tag{3.30}$$

while the covariance matrix Q_x of the state vector $\underline{x}_k$ is given by $Q_x = \sigma_{wn}^2\bar{Q}_x$, where using Eq. 3.1 under stationary conditions and with $\underline{w}_k = 0$, the covariance matrix $\bar{Q}_x$ can be obtained by solving the discrete Liapunov equation

$$A\bar{Q}_xA^T - \bar{Q}_x + BB^T = 0 \tag{3.31}$$

The estimated value of Q_x is used in Eq. 3.28, the value of Q_z is used in Eq. 3.27, while the value of Q_y in Eq. 3.26 is obtained by setting $\underline{z} = \underline{y}$ in Eq. 3.30.

The value of σ_e of the model error in Eq. 3.26 and the values of σ_ε of the prediction error in Eq. 3.27 are selected to be $\sigma_e = \sigma_\varepsilon = 0.001$, 0.01 and 0.1 corresponding to a small, moderate and large model error.

To complete the formulation for the errors, one needs to select the values of the measurement error parameter s in Eq. 3.26. For this, the intensities of the acceleration at all nodes and the strains for all finite elements along the x direction of the plate surface are shown in

Fig. 3.2, normalized by the strength σ_{wn} of the white noise.

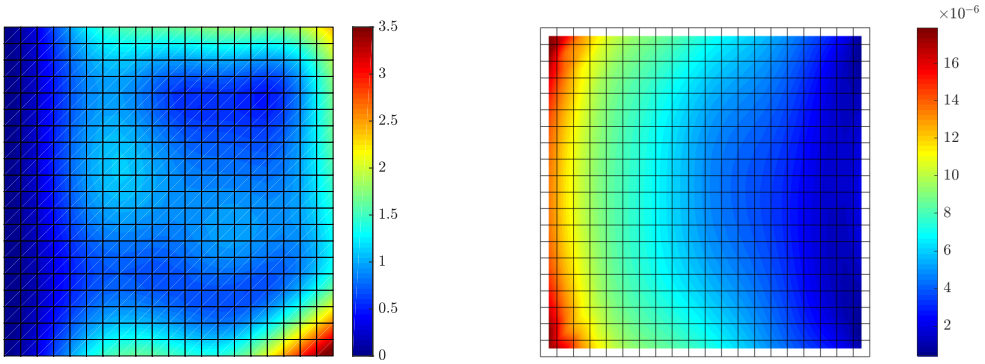

(a) **(b)**

Fig. 3.2. Intensities of (a) accelerations and (b) strains when the plate analysed is subjected to a discrete zero-mean white noise input sequence applied at point A, with standard deviation equal to 1.

The selected values of the measurement error parameter s corresponding to three cases of small, moderate and measurement errors are given in Table 3.2 for acceleration and strain sensors. In Table 3.2, ϵ_{min} is the minimum value of the strain and acceleration that covers 98% of the plate surface. The values in the table for moderate error indicate that the measurement error parameter s is selected in a way that it corresponds to the $1\% - 2\%$ of the average value of the intensity of the response QoI (acceleration or strain). Finally, the value of the covariance matrix S is selected to be $S = 1$, which for the nominal white noise excitation used it corresponds to $\sigma_{wn} = 1$.

Table 3.2: Model, measurement and prediction error, process noise, and load model error parameters. $\epsilon_{\min}$ is the minimum value of the nodal accelerations or element strains that cover 98% of the plate surface. $\epsilon_{\max}$ and ϵ_{rms} are respectively the maximum value and the intensity (root mean square) of the nodal acceleration or element strain in the plate surface.

Error	Sensor type	$\sigma_e, \sigma_\epsilon$	s	s/ϵ_{rms}	$s/\epsilon_{\min}$	$s/\epsilon_{\max}$	σ_x	α
Small	Acceleration	10^{-3}	10^{-3}	10^{-3}	1.4×10^{-2}	2.7×10^{-4}	10^{-3}	1
Small	Strain	10^{-3}	10^{-8}	1.6×10^{-3}	10^{-2}	5.6×10^{-4}	10^{-3}	1
Moderate	Acceleration	10^{-2}	10^{-2}	10^{-2}	1.4×10^{-1}	2.7×10^{-3}	10^{-3}	1
Moderate	Strain	10^{-2}	10^{-7}	1.6×10^{-2}	10^{-1}	5.6×10^{-3}	10^{-3}	1
Large	Acceleration	10^{-1}	10^{-1}	10^{-1}	1.4×10^{0}	2.7×10^{-2}	10^{-3}	1
Large	Strain	10^{-1}	10^{-6}	1.6×10^{-1}	10^{0}	5.6×10^{-2}	10^{-3}	1

3.4.2 Strain Predictions Using a Combination of Acceleration and Strain Observations

The positions of the acceleration and strain sensors are optimized for reliable strain prediction in all 400 finite elements of the plate. The strain sensors are assumed to be placed at the midpoint of each finite element, measuring the normal strain along the x direction on the plate surface.

Taking into account that a single load at A is applied, to be able to have a stable estimation with AKF to be used in the utility function, at least one acceleration sensor is required. Thus, in the optimization procedure, the first sensor is forced to be an acceleration sensor.

3.4.2.1 Information Gain versus Number of Sensors

The utility results estimated using GA and SSP algorithms as a function of the number of sensors are given in Fig. 3.3 for up to 30 sensors for the moderate error case presented in Table 3.2. The maximum information $U_{\max}^{all}$ that can be reached (shown by horizontal line in Fig. 3.3(a)) is calculated by assuming that 420 acceleration and 400 strain sensors are placed at all possible locations. Comparing the utility values calculated by the SSP and the GA algorithm, it can be seen that very similar maximum utility values are obtained for most of the sensor numbers in a sensor configuration (Fig. 3.3(a)). For less than 9 sensors the GA is more accurate than the SSP method. The SSP algorithm gives overall higher utility values for 9 or more sensors, demonstrating in this case an improved accuracy compared to the GA algorithm. However, it is expected that the estimates from the GA algorithm can be improved at a higher computational cost if one uses lower tolerance values for stopping the GA algorithm.

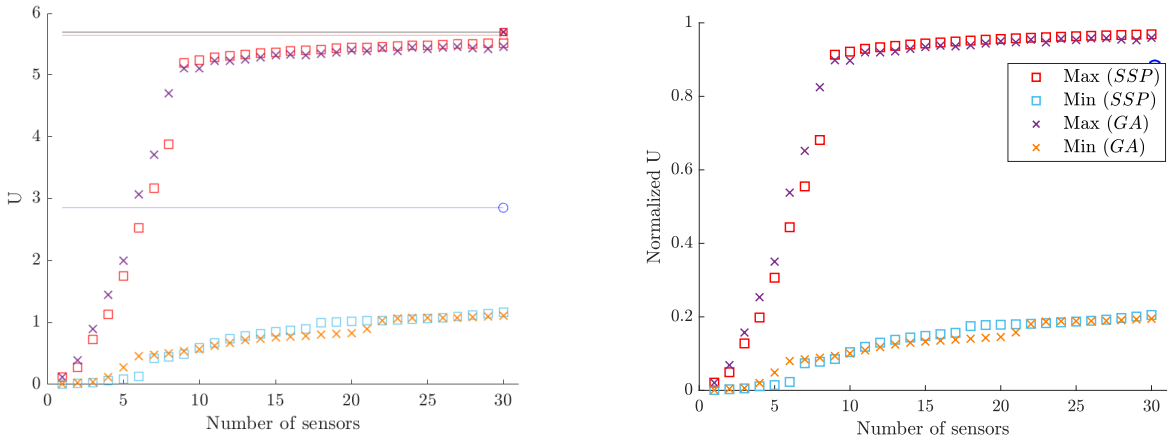

(a) **(b)**

Fig. 3.3. (a) Utility values, and (b) normalized utility values. The maximum utility is obtained by using 820 acceleration and strain sensors, 400 strain sensors, and 420 acceleration sensors, placed at all possible positions, is shown with black, red, and blue horizontal lines, respectively.

Observing the utility values as a function of the number of sensors, it is seen that the information gain increases as additional sensors are placed at their optimal locations. Significant information is gained by each additional sensor for up to 9 sensors placed in the structure. Adding more than 9 sensors, the information gain for each additional sensor placed in the structure is relatively small compared to the information gained for the first nine sensors. Normalized utility values obtained by dividing the utility values in Fig. 3.3(a) by the maximum utility value that can be achieved by placing the maximum number of 420 acceleration and 400 strain sensors are presented in Fig. 3.3(b). Tracking the maximum normalized information gain values as a function of the number of sensors helps decide on the number of sensors to be kept in a sensor configuration. The number of sensors is considered to be adequate when the maximum information gained is a large percentage of the maximum information $U_{\max}^{all}$ or the information gained by each additional sensors is not significant compared to the information gained by the existing sensors. Based on the results in Fig. 3.3(b), it is reasonable to use 9 sensors placed at their optimal positions since the information gained is 91% of $U_{\max}^{all}$ and the increase in information gain by adding a sensor at a time is relatively small. Such information gain should be weighted with the cost of the information [67] so that a cost-effective and highly informative sensor configuration is obtained.

Comparison of FSSP, BSSP and GA algorithms can be seen in Fig. 3.4. It is evident that the GA algorithm also provides a near optimal solution, as the heuristic FSSP and BSSP

algorithms do. The BSSP provides the best accuracy for 9 or more sensors, while GA provides more accurate solutions for less than 9 sensors. The FSSP gives better accuracy than BSSP for less than 9 sensors. The GA estimate depends on the tolerance values used. Improving this estimate using lower tolerance values for stopping the algorithm may be computationally a very costly procedure.

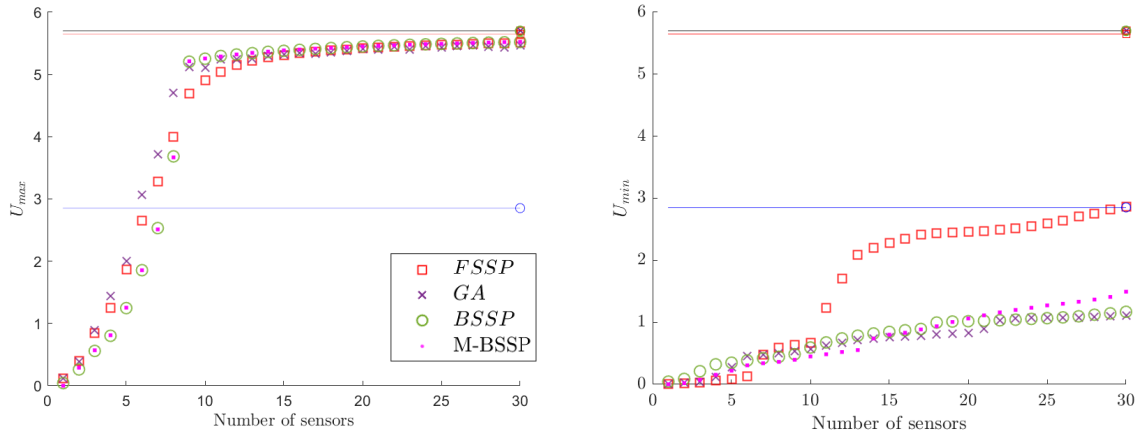

(a) **(b)**

Fig. 3.4. Comparison of FSSP, BSSP, M-BSSP and GA. (a) Maximum utility values, and (b) minimum utility values. The max utility obtained by using 820 acceleration and strain sensors, 400 strain sensors, and 420 acceleration sensors, placed at all possible positions, is shown with black, red, and blue horizontal lines, respectively.

The time-to-solution (TTS) required for estimating the optimal and worst sensor placement results for 1 to 30 sensors from the different algorithms is given in Table 3.3. This TTS is 1 min for FSSP, 842 min for BSSP, 843 min for SSP, and 32 min for GA. The results reveal that the FSSP method is computationally very efficient, while the BSSP method can be very inefficient if the number of possible sensor positions N_{all} is large.

The computational efficiency of GA is significantly less than FSSP and higher than BSSP. However, the computational cost for BSSP can be drastically improved by starting the BSSP with a configuration that involves significantly less number of sensors N_{start} selected to be higher than the number N_0 of sensors to be optimized. The starting sensor configuration with N_{start} sensors must be selected to be optimal. Such sensor configuration can be obtained using the FSSP or the GA algorithm. Following this procedure, results from the modified BSSP (M-BSSP) algorithm for $N_{start} = 100$ and 200, instead of 820, are given in Table 3.3 and also in Fig. 3.4 for $N_{start} = 100$. It is clearly seen in Fig. 3.4 that the estimates of the utility values almost coincide with those of the original BSSP algorithm. Estimating the starting sensor

configuration for $N_{start} = 100$ using FSSP, the total computation time for running M-BSSP is 5.7 min. Specifically, the TTS is 0.7 min to compute the optimal sensor configuration for 1-100 sensors using BSSP and 5 min the required time to run FSSP for 1-100 sensors. Estimating the starting sensor configuration using the GA algorithm for 100 sensors, the TTS drops to 1 min (0,7 min to compute the optimal sensor configuration for 1-100 sensors using BSSP and 0.3 min the required time to run GA for 100 sensors) which is approximately the same as the TTS required to compute the optimal sensor configuration for 1-30 sensors using FSSP. As a results, the computational time using M-BSSP is approximately two to three orders of magnitude less than the computational time of 842 min required for the original BSSP algorithm.

Table 3.3: Time-to-solution (TTS) for computing the optimal and worst sensor configurations for 1 to 30 sensors from different algorithms.

Method	FSSP	BSSP	SSP	GA	FSSP	GA	M-BSSP	FSSP	GA	M-BSSP
Sensors	1-30	1-30	1-30	1-30	1-100	100	1-100	1-200	200	1-200
TTS (min)	1	842	843	32	5	0.3	0.7	14	0.1	3

3.4.2.2 Optimal Location of Acceleration and Strain Sensors

Fig. 3.5(a) shows the best acceleration (circle) and strain (square) sensor locations (estimated using GA and SSP algorithms) for 9 sensors. For SSP results, the best type of sensors to be used are 5 acceleration sensors and 4 strain sensors out of the total of 9 sensors. The 4 strain sensors are placed on the plate at a reasonable distance from each other and far from the right edge which has a very small strain intensity and so the noise-to-signal ratio is expected to be large. The acceleration sensors are placed closer to the right edge, far away from the fixed support, since there again the noise-to-signal ratio is expected to be smaller than places close to the fixed support. Similar results in terms of the number and location of the acceleration and strain sensors are obtained using GA, promoting 5 acceleration sensors and 4 strain sensors. For the worst sensor positions (Fig. 3.5(b)), SSP and GA results are consistent in terms of showing that nine acceleration sensors (no strain sensors) placed close to the left edge, where the noise-to-signal ratio in acceleration time histories is large, will give the worst strain predictions.

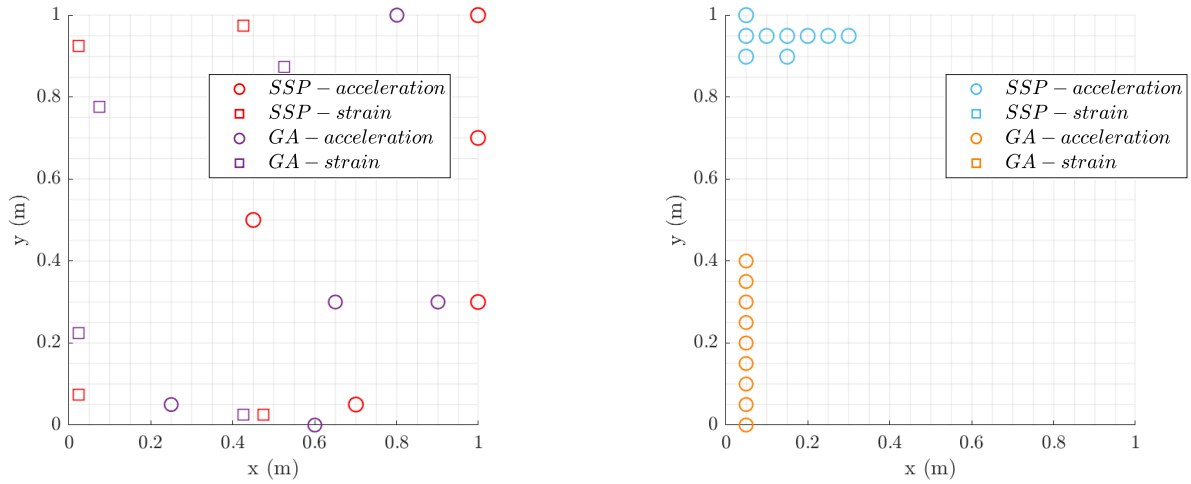

Fig. 3.5. (a) Best 9 sensor positions, and (b) worst 9 sensor positions.

The optimal sensor configuration for 6 sensors is found to involve 4 acceleration sensors and 2 strain sensors (Fig. 3.5(a)). It is worth noting that the maximum information gain that can be achieved for 6 sensors is 3.28, which is slightly higher (see Fig. 3.3) than the maximum information gained with 420 acceleration sensors placed at all possible positions (blue horizontal line in Fig. 3.3). It is thus obvious that a combination of the two type of sensors can give a very effective sensor configuration with a very small number of 6 sensors, avoiding the use of the large number of 420 acceleration sensors that achieves inferior information.

It should be pointed out that based on the utility values presented in Fig. 3.3, the SSP results for the optimal sensor configuration are slightly more informative than the GA results. Nevertheless, it is expected that both algorithms will give reasonable near optimum sensor configurations. The observed variability in the near optimal sensor configuration between the predictions from the SSP and GA algorithms is due to the fact that among all 4.4e+20 possible sensor configurations of 9 sensors placed at 820 positions, a small fraction of them give near optimum solutions. This small fractions can be a large number of sensor configurations that are promoted by the SSP and GA algorithms used.

The AKF method for response reconstruction and virtual sensing is able to fuse acceleration and strain sensors. Despite the fact that the predictions are strains throughout the plate, the type of sensors that are promoted for monitoring are both acceleration and strain sensors. In contrast, the optimal sensor placement based on modal expansion [66] limits the type of sensors that can be used. For example, for strain predictions, only strain or displacement sensors

can be used.

3.4.2.3 *Effect of Measurement and Model Errors*

The effect of the measurement and model errors on the OSP results is next investigated. OSP results for small, moderate, and large measurement errors are obtained by selecting the values of the error covariance matrix parameter s (in Eq. 3.26) to vary as indicated in Table 3.2 and letting the model error parameters to be $\sigma_e = \sigma_\varepsilon = 0.01$, corresponding to moderate model error. The utility results for the three measurement error cases estimated using the M-BSSP and GA algorithms are presented in Fig. 3.6. Similar results for moderate measurement error are compared in Fig. 3.7 for three different values of the model error selected to be $\sigma_e = \sigma_\varepsilon = 10^{-3}$ (small model error), 10^{-2} (moderate model error) and 10^{-1} (large model error). It is clear that the information gain decreases as the measurement error or the model error increases, signifying that less information is gained from noisy measurements or less accurate models.

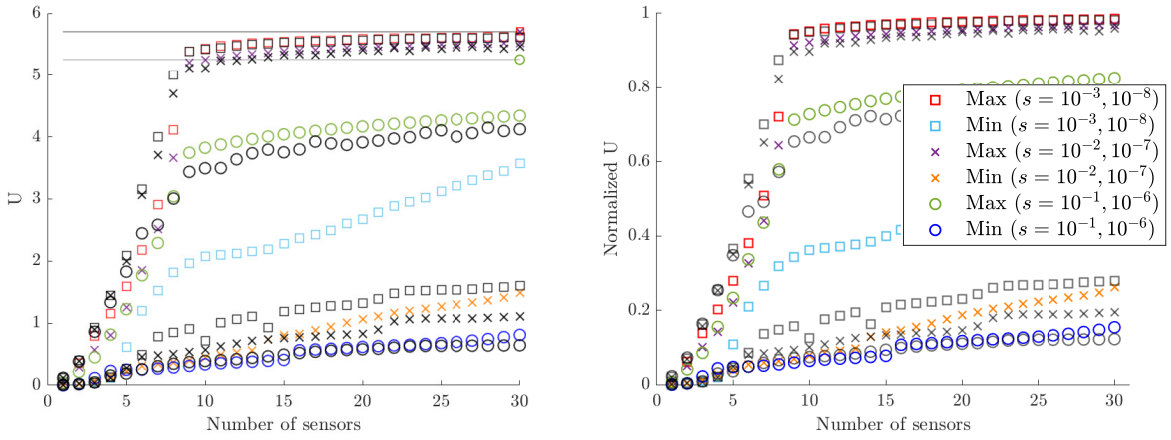

(a) **(b)**

Fig. 3.6. Comparison of utility (information gain) results for different measurement error cases. Color and black symbols represent results obtained from M-BSSP and GA algorithms, respectively. (a) Utility values, (b) normalized utility values. The max utility obtained by using 820 acceleration and strain sensors, 400 strain sensors, and 420 acceleration sensors, placed at all possible positions, is shown with black horizontal lines.

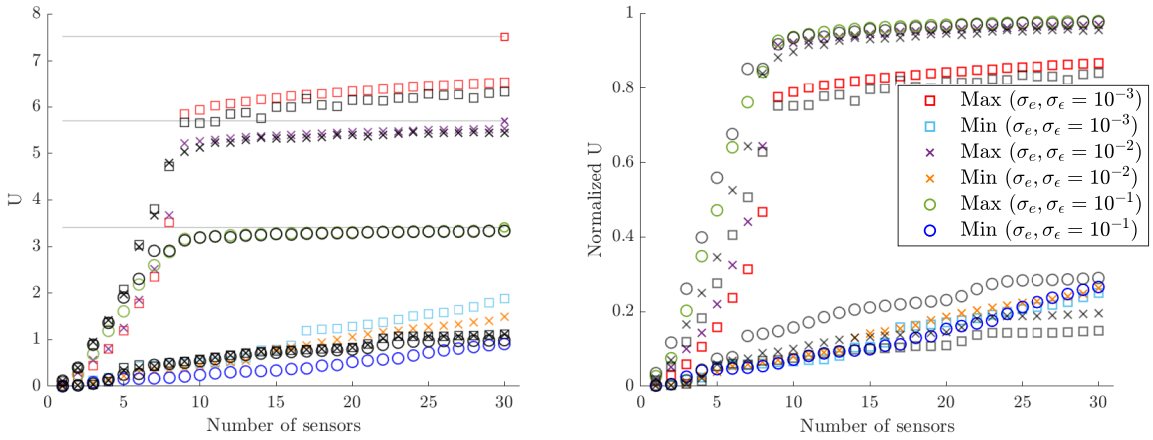

(a) **(b)**

Fig. 3.7. Comparison of utility (information gain) results for different model error cases. Color and black symbols represent results obtained from M-BSSP and GA algorithms, respectively. (a) Utility values, (b) normalized utility values. The max utility obtained by using 820 acceleration and strain sensors, 400 strain sensors, and 420 acceleration sensors, placed at all possible positions, is shown with black horizontal lines.

For small to moderate measurement errors (see Fig. 3.6b), nine sensors placed at their optimal location account for 95% to 90% approximately of the maximum information $U^{all}_{\max}$ that can be achieved by adding 820 strain and acceleration sensors at all possible locations. In contrast, for large measurement error the information gain that can be achieved with 9 sensors placed at their optimal locations is 65% of the maximum information gain $U^{all}_{\max}$. This significantly lower information extracted from the measurements is due to the higher noise to signal ratio in the measurements. Specifically, more sensors are needed to extract significant information, with 30 sensors providing only 75% of $U^{all}_{\max}$. The higher the measurement error, the less the information extracted from the sensors, which is consistent with the results obtained from a similar work based on modal expansion technique for response reconstruction [66].

Similar observations can be made for the different model errors. The higher the model error, the less the information gained from a sensor configuration involving a fixed number of sensors. There is, however, a qualitative difference for the effect of the number of sensors on the information gain for the two different types of errors. As the measurement error increases, the maximum information gain $U^{\max}_{all}$ that can be achieved with 820 strain and acceleration sensors does not deteriorate significantly as can be seen by the horizontal lines in Fig. 3.6(a). However, increasing the measurement error to large values, the information gained by using 9 sensors is only 60% of $U^{all}_{\max}$, and a large number of sensors are required to gain the remaining

40% of the information. In contrast, increasing the model error to large values (Fig. 3.7(a)), the maximum information gain that can be achieved with 820 strain and acceleration sensors reduces substantially to 60% and 45% of the maximum information gained for moderate and small model error values, respectively. However, for large model error, a large percentage, around 94%, of the maximum information gain $U_{all}^{\max}$, can be achieved with as many as 9 sensors placed at their optimal locations. Adding more sensors from 10 to 820 will only result in a very small increase (5%) of the maximum information gain. Thus, for high model error a small number of sensors placed at their optimal locations will obtain most of the information that can be achieved by fully populating the structure with sensors, while for high measurement error, the same small number of sensors will only contain a percentage of the information gain and many more sensors are required to gain the large amount of the remaining information.

The optimal sensor positions for nine sensors obtained using the combined M-BSSP estimates are compared for the different values of the measurement errors and moderate model error in Fig. 3.8(a) and for moderate measurement error and different values of model error in Fig. 3.8(b). For small measurement errors in Fig. 3.8(a), the strain sensors are placed towards the right edge of the plate where, although the strains are relatively small, the noise to signal ratio is small and the quality of information is very good. For large measurement errors in Fig. 3.8(a), placing strain sensors in the right edge is avoided since the signal to noise ratio for strains decreases and the quality of information from strain sensors placed towards the right edge is substantially deteriorated. In addition, for the large error case, the strain sensors towards the right edge tend to be replaced by acceleration sensors. The worst sensors are found to be acceleration sensors (not shown in the figures) for all error cases placed at the nodes closest to the left support.

From Fig. 3.8(b) it can be seen that there is not a clear trend in the placement of sensors for different levels of model error. One does not expect to have the tendency observed with increasing measurement error since the model error, quantified at each point in the plate as a fixed error with respect to the intensity of the measured/predicted QoI at this point, is set to be the same over the whole surface. So locations with higher or lower signal-to-noise ratio should not be preferred.

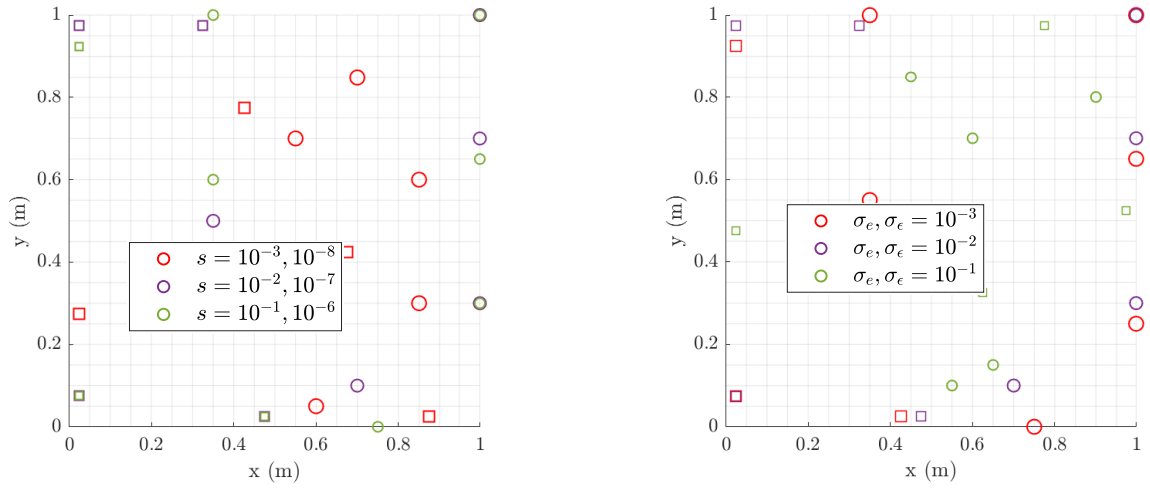

(a) **(b)**

Fig. 3.8. Comparison of best sensor locations for 9 sensors using M-BSSP (a) for different measurement error cases, (b) for different model error cases. Acceleration and strain sensors are shown with circle and square, respectively.

3.4.2.4 Robustness to Measurement and Model Error Uncertainties

The level of noise to signal ratio are not known a priori since the intensity and frequency content of the excitation and thus the level of measured response is not known. The size of model/prediction errors due to unmodelled dynamics is also not known a priori. Thus, it is more rational to use a robust design to better account for uncertainty in measurements and model/prediction errors. Two robust designs $R1$ and $R2$ are next considered. In robust design $R1$, the uncertainties for measurement errors are considered by letting $s = 10^{\beta}$ and assigning a uniform prior distribution of the measurement error parameter β with large enough bounds, given by $\beta \sim U(-8, -6)$ for strain sensors and $\beta \sim U(-3, -1)$ for acceleration sensors, covering the domain in the parameter space that correspond to small, moderate and large measurement errors. The uncertain parameter space has dimension two since it involves one parameter for the measurement error for accelerations and one parameter for strains. Similarly, in robust design $R2$, the uncertainties for model errors are considered by letting $\sigma_e = \sigma_\varepsilon = 10^{\gamma}$ and assigning a uniform prior distribution of the model error parameter γ with large enough bounds, given by $\gamma \sim U(-3, -1)$ for strain and acceleration sensors, covering the domain in the parameter space that corresponds to small, moderate and large model errors. The uncertain parameter space has dimension one. OSP robust results are calculated for moderate measurement error using the sparse grid algorithm of order 10.

The number of strain and acceleration sensors estimated for each optimal sensor configuration for N_0 ranging from 1 to 30 for the two robust cases $R1$ and $R2$ are compared in Fig. 3.9 with the ones obtained for the deterministic case for moderate model and measurement error. It can be seen that there is an increase in strain sensors in the robust case $R1$ compared to the strain sensors required in the deterministic case. The number of acceleration sensors in the robust case $R1$ is two for all values of $N_0 > 1$ considered. Also for the robust case $R2$, there is no clear change in the number of strain and acceleration sensors in a sensor configuration when compared to the deterministic case. The optimal sensor configuration obtained for 1 to 30 sensors for the robust case $R1$ (or the robust case $R2$), is used to estimate the utility values, denoted by U_s^{R1}, U_m^{R1} and U_l^{R1} (or U_s^{R2}, U_m^{R2} and U_l^{R2}) for the three deterministic cases corresponding to small, moderate and large measurement error, respectively. The ratio $U_s^{R1,2}/U_s^{\max}$, $U_m^{R1,2}/U_m^{\max}$ and $U_l^{R1,2}/U_l^{\max}$ of the computed utility values to the maximum utility values $U_s^{\max}$, $U_m^{\max}$ and $U_l^{\max}$ for the deterministic cases for small, moderate and measurement (respectively model) errors are shown in Fig. 3.10. Such ratios provide the percentage of information gain that the robust OSP can achieve for the three measurement or model error cases in relation to the maximum information gain that could be achieved by the three deterministic cases. The closeness of these values to unity indicates the effectiveness of the OSP robust case when applied to the three deterministic cases of small, moderate and large error. It can be seen that the robust case is effective for large model or measurement errors. Decreasing these errors, the effectiveness of the robust cases deteriorates, reaching information gain values that are as low as 88% of the information entropy values that can be achieved by the OSP obtained for the deterministic cases.

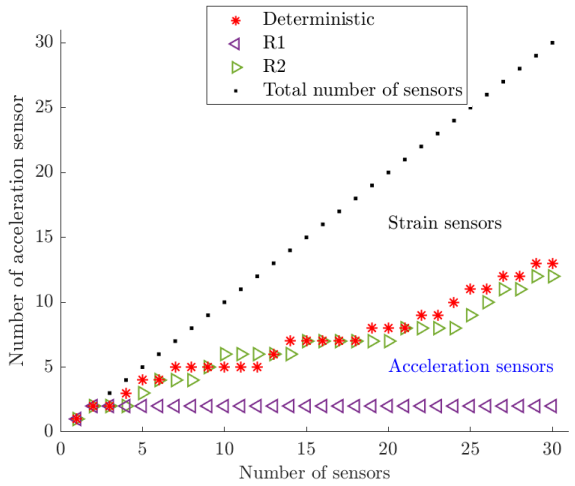

Fig. 3.9. Number of acceleration sensors and total number of sensors versus number of sensors for deterministic and robust cases $R1$ and $R2$. The number of strain sensors is the difference between the total number of sensors and the number of acceleration sensors.

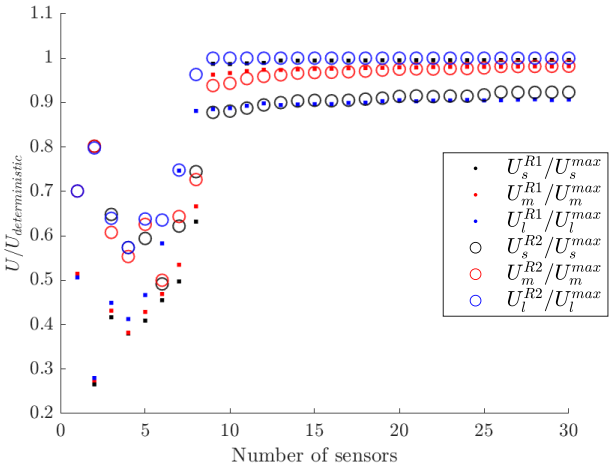

Fig. 3.10. Ratios $U_s^{R1,2}/U_s^{\max}$, $U_m^{R1,2}/U_m^{\max}$ and $U_l^{R1,2}/U_l^{\max}$ for the robust cases $R1$ and $R2$, computed using (a) GA for 1 to 8 sensors, and (b) M-BSSP for 9 to 30 sensors.

3.4.3 OSP for Strain Prediction using Acceleration-Only or Strain-Only Measurements

Next, the optimal sensor placement for reliable strain prediction in all 400 finite elements is performed using either acceleration or strain sensors. For optimally locating acceleration sensors, the maximum utility results calculated using SSP and GA algorithms are given in Fig. 3.11(a) for moderate model and measurement error (see Table 3.2) as a function of the number of sensors. For 8 or more sensors, the utility values found by the SSP and the GA algorithms are almost the same (Fig. 3.11(a)). For 5 to 7 sensors, the GA algorithm is more accurate providing slightly higher values than the ones predicted by SSP. It is apparent that the

optimal number of acceleration sensors is 8 placed at their optimal positions since the information gain is almost the same as the information gained by populating the plate with as many as 420 acceleration sensors at all possible locations. Comparing the maximum information gain $U_{all}^{\max}$ in Fig. 3.11(a) with the one in Fig. 3.3(a), it can be seen that an optimal sensor configuration consisting of a combination of strain and acceleration sensors provides significantly higher information than an optimal sensor configuration consisting of acceleration sensors only.

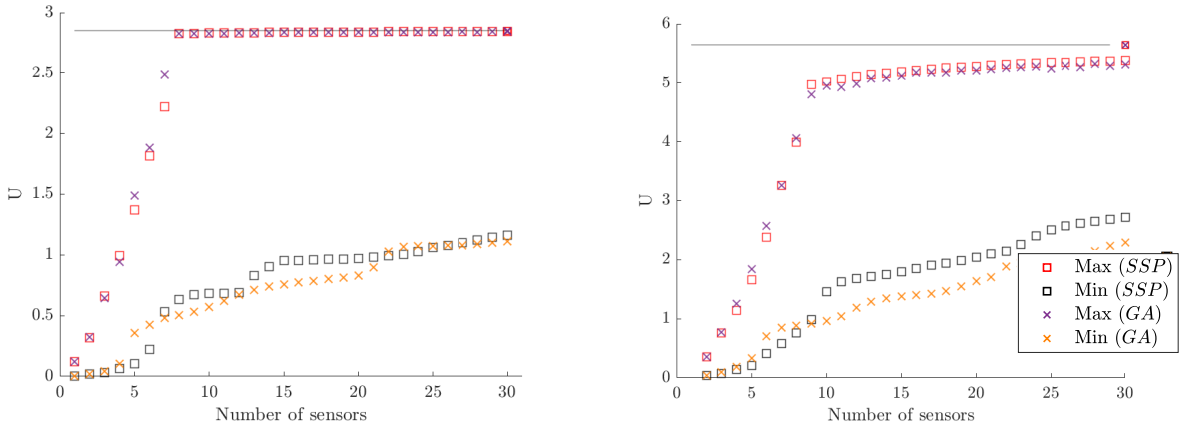

(a) **(b)**

Fig. 3.11. Comparison of SSP and GA. Utility values obtained by (a) acceleration sensors, (b) strain sensors. The max utility values obtained by using acceleration or strain sensors placed at all possible positions are shown with a horizontal line (420 acceleration sensors in (a), 400 strain sensors (with one acceleration) in (b).

The maximum utility values as a function of strain sensors optimally located in the plate are given in Fig. 3.11(b). To maintain stability of the Kalman filter, the positions of the strain sensors are optimized by introducing an acceleration sensor at the input location. For 8 or more strain sensors, the utility values estimated by SSP are slightly higher than the ones estimated by GA, while for less than 8 sensors GA provides slightly better results than SSP. Comparing the results in Fig. 3.11(b) for strain sensors and 1 acceleration sensor at the load location, with the ones in Fig. 3.3(a) for a combination of strain and acceleration sensors optimally placed in the structure, the information gain obtained using strain sensors only (and 1 acceleration sensor) is not significantly less than the information provided by sensor configurations consisting of a combination of optimally placed acceleration and strain sensors. As a result, in contrast to the significantly less informative sensor configurations consisting of acceleration sensors (compare Fig. 3.11(a) with Fig. 3.3(a)), sensor configurations involving strain sensors only (and one acceleration sensor to maintain filter stability) can provide almost as good information

as the combination of strain and acceleration sensors (compare Fig. 3.11(b) and Fig. 3.3(a)). However, installation, calibration and maintenance complexities involved with strain sensors make their use less favorable than acceleration sensors. Thus, a combination of acceleration and strain sensors is the most preferred sensor configuration as presented in Section 3.4.2.

The TTS required for optimizing the acceleration or the strain sensors for 1 to 30 sensors from different algorithms is given in Table 3.4. The TTS for computing the optimal and worst locations of acceleration sensors is 17 min for SSP algorithm (0.7 min for FSSP) and 30 min for GA algorithm. The TTS for computing the optimal and worst locations of strain sensors is 32 min with SSP (0.7 min for FSSP) and 18 min with GA algorithm.

The computational effort for SSP (combination of FSSP and BSSP) algorithm can be substantially reduced by one to two orders of magnitude by using M-BSSP algorithm with $N_{start} = 100$ sensors. Specifically, the TTS for acceleration sensors drops from 17 min for SSP to 3.1 and 0.7 min for M-BSSP using respectively FSSP and GA algorithm to compute the starting sensor configuration for $N_{start} = 100$ sensors, while for strain sensors drops from 32 min for SSP to 3.1 and 0.7 min for M-BSSP using respectively FSSP and GA algorithm to compute the starting sensor configuration for $N_{start} = 100$ sensors. The results reveal that the FSSP method is computationally very efficient, while the BSSP method can be inefficient if the number of possible sensor positions N_{all} is large, leading to computational effort that might exceed that of GA algorithm. The proposed M-BSSP algorithm exploits the computational efficiency of FSSP and the accuracy of BSSP. These results are consistent with the results reported in Table 3.3. Comparing the computational savings gained using M-BSSP in Table 3.3 for $N_{all} = 820$ and Table 3.4 for $N_{all} = 400$ or 420, it can be concluded that higher savings are expected as N_{all} increases.

Table 3.4: Time-to-solution (TTS) for computing the optimal and worst sensor configurations for 1 to 30 acceleration only or strain only sensors from different algorithms.

Method	FSSP	BSSP	SSP	GA	FSSP	GA	M-BSSP	FSSP	GA	M-BSSP
Sensors	1-30	1-30	1-30	1-30	1-100	100	1-100	1-200	200	1-200
TTS (min) - Accel. sensors	0.7	16	17	30	2.5	0.1	0.6	5.4	0.1	2.6
TTS (min) - Strain sensors	0.7	31	32	18	2.5	0.1	0.6	5.6	0.1	2

The best sensor locations for 8 sensors obtained using the GA and SSP algorithms are given in Fig. 3.12(a) for acceleration sensors only and in Fig. 3.12(b) for strain sensors only. For each case, both SSP and GA provide qualitatively similar sensor positions. The acceleration sensors

are distributed towards to the right edge which has higher acceleration intensity and thus low noise to signal ratio. Similarly, the strain sensors are distributed towards the left edge since the strain values are higher and the noise to signal ratio is low.

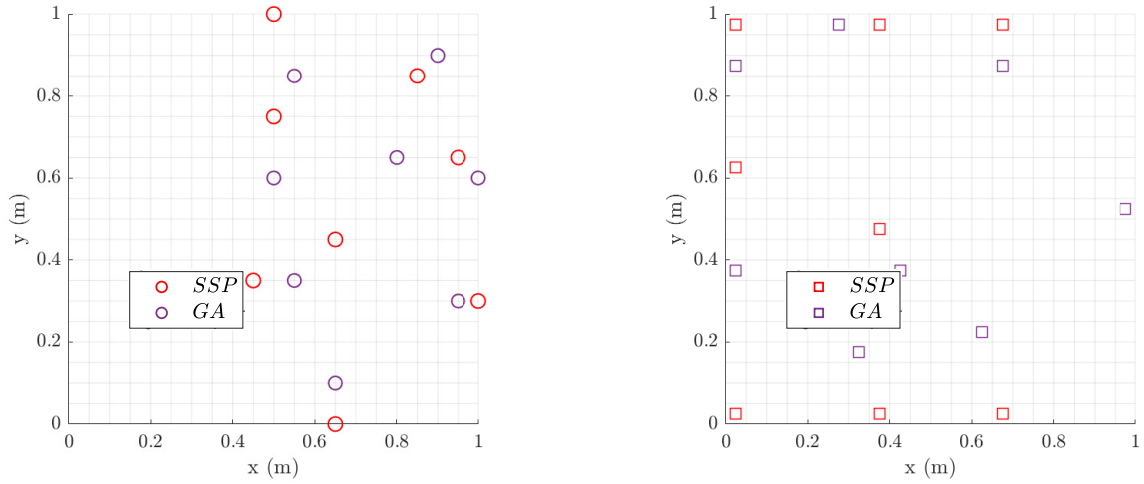

(a) **(b)**

Fig. 3.12. (a) Best 8 acceleration sensor positions, (b) best 8 strain sensor positions.

3.4.4 Optimal Sensor Configuration for Input Estimation

The optimal design of sensor configuration for input reconstruction is next considered. The maximum and minimum information gain values estimated by the M-BSSP algorithm as a function of the number of sensors is given in Fig. 3.13(a). These values are compared with the maximum and minimum information gain values estimated for strain response predictions. A similar trend is observed, although the maximum information gain for input estimation is less than the maximum information gain for strain response predictions. In contrast to the strain response predictions where 9 sensors provide more than 90% of the maximum information $U_{\max}^{all}$, 7-9 sensors and as many as 30 sensors optimally placed for input estimation provide approximately 70% and 80% of the $U_{\max}^{all}$, respectively. One needs more than 30 sensors to achieve an information gain higher than 90% of the $U_{\max}^{all}$.

Comparison of the optimal sensor configurations involving 9 sensors for input and response reconstruction is shown in Fig. 3.13(b). The optimal sensor configurations present some differences which are expected, since the objectives differ in the two design cases. Fig. 3.13(a) also includes the information gain values $U_s(\delta_{in})$ for the strain predictions for 1 to 30 sensors that can be achieved for the sensor configuration optimally designed for reconstructing the input.

Similarly, the information gain curve $U_{in}(\delta_s)$ for input estimation that can be achieved for the sensor configuration optimally designed for estimating strains is also presented. It can be seen that in both cases of the optimal sensor configuration for a design objective is suboptimal for another design objective. The information loss is of the order of approximately 20% loss.

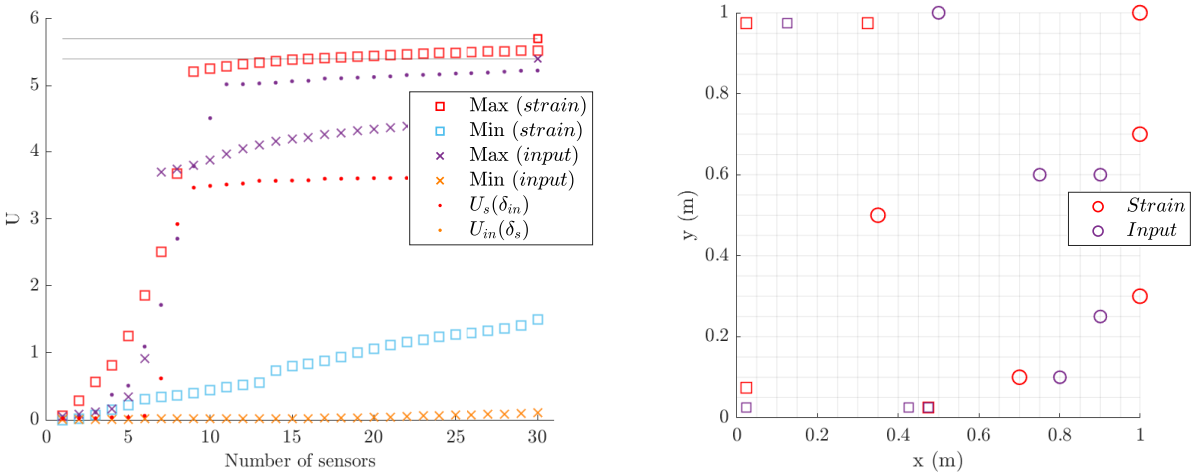

(a) **(b)**

Fig. 3.13. Comparison of OSP results for strain or input reconstruction. (a) utility values, (b) best sensor positions found by M-BSSP. The maximum utility obtained by using 820 acceleration and strain sensors, 400 strain sensors, and 420 acceleration sensors, placed at all possible positions, is shown with black lines. Acceleration and strain sensors are shown with circle and square symbols, respectively. $U_s(\delta_{in})$ (respectively $U_{in}(\delta_s)$) is the information gain for the strain (respectively input) reconstruction using the sensor configuration optimally designed for reconstructing the input (respectively strain).

3.4.5 Effectiveness of Optimal Sensor Configuration for Response Predictions

The effectiveness of the best sensor configuration is next investigated using simulated measurements. For this, a white noise input at location A (Fig. 3.1) is first used to simulate strain response time histories at all finite elements considering up to eight contributing modes. The standard deviation of the Gaussian white noise sequence is set to $\sigma_{wn} = 1$. A sampling period of $\Delta t = 0.01$ seconds and a response duration of 10 seconds are used to generate the simulated time histories. To simulate noise contaminated measurements and thus consider the effect of the measurement error (noise from sensors), independent zero-mean Gaussian white noise sequences with standard deviation equal to 2% of the intensity of the simulated response is added to each simulated strain response time history.

The relative errors between the strain responses predicted by AKF with a fixed number

of sensors and the simulated, noise contaminated measurements are used to demonstrate the effectiveness of the optimal sensor configuration in the presence of measurement error. The relative strain error at each location is defined as the ratio of the root mean square error between the predicted and measured responses over the root mean square value (intensity) of the measured strain response time history. The relative errors for the strain predictions obtained using AKF for 9 best sensor positions found by SSP algorithm for moderate measurement and model errors are presented in Fig. 3.14(a). The information gain for the best sensor configuration is 91% of $U_{\max}$. These errors should be compared with the relative errors shown in Fig. 3.14(b), obtained using 9 sensors placed at arbitrarily selected sensor positions and corresponding to lower utility value of 68% of $U_{\max}$. It is clear that the errors for the arbitrarily selected sensor configuration are significantly higher than the ones for the optimal sensor configuration. In particular, the average relative error over the plate surface is 4.23% for the arbitrary sensor configuration, which should be compared to the average relative error of 1.67% for the optimal sensor configuration. The average relative errors computed between input time history predicted by AKF and the simulated input are found to be 16.21% and 11.87% for the arbitrary and optimal sensor configuration, respectively. These higher errors are consistent with the finding in Section 3.4.4 where optimal sensor placement for response reconstruction is suboptimal for input reconstruction and that a small number of sensors (9 sensors in this case) contain 60% of the maximum information gain that can be achieved by fully populating the plate with sensors. In general, the aforementioned results confirm the effectiveness of the proposed OSP methodology.

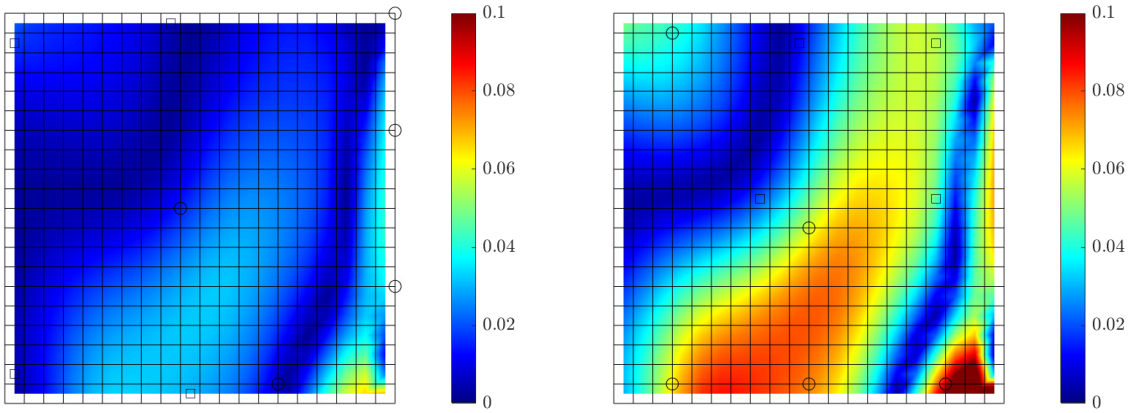

(a) **(b)**

Fig. 3.14. Relative errors in strain response for white noise excitation using simulated data with 2% added Gaussian noise (measurement error). (a) Best sensor configuration with 9 sensors obtained for moderate measurement and model error; $U = 5.21$ corresponding to 91.32% of U_{max}; average strain error 1.67%; average input error 11.87%. (b) Arbitrarily selected sensor configuration with 9 sensors; $U = 3.88$ corresponding to 68% of U_{max}; average strain error 4.23%; average input error 16.21%.

Similar results are presented in Fig. 3.15, corresponding to inflicted model errors instead of measurement errors. The model errors are introduced by simulating measurements from a finite element model of the plate with all nodal masses perturbed independently by 10% (a zero-mean Gaussian perturbation with standard deviation 0.1 is used) around their nominal values. The relative errors in the strain predictions using the optimal sensor configuration for moderate measurement and large model error corresponding to information gain of 93% of $U_{\max}$ remain less than approximately 3% with an average relative error to be 1.14% over the plate surface, while the relative errors for the arbitrarily selected sensor configuration corresponding to lower information gain of 71% of $U_{\max}$ is significantly higher with an average relative error of 5.6%. The average relative errors computed for the input predicted by AKF and simulated input are found to be 49.4% and 21.74% for the arbitrary and the optimal sensor configuration, respectively.

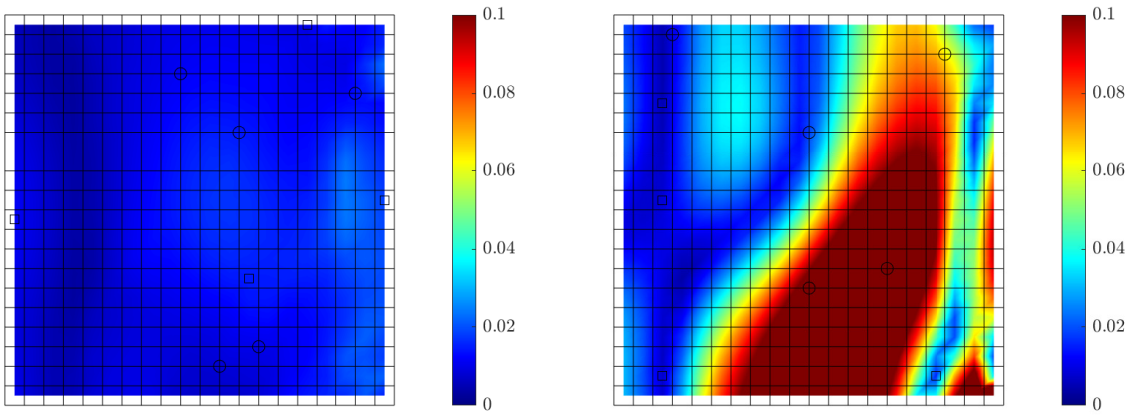

(a) **(b)**

Fig. 3.15. Relative errors in strain response predictions for white noise excitation using simulated data with 10% model error. (a) Best sensor configuration with 9 sensors obtained for moderate measurement and large model error; $U = 3.16$ corresponding to 93% of U_{max}; average strain error 1.14%; average input error 21.74%. (b) Arbitrarily selected sensor configurations with 9 sensors; $U = 2.41$ corresponding to 71% of U_{max}; average strain error 5.60%; average input error 49.4%.

The study is repeated for impulse excitation applied at location A. The impulse is simulated as a triangular excitation of maximum value of one and duration equal to $t_0 = T_8/5$, where T_8 is the modal period of the last contributing mode. For $t > t_0$ the triangular excitation is set to zero. The discretization time is $\Delta t = t_0/6$. The duration of the response to impulse excitation is selected to be approximately $T = -log(0.1)/(\zeta_1\omega_1)$, where $\omega_1 = 2\pi f_1$ is the first modal frequency with f_1 is the value of the fundamental modal frequency in Hz given in Table 1. At the end of the duration T, the response is expected to fall off to approximately 10% of the maximum response values observed in the beginning of the excitation. Simulated data for the acceleration and strain response time histories over the plate surface are generated by adding in each time history a Gaussian noise of standard deviation equal to 2% of the acceleration and strain intensity.

Results for the effectiveness of the optimal and arbitrary sensor configurations involving 9 sensors are shown in Fig. 3.16(a) and Fig. 3.16(b), respectively. The average relative error over the plate surface is 25% for the arbitrary sensor configuration which should be compared to the average relative error of 13% for the optimal sensor configuration. The average relative errors computed between input time history predicted by AKF and the simulated input for the duration $0 - t_0$ sec are found to be 27% and 18% for the arbitrary and optimal sensor configuration (for $0 - t_0$ sec). The errors for the arbitrarily selected sensor configuration are

found to be significantly higher than the ones for the optimal sensor configuration, confirming the effectiveness of the proposed optimal sensor placement methodology.

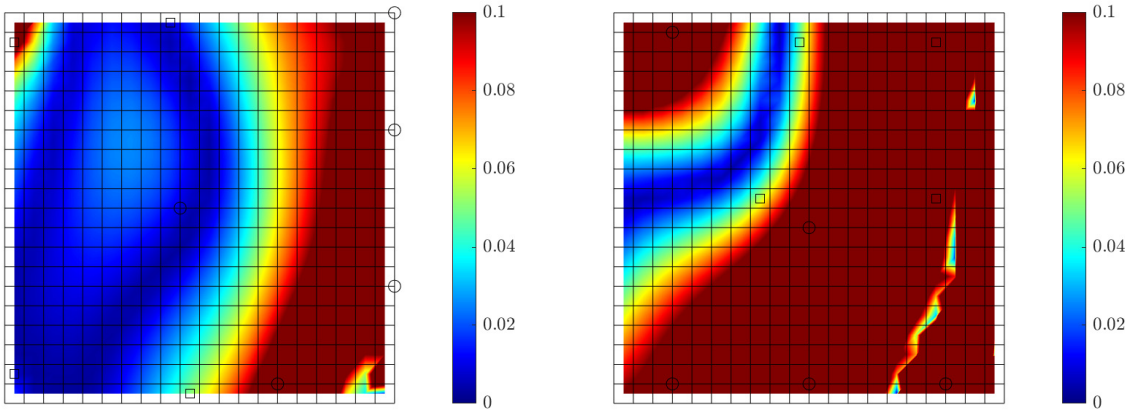

(a) **(b)**

Fig. 3.16. Relative errors in strain response predictions for impulse excitation using simulated data with 2% added Gaussian noise (measurement error). (a) Best sensor configuration with 9 sensors obtained for moderate measurement and model error; $U = 5.21$, 91.3% of U_{max}, average strain error 13%, average input error 18%. (b) Arbitrarily selected sensor configuration with 9 sensors; $U = 3.88$, 68% of U_{max}, average strain error 25%, average input error 27%.

3.5 Conclusions

A methodology is presented for optimizing the type and location of sensors in a structure for reliable response and input reconstruction (virtual sensing) in the challenging case of output-only vibration measurements. AKF is used for input-state estimation and virtual sensing. The utility function to be optimized with respect to the type and location of sensors is defined as the information gained from the data during the measurement update step of the AKF, quantified as the KL-div between the prior and the posterior PDF of the response QoI obtained during the AKF update and measurement step. Exploiting the linearity of the dynamic system and the Gaussian nature of the input and response predictions, the utility is formulated in terms of the corresponding variances of the errors in the predictions of the input and/or response QoI, readily obtained by solving the steady-state Riccati equation. The utility is extended to account for uncertainties in structural model parameters, as well as measurement and model error parameters.

Two types of optimization methods, a heuristic algorithm and a GA algorithm, are used to

estimate the optimal and worst sensor configurations as a function of the number of sensors. For the heuristic algorithm, various versions of the SSP algorithm are introduced and tested for computational efficiency and accuracy. Comparisons with the GA algorithm are made. The FSSP algorithm is by far the computationally most efficient one but may suffer from accuracy problems. For a sufficiently large number of sensors, the BSSP algorithm is the most accurate one, but it requires orders of magnitude higher computational cost than FSSP or GA. A new modified M-BSSP heuristic algorithm is also proposed to drastically reduce the computational burden to levels that are orders of magnitude less than the GA algorithm, while maintaining the accuracy of the original BSSP algorithm. GA provides nearly optimal solutions, which for a sufficiently large number of sensors are less accurate than the ones estimated by BSSP or M-BSSP. Results suggest that the combined estimate of heuristic FSSP, M-BSSP, and GA algorithms can be used to optimize a sensor configuration.

The proposed methodology was demonstrated by designing the optimal location of strain and/or acceleration sensors over the surface of a plate structure subjected to a single excitation at a known location. A thorough investigation of the effect of plant/process, measurement and model/prediction errors, and the intensity of the excitation was conducted, considering the uncertainties in these errors on the optimal type and location of sensors and on the variation of the highest and lowest information gain as a function of the number of sensors. It is demonstrated that an increase in measurement and model error has an effect of decreasing the information gain. The effect of the two types of errors is qualitatively different. For small measurement error or large model error, a fixed number of 9 sensors placed at their optimal location provide most of the information that can be achieved by fully populating the structure with 820 sensors. In contrast, for large measurement error or small model error, a fixed number of 9 sensors placed at their optimal locations provides only a fraction of the information that can be achieved by fully populating the plate with 820 sensors and thus there is significant information that can be gained by adding a large number of sensors. It was also found that the optimal sensor configuration fuses a mixed-type of acceleration and strain sensors which can be significantly more informative than sensor configurations involving only acceleration sensors.

The framework also provides optimal sensor configurations that are robust to uncertainties in model parameters as well as in model/prediction and measurement errors. Such uncertainties are not known in the initial optimal experimental design phase and thus are postulated

using prior distributions. The robust designs over wide uncertainty bounds of errors leads to optimal sensor placement designs that are closer to the ones obtained for high measurement and model/prediction errors. Finally, the effectiveness of the optimal designs was validated against sub-optimal ones by comparing errors in the predictions between the AKF method and simulated measurements contaminated by noise or model errors.

The proposed general OSP framework can be used to reliably reconstruct responses and inputs that are important for providing data-driven safety and performance estimates of systems. In particular, it can be used in reconstructing stress response time histories that are important for reliably predicting fatigue damage accumulation estimates.

3.6 References

[1] H. P. Hjelm, R. Brincker, J. Graugaard-Jensen, and K. Munch. Determination of stress histories in structures by natural input modal analysis. In *Proceedings of the 23rd International Modal Analysis Conference,IMAC*, pages 838–844, 2005.

[2] P. Pingle and P. Avitabile. Full-field dynamic stress/strain from limited sets of measured data. *Sound and Vibration*, 2(8):187–200, 2011.

[3] J. Baqersad, K. Bharadwaj, and P. Poozesh. Modal expansion using strain mode shapes. In *Shock & Vibration, Aircraft/Aerospace, Energy Harvesting, Acoustics & Optics,*, volume 9, pages 219–226. Springer New York LLC, 2017.

[4] P. Avitabile, E. Harvey, and J. Ruddock. Comparison of full field strain distributions to predicted strain distributions from limited sets of measured data for SHM applications. *Key Engineering Materials*, 569-570:1140–1147, 2013.

[5] J. Kullaa. Bayesian virtual sensing for full-field dynamic response estimation. In *Procedia Engineering*, volume 199, pages 2126–2131. Elsevier Ltd, 2017.

[6] J. Kullaa. Bayesian virtual sensing in structural dynamics. *Mechanical Systems and Signal Processing*, 115:497–513, 1 2019.

[7] E. Lourens, E. Reynders, G. De Roeck, G. Degrande, and G. Lombaert. An augmented kalman filter for force identification in structural dynamics. *Mechanical systems and signal processing*, 27:446–460, 2012.

[8] E. Lourens, C. Papadimitriou, S. Gillijns, E. Reynders, G. De Roeck, and G. Lombaert. Joint input-response estimation for structural systems based on reduced-order models and vibration data from a limited number of sensors. *Mechanical Systems and Signal Processing*, 29:310–327, 2012.

[9] S. E. Azam, E. Chatzi, and C. Papadimitriou. A dual kalman filter approach for state estimation via output-only acceleration measurements. *Mechanical systems and signal processing*, 60:866–886, 2015.

[10] F. Naets, J. Cuadrado, and W. Desmet. Stable force identification in structural dynamics using kalman filtering and dummy-measurements. *Mechanical Systems and Signal Processing*, 50:235–248, 2015.

[11] K. Erazo and E. M. Hernandez. A model-based observer for state and stress estimation in structural and mechanical systems: Experimental validation. *Mechanical Systems and Signal Processing*, 43(1-2):141–152, 2014.

[12] V. K. Dertimanis, E. N. Chatzi, S. E. Azam, and C. Papadimitriou. Input-state-parameter estimation of structural systems from limited output information. *Mechanical Systems and Signal Processing*, 126:711–746, 2019.

[13] R. Álvarez-Briceño and L. P. R. de Oliveira. Combining strain and acceleration measurements for random force estimation via kalman filtering on a cantilevered structure. *Journal of Sound and Vibration*, 469:115112, 2020.

[14] M. Impraimakis and A. W. Smyth. An unscented kalman filter method for real time input-parameter-state estimation. *Mechanical Systems and Signal Processing*, 162:108026, 2022.

[15] S. P. Tchemodanova, M. Sanayei, B. Moaveni, K. Tatsis, and E. Chatzi. Strain predictions at unmeasured locations of a substructure using sparse response-only vibration measurements. *Journal of Civil Structural Health Monitoring*, 11(4):1113–1136, 2021.

[16] O. Sedehi, C. Papadimitriou, D. Teymouri, and L. S. Katafygiotis. Sequential bayesian estimation of state and input in dynamical systems using output-only measurements. *Mechanical Systems and Signal Processing*, 131:659–688, 2019.

[17] D. Teymouri, O. Sedehi, L. S. Katafygiotis, and C. Papadimitriou. A Bayesian Expectation-Maximization (BEM) methodology for joint input-state estimation and virtual sensing of structures. *Mechanical Systems and Signal Processing*, 169:108602, 2022.

[18] C. Papadimitriou, C. P. Fritzen, P. Kraemer, and E. Ntotsios. Fatigue predictions in entire body of metallic structures from a limited number of vibration sensors using Kalman filtering. *Structural Control and Health Monitoring*, 18(5):554–573, 2011.

[19] C. Papadimitriou, E. M. Lourens, G. Lombaert, G. De Roeck, and K. Liu. Prediction of fatigue damage accumulation in metallic structures by the estimation of strains from operational vibrations. In *Life-Cycle and Sustainability of Civil Infrastructure Systems - Proceedings of the 3rd International Symposium on Life-Cycle Civil Engineering, IALCCE*, pages 304–310, 2012.

[20] K. Maes, A. Iliopoulos, W. Weijtjens, C. Devriendt, and G. Lombaert. Dynamic strain estimation for fatigue assessment of an offshore monopile wind turbine using filtering and modal expansion algorithms. *Mechanical Systems and Signal Processing*, 76:592–611, 2016.

[21] A. Iliopoulos, R. Shirzadeh, W. Weijtjens, P. Guillaume, D. Van Hemelrijck, and C. Devriendt. A modal decomposition and expansion approach for prediction of dynamic responses on a monopile offshore wind turbine using a limited number of vibration sensors. *Mechanical Systems and Signal Processing*, 68:84–104, 2016. ISSN 10961216.

[22] M. S. Nabiyan, H. Ebrahimian, B. Moaveni, and F. Khoshnoudian. Structural identification for dynamic strain estimation in wind turbine towers. In *Proceedings of the 36th International Modal Analysis Conference,IMAC*, pages 239–245. Springer, 2019. doi: 10.1007/978-3-319-74421-6_32.

[23] M. S. Nabiyan, F. Khoshnoudian, B. Moaveni, and H. Ebrahimian. Mechanics-based model updating for identification and virtual sensing of an offshore wind turbine using sparse measurements. *Structural Control and Health Monitoring*, 28(2):e2647, 2021.

[24] M. Henkel, J. Häfele, W. Weijtjens, C. Devriendt, C. G. Gebhardt, and R. Rolfes. Strain estimation for offshore wind turbines with jacket substructures using dual-band modal expansion. *Marine Structures*, 71:102731, 2020.

[25] P. Ren and Z. Zhou. Strain estimation of truss structures based on augmented Kalman filtering and modal expansion. *Advances in Mechanical Engineering*, 9(11):1–10, 2017.

[26] Y. Chen, D. Joffre, and P. Avitabile. Underwater dynamic response at limited points expanded to full-field strain response. *Journal of Vibration and Acoustics, Transactions of the ASME*, 140(5):1–9, 2018.

[27] S. Vettori, E. Di Lorenzo, B. Peeters, and E. Chatzi. Kalman-based coupled response-input estimation during environmental tests on the box assembly with removable component structure. In *Proceedings of the 11th International Conference on Structural Dynamics,EURODYN*, pages 3878–3885. EASD Procedia, 2020.

[28] S. Vettori, E. Di Lorenzo, R. Cumbo, U. Musella, T. Tamarozzi, B. Peeters, and E. Chatzi. Kalman-based virtual sensing for improvement of service response replication in environmental tests. In *Model Validation and Uncertainty Quantification, Volume 3*, pages 93–106. Springer, 2020.

[29] A. Iliopoulos, W. Weijtjens, D. Van Hemelrijck, and C. Devriendt. Fatigue assessment of offshore wind turbines on monopile foundations using multi-band modal expansion. *Wind Energy*, 20(8):1463–1479, 8 2017.

[30] D. Giagopoulos, A. Arailopoulos, V. Dertimanis, C. Papadimitriou, E. Chatzi, and K. Grompanopoulos. Computational framework for online estimation of fatigue damage using vibration measurements from a limited number of sensors. In *Procedia Engineering*, volume 199, pages 1906–1911, 2017.

[31] S. P. Tchemodanova, K. Tatsis, V. Dertimanis, E. Chatzi, and M. Sanayei. Remaining fatigue life prediction of a roller coaster subjected to multiaxial nonproportional loading using limited measured strain locations. In *Structures Congress 2019: Bridges, Nonbuilding and Special Structures, and Nonstructural Components*, pages 112–121, 2019.

[32] M. Tarpø, B. Nabuco, C. Georgakis, and R. Brincker. Expansion of experimental mode shape from operational modal analysis and virtual sensing for fatigue analysis using the modal expansion method. *International Journal of Fatigue*, 130:105280, 2020.

[33] K. Maes and G. Lombaert. Fatigue monitoring of railway bridges by means of virtual sensing. In *Proceedings of the Belgian and Dutch National Groups of IABSE - Young Engineers Colloquium 2019,YEC2019*, pages 24–25, 2019.

[34] D. Giagopoulos, A. Arailopoulos, V. Dertimanis, C. Papadimitriou, E. Chatzi, and K. Grompanopoulos. Structural health monitoring and fatigue damage estimation using vibration measurements and finite element model updating. *Structural Health Monitoring*, 18(4):1189–1206, 2019.

[35] D. C. Papadioti. *Management of uncertainties in structural response and reliability simulations using measured data*. PhD thesis, University of Thessaly, 2015.

[36] D. Giagopoulos, A. Arailopoulos, S. E. Azam, C. Papadimitriou, E. Chatzi, and K. Grompanopoulos. Dynamic response estimation and fatigue prediction in a linear substructure of a complex mechanical assembly. In *Proceedings of 8th European Workshop on Structural Health Monitoring, EWSHM*, volume 2, pages 890–899, 2016.

[37] M. Tarpø, T. Friis, B. Nabuco, S. Amador, E. Katsanos, and R. Brincker. Operational modal analysis based stress estimation in friction systems. In *Conference Proceedings of the Society for Experimental Mechanics Series*, volume 1, pages 143–153. Springer, 2019.

[38] K. E. Tatsis, V. K. Dertimanis, C. Papadimitriou, E. Lourens, and E. N. Chatzi. A general substructure-based framework for input-state estimation using limited output measurements. *Mechanical Systems and Signal Processing*, 150:107223, 2021.

[39] R. J. Barthorpe and K. Worden. Emerging trends in optimal structural health monitoring system design: From sensor placement to system evaluation. *Journal of Sensor and Actuator Networks*, 9(3):31, 2020.

[40] E. M. Hernandez. Efficient sensor placement for state estimation in structural dynamics. *Mechanical Systems and Signal Processing*, 85:789–800, 2017.

[41] Z. Peng, K. Dong, and H. Yin. A modal-based Kalman filter approach and OSP method for structural response reconstruction. *Shock and Vibration*, 2019, 2019.

[42] R. Cumbo, L. Mazzanti, T. Tamarozzi, P. Jiranek, W. Desmet, and F. Naets. Advanced optimal sensor placement for kalman-based multiple-input estimation. *Mechanical Systems and Signal Processing*, 160:107830, 2021.

[43] T. Tamarozzi, E. Risaliti, W. Rottiers, K Janssens, and W Desmet. Noise, ill-conditioning and sensor placement analysis for force estimation through virtual sensing. In *International Conference on Noise and Vibration Engineering (ISMA2016)*, pages 1741 – 1756, Leuven, 2016.

[44] X.H. Zhang, S. Zhu, Y. L. Xu, and X.J. Homg. Integrated optimal placement of displacement transducers and strain gauges for better estimation of structural response. *International journal of structural stability and dynamics*, 11(03):581–602, 2011.

[45] S. Zhu, X. H. Zhang, Y. L. Xu, and S. Zhan. Multi-type sensor placement for multi-scale response reconstruction. *Advances in Structural Engineering*, 16(10):1779–1797, 2013.

[46] M. Khalil, I. Kouroudis, R. Wüchner, and K. U. Bletzinger. Optimal sensor configuration for fatigue life prediction in structural applications. In *Dynamic Systems and Control Conference*, volume 59148, page V001T06A001, 2019.

[47] C. D. Zhang and Y. L. Xu. Optimal multi-type sensor placement for response and excitation reconstruction. *Journal of Sound and Vibration*, 360:112–128, 1 2016.

[48] S. Gillijns and B. De Moor. Unbiased minimum-variance input and state estimation for linear discrete-time systems with direct feedthrough. *Automatica*, 43(5):934–937, 2007.

[49] C. Papadimitriou. Optimal sensor placement methodology for parametric identification of structural systems. *Journal of Sound and Vibration*, 278(4-5):923–947, 2004.

[50] E. Lourens and D. J. M. Fallais. Full-field response monitoring in structural systems driven by a set of identified equivalent forces. *Mechanical Systems and Signal Processing*, 114:106–119, 2019.

[51] E. Risaliti, T. Tamarozzi, M. Vermaut, B. Cornelis, and W. Desmet. Multibody model based estimation of multiple loads and strain field on a vehicle suspension system. *Mechanical Systems and Signal Processing*, 123:1–25, 2019.

[52] K. Maes, E. Lourens, K. Van Nimmen, E. Reynders, G. De Roeck, and G. Lombaert. Design of sensor networks for instantaneous inversion of modally reduced order models in structural dynamics. *Mechanical Systems and Signal Processing*, 52-53(1):628–644, 2015.

[53] C. Papadimitriou, J. L. Beck, and S. K. Au. Entropy-based optimal sensor location for structural model updating. *JVC/Journal of Vibration and Control*, 6(5):781–800, 2000.

[54] K. V. Yuen and S. C. Kuok. Efficient Bayesian sensor placement algorithm for structural identification: a general approach for multi-type sensory systems. *Earthquake Engineering & Structural Dynamics*, 44(5):757–774, 2015.

[55] B. Li and A. Der Kiureghian. Robust optimal sensor placement for operational modal analysis based on maximum expected utility. *Mechanical Systems and Signal Processing*, 75:155–175, 2016.

[56] R. Pasquier, J. A. G., and I. F. Smith. Measurement system design for civil infrastructure using expected utility. *Advanced Engineering Informatics*, 32:40–51, 2017.

[57] C. Papadimitriou and C. Argyris. Bayesian optimal experimental design for parameter estimation and response predictions in complex dynamical systems. In *Procedia Engineering*, volume 199, pages 972–977. Elsevier Ltd, 2017.

[58] C. Argyris. *Bayesian uncertainty quantification and optimal experimental design in data driven simulations of engineering systems*. PhD thesis, University of Thessaly, 2010.

[59] N. J. Bertola, M. Papadopoulou, D. Vernay, and I. F. Smith. Optimal multi-type sensor placement for structural identification by static-load testing. *Sensors*, 17:2904, 2017.

[60] G. Capellari, E. Chatzi, and S. Mariani. Structural health monitoring sensor network optimization through Bayesian experimental design. *ASCE-ASME Journal of Risk and Uncertainty in Engineering Systems, Part A: Civil Engineering*, 4(2):04018016, 2018.

[61] G. Capellari, E. Chatzi, and S. Mariani. Cost–benefit optimization of structural health monitoring sensor networks. *Sensors*, 18(7):1–22, 2018.

[62] H. Ebrahimian, R. Astroza, J. P. Conte, and R. R. Bitmead. Information-theoretic approach for identifiability assessment of nonlinear structural finite-element models. *Journal of Engineering Mechanics*, 145(7):04019039, 2019.

[63] P. Bhattacharyya and J. Beck. Exploiting convexification for Bayesian optimal sensor placement by maximization of mutual information. *Structural Control and Health Monitoring*, 27(10):1–18, 2020.

[64] C. Argyris, C. Papadimitriou, G. Samaey, and G. Lombaert. A unified sampling-based framework for optimal sensor placement considering parameter and prediction inference. *Mechanical Systems and Signal Processing*, 161:107950, 2021.

[65] C. Papadimitriou, Y. Haralampidis, and K. Sobczyk. Optimal experimental design in stochastic structural dynamics. *Probabilistic Engineering Mechanics*, 20(1):67–78, 2005.

[66] T. Ercan and C. Papadimitriou. Optimal Sensor Placement for Reliable Virtual Sensing Using Modal Expansion and Information Theory. *Sensors*, 21(10):3400, 2021. doi: doi.org/10.3390/s21103400.

[67] A. Mehrjoo, M. Song, B. Moaveni, C. Papadimitriou, and E. Hines. Optimal sensor placement for parameter estimation and virtual sensing of strains on an offshore wind turbine considering sensor installation cost. *Mechanical Systems and Signal Processing*, 169:108787, 2022.

[68] C. Papadimitriou. Optimal sensor placement for response reconstruction in structural dynamics. In *Model Validation and Uncertainty Quantification, Volume 3*, pages 205–210. Springer, 2020.

[69] T. Ercan, O. Sedehi, C. Papadimitriou, and L. S. Katafygiotis. Robust optimal sensor placement for response reconstruction using output only vibration measurements. In *Proceedings of the 29th European Safety and Reliability Conference, ESREL*, pages 1270–1276. Research Publishing Services, 2019.

[70] S. Kullback and R. A. Leibler. On information and sufficiency. *The Annals of Mathematical Statistics*, 22(1):79–86, 1951.

[71] D. V. Lindley. On a measure of the information provided by an experiment. *The Annals of Mathematical Statistics*, 27(4):986–1005, 1956.

[72] K. J. Ryan. Estimating Expected Information Gains for Experimental Designs with Application to the Random Fatigue-Limit Model. *Journal of Computational and Graphical Statistics*, 12(3):585–603, 2003.

[73] R. Cumbo, T. Tamarozzi, K. Janssens, and W. Desmet. Kalman-based load identification and full-field estimation analysis on industrial test case. *Mechanical Systems and Signal Processing*, 117:771–785, 2019. doi: 10.1016/j.ymssp.2018.08.045.

[74] T. Gerstner and M. Griebel. Numerical integration using sparse grids. *Numerical Algorithms*, 18(3):209–232, 1998.

[75] F. Heiss and V. Winschel. Likelihood approximation by numerical integration on sparse grids. *Journal of Econometrics*, 144(1):62–80, 2008.

[76] C. Papadimitriou and G. Lombaert. The effect of prediction error correlation on optimal sensor placement in structural dynamics. *Mechanical Systems and Signal Processing*, 28:105–127, 4 2012.

[77] D. I. Papadimitriou and C. Papadimitriou. Optimal Sensor Placement for the Estimation of Turbulence Model Parameters in CFD. *International Journal for Uncertainty Quantification*, 5(6):545–568, 2015.

Chapter 4. Bayesian Optimal Experimental Design for Parameter Estimation under Structural Modeling and Input Uncertainty

ABSTRACT

A Bayesian optimal experimental design (OED) framework for model parameter estimation in nonlinear structural dynamics models is proposed, based on maximizing a utility function built from appropriate measures of information contained in the input-output response time history data. The information gain is quantified using Kullback-Leibler divergence (KL-div) between the prior and posterior distribution of the model parameters. The design variables may include the location of sensors, as well as the actuator location and/or the characteristics of the excitation (amplitude variation and frequency content). Asymptotic approximations, valid for large number of data, provide valuable insight into the measure of information. Robustness to uncertainties in nuisance (non-updatable) parameters associated with modeling and excitation uncertainties is considered by maximizing the expected information gain over all possible values of the nuisance parameters. In particular, the framework handles the case where the excitation time history is measured by installed sensors but remains unknown at the experimental design phase. Introducing stochastic excitation models, the expected information gain is taken over the large number of uncertain parameters used to model the random variability in the input time histories. Monte Carlo or sparse grid methods estimate the multidimensional probability integrals arising in the formulation. Heuristic algorithms are used to solve the optimization problem. The effectiveness of the method is demonstrated for a multi-degree of freedom (DOF) spring-mass chain system with restoring elements that may exhibit hysteretic nonlinearities.

4.1 Introduction

Experimental data are used to inform a digital twin of a system operating under various conditions, selecting models of system components, estimating model parameters, improving virtual sensing capabilities and model-based predictions of important output quantities of interest (QoI). Combining data with models of systems are crucial in making decisions regarding per-

formance, structural health, safety and maintenance. Optimally designed experiments and sensor systems provide substantial benefits to update models and model-based predictions and to support decisions in many fields of science, health and engineering, as well as to reduce cost of experimentation, instrumentation, or monitoring. By designing an optimal experimental set-up, it is possible to cost-effectively improve structural models, narrow the uncertainties in the model parameters and the model-based predictions of output QoI. A recent review of optimal sensor placement (OSP) strategies is covered in [1].

Information theoretic-based approaches provide useful measures of the information contained in the data collected by a sensor configuration for estimating the model parameters. Past OSP approaches for parameter estimation have used measures of information such as Fisher Information Matrix (FIM) [2–7], information entropy [8–20], joint entropy [21, 22], KL-div [23–26], mutual information [27, 28] and value of information [29–31]. The aforementioned OSP techniques address parameter estimation of linear models of structures subjected to known inputs [10–13, 19, 27]. Such studies cover applications to model updating [8, 17], modal identification [15, 28, 32], model selection [14], structural health monitoring and damage detection [16, 18, 25, 33]. OSP for parameter estimation under unknown input can be found in [9] using spectral estimators. Information theoretic measures have also been introduced to measure the information gain for the purpose of response reconstruction for the case of known input [34, 35] as well as the case of output-only vibration measurements [36, 37] for linear models of structures. The response reconstruction under unknown input is carried out using Bayesian modal expansion techniques [36–39] and/or filtering techniques [40, 41].

These studies have mostly concentrated on linear models of structural dynamics. Limited studies are available for OSP for parameter estimation of nonlinear models based on information theoretic approaches. Information entropy and mutual information are used to design the optimal locations of sensors in for parameter estimation of nonlinear suspension models of vehicles [42], nonlinear elastic models [43] and nonlinear hysteretic laws in finite element models of civil infrastructure [20]. For nonlinear models, an issue that is also related to OED is the optimal design of actuator configuration (location and number of actuators) and the optimal design of input characteristics (frequency and amplitude content) so that the model nonlinearities are sufficiently activated, and thus the parameters related to model nonlinearities can be inferred from the measured data. The information entropy based approach introduced in [8] was used for the design of optimal input characteristics for linear and nonlinear suspension

models of vehicles in [42].

In this work, the problem of optimizing the sensor configuration (type, number and location of sensors) and excitation characteristics (amplitude and frequency content) is investigated for reliable parameter estimation of nonlinear models under modeling and input uncertainties. It is assumed that the excitation time histories and the response time histories at the sensor locations are measured. Investigating the actuating forces known to enhance the information provided from sensors is important especially for nonlinear models. By optimizing the actuating characteristics (e.g. exciting at resonance frequency or with large amplitudes), nonlinear features can be activated and the quality of experimental data can be improved. The OED problem is addressed using information theoretic-based approaches. Such approached include sampling [23] and asymptotic techniques [8]. In particular, asymptotic approximations, valid for large number of data, were demonstrated to provide useful insight into the measure of the information [8, 10, 44, 45] from a sensor configuration and it is the preferred techniques used in the present study. Past studies on OSP for parameter estimation using input-output vibration measurements assume that the input is available at the experimental design phase (e.g. [8, 10, 20, 42, 43]). This is the case of laboratory experiments where one can control the input or the case of full-scale experiments performed on civil infrastructure using actuators where the input can also be controlled. However, there are a number of cases and physical phenomena, such as earthquakes, where the excitation is measured using sensors but is completely unknown during the experimental design phase. As a result, the OED should take into account the input uncertainty.

This study is mainly focused on nonlinear models of systems. The purpose is twofold. First, the modeling and input uncertainties are taken into account in the design of the OSP. Modeling uncertainties are associated with non-updatable (nuisance) parameters that their values are uncertain. Such uncertainties can be quantified by assigning a prior probability distribution function (PDF) and included in the formulation for OSP by generalizing the definition of the information gain so that such uncertainties are taken into account in the design. This work also addresses for the first time the uncertainty of the input response time history in the OSP design. Input uncertainties are associated with the fact that the sensor system installed in a structure is designed to measure the time history of the excitation(s) when it occurs, but such measurements are not available at the experimental design phase. An application is on earthquake excited civil infrastructure (e.g. building, bridges) where sensors (mainly acceleration

sensors) are installed to measure the excitation(s) at the base(s) of the structure. However, such excitation is unavailable during the experimental design phase. OSP design should take into account such uncertainties. Stochastic processed/fields can be used to model the variability in ground motion. For example, such variability can be described by simplified ground motion models (e.g. [46, 47]) and seismological models [48] used in the past to represent the ground motion by a large number of random parameters [49, 50]. The input can then be obtained as a specific realization of the underlining stochastic process, and the OSP should account for all such input realizations. The high computational cost associated with the proposed framework is pointed out, and computational issues for carrying out the OSP under model and input uncertainties are also addressed. The second purpose of the work is to point out the differences between the design of optimal sensor configuration and the design of optimal actuator and excitation characteristics.

The presentation is organised as follows. Section 4.2 introduces briefly the Bayesian inference formulation for parameter estimation. The formulation is used in Section 4.3 to introduce the utility function built from the information gain quantified by the KL-div between the prior and posterior distribution of the model parameters to be inferred. The information gain is generalized to account for uncertainties in nuisance (non-inferred) parameters associated with model and input uncertainties. In addition, the problem of optimally designing the actuator configuration and excitation characteristics is formulated. The application of the proposed methodology in a spring-mass chain model of Bouc-Wen nonlinear hysteretic restoring force introduced to represent a high-rise building excited by stochastic earthquake excitation models is presented in Section 4.4. Numerical results demonstrating the applicability and effectiveness of the methodology are presented in Section 4.5. Concluding remarks are drawn in Section 4.6.

4.2 Bayesian Inference for Parameter Estimation

Consider a parameterized structural model and let $\underline{\theta} \in R^{n_\theta}$ be the model parameters to be estimated using a set of data $D = \{\underline{y}_\delta(k) \in R^{n_y},\ \underline{u}_\delta(k) \in R^{n_u},\ \ k = 1, \ldots, n_d\}$, where $\underline{y}_\delta(k)$ is the data of n_y output quantities (acceleration, velocity, displacement or strain) provided by a sensor network, $\underline{u}_\delta(k)$ is the input data of n_u input forces assumed to be measured by the sensor network, k denotes the time index at time t ($t = k\Delta t$) for n_d sampled data and Δt is the sampling period. The data $\underline{y}_\delta(k)$ depends on the sensor configuration $\underline{\delta}$ related

to the number, location and measurement direction of sensors placed on the structure. Let $\underline{g}(k;\underline{\theta},\underline{\varphi}) \in R^n$ be the time histories of n response QoI predicted for the specific values of the parameter set $\underline{\theta}$ by the structural model at all possible locations or DOF given the input time histories. These predictions depend also on a parameter set $\underline{\varphi}$ that may include the excitation characteristics (e.g. amplitude and frequency content, random variables such as white noise variables defining the uncertain temporal and spatial variability of the excitation, number and location of actuators), and nuisance parameters associated with non-updatable parameters of the structural and/or prediction error model.

To account for modeling errors in the predictions, quantified by additive zero-mean Gaussian noise terms, the prediction from the model at the locations defined by the sensor configuration $\underline{\delta}$ are expressed as:

$$\underline{\tilde{g}}_{\underline{\delta}}(k;\underline{\theta},\underline{\varphi}) = L(\underline{\delta})\ \underline{g}(k;\underline{\theta},\underline{\varphi}) + L(\underline{\delta})\ \underline{e}(k;\Sigma_e) \tag{4.1}$$

where $L(\underline{\delta}) \in R^{n_y \times n}$ is the selection matrix that selects the DOF from the response vector $\underline{g}(k;\underline{\theta},\underline{\varphi})$ that correspond to sensor configuration $\underline{\delta}$, $\underline{e} \sim N(0,\Sigma_e)$ is a zero-mean Gaussian measurement and model error term with a covariance equal to $\Sigma_e \in R^{n\times n}$. Models for the prediction error covariance Σ_e are introduced by following the approach used in [13, 37, 45]. The covariance matrix Σ_e is taken as

$$\Sigma_e(\underline{\vartheta},\underline{\varphi}) = s^2 I + \sigma_e^2 \tilde{Q}_g^{1/2}(\underline{\vartheta},\underline{\varphi}) \tag{4.2}$$

where I is the identity matrix and the notation $\tilde{Q}$ denotes a diagonal matrix that contains in the i-th diagonal entry the square of the intensity of the i-th element of $\underline{g}(k;\underline{\theta},\underline{\varphi})$. The first term in Eq. 4.2 accounts for the measurement error with error values to be independent of the response intensity, with the level s of the error to depend on the sensor accuracy and characteristics. The second term in Eq. 4.2 accounts for the model error. A reasonable choice of the model error variance at the i-th DOF is to have it proportional to the square of the intensity of the QoI at DOF i, given by $\underline{g}_i^2(k;\underline{\theta},\underline{\varphi})$, where σ_e denotes the level of model error in relation to the intensity of the QoI. Spatial correlation between prediction errors is neglected in the aforementioned formulation. Details about the correlation structure and its significance in structural dynamics can be found in [13].

Applying the Bayesian theorem, the posterior probability density function (PDF) of the parameter set $\underline{\theta}$, given the measured data D, takes the form

$$p(\underline{\theta}|D,\underline{\delta},\underline{\varphi}) = \tilde{c}\frac{1}{(\sqrt{2\pi})^{n_d}\sqrt{\det[L(\underline{\delta})\Sigma_e L^T(\underline{\delta})]}} \times \exp[-\frac{n_d n_y}{2} J(\underline{\theta}|D,\underline{\delta},\underline{\varphi})]\pi(\underline{\theta}) \tag{4.3}$$

where

$$\begin{aligned} J(\underline{\theta}|D,\underline{\delta},\underline{\varphi}) = \frac{1}{n_d n_y}\sum_{k=1}^{n_d}[\underline{y}_\delta(k) - L(\underline{\delta})\ \underline{g}(k;\underline{\theta},\underline{\varphi})]^T[L(\underline{\delta})\ \Sigma_e(\underline{\theta};\underline{\varphi})\ L^T(\underline{\delta})]^{-1} \\ [\underline{y}_\delta(k) - L(\underline{\delta})\ \underline{g}(k;\underline{\theta},\underline{\varphi})] \end{aligned} \tag{4.4}$$

expresses the deviation between the measured and model predicted quantities. $\pi(\underline{\theta})$ is the prior distribution for $\underline{\theta}$ and $\tilde{c}$ is a normalization constant guaranteeing that the posterior PDF $p(\underline{\theta}|D,\underline{\delta})$ integrates to one. Eq. 4.3 quantifies the posterior uncertainty in the parameter values $\underline{\theta}$ based on the information contained in the measured data.

4.3 Bayesian Optimal Experimental Design Methodology for Parameter Estimation

4.3.1 Information Content from Sensor Network for Parameter Estimation

The information content in the data is quantified through a utility function selected as the information gained by the experiment. The utility function is related to the relative entropy or the KL-div [51] between the prior and posterior PDF of the model parameters obtained from an experimental design $\underline{\delta}$. Using utility theory [52], the OED is accomplished by maximizing the expected information gain over all possible data generated from the prediction error model. It can be shown that asymptotically for large number of data and small prediction errors, the utility function that measures the expected information gain from the data for given $\underline{\varphi}$, can be simplified as follows [20, 27, 28, 37]:

$$U(\underline{\delta},\underline{\varphi}) = H_\theta(\underline{\varphi}) - \int_\theta H_{\theta|D}(\underline{\delta};\underline{\theta},\underline{\varphi})\ \pi(\underline{\theta})d\underline{\theta} \tag{4.5}$$

where, using Eq. 4.3, $H_\theta(\underline{\varphi})$ is the information entropy of the prior PDF of the model parameters, $H_{\theta|D}(\underline{\delta};\underline{\theta},\underline{\varphi})$ is the average information entropy of the posterior PDF of the model parameters over all data, asymptotically approximated for large number of data by the expres-

sion [10, 45]

$$H_{\theta|D}(\underline{\delta};\underline{\theta},\underline{\varphi}) = \frac{1}{2}n_\theta[\ln(2\pi)+1] - \frac{1}{2}\ln\det[Q(\underline{\delta};\underline{\theta},\underline{\varphi}) + Q_\pi(\underline{\varphi})] \tag{4.6}$$

where $Q(\underline{\delta};\underline{\theta},\underline{\varphi}) \in R^{n_\theta \times n_\theta}$ is the Fisher information matrix, a semi-positive definite matrix given by:

$$Q(\underline{\delta};\underline{\theta},\underline{\varphi}) = \sum_{k=1}^{n_d} \nabla_{\underline{\theta}}[L(\underline{\delta})\ \underline{g}(k;\underline{\theta},\underline{\varphi})]^T\ [L(\underline{\delta})\ \Sigma_e(\underline{\theta};\underline{\varphi})\ L^T(\underline{\delta})]^{-1}\ \nabla_{\underline{\theta}}^T\ [L(\underline{\delta})\ \underline{g}(k;\underline{\theta},\underline{\varphi})] \tag{4.7}$$

$\nabla_{\underline{\theta}} = [\partial/\partial\theta_1, \cdots, \partial/\partial\theta_{n_\theta}]$ is the gradient operator and $\underline{g}(k;\underline{\theta},\underline{\varphi})$ is the vector of response time histories at all possible sensor locations.

For truncated Gaussian prior distribution $\pi(\underline{\theta}) = N_T(\underline{\theta};\underline{\mu},\Sigma_\pi,\underline{a},\underline{b})$, where $\underline{a}$ and $\underline{b}$ are vectors defining the lower and upper truncation bounds of the distribution, the information entropy of the prior distribution of the model parameters is given by

$$H_{\underline{\theta}}(\underline{\varphi}) = \frac{1}{2}n_\theta[\ln(2\pi)+1] - \frac{1}{2}\ln\det[Q_\pi(\underline{\varphi})] + h_T(\underline{\mu},\Sigma_\pi,\underline{a},\underline{b}) \tag{4.8}$$

where $Q_\pi(\underline{\varphi})$ is the inverse of the covariance matrix Σ_π of the prior. For a Gaussian distribution $\pi(\underline{\theta}) = N(\underline{\theta};\underline{\mu},\Sigma_\pi)$, the last term $h_T(\underline{\mu},\Sigma_\pi,\underline{a},\underline{b}) = 0$. For independent components in $\underline{\theta}$, each one following a truncated Gaussian normal distribution, denoted as $N_T(\theta_i;\mu_i,\sigma_i,a_i,b_i) =$ for the parameter θ_i, the function $h_T(\underline{\mu},\Sigma_\pi,\underline{a},\underline{b})$ takes the form

$$h_T(\underline{\mu},\Sigma_\pi,\underline{a},\underline{b}) = \sum_{i=1}^{N_\theta}\left[\ln\left(\Phi(\beta_i)-\Phi(\alpha_i)\right) - \frac{1}{2}\frac{\beta_i\phi(\beta_i)-\alpha_i\phi(\alpha_i)}{\Phi(\beta_i)-\Phi(\alpha_i)}\right] \tag{4.9}$$

where ϕ and Φ is the probability and the cumulative distribution function of a standard normal variable, respectively, $\beta_i = (b_i-\mu_i)/\sigma_i$ and $\alpha_i = (a_i-\mu_i)/\sigma_i$, a_i and b_i are the lower and upper bounds of the truncated normal distribution for the parameter θ_i, μ_i is the mean and σ_i is the standard deviation.

The expected utility function finally takes the form

$$U(\underline{\delta},\underline{\varphi}) = \Delta\bar{H}(\underline{\delta},\underline{\varphi}) = E_{\underline{\theta}}[\Delta H(\underline{\delta},\underline{\varphi},\underline{\theta})] = \int_\Theta \Delta H(\underline{\delta},\underline{\varphi},\underline{\theta})\ \pi(\underline{\theta})\ d\underline{\theta} \tag{4.10}$$

where $\Delta H(\underline{\delta},\underline{\varphi},\underline{\theta}) = H_{\underline{\theta}}(\underline{\varphi}) - H_{\theta|D}(\underline{\delta};\underline{\theta},\underline{\varphi})$ is the change of the information entropy between

the prior and the posterior distribution estimated at a parameter value $\underline{\theta}$ within the support of the prior distribution, given by

$$\Delta H(\underline{\delta}, \underline{\varphi}, \underline{\theta}) = \frac{1}{2} \ln \frac{\det[Q(\underline{\delta}; \underline{\theta}, \underline{\varphi}) + Q_{\pi}(\underline{\varphi})]}{\det Q_{\pi}(\underline{\varphi})} + h_T(\underline{\mu}, \Sigma_{\pi}, \underline{a}, \underline{b}) \tag{4.11}$$

The utility function is based on the Fisher information matrix and it is an average of the information gain over all possible values of the model parameters over the support of the prior distribution, weighted by the values of the prior distribution. An estimate of the integral in Eq. 4.10 can be obtained using either Monte Carlo or Sparse Grids methods [53, 54] as follows:

$$U(\underline{\delta}, \underline{\varphi}) = -E_{\underline{\theta}}[\Delta H(\underline{\delta}, \underline{\varphi}, \underline{\theta})] \approx -\sum_{j=1}^{N} w_j \Delta H(\underline{\delta}, \underline{\varphi}, \underline{\theta}^{(j)}) \tag{4.12}$$

where $\underline{\theta}^{(j)}$, $j = 1, \ldots, N$ are sparse grid points or samples from the prior distribution $\pi(\underline{\theta})$ and w_j are the sparse grid or Monte Carlo weights.

4.3.2 Optimal Sensor Placement Conditional on φ

The optimal values $\underline{\delta}_{opt}$ of the design variables are obtained by maximizing the utility $U(\underline{\delta}, \underline{\varphi})$ or, equivalently, minimizing the expected change in information entropy $\Delta\bar{H}(\underline{\delta}.\underline{\varphi})$ taken with respect to $\underline{\theta}$ values over the support of the prior distribution, that is,

$$\underline{\delta}_{opt}(\underline{\varphi}) = \underset{\underline{\delta}}{\text{argmax}}\, U(\underline{\delta}, \underline{\varphi}) = \underset{\underline{\delta}}{\text{argmin}}\, \Delta\bar{H}(\underline{\delta}, \underline{\varphi}) \tag{4.13}$$

The optimization problem involves discrete design variables $\underline{\delta}$ (e.g. DOF at nodes for placing displacement/acceleration sensors or Gauss integration points for placing strains sensors in a finite element mesh). Heuristic algorithms (e.g. [27]), including forward and backward sequential sensor placement (FSSP/BSSP) algorithms [10, 13], or genetic algorithms [1, 55, 56] can be employed to solve the optimization problem. The heuristic FSSP/BSSP algorithms bypass the problem of multiple local/global optima manifested in OEDs, providing near optima solutions in a fraction of the computational effort required in stochastic optimization algorithms or exhaustive search methods [8]. The heuristic FFSP algorithms is used in this study.

4.3.3 Optimal Sensor Placement Considering Modeling and Input Uncertainties

The utility function in Eq. 4.10 depends on the values of the parameter set $\underline{\varphi}$. The values of $\underline{\varphi}$ are usually uncertain and this has to be accounted in the design of the optimal sensor configuration. The source of uncertainties vary from excitation uncertainties to structural model and prediction error model uncertainties. The excitation uncertainties are associated with the uncertain characteristics of environmental loads. Such loads are usually modelled by stochastic processes that correspond to a parameterized spectrum. For example, earthquake loads are often represented by the Kanai-Tajimi spectrum [46, 47] which belongs to a class of filtered white noise processes where the filter is represented by a second-order differential equation excited by white noise. More involved models [48–50] connected with the physics-based parameters such as earthquake source, source to site propagation properties, directional effects and local soil conditions also exist to characterize the earthquake excitation uncertainties at a site by a stochastic process corresponding to a parameterized spectrum. The uncertain parameters $\underline{\varphi}$ are associated with the Gaussian white noise sequence used to generate realization of the stochastic load [49, 50] and also with the Gaussian, lognormal or other distributions used to quantify the uncertainties in the parameters defining the spectrum. The OSP should be designed to cover all possible realizations of the stochastic process generated by all realizations of the load spectrum parameters.

The parameter vector $\underline{\varphi}$ is composed of two independent parameter sets, $\underline{\varphi} = (\underline{\varphi}_{wn}, \underline{\varphi}_{nu})$, where the set $\underline{\varphi}_{wn}$ is associated with the Gaussian white noise sequence used for representing the stochastic nature of the excitation and the set $\underline{\varphi}_{nu}$ contains the parameter of the load spectrum, as well as the nuisance (non-updatable) parameters of the structural and prediction error models, such as the parameter set $\underline{\sigma} = (s, \sigma_e)$ in Eq. 4.2. Using the fact that the parameter vector $\underline{\varphi}$ is an uncertain vector modelled by a prior probability distribution $\pi(\underline{\varphi}) = \pi(\underline{\varphi}_{wn})\ \pi(\underline{\varphi}_{nu})$, the information contained in the sensor measurements is defined to be the expected information gain, quantified by the expected utility function

$$U(\underline{\delta}) = \int_{\Phi} U(\underline{\delta}, \underline{\varphi})\ \pi(\underline{\varphi})\ d\underline{\varphi} = -\int_{\Phi}\int_{\Theta} \Delta H(\underline{\delta}, \underline{\varphi}, \underline{\theta})\ \pi(\underline{\varphi})\pi(\underline{\theta})\ d\underline{\varphi}\ d\underline{\theta} \equiv -\Delta\bar{H}(\underline{\delta}) \tag{4.14}$$

over all possible values of the parameter set $\underline{\varphi}$. The optimal sensor configuration $\underline{\delta}_{opt}$ is selected

to optimize the expected utility function, i.e.

$$\underline{\delta}_{opt} = \underset{\underline{\delta}}{\text{argmax}}\, U(\underline{\delta}) = \underset{\underline{\delta}}{\text{argmin}}\, \Delta\bar{H}(\underline{\delta}) \tag{4.15}$$

over all possible sensor configurations $\underline{\delta}$, where $\Delta\bar{H}(\underline{\delta})$ is the expected change in the information entropy between the prior and posterior distribution.

An estimate of the multidimensional integral in Eq. 4.14 can be obtained using Monte Carlo sampling for the white noise sequence parameters, while the parameters of the spectrum can be treated exactly the same as the model parameters $\underline{\theta}$ so that sparse grid or Monte Carlo estimates can be used to estimate the integral in the form

$$U(\underline{\delta}) = \frac{1}{M}\sum_{i=1}^{M} U(\underline{\delta}, \underline{\varphi}_{wn}^{(i)}) \tag{4.16}$$

where

$$U(\underline{\delta}, \underline{\varphi}_{wn}) = -E_{\underline{\theta},\underline{\varphi}_{nu}}[\Delta H(\underline{\delta}, \{\underline{\varphi}_{wn}, \underline{\varphi}_{nu}\}, \underline{\theta})] \approx -\sum_{j=1}^{N} w_j \Delta H(\underline{\delta}, \{\underline{\varphi}_{wn}, \underline{\varphi}_{nu}^{(j)}\}, \underline{\theta}^{(j)}) \tag{4.17}$$

For each white noise sequence, Eq. 4.17 averages over all possible values of the model parameters in the support of the prior distributions of the updatable and non-updatable parameters. Eq. 4.16 averages the utility function over different realizations of the white noise sequence and represents robustness in the time history details of the stochastic excitation.

4.3.4 Optimal Sensor, Actuator and Excitation Characteristics

The problem of selecting the number and location of sensors and actuators, as well as the excitation characteristics is next considered. For this, the parameter set $\underline{\varphi}$ is augmented to include the design variables $\underline{d}$ associated with the location of actuators and the excitation characteristics, along with the rest of the uncertain parameters $\{\underline{\varphi}_{wn}, \underline{\varphi}_{u}\}$ that include the white noise sequence parameters for the case of stochastic excitations and the nuisance parameters.

Thus, the parameter set $\underline{\varphi}$ is partitioned to the set $\underline{d}$ of design variables to be selected so that the information in the data is the highest, and the set $\{\underline{\varphi}_{wn}, \underline{\varphi}_{un}\}$ of uncertain parameters. The expected utility function quantifying the expected information gain over all possible values of

the uncertain parameter set $\{\underline{\varphi}_{wn}, \underline{\varphi}_{un}\}$ takes the form

$$
\begin{aligned}
U(\underline{\delta}, \underline{d}) &= -E_{\underline{\theta}, \underline{\varphi}_{un}, \underline{\varphi}_{un}}[\Delta H(\underline{\delta}, \{\underline{d}, \underline{\varphi}_{wn}, \underline{\varphi}_{un}\}, \underline{\theta})] \\
&\approx -\frac{1}{M} \sum_{i=1}^{M} \sum_{j=1}^{N} w_j \Delta H(\underline{\delta}, \{\underline{d}, \underline{\varphi}_{wn}^{(i)}, \underline{\varphi}_{un}^{(j)}\}, \underline{\theta}^{(j)})
\end{aligned}
\tag{4.18}
$$

It should be noted that the utility is a function of the sensor configuration $\underline{\delta}$, the actuator locations and the excitation characteristics included in the set $\underline{d}$. The optimal values $\underline{\delta}_{opt}$ and $\underline{d}_{opt}$ are selected to maximize the expected information gain, i.e.

$$
\{\underline{\delta}_{opt}, \underline{d}_{opt}\} = \underset{\{\underline{\delta}, \underline{d}\}}{\operatorname{argmax}}\, U(\underline{\delta}, \underline{d}) \tag{4.19}
$$

with respect to the sensor configuration $\underline{\delta}$, the actuator locations and the excitation characteristics $\underline{d}$.

There are qualitative structural differences between the design of optimal sensor configuration and the design of optimal actuator and excitation characteristics. The expected utility function is a scalar measure of the sensitivity of the responses at the measured locations with respect to the parameters to be inferred. A sensor configuration affects which response sensitivities are involved in the information gain measure. An actuator configuration and the excitation characteristics affects the value of the information gain but does not alter the structure of the information gain built from the response sensitivities corresponding to a sensor configuration.

4.3.5 Computational Cost and Storage Requirements

The computationally most efficient algorithm to perform the OSP is to avoid re-computing the sensitivities of the time history responses in Eq. 4.7 with respect to the parameters $\underline{\theta}$ for sensors configuration that contain common locations. These sensitivities have to be computed once and then stored for all possible sensor locations. This computation has to be repeated for each sample $\underline{\theta}^{(j)}$ and $\underline{\varphi}^{(j)}$ of the updatable and non-updatable (nuisance) model parameter drawn from the prior distribution and for each realization ${\varphi_{wn}}^{(i)}$ of the stochastic input. These sensitivity computations can substantially increase the computational burden of the methodology as well as the storage requirements, especially when the number n of possible sensor

locations, number N of samples drawn from the prior distribution and the number M of input realizations are large. The computational burden depends on the number of runs required to compute the response sensitivities. For the case that the response sensitivities can be obtained analytically by direct differentiation methods, the number of simulation runs for solving the equations for the sensitivities of the response to each parameter are as many as the number of model parameters n_θ. For n number of possible sensor locations, N number of samples in Eq. 4.17, M input realizations in Eq. 4.16, n_θ number of updatable model parameters, and n_d points in a time history, the total number of simulation is thus $n_\theta NM$, while the storage requirements are of the order of $8n_\theta n n_d NM10^{-9}$ GB. Once the response sensitivities have been stored, the optimization of the utility function is performed with the utility built from the stored response sensitivities.

To get an idea of the computational cost and the storage requirements, for the small case of $n_\theta = 10$, $n = 100$, $N = 100$, $M = 100$ and $n_d = 100$ and $n_d = 100$ the system simulation runs is of the order of 10^5 and the storage requirement is 8GB, while for a moderate case of $n_\theta = 10$, $n = 1000$, $N = 1000$, $M = 1000$ and $n_d = 1000$ the simulation runs is of the order of 10^7 and the storage requirements is 8×10^4 GB. It is obvious that the computational cost and especially the storage requirements can become excessive even for moderate cases encountered in structural dynamics. Parallel computing can help to scale the computational effort by the number of available cores available.

4.4 Application in Nonlinear Spring-Mass Chain Model

Without loss of generality, the application in this work is confined to MDOF nonlinear spring-mass chain models shown in Fig. 4.1. The restoring force is considered to be hysteretic, modelled by Bouc-Wen model [57, 58]. The equations of motion are briefly summarized in Section 4.4.1 and extended in Section 4.4.2 for ground excitations modelled by filtered white noise input. Direct differentiation techniques are used to develop the equations for the response sensitivities with respect to the model parameters for the Bouc-Wen restoring force nonlinearity, required in the OSP formulation (see Eq. 4.7).

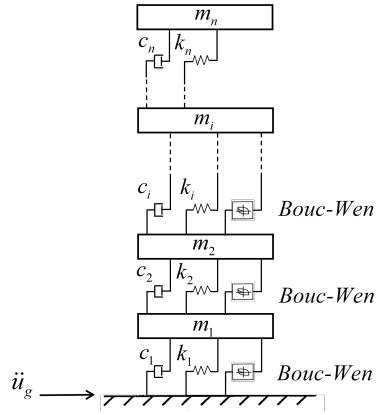

Fig. 4.1. Multi DOF nonlinear spring-mass chain model.

4.4.1 Formulation of Dynamic Equations of Motion

Let $q_i(\underline{u}, \underline{\dot{u}}, t)$ be the restoring force for the nonlinear link i, where u_i and $\dot{u}_i$ are the relative displacement and velocity time histories of floor i with respect to the base. The restoring force is given by

$$\underline{q}(\underline{u}, \underline{\dot{u}}, \underline{z}) = \underline{c} \circ (\tilde{L}\underline{\dot{u}}(t)) + diag(\underline{\alpha} \circ \underline{k})(\tilde{L}\underline{u}(t)) + diag((\underline{1} - \underline{\alpha}) \circ \underline{k})\underline{z}(t) \tag{4.20}$$

where $\underline{c}$ is a vector related to damping values and $\underline{k}$ is a vector containing the stiffness parameters of each floor. $\underline{\alpha}$ is a vector of the rigidity ratios (i.e. the ratio of final tangent stiffness k_N to initial stiffness k_i, with $(0 < \alpha < 1)$ and $\underline{\alpha} = \underline{1}$ corresponds to linear system) and z_i is the hysteresis displacement of each floor. Here the notation $\underline{a} \circ \underline{b}$ denotes the element-wise product of the vectors $\underline{a}$ and $\underline{b}$, and $\tilde{L} \in R^{N \times N}$ is a lower triangular transformation matrix given by

$$\tilde{L} = \begin{bmatrix} 1 & & & & \\ -1 & 1 & & & \\ 0 & \ddots & \ddots & & \\ \vdots & \ddots & -1 & 1 & \\ 0 & \cdots & 0 & -1 & 1 \end{bmatrix} \tag{4.21}$$

The non linearity is represented by Bouc-Wen hysteretic model given by

$$\dot{\underline{z}} = \underline{A} \circ (L\underline{\dot{u}}) - \underline{\beta} \circ |L\underline{\dot{u}}| \circ \underline{z} \circ |\underline{z}|^{\circ(\underline{n}-\underline{1})} - \underline{\gamma} \circ (L\underline{\dot{u}}) \circ |\underline{z}|^{\circ \underline{n}} \tag{4.22}$$

where parameter $\underline{A}$ and $\underline{n}$ controls the hysteresis amplitude and the smoothness of the hysteretic curve respectively. Along with $\underline{n}$, the hysteretic parameters $\underline{\beta}$, $\underline{\gamma}$ determine the basic shape of the hysteretic loop. Their sum or difference will define a hardening or softening relationship. Pinching effect, stiffness and strength degradation are neglected in this hysteresis formulation. Using the vector of restoring force $q(\underline{u}, \dot{\underline{u}}, t) \in R^n$, the equations of motion for the nonlinear system can be written as follows:

$$M\ddot{\underline{u}}(t) + \tilde{L}^T \underline{q}(\underline{u}, \dot{\underline{u}}, t) = L_f F(t) \tag{4.23}$$

and using Eq. 4.20, Eq. 4.23 it can be rearranged as:

$$M\ddot{\underline{u}}(t) + C\dot{\underline{u}}(t) + \tilde{L}^T diag(\underline{\alpha} \circ \underline{k})\tilde{L}\underline{u}(t) + \tilde{L}^T diag((\underline{1} - \underline{\alpha}) \circ \underline{k})\underline{z}(t) = L_f F(t) \tag{4.24}$$

The system of equations of motion Eq. 4.24 can be solved by introducing the state space vector

$$\begin{Bmatrix} \underline{y}_1(t) \\ \underline{y}_2(t) \\ \underline{y}_3(t) \end{Bmatrix} = \begin{Bmatrix} \underline{u}(t) \\ \dot{\underline{u}}(t) \\ \underline{z}(t) \end{Bmatrix} \tag{4.25}$$

and deriving the state space form:

$$\begin{Bmatrix} \dot{\underline{y}}_1(t) \\ \dot{\underline{y}}_2(t) \\ \dot{\underline{y}}_3(t) \end{Bmatrix} = \begin{Bmatrix} \underline{y}_2(t) \\ -M^{-1}(C\underline{y}_2(t) + L^T diag(\underline{\alpha} \circ \underline{k})L\underline{y}_1(t) + L^T diag((\underline{1} - \underline{\alpha}) \circ \underline{k})\underline{y}_3(t)) \\ \underline{A} \circ (L\underline{y}_2(t)) - \underline{\beta} \circ |L\underline{y}_2(t)| \circ \underline{y}_3(t) \circ |\underline{y}_3(t)|^{\underline{n}-\underline{1}} - \underline{\gamma} \circ [L\underline{y}_2(t)] \circ |\underline{y}_3(t)|^{\underline{n}} \end{Bmatrix} + \begin{Bmatrix} \underline{0} \\ \underline{f}(t) \\ \underline{0} \end{Bmatrix} \tag{4.26}$$

where

$$\underline{f}(t) = M^{-1} L_f \underline{F}(t) \tag{4.27}$$

The equations of motion for a ground acceleration input $\ddot{u}_g(t)$ are obtained by setting $L_f \underline{F}(t) = -M\underline{1}\ddot{u}_g(t)$, leading to $\underline{f}(t) = M^{-1} L_f \underline{F}(t) = -M^{-1} M \underline{1}\ddot{u}_g(t) = -\underline{1}\ddot{u}_g(t)$.

The nonlinear hysteretic part $\underline{q}_{nl}$ of the restoring force $\underline{q}$ is defined in matrix form as:

$$\underline{q}_{nl} = diag((\underline{1} - \underline{\alpha}) \circ k)\underline{y}_3 \tag{4.28}$$

Let $\underline{y}_{i\theta} = \frac{\partial \underline{y}_i(t)}{\partial \theta}$ be the sensitivity of the response $\underline{y}_i(t)$ with respect to a parameter θ. Then the equations for the sensitivities are readily obtained by direct differentiation of Eq. 4.26 in the form:

$$\dot{\underline{y}}_{1\theta} = \underline{y}_{2\theta} + \underline{0} \tag{4.29}$$

$$\begin{aligned}\dot{\underline{y}}_{2\theta} =& - M_\theta^{-1}(C\underline{y}_2 + L^T diag(\underline{\alpha} \circ \underline{k})L\underline{y}_1 + L^T diag((\underline{1} - \underline{\alpha}) \circ \underline{k})L\underline{y}_3) \\ & - M^{-1}(C_\theta \underline{y}_2 + C\underline{y}_{2\theta} + L^T diag(\underline{\alpha}_\theta \circ \underline{k} + \underline{\alpha} \circ \underline{k}_\theta)L\underline{y}_1 + L^T diag(\underline{\alpha} \circ \underline{k})L\underline{y}_{1\theta} \\ & + L^T diag(-\underline{\alpha}_\theta \circ \underline{k} + (\underline{1} - \underline{\alpha}) \circ \underline{k}_\theta)\underline{y}_3 + L^T diag((\underline{1} - \underline{\alpha}) \circ \underline{k})\underline{y}_{3\theta}) + \underline{f}_\theta(t)\end{aligned} \tag{4.30}$$

$$\begin{aligned}\dot{\underline{y}}_{3\theta} =& \underline{A}_\theta \circ (L\underline{y}_2) + \underline{A} \circ (L\underline{y}_{2\theta}) - \underline{\beta}_\theta \circ |L\underline{y}_2| \circ \underline{y}_3 \circ |\underline{y}_3|^{\circ(\underline{n}-\underline{1})} \\ & - \underline{\beta} \circ sign(L\underline{y}_2) \circ (L\underline{y}_{2\theta}) \circ \underline{y}_3 \circ |\underline{y}_3|^{\circ(\underline{n}-\underline{1})} \\ & - \underline{\beta} \circ |L\underline{y}_2| \circ \underline{n} \circ |\underline{y}_3|^{\circ(\underline{n}-\underline{1})}\underline{y}_{3\theta} - \underline{\gamma}_\theta \circ (L\underline{y}_2) \circ |\underline{y}_3|^{\circ\underline{n}} - \underline{\gamma} \circ (L\underline{y}_{2\theta}) \circ |\underline{y}_3|^{\circ\underline{n}} \\ & - \underline{\gamma} \circ (L\underline{y}_2) \circ \underline{n}sign(\underline{y}_3)|\underline{y}_3|^{\circ(\underline{n}-\underline{1})}\underline{y}_{3\theta} - \underline{\beta} \circ |L\underline{y}_2(t)| \circ \underline{y}_3(t) \circ |\underline{y}_3(t)|^{\circ(\underline{n}-\underline{1})} \circ log(|\underline{y}_3(t)|) \circ \underline{n}_\theta \\ & - \underline{\gamma} \circ (L\underline{y}_2(t)) \circ |\underline{y}_3(t)|^{\circ\underline{n}} \circ log(|\underline{y}_3(t)|) \circ \underline{n}_\theta + \underline{0}\end{aligned} \tag{4.31}$$

4.4.2 Implementation of Kanai-Tajimi Model

The Kanai-Tajimi filter is a commonly used model to represent the strong motion content, and it is given as [59],

$$\ddot{u}_g = \ddot{x}_g + cw_t = -2\zeta_g\omega_g\dot{x}_g - \omega_g^2 x_g \tag{4.32}$$

where $\ddot{u_g}$ is the base acceleration, ω_g is the characteristic frequency of the soil layer, ζ_g is the damping ratio of the filter, c is the intensity of the white noise input, and w_t is a zero-mean Gaussian white noise input sequence, with sample at discrete time t following a Gaussian distribution $N(w_t|0,1)$ of unit variance. The equation of motion of the filter can be written as,

$$\ddot{x}_g + 2\zeta_g\omega_g\dot{x}_g + \omega_g^2 x_g = -cw_t \tag{4.33}$$

with $x_g(0) = \dot{x}_g(0) = 0$. Introducing the state vector

$$\begin{Bmatrix} y_4(t) \\ y_5(t) \end{Bmatrix} = \begin{Bmatrix} x_g(t) \\ \dot{x}_g(t) \end{Bmatrix} \tag{4.34}$$

to augment the state vector in Eq. 4.25, the additional equations for the state vector Eq. 4.34 are given by

$$\begin{Bmatrix} \dot{y}_4(t) \\ \dot{y}_5(t) \end{Bmatrix} = A_c \begin{Bmatrix} y_4(t) \\ y_5(t) \end{Bmatrix} - B_c c w_t \tag{4.35}$$

where

$$A_c = \begin{bmatrix} 0 & 1 \\ -\omega_g^2 & -2\zeta_g\omega_g \end{bmatrix}, \quad B_c = \begin{bmatrix} 0 \\ 1 \end{bmatrix} \tag{4.36}$$

and the forcing term in Eq. 4.26 takes the form $\underline{f}(t) = \underline{1}(2\zeta_g\omega_g y_5 + \omega_g^2 y_4)$. The sensitivity equations Eq. 4.29, Eq. 4.30 and Eq. 4.31 can be augmented by the equations

$$\begin{Bmatrix} \dot{y}_{4\theta} \\ \dot{y}_{5\theta} \end{Bmatrix} = \begin{Bmatrix} y_{5\theta} \\ -2\zeta_g\omega_g y_{5\theta} - \omega_g^2 y_{4\theta} - 2(\zeta_{g\theta}\omega_g + \zeta_g\omega_{g\theta})y_5 - 2\omega_g\omega_{g\theta}y_4 \end{Bmatrix} \tag{4.37}$$

where the sensitivity of the forcing term in Eq. 4.26 is given by $\underline{f}_{\theta}(t) = \underline{1}[2\zeta_g\omega_g y_{5\theta} + \omega_g^2 y_{4\theta} + 2(\zeta_{g\theta}\omega_g + \zeta_g\omega_{g\theta})y_5 + 2\omega_g\omega_{g\theta}y_4]$.

In the analysis, for a fair comparison of the utilities, the intensity of filtered input is kept the same for different values of uncertain filtered parameters ω_g and ζ_g. This is accomplished by selecting the value of the white noise input intensity c. Specifically, using a discrete state space representation of the Kanai-Tajimi model Eq. 4.33, applying the Liapunov equation, and assuming a scalar stationary zero-mean Gaussian white noise excitation with variance

$\sigma_{wn}^2 = c^2$, the variance of the ground motion acceleration is given by

$$\sigma_{\ddot{u}_g}^2 = c^2(G\bar{Q}_x G^T + JJ^T) \tag{4.38}$$

where $\bar{Q}_x$ can be obtained by solving the discrete Liapunov equation

$$A\bar{Q}_x A^T - \bar{Q}_x + BB^T = 0 \tag{4.39}$$

with the discrete state space matrices given, using zero-order hold, as $A = exp(A_c \Delta t)$ and $B = (A - I)A_c^{-1}B_c$, and Δt is the sampling time, and $G = [\ -\omega_g^2 \quad -2\zeta_g\omega_g\ ]$. Given the intensity $\sigma_{\ddot{u}_g}$ of the excitation and the filter parameters ω_g and ζ_g, the intensity c of the white noise input is computed from Eq. 4.38.

4.5 Numerical Results

4.5.1 6-DOF nonlinear spring-mass system

A 6 DOF nonlinear spring-mass chain model of the structure is first considered (Fig. 4.1). The structure could be a 6-story building represented by a shear model with each link modeling the interstory stiffness and each mass modelling the floor mass. Rayleigh damping $C = \alpha_R M + \beta_R K$ is assumed with $\alpha_R = 0.23$ and $\beta_R = 0.001$, where M and K are the mass and stiffness matrices of the linear model of the system. The parameter set $\underline{\theta}$ is introduced for the 1st and the 2nd links of the chain model. The parameter set $\underline{\theta}$ includes the stiffness k and the Bouc-Wen model parameters A, β, α, n of the 1st and 2nd links. γ is assigned to be $1 - \beta$. The model parameters of two links are assumed to be independent from each other. Thus the number of model parameters to be inferred is 10. It is assumed that the other springs are linear. A normal prior PDF is assumed for each model parameter in $\underline{\theta}$ with mean μ and standard deviation σ given in Table 4.1. The bounds of Bouc–Wen model parameters are selected to meet the following conditions: $A > 0, n > 1, \beta > 0, \alpha \in (0, 1)$.

Table 4.1: Mean and standard deviation of normal distribution, $\theta_i \sim N(\mu, \sigma)$, quantifying the prior information of the model parameters θ_i.

Parameter	(μ, σ)
k_1, k_2	(1, 0.2)
A_1, A_2	(1, 0.2)
β_1, β_2	(0.7, 0.2)
n_1, n_2	(2, 0.2)
α_1, α_2	(0.5, 0.1)

The objective of the application is to find an optimal acceleration sensor placement layout that maximizes the information for computing the model parameters $\underline{\theta}$. The time histories of the response used for the OED are contained in the interval $[t_1, t_1 + T]$ where the variable t_1 is chosen to be $t_1 = 1$ sec in order to reduce the transient effects and T is chosen to be $T = 10$ sec in order to have a reasonable signal duration to be a multiple of the largest modal period of 0.92 sec for the nominal values of the model parameters.

The structure is subjected to a base acceleration modelled by a zero-mean Gaussian white noise process with variance c^2, defined at discrete times with time step $dt = 0.01sec$. The amplitude c is selected to be $c = 100$ in order to activate model nonlinearities. The nonlinear restoring force of the 1st and 2nd links to the white noise input is presented in Fig. 4.2 for the nominal values of the model parameters. Fig. 4.3 shows the intensities (root-mean-square of the responses) of the acceleration responses at the six DOF.

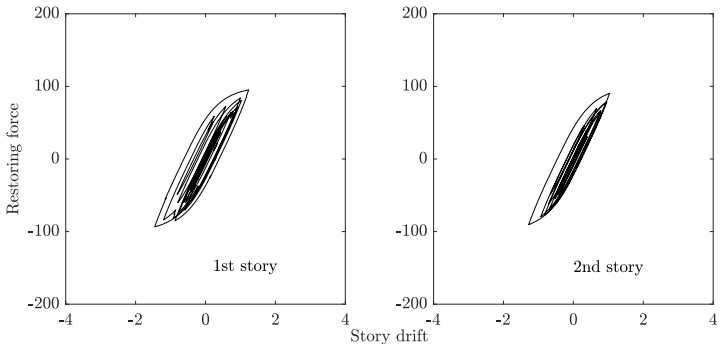

Fig. 4.2. Hysteretic force vs story drift for the first and second link computed for the nominal (mean) values of model parameters $(k = 1, A = 1, \beta = 0.7, \gamma = 0.3, n = 2, \alpha = 0.5)$.

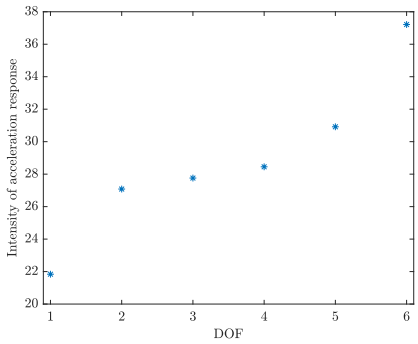

Fig. 4.3. Intensities of absolute accelerations for mean values of the model parameters vs DOF.

4.5.2 Effect of model and measurement error parameters

The effects of the model and measurement error parameters on OSP is explored by considering different measurement and model error cases given in Table 4.2. For error cases 1 and 5, the standard deviations for the error covariance matrices are selected so that the model error corresponds to 1% (small model error) and 10% (large model error) of the intensity of measured QoI, while the measurement error is fixed to 0.4% (small measurement error) of the average intensity of the measured QoI given in Fig. 4.3. For cases 1 to 4, the model error is fixed to 1% (small) of the intensity of measured QoI, while the measurement error corresponds to 0.4% (small), 1% (moderate), 4% (large) and 40% (very large) of the average intensity of measured QoI given in Fig. 4.3.

Table 4.2: Different cases of model and measurement error parameters. ϵ_{rms} is the intensity (root mean square) of the floor absolute accelerations.

Case	model error	measurement error	σ_e	s	s/ϵ_{rms}
1	small	very small	0.01	0.1	$\sim 0.4\%$
2	small	small	0.01	0.3	$\sim 1\%$
3	small	moderate	0.01	1	$\sim 4\%$
4	small	large	0.01	10	$\sim 40\%$
5	large	small	0.1	0.1	$\sim 0.4\%$

To consider the uncertainty in the unknown temporal variability of the input, the OSP design is based on 100 realizations of the white noise input. The expectation over the uncertain input parameter space is calculated using the expected information gain (utility) values in Eq. 4.14 as a function of the number of sensors placed at their optimal locations. Results are

presented in Fig. 4.4(a). Fig. 4.4(b) shows the utility values normalized by the maximum utility value for the sensor configuration containing six sensors. Results obtained from different error cases are compared in these figures.

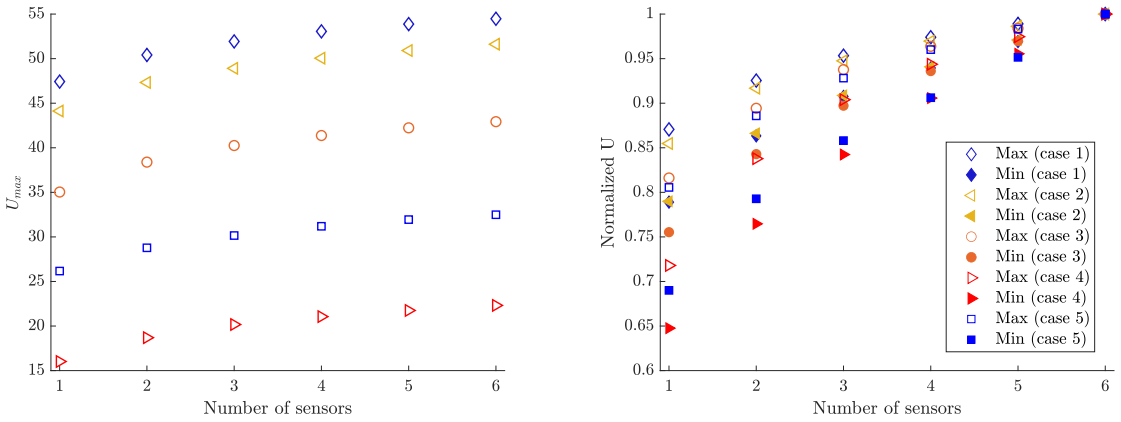

(a) **(b)**

Fig. 4.4. (a) Maximum utility values and (b) normalized maximum and minimum utilities values as a function of the number of sensors.

As observed from the expected utility values, there is a significant information gain when sensors are placed to the system to estimate the model parameters. Depending on the model and measurement error case, the first sensor optimally located on the structure provides 71-87% of the information that one would get by placing all six acceleration sensors in all six DOF. Each additional sensor provides some extra information for estimating the model parameters, until the maximum information is reached for 6 sensors. From Fig. 4.4(a) results, as measurement error increases from case 1 to case 4, the information gain decreases, which is consistent with intuition that higher measurement error corresponds to higher noise to signal ratio in the measurements and thus the information recovered is less. In the presence of noisy signals, one requires more sensors to gain the same information for parameter estimation. A similar trend can be observed for the model error comparison between case 1 and case 5. Higher model error requires more sensors to gain the same information as one gains with smaller model error.

The optimal and the worst sensor locations are shown in Fig. 4.5 as a function of the number of sensors. The best locations for the most informative sensor configurations and the worst locations for the least informative sensor configurations for all sensors are found to slightly depend on the model and measurement error cases. According to the optimal sensor

location result, the 1st sensor should be placed in the 1st DOF, independently of the model and measurement error case considered, to reliably estimate the model parameters associated with the 1st and 2nd links. This optimal location turns out to be the location between the two links that involve the unknown parameters to be inferred from the measurements. The best location of the second sensors turns out to be the 2nd DOF for most error cases and DOF 6 for the case of large measurement error. For almost all cases, the worst location of one sensor is 5th or 6th DOF, which correspond to DOF that are further away from the parameterized first two links.

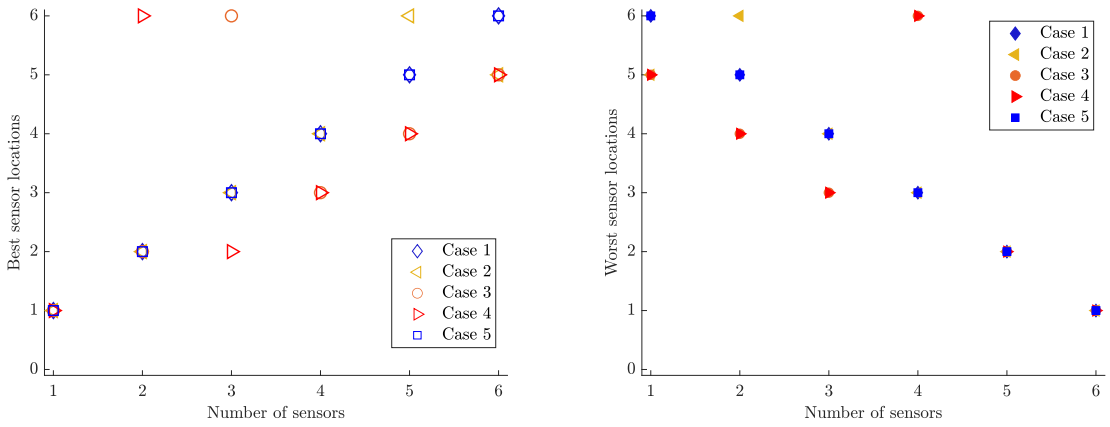

(a) **(b)**

Fig. 4.5. The best and worst sensor locations as a function of the number of sensors.

4.5.3 Computational Issues

For the 6 DOF system, the size of the input file (the actual storage requirements) for 100 white noise input realizations is $8n_\theta n n_d N M 10^{-9} = 8 \times 10 \times 6 \times 1001 \times 400 \times 100 \times 10^{-9} = 19$ GB. To create the input file for 100 white noise input cases, $n_\theta N M = 10 \times 400 \times 100 = 4 \times 10^5$ runs of the response sensitivity equations is required which amounts to 4.5 hours of computation time performed in a 32-core computer to handle the problem in parallel workers. Finally, the optimization over the sensor configuration, performed using the stored values for the response sensitivities, takes around 30 min with FSSP algorithm, which amounts to 10% of the time required to compute and store the response sensitivities.

4.5.4 Effect of input intensity

To explore the effect of the input intensity, the OSP problem is solved with different values c of the white noise excitation intensity, ranging from 0.1 to 500, and for the measurement and

model error case 3 (small model error and moderate measurement error) presented in Table 4.2. In this analysis, only 1 white noise input realization is considered. Results for the maximum information gain are presented in Fig. 4.6 for three different sensor configurations corresponding to 1, 3 and 6 number of sensors. As expected, the information gain is increasing with the input amplitude since as the values of the input intensity increase, the level of nonlinearity in the system links are progressively activated into higher levels and thus more information can be extracted from the data to reliably estimate parameters related to the nonlinearity. The higher the value of the input intensity, the smaller the increase in the information gain. As the value of the intensity increases, a sharper increase of the information gain is observed for smaller values of the input intensity c since the system moves progressively from a linear or weakly nonlinear state to a strongly nonlinear state. Once the nonlinearities are strongly activated, further increase of the intensity causes the system nonlinearities to increase further but the extra information gain is relatively small compared to the information gain obtained for smaller intensities that strongly activate the nonlinearities. Specifically, it can be noted that the increase of the intensity from 200 to 500 results in an extra information gain of 3 for one optimally placed sensor, which is only a small fraction of approximately 10% of the information gain of 27 obtained from an increase of c from 0.1 to 200.

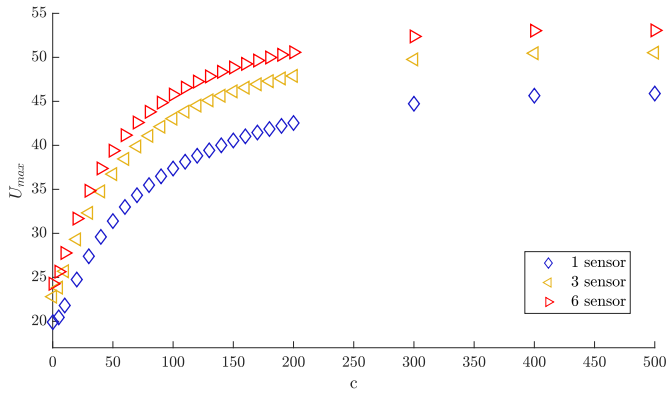

Fig. 4.6. Maximum utility values versus input intensity for white noise input obtained with 1, 3 and 6 sensors.

4.5.5 Effect of prior uncertainty

To investigate the effect of prior uncertainty, the problem is solved with truncated Gaussian prior distributions. The truncated Gaussian distribution $N_T(\theta; \mu, \sigma, a, b)$ is used in order to be able to increase the uncertainty in the prior of the updated parameters, avoiding the violation

of hard constrains in the allowable values of the model parameters. The parameters μ, σ and the bounds a and b of the truncated prior distribution are given in Table 4.3. Results are obtained for only a single input white noise realization and for model and measurement error case 3. Results are compared in Fig. 4.7 for different values of the standard deviation σ: 0.1, 0.5, 1 and 10. The increase of the uncertainty of prior distribution leads to an increase in the utility values. This is consistent with the fact that the apparent information gain that a given set of data provides is larger for larger uncertainty in the prior. This is due to the fact that large prior uncertainty corresponds to smaller values of $\det Q_\pi$ in Eq. 4.11, while for a fixed Fisher information matrix Q determined from the data, the contribution of Q_π in $Q + Q_\pi$ is negligible. As a result, the increase in the uncertainty in the prior results in a decrease in the denominator in Eq. 4.11 which corresponds to an increase in the utility value. From the normalized utility values in Fig. 4.7(b), it can be concluded that the normalized information gain, seen as a fraction of the maximum information gain that can be achieved for 6 sensors, is almost independent of the large differences in the prior uncertainty.

Table 4.3: Mean, standard deviation and bounds of truncated normal distribution, $\theta_i \sim N_T(\mu, \sigma, a, b)$, quantifying the prior information of the model parameters θ_i.

Parameter	(μ, σ, a, b)
k_1, k_2	$(1, \sigma, 0.4, 1.6)$
A_1, A_2	$(1, \sigma, 0.1, 10)$
β_1, β_2	$(0.7, \sigma, 0.1, 2)$
n_1, n_2	$(2, \sigma, 1.1, 5)$
α_1, α_2	$(0.5, \sigma, 0.1, 0.9)$

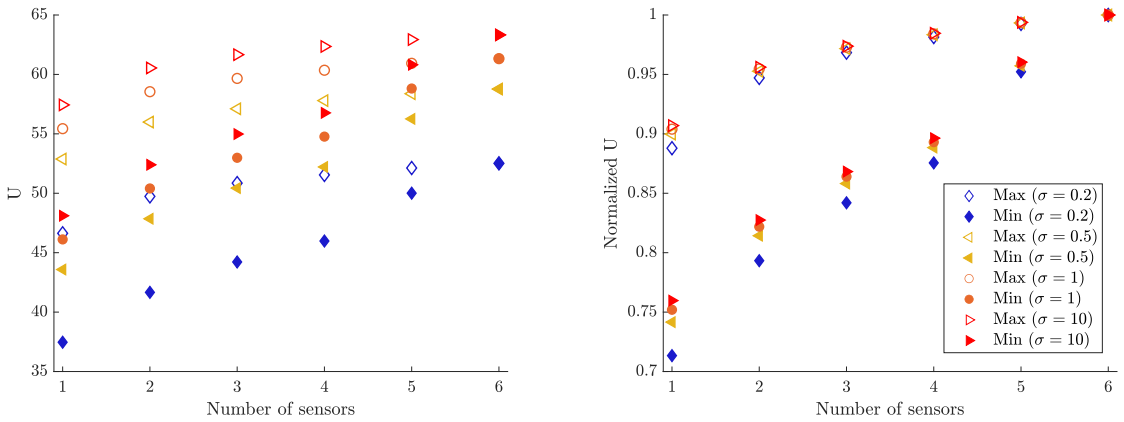

(a) **(b)**

Fig. 4.7. Maximum and minimum (a) utility values and (b) normalized utility values using truncated Gaussian priors.

4.5.6 Optimal excitation characteristics

To study the effect of excitation characteristics on the information gain, the optimal excitation frequency of a harmonic base acceleration given by $F(t) = c\sin(2\pi\Omega_i t)$ is obtained. For this the maximum information gain is estimated for different excitation frequency values Ω_i, ranging from 0.2 to 10Hz with $\Delta\Omega_i = 0.1Hz$. The intensity of the harmonic input is selected as $c = 30$, $c = 60$ and $c = 90$ to progressively activate the nonlinearities. The maximum utility values are calculated with acceleration sensors placed at all 6 DOF of the chain and the results are compared with the ones obtained from a linearized system by using the same input.

The time histories of the response used for the OED are contained in the interval $[t_1, t_1+T]$. The variable t_1 is chosen to be 10 sec so that the effect of the transient part of the response disappears, while the duration of the response is chosen to be $T = 5T_i$, where $T_i = 2\pi/\Omega_i$ is the excitation period, so that there are at least 5 cycles of the excitation frequency in the response. Here the sampling period of the input signal is selected to be $dt = T_i/N_t$ where the number of points N_t within the excitation period T_i is selected to be 20. These selections guarantee that the number of points per period remain the same, independent of the excitation frequency. These selections are important in order to compare the utility values over different excitation frequencies.

The intensity of the drift response time history at the lowest story versus the input frequencies is presented in Fig. 4.8 for the linear and nonlinear system for the harmonic input intensities $c = 30$, 60 and 90. The natural frequencies of the linearised system are shown with the vertical lines. The intensity of the drift response close to the first and second linear resonance frequency attains its maximum at a value slightly lower than the natural frequency due to the softening nonlinearity that is activated. The level of nonlinearity increases with the level of excitation, increasing the distance between the excitation frequency for which the intensity peaks and the linear resonance frequency. The width of the resonance region also increases with the level of excitation c since it affects the level of nonlinearity activated.

The utility $U(\underline{\delta}, \Omega)$ as a function of the excitation frequency Ω is presented in Fig. 4.9. Comparing Fig. 4.9 with Fig. 4.8, it is observed that the optimal excitation frequency is close to the first and the second resonant frequencies of the linear model. The most optimal excitation frequency is the one closer and slightly lower than the lowest modal frequency of the linear model. Moreover, the width of the utility function, seen as a function of the excita-

tion frequency Ω, around the lowest resonance region is larger than the width of the intensity response function around the resonance region shown in Fig. 4.8, signifying that the the selection of the optimal excitation frequency is not that sensitive to the accuracy with which the resonance frequency is known.

The information gain in the neighborhood of the second resonance frequency increases as the intensity c of the excitation frequency increases due to the fact nonlinear mechanism is progressively activated and thus more information is gained for identifying the parameters of the nonlinear hysteretic behavior. This increase in the information gain is less evident in the resonance region very close to the lowest mode due to the fact that the response at all three levels of excitation c is very large, strongly exciting the nonlinearities at all these three levels, so the information gained from higher values of c are not more informative for estimating the hysteretic parameters than the information gained from lower c values. Also, for excitation frequencies higher than 4 Hz, it can be seen that the utility values $U(\underline{\delta}, \Omega)$ almost coincide for all three excitation levels, mostly demonstrating that the nonlinearities are not adequately activated in such excitation frequency and the system behaves close to the linear range, thus providing very similar information for the parameters associated with the nonlinearities. This is consistent with the results in Fig. 4.8 which shows that drift intensities in the first floor to be smaller in the frequency range $\Omega > 4$ Hz compared to the intensities in the lower frequency range. This is also consistent with the hysteretic curves shown in Fig. 4.10 for the first floor for the three different excitation intensity levels $c = 30$, 60 and 90 drawn for the four different excitation frequencies close to the resonance frequencies 1.08 Hz, 3.19 Hz, 5.11 Hz and 6.74 Hz. Specifically, for excitation frequencies close to the third and fourth resonance frequency, the nonlinearities are only very slightly activated, with the system behaving almost in the linear regime.

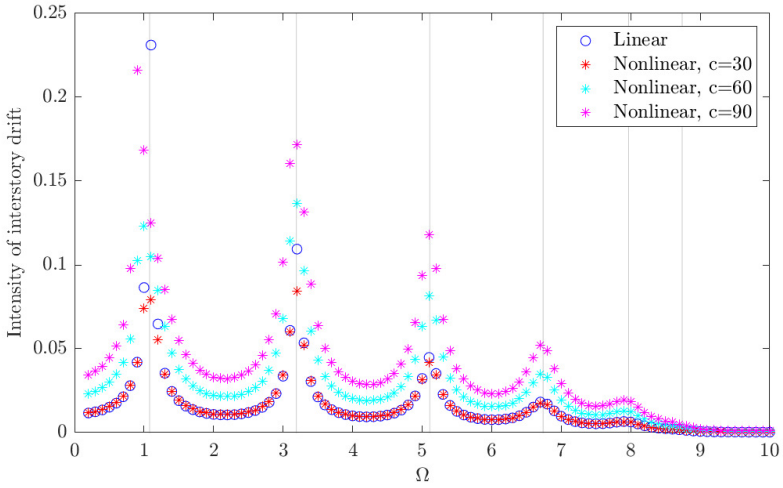

Fig. 4.8. Intensity of interstory drift for first story versus the input frequencies for linear and nonlinear systems.

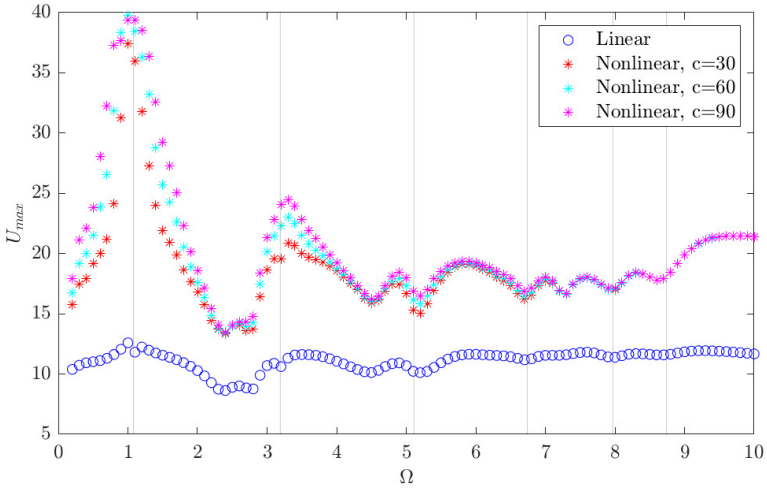

Fig. 4.9. Maximum utility versus input frequency for linear and nonlinear systems.

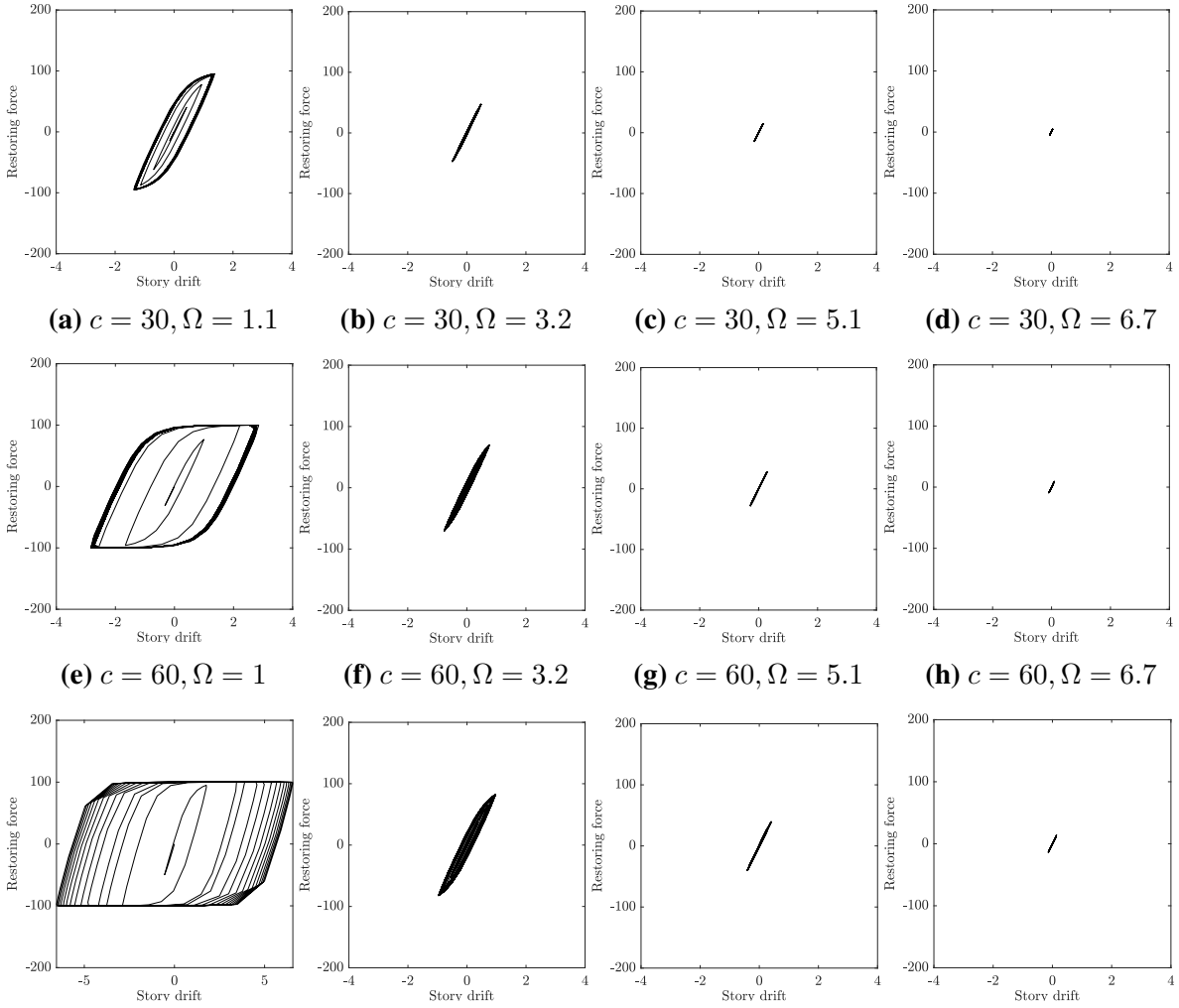

(a) $c = 30, \Omega = 1.1$ **(b)** $c = 30, \Omega = 3.2$ **(c)** $c = 30, \Omega = 5.1$ **(d)** $c = 30, \Omega = 6.7$

(e) $c = 60, \Omega = 1$ **(f)** $c = 60, \Omega = 3.2$ **(g)** $c = 60, \Omega = 5.1$ **(h)** $c = 60, \Omega = 6.7$

(i) $c = 90, \Omega = 0.9$ **(j)** $c = 90, \Omega = 3.2$ **(k)** $c = 90, \Omega = 5.1$ **(l)** $c = 90, \Omega = 6.7$

Fig. 4.10. Hysteretic force versus story drift for the first story for the three different excitation levels $c = 30$, 60 and 90 and four different excitation frequencies close to resonance frequencies 1.08 Hz, 3.19 Hz, 5.11 Hz and 6.74 Hz, estimated for the nominal (mean) values of model parameters

4.5.7 Optimal actuator location

To explore the effect of actuator location, OSP analysis is performed for the nonlinear system with harmonic excitation ($\Omega = 1.1$) for different locations of the actuator ranging from the 1st to the 6th DOF. To strongly activate the nonlinearities, the intensity c of the harmonic excitation is selected to be 1. The activation of the nonlinearities is evident in Fig. 4.11, showing the hysteretic curves of the restoring force at the first and second story versus story drift for actuator locations at 1st, 3rd and 6th DOF and for the nominal values of the model parameters. Results for the maximum utility values U as a function of the actuator location

are shown in Fig. 4.12(a) for one, two and six sensors placed at their optimal locations. It can be seen that different actuator locations provide different information. The best actuator location can be considered at the top floors (DOF 4, 5 or 6) as they provide similar information gain values. The optimal location of the sensors for different actuator locations, shown in Fig. 4.12(b), are found to be insensitive to input location for the first 3 sensors. Moreover, the 1st and 2nd DOF which are closest to the parameterized nonlinear links, are the best two sensor locations for all actuator location cases. The third best sensor location is the 6-th DOF.

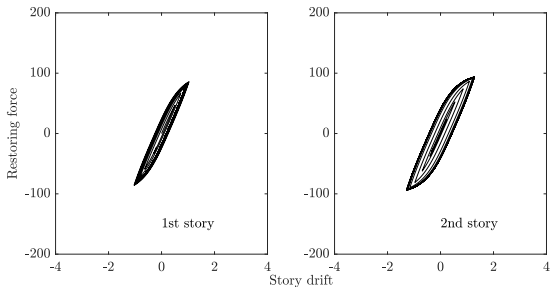

(a) actuator location: 1st DOF

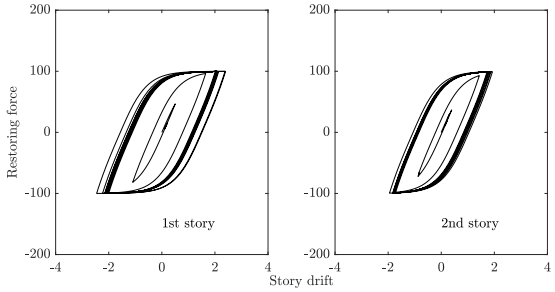

(b) actuator location: 3rd DOF

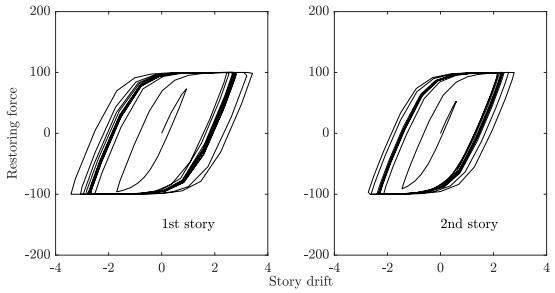

(c) actuator location: 6th DOF

Fig. 4.11. Hysteretic force versus story drift for the first and second story for actuator locations at 1, 3 and 6 DOF, for $\Omega = 1.1$ and for the nominal (mean) values of model parameters.

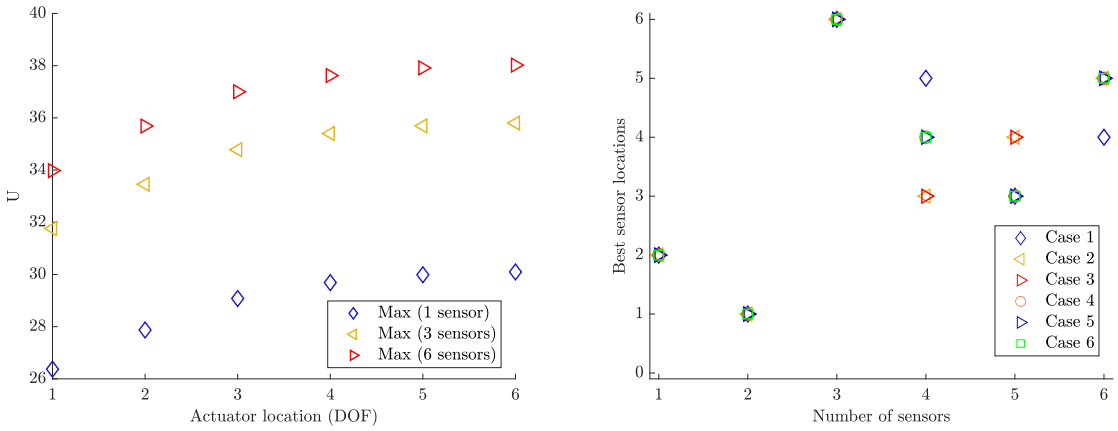

(a) **(b)**

Fig. 4.12. (a) Maximum utility values U for 1, 3 and 6 optimally located sensors, (b) Optimal sensor locations for different actuator locations. Case i corresponds to the actuator location at DOF i.

4.5.8 20-DOF nonlinear spring-mass system

As a second numerical example, a 20 DOF nonlinear spring-mass chain model of the structure shown in Fig. 4.1 is considered. The modal frequencies of the linear system are given in Table 4.4. The nonlinearity in the system is defined in the form of a Bouc-Wen hysteresis model for the links 1 to 5. It is assumed that the stiffness of the other links are linear. Rayleigh damping $C = \alpha_R M + \beta_R K$ is assumed with $\alpha_R = 0.48$ and $\beta_R = 0.04$, where M and K are the mass and stiffness matrices of the linear model of the system. The parameter set $\underline{\theta}$ includes the stiffness k and the Bouc-Wen model parameters A,β, n and α for each link from 1-5 floors. γ is assigned to be $1 - \beta$. The model parameters in $\underline{\theta}$ for links 1 to 4 are considered fully correlated. The model parameters of link 5 are treated as independent of the model parameters of link 1 to 4. Thus, the number of modal parameters is 10. A Normal prior PDF is assumed for each model parameter with mean μ and standard deviation σ given in Table 4.5. The case 3 of small model and moderate measurement error is considered. For each white noise input realization, the Monte Carlo method with 400 samples is used to calculate the integration in the utility calculation over the support of the prior values of model parameters $\underline{\varphi}_{nu}$ and $\underline{\theta}$.

Table 4.4: Modal frequencies of the linear system.

Mode	1	2	3	4	5	6	7	8	9	10	11	12	13
Freq. (Hz)	1.02	3.07	5.09	7.09	9.04	10.94	12.78	14.54	16.21	17.79	19.26	20.63	21.87
	14	15	16	17	18	19	20						
	22.99	23.97	24.80	25.50	26.04	26.43	26.66						

Table 4.5: Mean and standard deviation of normal distribution, $\theta_i \sim N(\mu, \sigma)$, quantifying the prior information of the model parameters.

Parameter	(μ, σ)
$k_{1,2,3,4}, k_5$	(1, 0.2)
$A_{1,2,3,4}, A_5$	(1, 0.2)
$\beta_{1,2,3,4}, \beta_5$	(0.7, 0.2)
$n_{1,2,3,4}, n_5$	(2, 0.2)
$\alpha_{1,2,3,4}, \alpha_5$	(0.5, 0.1)

4.5.9 Uncertainties in white-noise input characteristics

The structure is subjected to a broadband base acceleration modelled by a discrete zero-mean Gaussian white noise process with variance c^2 ($c = 800$) selected so that the nonlinearities are activated. The time samples are given every $dt = 0.01$ sec. The hysteresis force versus story drift calculated with the mean values of estimated parameters for the lowest five stories is given in Fig. 4.13 for a specific realization of the white noise excitation and for c values ranging from 400 to 1000. In Fig. 4.14 the intensities of the acceleration response time histories are given for all DOF. For the OED, the chosen time interval is $[t_1, t_1 + T]$ where $t_1 = 1$ sec is selected to reduce the effect of the transient part of the response, and $T = 2, T = 5$ and $T = 10$ sec are selected to be able to study the effect of time duration on the information gain. To consider the effect of the input uncertainty, the expectation over 100 different white noise input realizations is calculated using Eq. 4.14.

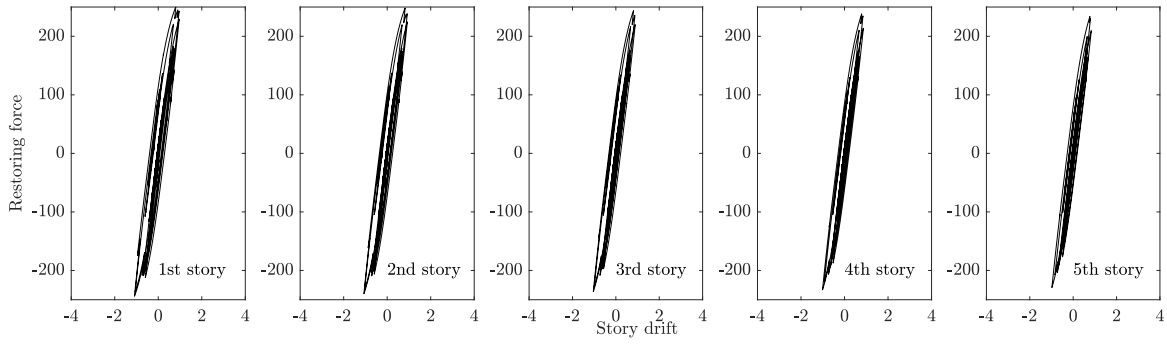

(a) $c = 400$

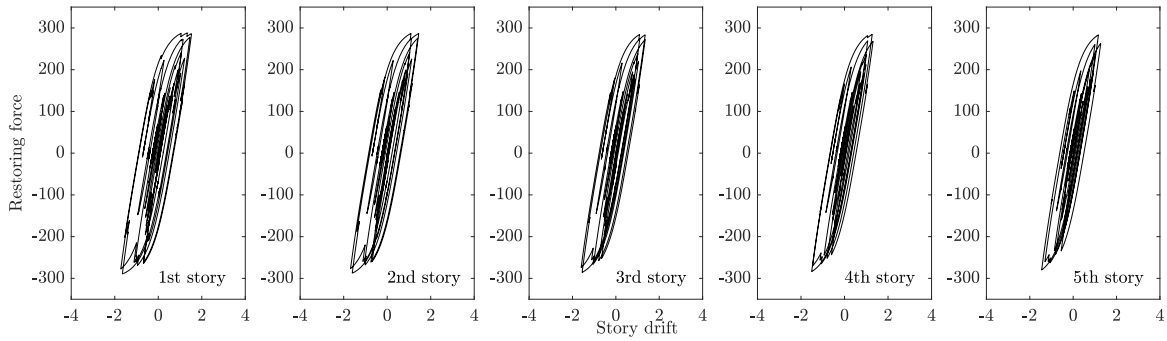

(b) $c = 600$

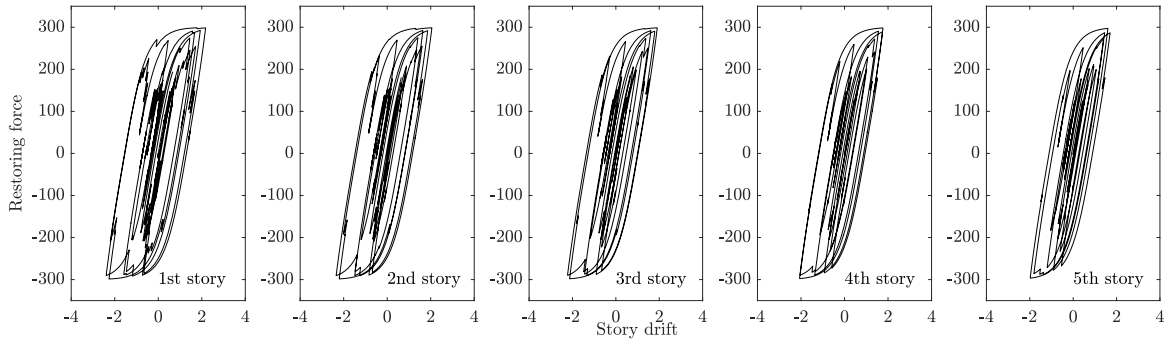

(c) $c = 800$

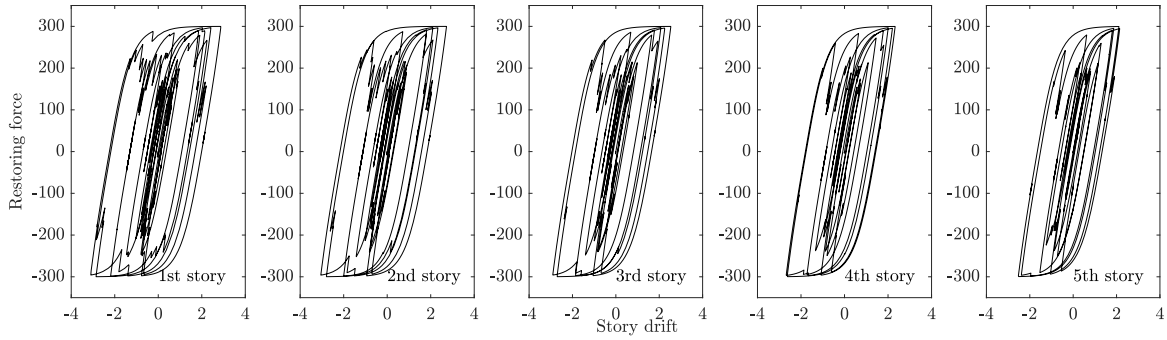

(d) $c = 1000$

Fig. 4.13. Hysteretic force vs story drift with mean values of updated parameters.

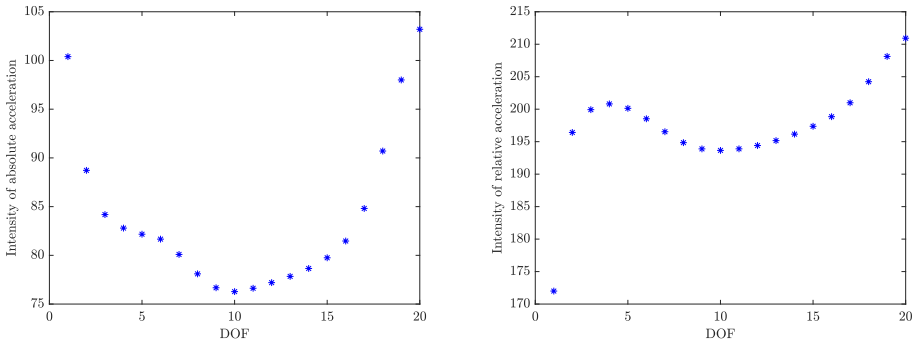

(a) **(b)**

Fig. 4.14. Intensities of the (a) absolute and (b) relative acceleration response estimated for the mean values of the model parameters versus DOF.

OSP results are presented for the three different signal durations of $T = 2$, 5 and 10 sec. The maximum and minimum utility values as well as the normalized utility values are presented in Fig. 4.15. The best and worst sensor locations are presented in Fig. 4.16. From the utility results, it can be seen that the information gain is affected by the signal duration. The higher the signal duration, the more the information provided from the data. However, from the normalized utility values in Fig. 4.15(b), it can be seen that the maximum information gain from an optimal sensor configuration involving a fixed number of sensors, measured as a fraction of the maximum information that can be gained by placing as many as 20 acceleration sensors, is almost independent of the duration of the excitation. From Fig. 4.16, the same can be concluded for the optimal and the worst sensor locations since these locations are almost independent of the signal duration. As a result, the OSP for a signal duration remains optimal for any other signal duration, in terms of normalized information gain and optimal sensor locations.

For the three cases of signal duration, there is a significant gain of approximately 75% of the maximum information when the first sensors is placed to its optimal location. According to the optimal sensor location result, the first 3 sensor locations are not affected from the signal duration and they should be placed to 4th, 5th and 3th DOF to reliably estimate the model parameters of the first 5 links. The best locations for more than 3 sensors are slightly different for the three different signal durations. However, these different sensor configurations are nearly optimal since they provide utility values that are close to the maximum utility values. The worst locations of the first sensor is the 17th DOF providing 57% to 66% of the maximum information that can be achieved by placing acceleration sensors at all 20 DOF.

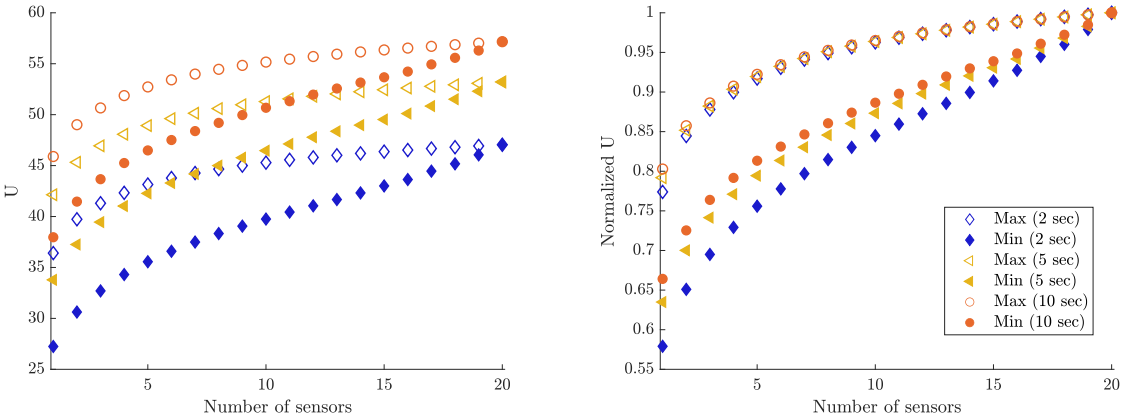

(a) **(b)**

Fig. 4.15. Maximum and minimum (a) Utility values, and (b) normalized utility values robust to input characteristics for different signal duration $T = 2$, 5 and 10 sec.

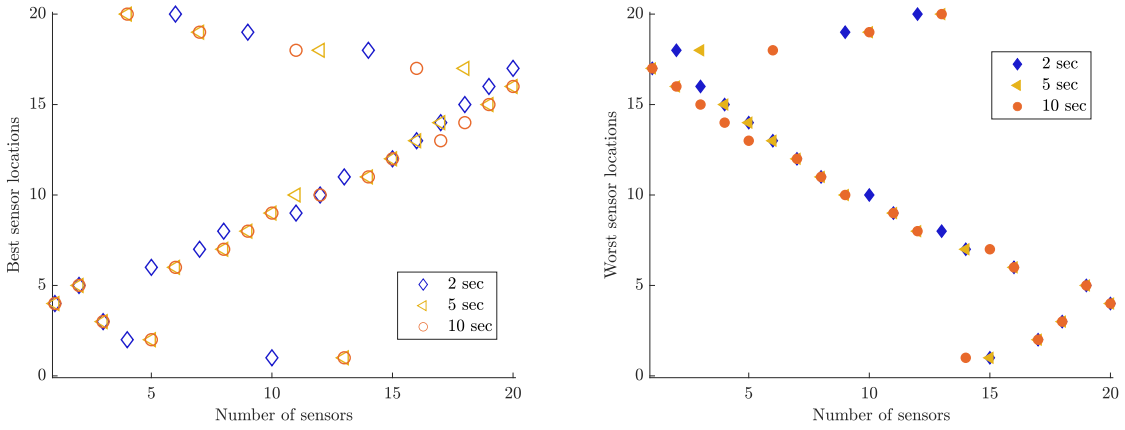

(a) **(b)**

Fig. 4.16. (a) Best and (b) worst sensor locations robust to input characteristics for different signal duration $T = 2$, 5 and 10 sec.

The optimal location of sensors as a function of the number of sensors are reported in Fig. 4.17 for 100 different realizations of the stochastic excitation. The optimal sensor locations corresponding to the expected utility values that take into account the input uncertainties are also shown in this figure. The optimal sensor locations show a slight dependence on the details of the input realizations of the stochastic excitation. The robust optimal location of the first sensor is DOF 4. This OSP at DOF 4 for the first sensor is preferred for all 100 input realizations. The robust optimal location of the second sensor is DOF 5. The DOF 5 is preferred as optimal location of the second sensor for 99 input realization cases. The second preferred location of the second sensor is DOF 3 for 1 input realization. For the third sensor, the robust

position is DOF 3, while the optimal position for each input realization is shared among DOF 3 (65% of the input realizations), DOF 20 (34% of the input realizations), and DOF 5 (1% of the input realizations).

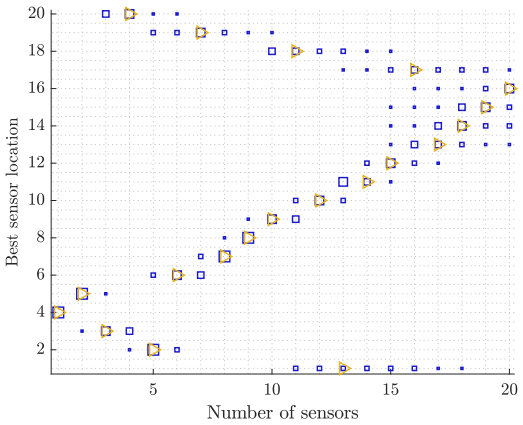

Fig. 4.17. Optimal sensor locations as a function of the number of sensors for 100 different stochastic input realizations. For a given number of sensors, more than one sensors locations can be predicted out of the 100 input realizations. The size of the blue square marker is selected to be proportional to the number of occurrence of each best/worst sensor locations counted among the 100 input realizations. Also, the robust optimal sensor locations are shown with yellow triangle.

For the 20 DOF system, the storage storage requirements for 100 white noise input realizations are $8n_\theta nn_d NM10^{-9} = 8 \times 10 \times 20 \times 1000 \times 400 \times 100 \times 10^{-9} = 64$ GB. To create the input file for 100 white noise input realizations, $n_\theta n_d NM = 10 \times 400 \times 100 = 4 \times 10^5$ runs of the sensitivity equations is required which amounts to 26 hours of computation time required in a 32-core computer to handle the problem in parallel workers. Finally, the optimization over the sensor configuration, performed using the stored values for each sensor involved in a sensor configuration to compute the utility, takes around 3 hours with FSSP, which amounts to almost 10% of the time required to compute and store the response sensitivities.

4.5.10 Uncertainties in white noise input intensity

To consider the uncertainty in white noise intensity, the parameter c is assumed to follow a truncated Gaussian distribution $N(c|\mu_c, \sigma_c, 0, \infty)$ with mean parameter $\mu_c = 800$ and standard deviation parameter $\sigma_c = 0.3\mu_c = 240$. For the OED, a time interval $[t_1, t_1 + T]$ is chosen with $t_1 = 1$ and $T = 10$ sec.

Results for the maximum utility values as a function of the number of acceleration sensors

placed at the optimal position, as well as the optimal and worst sensor locations are compared in Fig. 4.18 and Fig. 4.19 for the deterministic $c = 800$ value and the uncertain c case. The results for both the deterministic and the uncertain c cases are estimated for only a single realization of the white noise input. According to the utility results, the uncertain c case give information gain values that are higher than the ones for the deterministic case. This is due to the fact that in the uncertain case, the values of c increase significantly, activating large levels of nonlinearities, and thus there is more information in the data to estimate the parameters related to the nonlinear restoring force. From the results in Fig. 4.18, the maximum normalized information gain for both deterministic $c = 800$ case and the uncertain c case is almost the same for all optimal sensor configurations involving various number of sensors. In particular, approximately 80% of the maximum information can be obtained by using 1 sensor and after that each additional sensors provides some extra information for estimating the model parameters of lowest 5 nonlinear stories.

Results in Fig. 4.19 suggest that the optimal sensor configuration involving one, two or four sensors is not affected by the uncertainty in c. The optimal location of 3 sensors differs, with the third sensor placed optimally at the 20-th DOF for the uncertain c case as opposed to the 3-rd DOF placed for the deterministic c case. However, both optimal sensor configurations predicted by the deterministic and uncertain c cases for 3 sensors provide normalized information gains that are higher than 99% of the maximum information gain that can be achieved for 3 sensors. The optimal and worst sensor configurations for 1 to 20 sensors give almost the same pattern, as seen in Fig. 4.19, for both the deterministic and uncertain c cases.

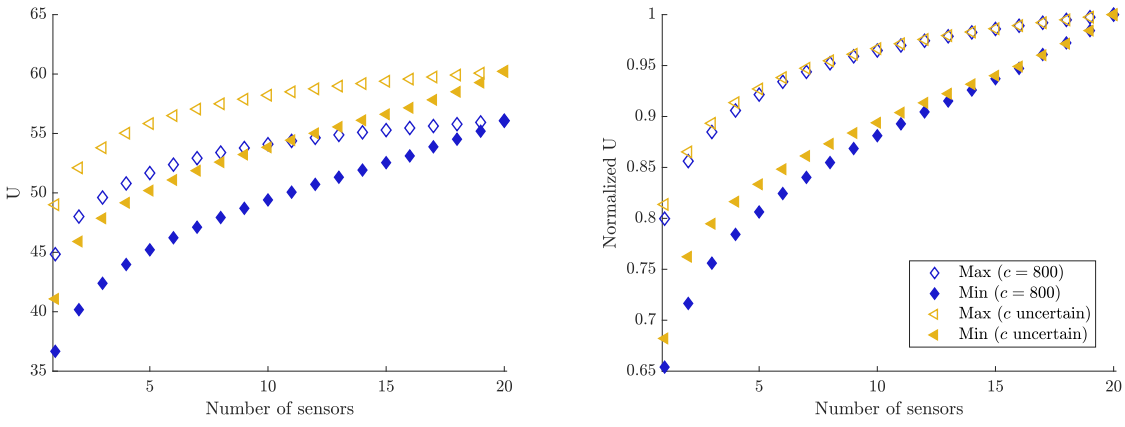

(a) **(b)**

Fig. 4.18. Comparison of (a) Utility values, and (b) normalized utility values for the deterministic ($c = 800$) and uncertain input intensity c.

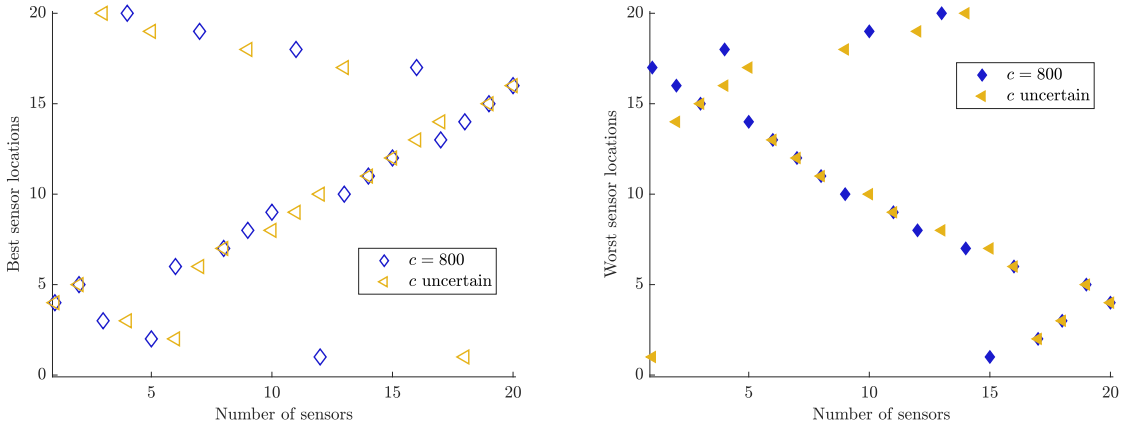

(a) **(b)**

Fig. 4.19. Comparison of (a) best and (b) worst sensor locations for the deterministic ($c = 800$) and uncertain input intensity c.

4.5.11 Uncertainties in filtered input characteristics

The structure is next subjected to a base excitation modelled by the output of the Kanai-Tajimi model used to simulated earthquake excitations. In [59] the use of $\zeta = 0.64$ and $\omega_g = 15.56(rad/sn)$ is recommended for firm soil conditions in a frequency range from $2.1(rad/sn)$ to $21(rad/sn)$. In this example, ζ_g is assumed to be constant equal to 0.64, and ω_g is assumed to be uncertain following a Gaussian distribution with mean $15(rad/sec)$ and standard deviation $1.5(rad/sec)$. The intensity of the filtered input is kept equal to $c_f = 400$ for all values of ω_f, in order to activate nonlinearities in the first five links. In Fig. 4.20, comparison of the white noise and the filtered input, and the hysteretic force and story drifts (for the first 5 stories) calculated by using the mean values of updated and uncertain model parameter is seen. Case 3 of the small model and moderate measurement error reported in Table 4.2 is considered.

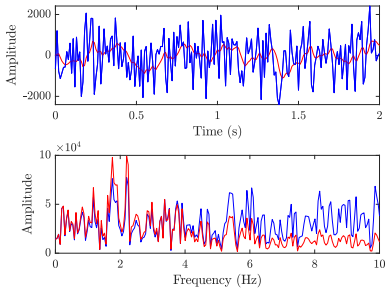

(a)

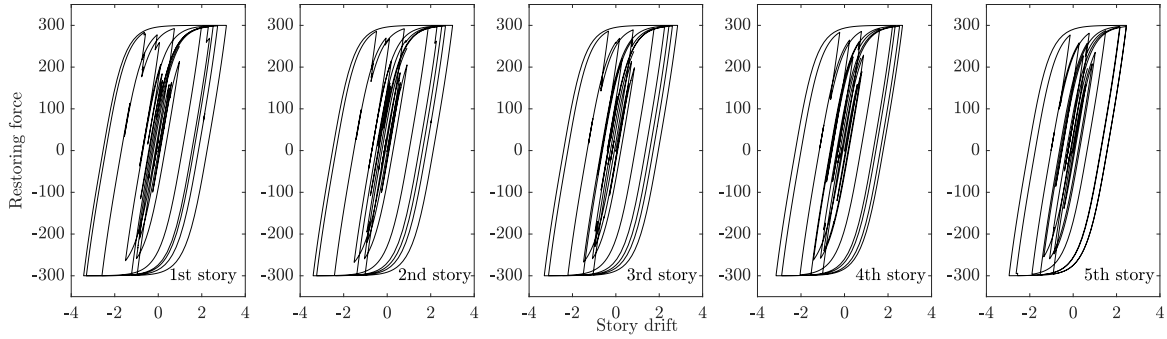

(b)

Fig. 4.20. (a) Comparison of the input (blue) and filtered input (red) in time and frequency domain, (b) hysteretic restoring force versus story drift for the first 5 stories estimated using the mean values of model parameters.

The portion of the response that is included in the utility estimation corresponds to the time interval $[t_1, t_1 + T]$, where t_1 is selected so that the transient part of the response decays sufficiently, while the duration T is chosen to be a multiple of the lower modal period of the linear system so that and the response within the interval T achieves stationarity. The following choices are made $t_1 = 1$ sec and $T = 10$ sec in order to keep the computational effort to manageable levels.

The OSP is computed to take into account the uncertainties of the filter parameter ω_g and the time history details of the earthquake excitation. To consider the earthquake acceleration uncertainty, 100 different filtered white noise input realizations are generated and the utility is averaged over all input representations. The Monte Carlo method is used to estimate the integral involved in the utility over the possible values of parameters to be inferred and the uncertain input parameter with 400 samples.

The robust OSP results obtained using the expected utility value over all realizations are compared with the results obtained by maximizing the utility value for each one of the 100 realizations of the stochastic excitation. For this, the upper and lower bounds in the maximum

and minimum utility values computed by using 100 realizations are shown in Fig. 4.21(a). The averaged maximum and minimum utility values over the 100 input realization is also presented in Fig. 4.21(a). The upper and lower bounds for the normalized information gain values are shown in Fig. 4.21(b).

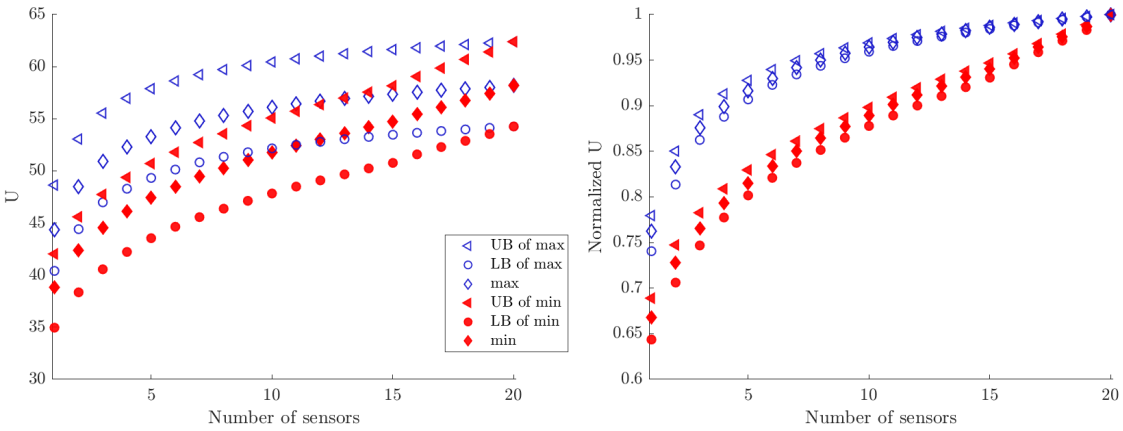

(a) **(b)**

Fig. 4.21. Upper bounds (UB) and lower bounds (LB) of maximum and minimum information gain for 100 different input realizations, as well as maximum and minimum of the expected information entropy robust to input uncertainties. (a) Expected utility values, and (b) normalized expected utility values.

It can be seen that the maximum and minimum utility values are affected from the details of the stochastic excitation. Specifically, the maximum and the minimum utility values depend on the input realization and may vary by approximately 20 to 30% depending on the number of sensors in a configuration. Similar variation is evident for the minimum utility values. However, the normalized utility values, normalized with respect to the maximum information gain that can be achieved by as many as 20 acceleration sensors, demonstrate a smaller variability, lower than 7%. In addition, the expected utility values and the normalized expected utility values that take into account the input uncertainties are contained within the aforementioned bounds. The results in Fig. 4.21(a) suggest that the uncertainty in the details of the input excitation does not considerably affect the information gain as a function of the number of optimally placed sensors in relation to the maximum information gain that can be achieved by populating the structure with the maximum of 20 sensors. 75% of the maximum information can be obtained by using 1 sensor and after that each additional sensors provides some extra information for estimating the model parameters of the lower 5 links in the chain.

The optimal and worst location of sensors as a function of the number of sensors are re-

ported in Fig. 4.22 for 100 different realizations of the stochastic excitation. The optimal and worst sensor locations corresponding to the expected utility values that take into account the input uncertainties are also shown in this figure. The optimal and worst sensor locations in Fig. 4.22 show a slight dependence on the details of the input realizations of the stochastic excitation. The robust optimal location of the first sensor is DOF 4, while the OSP at DOF 4 for the first sensor is preferred 88% of 100 input realizations, with the second preferred location of the first sensor to be DOF 3. Similar results are obtained for the second sensor. The robust optimal sensor location of the second sensor is DOF 1. The preferred locations of the second sensor are DOF 1 for 88 input realizations and DOF 20 for the rest 12 input realizations. For the third sensors, the robust position is found to be DOF 20, while the optimal position for each input realization is shared among DOF 20 (71% of the input realizations), DOF 5 (17% of the input realizations) and DOF 1 (12% of the input realizations). Finally, the robust OSP for 1 to 4 sensors are DOF 4, 1, 20 and 5, while the OSP predicted by the 100 input realizations is 4 (88% occurence), 1 (88% occurence), 20 (71% occurence) and 5 (60% occurence).

Similar to the best sensors location results, worst locations are also found to be less sensitive to the changes in the white noise input characteristics.

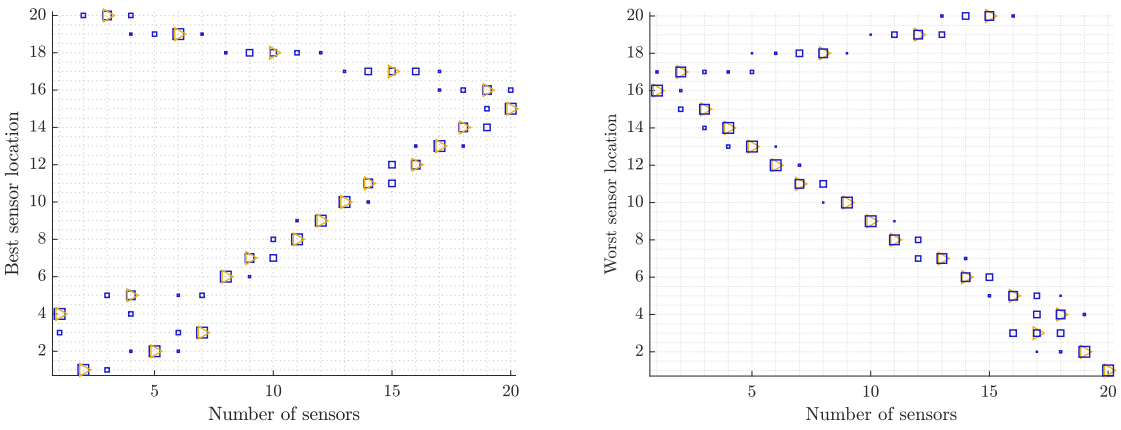

(a) **(b)**

Fig. 4.22. (a) Optimal and (b) worst sensor locations as a function of the number of sensors for 100 different stochastic input realizations. For a given number of sensors, more than one sensors locations can be predicted out of the 100 input realizations. The size of the blue square marker is selected to be proportional to the number of occurrence of each best/worst sensor locations counted among the 100 input realizations. Also, the robust (a) optimal and (b) worst sensor locations are shown with yellow triangle.

The different OSP estimates proposed by each one of the 100 input realizations do cor-

respond to near optimal solutions when the robust utility is computed. To demonstrate this, the optimal sensor configuration computed for each one of the 100 input realizations is used to compute the expected information gain taking into account the input uncertainty. The ratio of the resulting information gain values to the maximum expected information gain values is computed as a function of the number of sensors for all 100 input realizations. The lower and upper bounds of this ratio as a function of the number of sensors are plotted in Fig. 4.23. The values of the ratio are extremely close to one, ranging from 0.985 to 1.0, signifying that the information loss obtained by designing the optimal sensor configuration based on a single input realization, any single one out of the 100 input realizations, is not higher than 1 to 1.5%. This result promotes the idea of using a single realization of a stochastic excitation to design the optimal sensor configuration and find a near optimal solution, thus avoiding the very high computational cost and storage requirements associated with maximizing the expected information gain over all possible values of the input realizations.

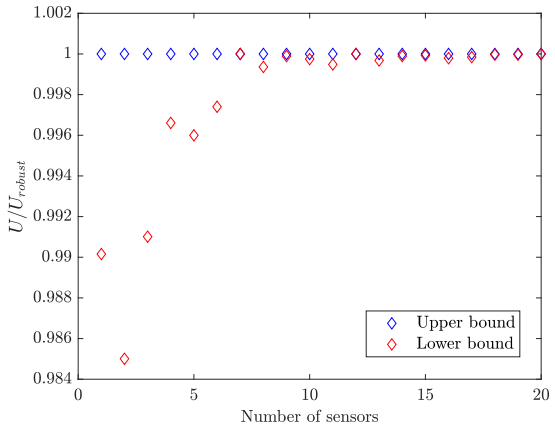

Fig. 4.23. Lower and upper bounds as a function of the number of sensors of the ratio of the expected information gain values computed from the OSP corresponding to each one of the 100 input realization and the maximum expected information gain values.

To investigate the effect of the number of parameters to be inferred and the spread of parameters along the structure, the final case considered is the OSP for estimating the parameters of the lower five links, assuming that the values of the five parameters k, A, β, n and α of each link are independent, totalling to as many as 25 parameters. A truncated Normal prior PDF is assumed for each model parameter θ with mean μ and standard deviation σ given in Table 4.5. The ground acceleration input is considered to follow the Kanai-Tajimi model with $\omega_g = 15$ Hz and $\zeta_g = 0.64$. The intensity of the filtered input is kept equal to be $c_f = 400$ in order

to activate nonlinearities in the lower five links. Case 3 of the model and measurement error reported in Table 4.2 is considered. Results for the maximum and minimum utility values as a function of acceleration sensors placed at their optimal locations are presented in Fig. 4.24 for 5 different realizations of the stochastic ground excitation. The corresponding optimal and worst sensors locations are given in Fig. 4.25. It is observed that there is no significant variability in the maximum information gain values among the 5 different input realizations, while the variability in the normalized utility values is extremely small. Also, the optimal sensor locations predicted by the five different input realizations coincide for sensor configuration involving 1 and up to 11 sensors. Similar results are obtained for the worst sensor configurations estimated from the 5 different realizations. These results confirm that it suffices to use a single input realization from a stochastic process to find a near optimum sensor configuration, thus avoiding the computationally very expensive process and reducing the storage requirements that may arise from averaging the utility function over all possible input realizations. Nevertheless, the last argument should be used with care since it is found to hold for the specific examples considered in this work and may not be generalizable to other systems and stochastic representations of loads. However, given the necessary computing facilities, the proposed technique can properly find the robust OSP that accounts for the uncertainties arising from variabilities in the input time histories.

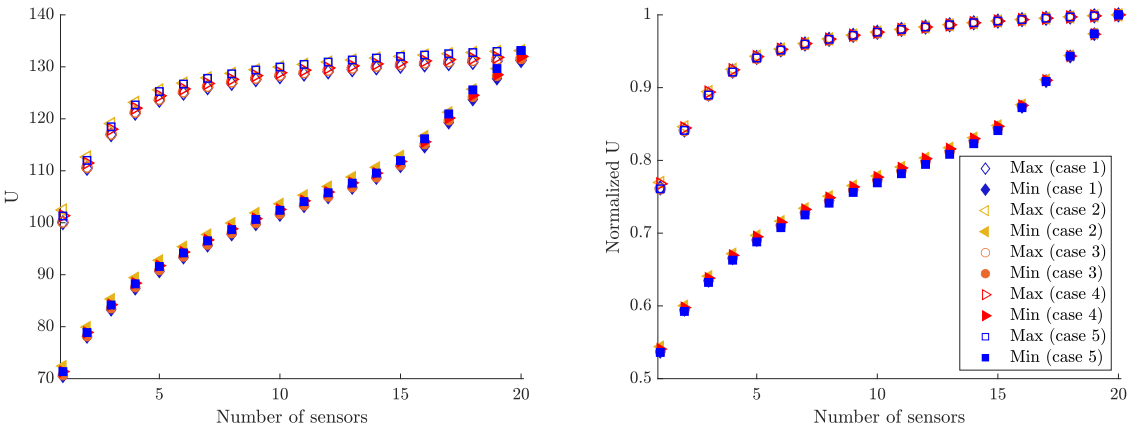

(a) **(b)**

Fig. 4.24. Maximum and minimum (a) Utility values, and (b) normalized utility values for different realizations of the excitation.

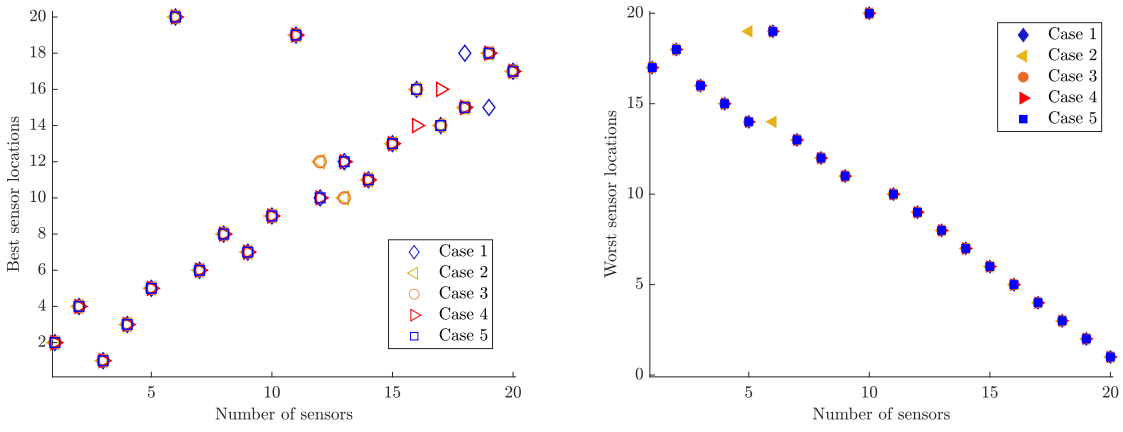

(a) **(b)**

Fig. 4.25. (a) Best and (b) worst sensor locations for different realizations of the excitation.

4.6 Conclusion

A Bayesian OED framework is presented for parameter estimation of linear and nonlinear models in structural dynamics using input-output response time history measurements. The effects of modeling and input uncertainties are comprehensively investigated in this study. Past studies considered in the OED that the excitation is available. However, although the time histories of the inputs can be measured during the inference process with appropriately installed sensors, such inputs are not available during OED phase. For this, the temporal variability of the inputs is described in this work using stochastic process models. An example includes the Kanai-Tajimi model or available seismological models for quantifying the earthquake excitation process. This study recognises the uncertainties in the excitation time histories and proposes an optimal design that is robust to such uncertainties.

The design variables include the locations of the sensors and actuators, as well as the input characteristics. Information and utility theory are used to define the objective function to be maximized, measuring the information gained from a sensor configuration. Asymptotic approximations simplify the information gain as a scalar measure of the Fisher information matrix built from the sensitivities of the response QoI at the sensor locations with respect to the parameters to be inferred. For the case of inadequate data, information is also borrowed from the prior distribution of the parameters to be inferred. It is demonstrated that the information gain for a given sensor configuration depends on location of actuators and the excitation characteristics. The OED problem involves a simultaneous optimization of the information

gain with respect to number and locations of sensors, as well as the number and location of the actuators and the excitation characteristics. The structural differences between the design of optimal sensor configuration and the design of optimal actuator and excitation characteristics is pointed out. Based on asymptotic approximation, valid for large number of data, the expected utility function to be maximized is a scalar measure of the sensitivity of the responses at the measured locations with respect to the parameters to be inferred. A sensor configuration affects which response sensitivities are involved in the information gain measure. An actuator configuration and the excitation characteristics affects the value of the information gain but does not alter the structure of the information gain built from the response sensitivities corresponding to a sensor configuration.

To take into account the model and input uncertainties the expected information gain is introduced over all possible model and input uncertainties. The resulting multi-dimensional probability integrals are estimated using Monte Carlo sampling techniques. Heuristic SSP algorithms as well as genetic algorithms can be used to optimize the objective function. The large computational burden associated with the OED robust to model and input uncertainties is also pointed out and remedies are provided to reduce the computational effort.

The proposed framework is validated using a 6 and a 20-DOF nonlinear spring-mass chain models with internal spring forces represented by hysteretic nonlinearities of the Bouc-Wen type. The effect of the model and measurement error parameters and the various input characteristics (amplitude variation and frequency content) on sensor placement is investigated. It is demonstrated that designing the OSP for a single realization of a stochastic input may suffice to obtain a very good design for the robust case that takes into account the uncertainty in the details of the stochastic input.

It is also shown that optimal input characteristics and actuator locations can be calculated by using the proposed method. According to the results for harmonic input, the information obtained will be maximum when the system is excited in the neighborhood of the resonance frequency of the linearized model. The optimal excitation frequency is not sensitive to the accuracy of the resonant frequency values.

4.7 References

[1] R. J. Barthorpe and K. Worden. Emerging trends in optimal structural health monitoring system design: From sensor placement to system evaluation. *Journal of Sensor and Actuator Networks*, 9(3):31, 2020.

[2] P. C. Shah and F. E. Udwadia. A methodology for optimal sensor locations for identification of dynamic systems. *Journal of Applied Mechanics*, 45(1):188–196, 3 1978.

[3] F. E. Udwadia. Methodology for optimum sensor locations for parameter identification in dynamic systems. *Journal of Engineering Mechanics*, 120(2):368–390, 1994.

[4] P. H. Kirkegaard and R. Brincker. On the optimal location of sensors for parametric identification of linear structural systems. *Mechanical Systems and Signal Processing*, 8 (6):639–647, 11 1994.

[5] D. Ucinski. Optimal sensor location for parameter estimation of distributed processes. *International Journal of Control*, 73(13):1235–1248, 2000.

[6] Z. H. Qureshi, T. S. Ng, and G. C. Goodwin. Optimum experimental design for identification of distributed parameter systems. *International Journal of Control*, 31(1):21–29, 1 1980.

[7] D. C. Kammer. Sensor placement for on-orbit modal identification and correlation of large space structures. *Journal of Guidance, Control, and Dynamics*, 14(2):251–259, 1991.

[8] C. Papadimitriou, J. L. Beck, and S. K. Au. Entropy-based optimal sensor location for structural model updating. *JVC/Journal of Vibration and Control*, 6(5):781–800, 2000.

[9] K. V. Yuen, L. S. Katafygiotis, C. Papadimitriou, and N. C. Mickleborough. Optimal sensor placement methodology for identification with unmeasured excitation. *Journal of Dynamic Systems, Measurement and Control, Transactions of the ASME*, 123(4):677–686, 2001.

[10] C. Papadimitriou. Optimal sensor placement methodology for parametric identification of structural systems. *Journal of Sound and Vibration*, 278(4-5):923–947, 2004.

[11] Y. Robert-Nicoud, B. Raphael, and I. F. Smith. Configuration of measurement systems using Shannon's entropy function. *Computers and Structures*, 83(8-9):599–612, 2005.

[12] K. V. Yuen and S. C. Kuok. Efficient Bayesian sensor placement algorithm for structural identification: a general approach for multi-type sensory systems. *Earthquake Engineering & Structural Dynamics*, 44(5):757–774, 2015.

[13] C. Papadimitriou and G. Lombaert. The effect of prediction error correlation on optimal sensor placement in structural dynamics. *Mechanical Systems and Signal Processing*, 28:105–127, 4 2012.

[14] N. J. Bertola, S. G. Pai, and I. F. Smith. A methodology to design measurement systems when multiple model classes are plausible. *Journal of Civil Structural Health Monitoring*, 11(2):1–22, 2021. ISSN 2190-5479.

[15] C. Stephan. Sensor placement for modal identification. *Mechanical Systems and Signal Processing*, 27(1):461–470, 2012.

[16] S. Q. Ye and Y. Q. Ni. Information entropy based algorithm of sensor placement optimization for structural damage detection. *Smart Structures and Systems*, 10(4_5):443–458, 2012. ISSN 17381991. doi: 10.12989/sss.2012.10.4_5.443.

[17] H. M. Chow, H. F. Lam, T. Yin, and S. K. Au. Optimal sensor configuration of a typical transmission tower for the purpose of structural model updating. *Structural Control and Health Monitoring*, 18(3):305–320, 4 2011.

[18] T. Yin, H. F. Lam, and H. M. Chow. A Bayesian probabilistic approach for crack characterization in plate structures. *Computer-Aided Civil and Infrastructure Engineering*, 25 (5):375–386, 2010.

[19] T. Yin, K. V. Yuen, H. F. Lam, and H. P. Zhu. Entropy-based optimal sensor placement for model identification of periodic structures endowed with bolted joints. *Computer-Aided Civil and Infrastructure Engineering*, 32(12):1007–1024, 12 2017.

[20] H. Ebrahimian, R. Astroza, J. P. Conte, and R. R. Bitmead. Information-theoretic approach for identifiability assessment of nonlinear structural finite-element models. *Journal of Engineering Mechanics*, 145(7):04019039, 2019.

[21] N. J. Bertola, M. Papadopoulou, D. Vernay, and I. F. Smith. Optimal multi-type sensor placement for structural identification by static-load testing. *Sensors*, 17:2904, 2017.

[22] M. Papadopoulou, B. Raphael, I. F. Smith, and C. Sekhar. Hierarchical sensor placement using joint entropy and the effect of modeling error. *Entropy*, 16(9):5078–5101, 2014.

[23] X. Huan and Y. M. Marzouk. Simulation-based optimal Bayesian experimental design for nonlinear systems. *Journal of Computational Physics*, 232(1):288–317, 1 2013.

[24] C. Argyris and C. Papadimitriou. Bayesian optimal experimental design using asymptotic approximations. In *Proceedings of the 35th International Modal Analysis Conference, IMAC*, volume 3, pages 273–275, 2017.

[25] G. Capellari, E. Chatzi, and S. Mariani. Cost–benefit optimization of structural health monitoring sensor networks. *Sensors*, 18(7):1–22, 2018.

[26] C. Argyris, S. Chowdhury, V. Zabel, and C. Papadimitriou. Bayesian optimal sensor placement for crack identification in structures using strain measurements. *Structural Control and Health Monitoring*, 25(5):2137, 5 2018.

[27] P. Bhattacharyya and J. Beck. Exploiting convexification for Bayesian optimal sensor placement by maximization of mutual information. *Structural Control and Health Monitoring*, 27(10):1–18, 2020.

[28] C. Argyris. *Bayesian uncertainty quantification and optimal experimental design in data driven simulations of engineering systems*. PhD thesis, University of Thessaly, 2010.

[29] C. Malings and M. Pozzi. Value of information for spatially distributed systems: Application to sensor placement. *Reliability Engineering and System Safety*, 154:219–233, 2016.

[30] C. Malings and M. Pozzi. Submodularity issues in value-of-information-based sensor placement. *Reliability Engineering and System Safety*, 183:93–103, 2019.

[31] S. Cantero-Chinchilla, J. Chiachío, M. Chiachío, D. Chronopoulos, and A. Jones. Optimal sensor configuration for ultrasonic guided-wave inspection based on value of information. *Mechanical Systems and Signal Processing*, 135:106377, 2020.

[32] C. Leyder, V. Ntertimanis, E. Chatzi, and A. Frangi. Optimal sensor placement for the modal identification of an innovative timber structure. In *Proceedings of the 1st International Conference on Uncertainty Quantification in Computational Sciences and Engineering, UNCECOMP*, pages 467–476, 2015.

[33] G. Capellari, E. Chatzi, and S. Mariani. Structural health monitoring sensor network optimization through Bayesian experimental design. *ASCE-ASME Journal of Risk and Uncertainty in Engineering Systems, Part A: Civil Engineering*, 4(2):04018016, 2018.

[34] C. Papadimitriou and C. Argyris. Bayesian optimal experimental design for parameter estimation and response predictions in complex dynamical systems. In *Procedia Engineering*, volume 199, pages 972–977. Elsevier Ltd, 2017.

[35] C. Argyris, C. Papadimitriou, G. Samaey, and G. Lombaert. A unified sampling-based framework for optimal sensor placement considering parameter and prediction inference. *Mechanical Systems and Signal Processing*, 161:107950, 2021.

[36] C. Papadimitriou, Y. Haralampidis, and K. Sobczyk. Optimal experimental design in stochastic structural dynamics. *Probabilistic Engineering Mechanics*, 20(1):67–78, 2005.

[37] T. Ercan and C. Papadimitriou. Optimal Sensor Placement for Reliable Virtual Sensing Using Modal Expansion and Information Theory. *Sensors*, 21(10):3400, 2021. doi: doi.org/10.3390/s21103400.

[38] J. Kullaa. Bayesian virtual sensing for full-field dynamic response estimation. In *Procedia Engineering*, volume 199, pages 2126–2131. Elsevier Ltd, 2017.

[39] A. Mehrjoo, M. Song, B. Moaveni, C. Papadimitriou, and E. Hines. Optimal sensor placement for parameter estimation and virtual sensing of strains on an offshore wind turbine considering sensor installation cost. *Mechanical Systems and Signal Processing*, 169:108787, 2022.

[40] C. Papadimitriou. Optimal sensor placement for response reconstruction in structural dynamics. In *Model Validation and Uncertainty Quantification, Volume 3*, pages 205–210. Springer, 2020.

[41] T. Ercan, O. Sedehi, C. Papadimitriou, and L. S. Katafygiotis. Robust optimal sensor placement for response reconstruction using output only vibration measurements. In *Proceedings of the 29th European Safety and Reliability Conference, ESREL*, pages 1270–1276. Research Publishing Services, 2019.

[42] P. Metallidis, G. Verros, S. Natsiavas, and C. Papadimitriou. Fault detection and optimal sensor location in vehicle suspensions. *Journal of Vibration and Control*, 9(3-4):337–359, 2003.

[43] P. L. Green, E. J. Cross, and K. Worden. Bayesian system identification of dynamical systems using highly informative training data. *Mechanical Systems and Signal Processing*, 56:109–122, 2015.

[44] C. Papadimitriou, E. M. Lourens, G. Lombaert, G. De Roeck, and K. Liu. Prediction of fatigue damage accumulation in metallic structures by the estimation of strains from operational vibrations. In *Life-Cycle and Sustainability of Civil Infrastructure Systems - Proceedings of the 3rd International Symposium on Life-Cycle Civil Engineering, IALCCE*, pages 304–310, 2012.

[45] D. I. Papadimitriou and C. Papadimitriou. Optimal Sensor Placement for the Estimation of Turbulence Model Parameters in CFD. *International Journal for Uncertainty Quantification*, 5(6):545–568, 2015.

[46] K. Kanai. Semi-empirical formula for the seismic characteristics of the ground. *Bulletin of the Earthquake Research Institute, University of Tokyo*, 35(2):309–325, 1957.

[47] H. Tajimi. A statistical method of determining the maximum response of a building structure during an earthquake. In *Proc. 2nd World Conf. Earthq. Eng.*, pages 781–797, 1960.

[48] D. M. Boore. Simulation of ground motion using the stochastic method. *Pure and applied geophysics*, 160(3):635–676, 2003.

[49] H. A. Jensen. Design and sensitivity analysis of dynamical systems subjected to stochastic loading. *Computers & structures*, 83(14):1062–1075, 2005.

[50] H. A. Jensen. Structural optimization of linear dynamical systems under stochastic excitation: a moving reliability database approach. *Computer methods in applied mechanics and engineering*, 194(12-16):1757–1778, 2005.

[51] C. Papadimitriou. Optimal sensor placement for response reconstruction in structural dynamics. In *Proceedings of the 37th International Modal Analysis Conference,IMAC*, pages 205–210. Springer, 2020. ISBN 9783030120740.

[52] D. V. Lindley. On a measure of the information provided by an experiment. *The Annals of Mathematical Statistics*, 27(4):986–1005, 1956.

[53] T. Gerstner and M. Griebel. Numerical integration using sparse grids. *Numerical Algorithms*, 18(3):209–232, 1998.

[54] F. Heiss and V. Winschel. Likelihood approximation by numerical integration on sparse grids. *Journal of Econometrics*, 144(1):62–80, 2008.

[55] K. Worden and W. J. Staszewski. Impact location and quantification on a composite panel using neural networks and a genetic algorithm. *Strain*, 36(2):61–68, 2000.

[56] L. Yao, W. A. Sethares, and D. C. Kammer. Sensor placement for on-orbit modal identification via a genetic algorithm. *AIAA Journal*, 31(10):1922–1928, 1993.

[57] R. Bouc. Forced Vibration of Mechanical Systems with Hysteresis. *4th Conference on Nonlinear Oscillations, Prague, Czechoslovakia*, 1967. ISSN 11749857.

[58] Y. K. Wen. Method for random vibration of hysteretic systems. *Journal of the engineering mechanics division*, 102(2):249–263, 1976.

[59] T. Neckel and F. Rupp. *Random differential equations in scientific computing*. De Gruyter Open Poland, 2013.

Chapter 5. Optimal Sensor Placement for Virtual Sensing: Applications to Wind Turbine and Helicopter Blade

Health monitoring practices for structures operating in a highly dynamic environment (i.e. energy structures, offshore structures) provide an important source for the understanding of their performance, improving damage evaluation and life prognostics of structural components. Considering the complexity of these dynamic systems, performing experiments to create and validate digital twins has crucial importance for predicting the loads or the responses (i.e. virtual sensing) in the parts where instrumentation is difficult or costly to implement. OSP strategies can be used to provide informative data by optimizing the experimental set up in terms of location, number, and type of sensors and eventually lead to reliable predictions.

In this chapter, the effectiveness of the proposed Bayesian optimal experimental design frameworks [1, 2] are demonstrated by applying it to two realistic structural components: a wind turbine blade and a helicopter blade. In the applications, the type, location and number of sensors are optimized for accurate virtual sensing (response and/or load reconstruction) under unknown excitation. Both a GA and heuristic SSP algorithms are used to solve the optimization problem in an effort to provide computationally efficient solutions. Validation studies have been also performed using the simulated, as well as available experimental data for the helicopter blade, to demonstrate that the proposed approach is applicable and reliable to optimize the experimental design of industrial structures in the presence of modelling errors and uncertainties in loads and environmental or operating conditions.

5.1 Application on Wind Turbine Blade (WTB)

The OSP methodology is applied to a small-scale composite WTB structure given in Fig. 5.1. The structure with its structural and geometrical properties as well as the monitoring campaign performed at ETH Zurich is presented in detail in references [3, 4]. The blade FE model is fixed at the left edge and the outer surface consists of 6189528 nodes and 242930 six-degree-of freedom thin shell elements. The first eight modal frequencies computed from the finite element model can be found in Table 5.1. The type, number and the locations of sensors are

optimized for reliable response predictions of unmeasured QoI under unknown excitation. Two different methods: modal expansion (ME) and Augmented Kalman Filter (AKF) techniques are used and the efficiency of the techniques is investigated using simulated measurements.

(a) **(b)**

Fig. 5.1. (a) Sonkyo Windspot 3.5 kW, (b) overview of the experimental set-up (Source: [3]).

Table 5.1: Modal frequencies of the wind turbine blade.

Mode	Mode 1	Mode 2	Mode 3	Mode 4	Mode 5	Mode 6	Mode 7	Mode 8
Natural Frequency (Hz)	14.59	38.66	66.18	89.97	113.84	116.64	137.40	152.60

5.1.1 OSP for Strain Predictions

OSP analysis is performed to optimize the location and number of strain sensors for strain response prediction on the locations marked with red dots in Fig. 5.2. For illustration purposes, it is assumed that the blade is subjected to a point load defined as a white noise input with a sampling period $\Delta t = 0.0025$ sec at the location shown in Fig. 5.2. It is assumed that only the lowest 8 modes contribute to the response. The modal damping ratios for all contributing modes are taken to be equal to 2%. The positions of strain sensors are optimized by using modal expansion to form the utility function. Then the same problem is solved by using AKF. Following that, OSP is performed for strain response and input predictions fusing different types of sensors by using AKF.

The effectiveness of the optimal sensor placement is investigated by using simulated noise contaminated measurements. To simulate strain response time histories, a white noise input is used with a standard deviation of $\sigma_{wn} = 1$, a sampling period of $\Delta t = 0.0025$ seconds and a response duration of 10 seconds. To be able to simulate noise contaminated measurements,

independent zero-mean Gaussian white noise sequences with standard deviation equal to 2% of the intensity of the simulated response is added to each simulated strain response time history.

The model and measurement error parameters σ_e, σ_ϵ and s (see Chapter 2 and 3 for definition) are selected according to the intensities of responses (observed QoI) and given in Table 5.2 with the prior parameter α and parameters for AKF for the process noise σ_x and the input uncertainty β (see [1] for the details of parameter selection for modal expansion and [2] for AKF). The values in Table 5.2 are given for different types of sensors and they correspond to small model error of the order of 1%, as well as medium to small measurement error ranging from 20% to 0.4% of the minimum and maximum reported observed QoI in the structure.

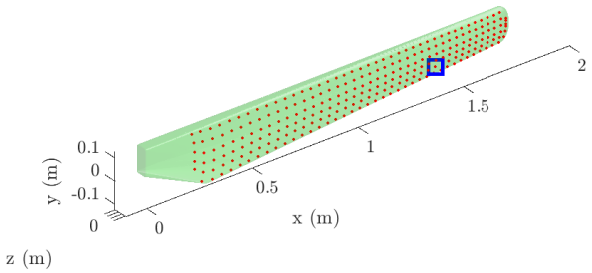

Fig. 5.2. Location of input (blue), predictions and possible sensors (red).

Table 5.2: Prior, prediction error, model and measurement error parameters for modal expansion. $\epsilon_{\min}$ is the minimum value of the nodal accelerations or element strains that cover 98% of the blade surface. $\epsilon_{\max}$ and ϵ_{rms} are respectively the maximum and the mean value of the intensity (root mean square) of the nodal acceleration, displacement or element strain in the blade surface.

Sensor type	α	$\sigma_e, \sigma_\epsilon$	s	$\sim s/\epsilon_{min}$	$\sim s/\epsilon_{rms}$	$\sim s/\epsilon_{max}$	σ_x	β
Acceleration	10^2	10^{-2}	10^2	2×10^{-1}	10^{-2}	2×10^{-3}	10^{-3}	1
Displacement	10^2	10^{-2}	10^{-3}	2×10^{-1}	10^{-2}	2×10^{-3}	10^{-3}	1
Strain	10^2	10^{-2}	10^{-7}	2×10^{-1}	10^{-2}	4×10^{-3}	10^{-3}	1

5.1.1.1 OSP results for strain sensors using ME

The OSP results for strain sensors are presented in Fig. 5.3 through the expected information gain (utility values) as a function of the number of sensors placed at their optimal (or worst) locations (Fig. 5.3(a)), and the optimal positions of 8 sensors (Fig. 5.3(b)). The maximum

utility value (U_{max}=9.17) which can be reached with 245 strain sensors is shown as a grey horizontal line in Fig. 5.3(a). For less than 8 sensors (the number of contributing modes) the problem of OSP is unidentifiable and subjective information for placing sensors is borrowed from the prior PDF. As a result, the information gain for a configuration up to 7 sensors is significantly less than the maximum information gain that can be achieved with as many as 8 to 245 strain sensors uniformly spread over the blade surface. Including an eight sensor in the sensor configuration leads to a sharp increase in the information gain, reaching a value which is very close to the maximum information gain. Adding more than eight sensors at the optimal locations results in a relatively small increase in information gain. From the optimal sensor configuration results in Fig. 5.3(b), it can be seen that the strain sensors are well distributed along the blade for reliable response prediction.

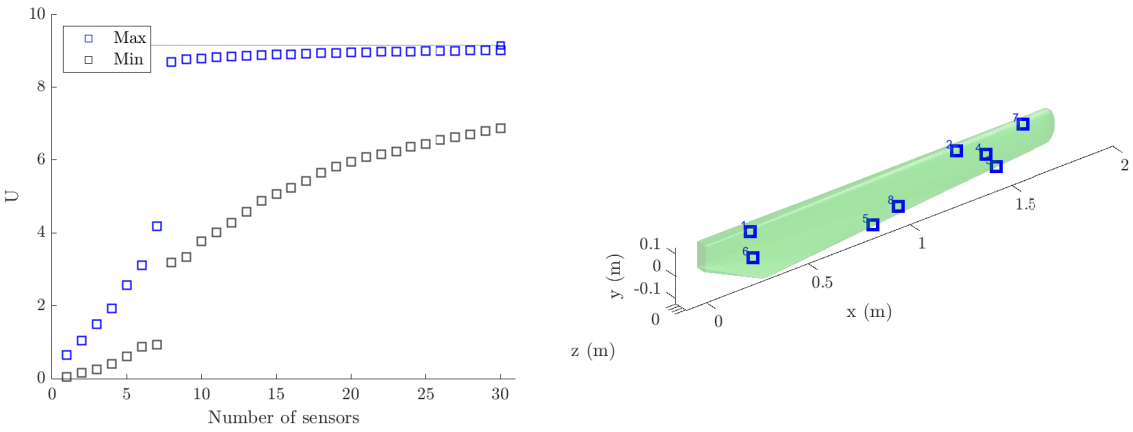

(a) **(b)**

Fig. 5.3. OSP results through (a) utility and (b) the best sensor locations. The maximum utility value U_{max} whichh can be reached with 245 strain sensors is shown as a grey horizontal line in (a).

For validation purposes, strain responses at the 245 locations shown in Fig. 5.2 are predicted with simulated measurements from the best, worst and an arbitrary sensor configurations, all involving 8 sensors. Relative root mean square (RRMS) errors between the predictions calculated with ME technique for the best and arbitrary configurations (with their utility values) are presented in Fig. 5.4. The relative strain error at each location is defined as the ratio of the root mean square error between the predicted and measured responses over the root mean square value (intensity) of the measured strain response time history.

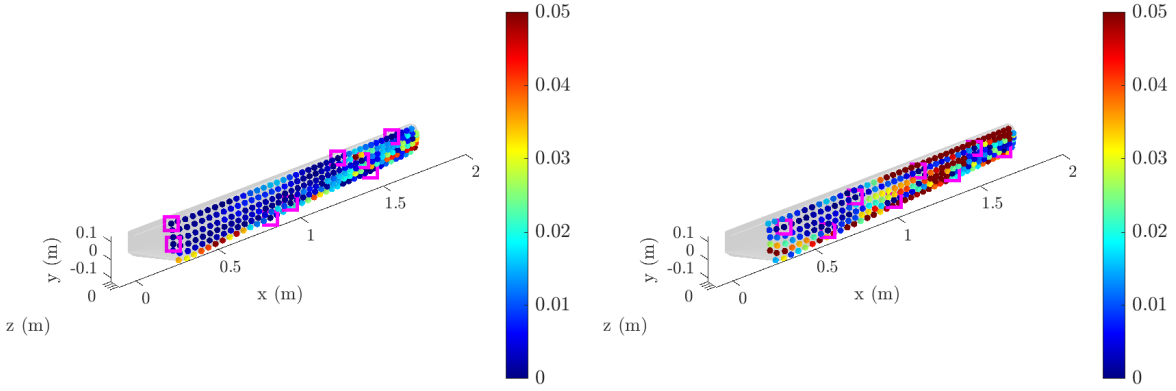

(a) $U = 8.71(95\%$ of $U_{max}), e_{avg} = 1.0\%$ **(b)** $U = 7.63(83\%$ of $U_{max}), e_{avg} 2.7\%$

Fig. 5.4. Relative error in response prediction locations using (a) best, and (b) arbitrary sensor configurations. Magenta shows measured locations.

Very good predictions with average RRMS error equal to 1% are obtained with the optimal sensor configuration. With the worst sensor locations, the average RRMS error (not shown in the Figure) in the unmeasured locations is around 20%, much higher than the one found with the best locations. The results also indicate that the selected arbitrary sensor layout, corresponding to a utility value that is approximately 20% less than the utility value for the optimal sensor configuration, also give a higher average RRMS error of 2.7% in the response prediction in the unmeasured locations.

5.1.1.2 OSP results for strain sensors using AKF

OSP for strain response prediction at locations in Fig. 5.2 is performed using AKF. The expected information gain as a function of the number of strain sensors placed at their optimal (or worst) locations is shown in Fig. 5.5(a), while the optimal positions of eight sensors are shown in Fig. 5.5(b). According to the utility result, the information gain increases as additional sensors are placed at their optimal locations. Significant information is gained by each additional sensor for up to 8 sensors placed in the structure. The information gain by adding more than 8 sensors, is relatively small compared to the information gained for the first 8 sensors. Best sensor positions are well distributed along the blade, and they are similar with the ones found by ME in Fig. 5.3.

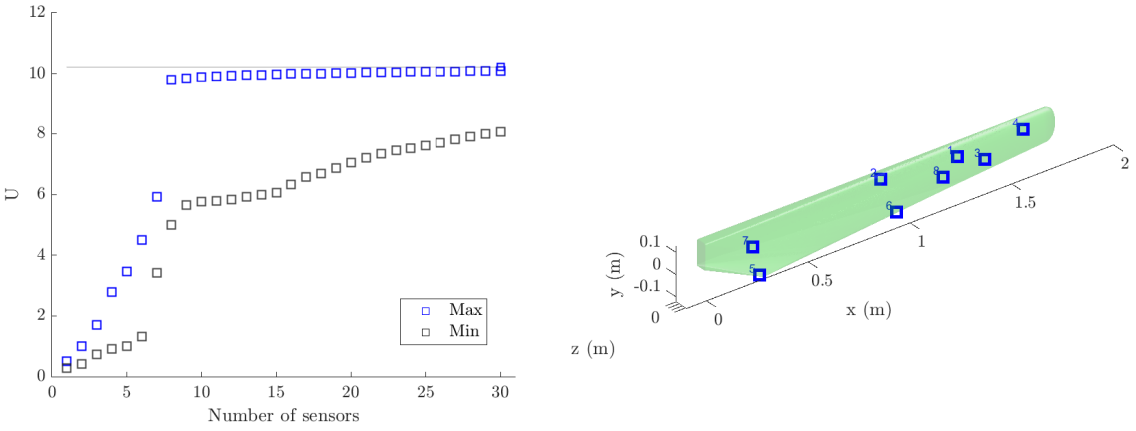

(a) **(b)**

Fig. 5.5. OSP results through (a) utility and (b) the best sensor locations. The maximum utility value U_{max} which can be reached with 245 strain sensors is shown as a grey horizontal line in (a).

The effectiveness of the optimal sensor placement in response prediction of selected locations is next investigated through the relative errors between the strain responses predicted by AKF with a fixed number of sensors and the simulated, noise contaminated measurements. Response prediction results computed with 8 best strain sensor locations with an acceleration sensor placed to the input location and 8 arbitrarily selected locations are presented in Fig. 5.6. In the calculations, Q_p is selected as 1. However results are the same for $Q_p = 10^8$ which is found by using the L curve.

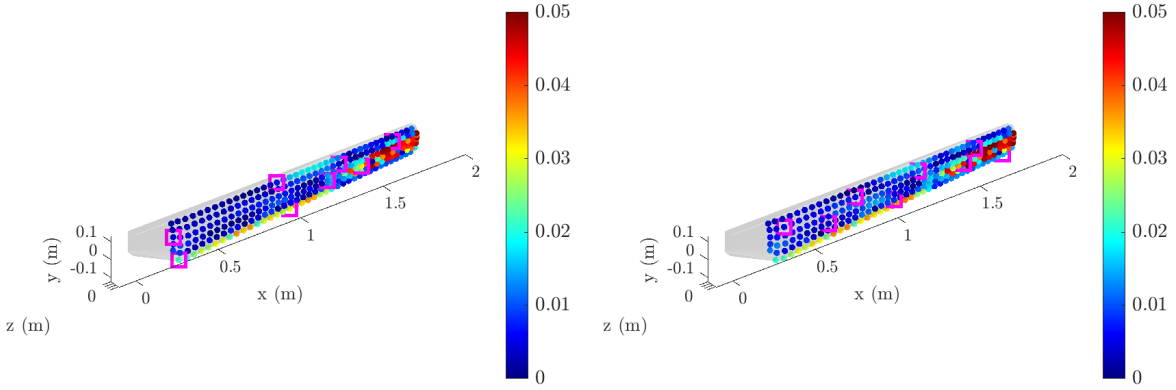

(a) $U = 9.79(96\%$ of $U_{max}), e_{avg} = 1.3\%, e_{input} = 9.4\%$

(b) $U = 8.73(87\%$ of $U_{max}), e_{avg} = 1.6\%, e_{input} = 10\%$

Fig. 5.6. Relative error in response prediction locations using (a) best and (b) arbitrary sensor locations. Magenta shows measured locations.

According to the results in Fig. 5.6, the relative error in the strain predictions is around 1.6% with best 8 strain sensors and 1.6% with arbitrarily selected 8 strain sensors that provide 87% of the U_{max}. The predictions are quite good except from the free end of the blade which has a lower strain response (high noise to signal ratio). The arbitrary sensor configuration correspond to relative high values of the information gain and thus the effectiveness of this configuration for response predictions is as good as the optimal sensor configuration. It is expected that the effectiveness of arbitrary sensor configurations corresponding to significantly lower values of information gain will be reduced.

5.1.1.3 Effect of the measurement and model error parameters

To investigate the effect of the measurement and model errors, OSP is performed with different values of measurement and model error parameters given in Table 5.3. In this analysis ME method is used. A comparison of the results obtained with three different values of measurement and model error parameters can be seen in Fig. 5.7 and Fig. 5.8, respectively. According to the results, the information extracted from sensors is affected by the model and measurement errors. When the noise in the measurements or the error in the model is higher, the information extracted from the sensors is less. However, there is a qualitative difference of the effect of the number of sensors on the information gain for the two different types of errors.

For small to medium measurement error (Fig. 5.7(a)), the maximum information gain is similar and 8 sensors provide 97-95% of the U_{max}. For large measurement error the information gain with 8 sensors placed at their optimal locations is 86% of the maximum information gain U_{max}. Due to the higher noise to signal ratio in the measurements, less information can be extracted by using the same number of sensors. Therefore, more sensors are needed. Comparison of the different model errors shows the similar results. Increasing the model error to large values (Fig. 5.8(a)), U_{max} reduces to 75% and 64% of the maximum information gained with moderate and small model error values, respectively. These results are consistent with the results presented in [1] based on ME technique and in [2] based on AKF technique. Expected utilies considering all possible values of model and measurement error parameters can be estimated as proposed in [1, 2]. Sensor positions robust to errors are more preferable for reliable response prediction.

Table 5.3: Model and measurement error parameters.

Error	Sensor type	σ_e,σ_ϵ	s	$\sim s/\epsilon_{min}$	$\sim s/\epsilon_{rms}$	$\sim s/\epsilon_{max}$
Small	Strain	10^{-3}	10^{-8}	2×10^{-2}	10^{-3}	4×10^{-4}
Moderate	Strain	10^{-2}	10^{-7}	2×10^{-1}	10^{-2}	4×10^{-3}
Large	Strain	10^{-1}	10^{-6}	2×10^{0}	10^{0}	4×10^{-1}

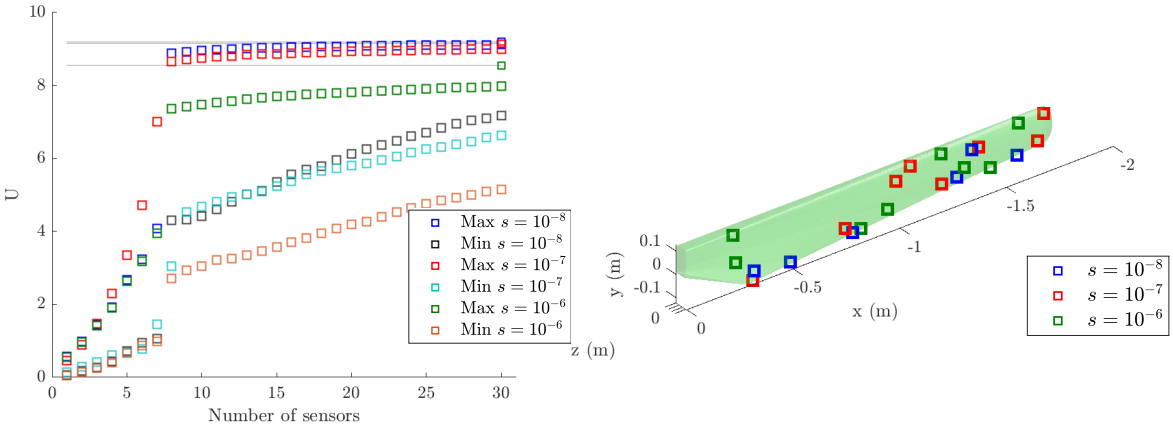

(a) **(b)**

Fig. 5.7. Comparison of utility (information gain) results for different measurement error cases. (a) Utility values and (b) best sensor locations. The maximum utility values U_{max} which can be reached with 245 strain sensors is shown as a grey horizontal lines in (a).

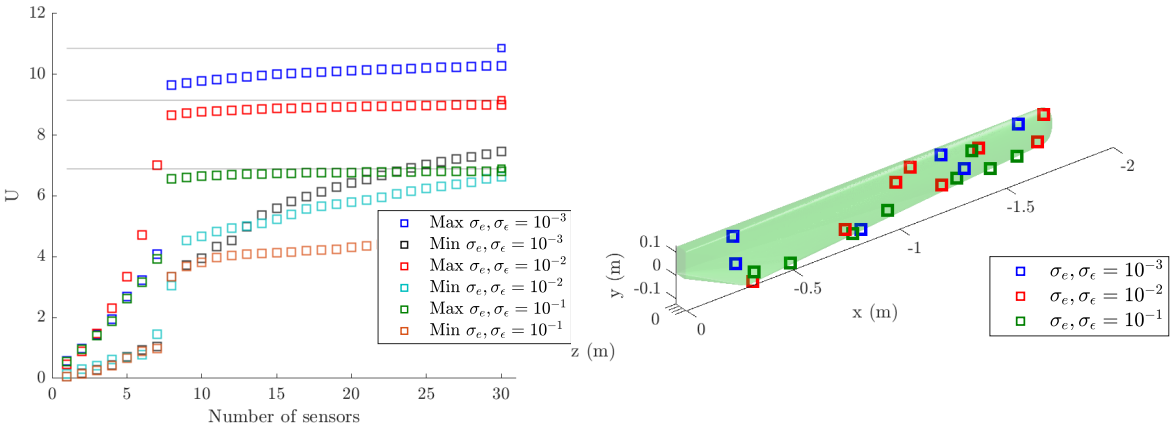

(a) **(b)**

Fig. 5.8. Comparison of utility (information gain) results for different model error cases. (a) Utility values, (b) best sensor locations. The maximum utility values U_{max} which can be reached with 245 strain sensors is shown as a grey horizontal lines in (a).

5.1.1.4 *OSP results for acceleration and strain sensors using AKF*

In this section, acceleration and strain sensors are optimized simultaneously for strain response prediction at selected 245 elements Fig. 5.2. Optimal sensor configuration is searched among 245 nodes for acceleration sensors and 245 elements for strain sensors (490 possible sensor location). Due to the large computational effort arising from the size of the matrices, FSSP and MBSSP with initial 100 points are used for optimization. An acceleration sensor that is required for FSSP to have a stable estimation with AKF is placed to its optimal location, before the optimization starts. Utility results estimated using FSSP and MBSSP as a function of number of sensors are given in Fig. 5.9(a). Results from both methods shows that significant information ($\sim 90\%$ of the maximum utility) can be gained for 9 sensors placed in the structure. MBSSP improve the results for 9 or more sensors. The best and worst acceleration (circle) and strain (square) sensor locations estimated using MBSSP are presented in Fig. 5.9(b) for 9 sensors. The best sensors are found to be strain sensors mostly. There are only two acceleration sensors.

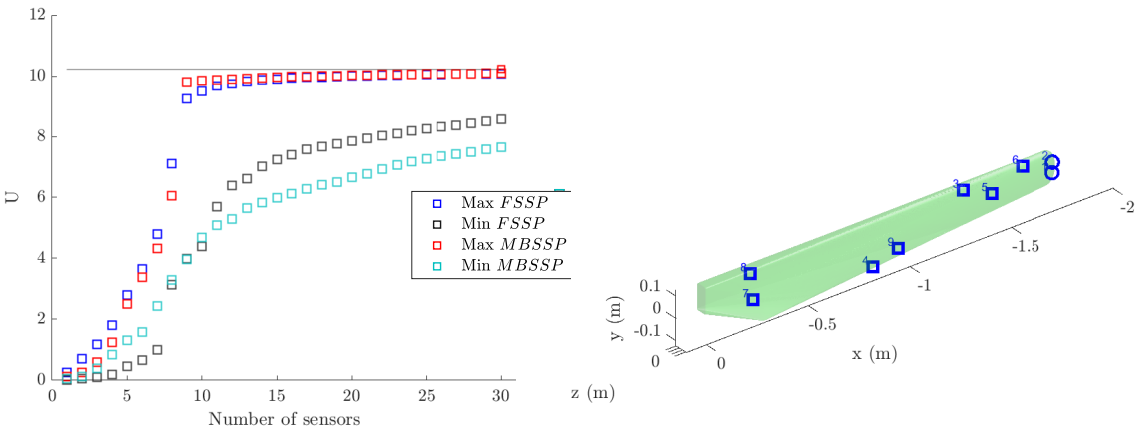

(a) **(b)**

Fig. 5.9. OSP results through (a) utility values and (b) best 9 sensor positions (MBSSP). The maximum utility value U_{max} which can be reached with 245 acceleration and 245 strain sensors are shown as a grey horizontal line in (a). Acceleration and strain sensors are shown with circle and square, respectively, in (b).

To validate the results, the relative errors in response prediction using best and worst locations are given in Fig. 5.10. According to the results in Fig. 5.10, the relative error in the strain predictions is around 1.5% with best 9 sensors and 1.8% with worst 9 sensors. Even with the worst sensors, prediction are quite good except from the free end of the blade which is not monitored with strain sensors and have a lower strain response. However, the average errors

in the input prediction is 3.5% for the optimal sensor configuration and as high as 12% for the worst sensor configuration. The relatively good predictions from the worst sensor configuration is also due to the fact that such sensor configuration correspond to 43% of the maximum information gain.

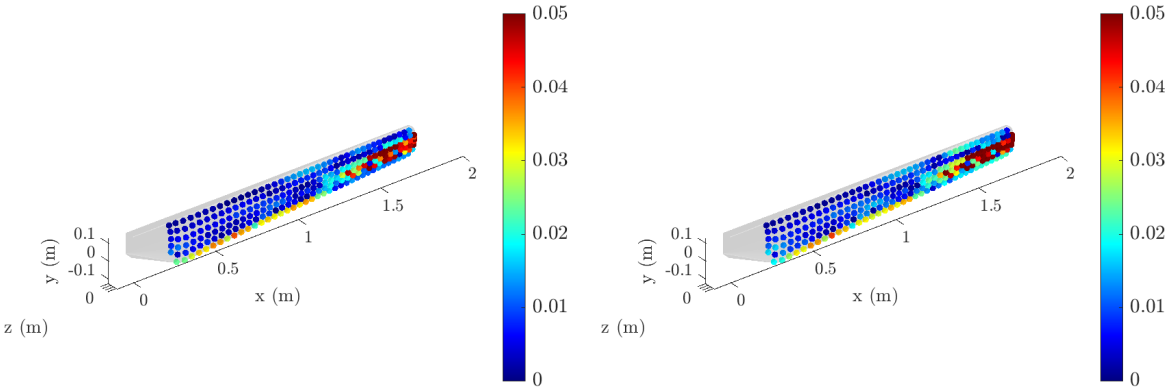

(a) $U = 9.81(96\%$ of $U_{max}), e_{avg} = 1.5\%, e_{input} = 3.5\%$

(b) $U = 4.39(43\%$ of $U_{max}), e_{avg} = 1.8\%, e_{input} = 12\%$

Fig. 5.10. Relative error in response prediction locations using (a) best and (b) worst sensor locations.

Response predictions by using arbitrarily selected sensor positions are presented in Fig. 5.11. The arbitrarily selected positions corresponding to lower utility value of 75% of U_{max}. The average errors for the arbitrarily selected sensor configuration are 2.6% for the response predictions and 13% for the input predictions which are higher than the ones for the optimal sensor configuration.

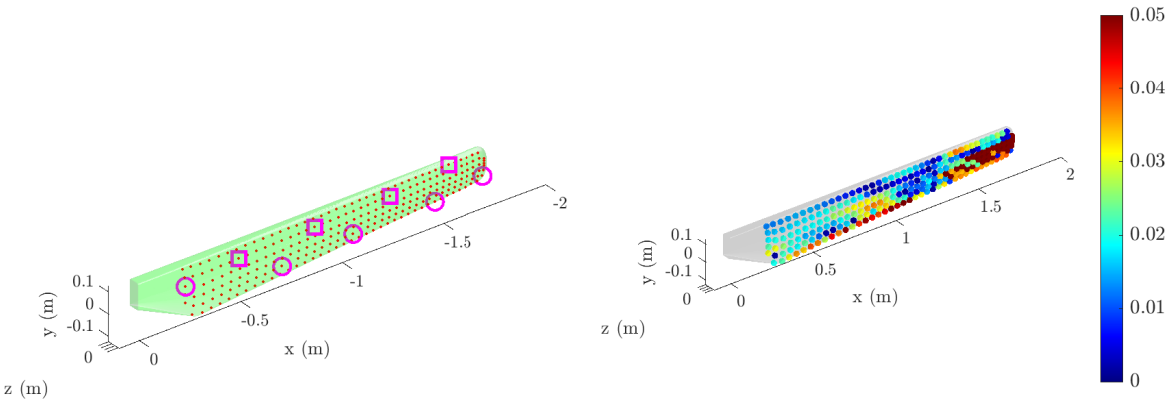

(a)

(b) $U = 7.65(75\%$ of $U_{max}), e_{avg} = 2.6\%, e_{input} = 13\%$

Fig. 5.11. Relative error in response prediction locations using arbitrary sensor locations (4 strain and 5 acceleration). Acceleration and strain sensors are shown with circle and square, respectively.

5.2 Application on Helicopter Blade

OSP studies are presented for a helicopter blade model that is hosted by University of Sheffield at the Laboratory for Verification and Validation (LVV) in Sheffield UK. The type, number, and the locations of sensors are optimized for reliable acceleration response predictions at unmeasured locations under unknown excitation. Verification studies are performed by using simulated measurements and validation studies using available experimental data.

5.2.1 Test Campaign

The test campaign which is the subject of this study is shown in Fig. 5.12. The test structure is exposed to a continuous random excitation to excite the blade up to 400 Hz. Fig. 5.13 shows the input and the 10 sensor locations where measurements (perpendicular to the "horizontal" blade surface) are obtained. From the experiment, acceleration measurements approximately for a duration of 7 min with a time step of 1.25e-03 sec are available for validation purposes. The response time histories and the Fourier transforms of the measured acceleration are presented in Fig. 5.14.

Fig. 5.12. Test photos.

The numerical model of the blade is built in ANSYS. The numerical modal frequencies computed from the ANSYS finite element model and the approximate experimental modal frequencies of the test structure estimated using peak picking are presented in Table 5.4 for up to 8 modes.

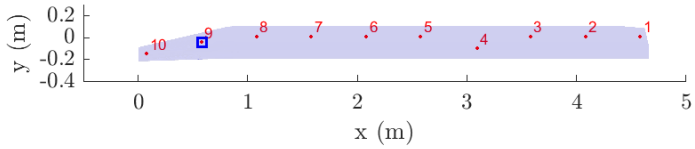

Fig. 5.13. Representation of the helicopter blade with the location of input (square) and acceleration sensors (points) in the experiment with their numbers.

Table 5.4: Modal frequencies (Hz).

Mode	ANSYS	Experimental (peak peaking)
1	0.963	0.92
2	3.699	3.56
3	5.963	5.90
4	16.566	16.34
5	21.076	21.67
6	32.538	31.70
7	37.403	51.56
8	53.559	72.79

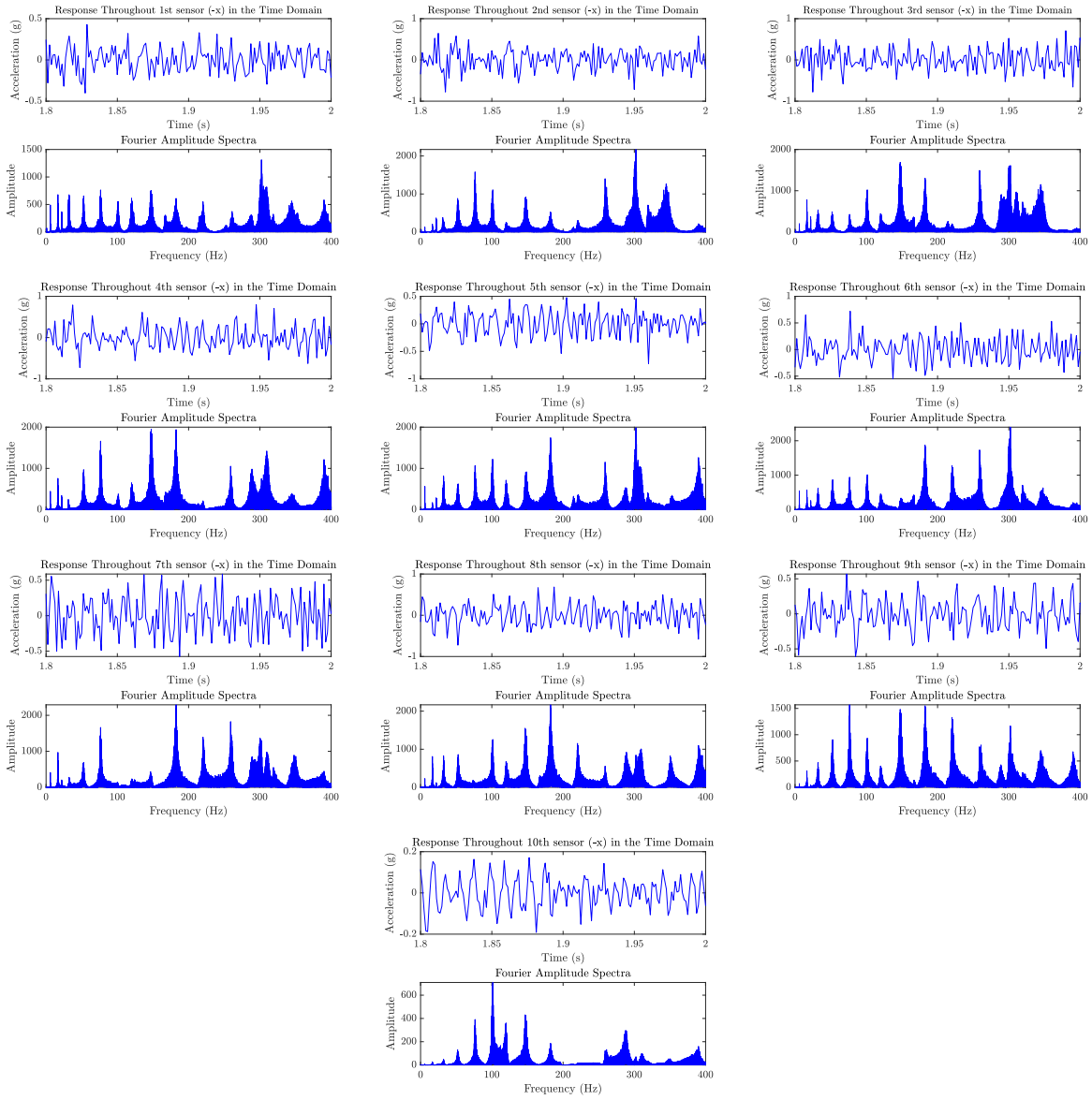

Fig. 5.14. Response time histories and Fourier transforms of the measured accelerations.

5.2.2 Case 1

In the first case, the positions of the acceleration sensors have been optimized to maximize the information collected from sensors for reliable model-based acceleration predictions. The location of the predictions and the possible sensor locations are only the 10 experimental sensor locations shown in Fig. 5.13. The optimal number and locations (among the 10 positions) are selected in order to make reliable predictions at the same 10 sensor locations used in the experiment. In applying the OSP methodology [1], it is assumed that the blade is subjected to white noise input with a sampling period $\Delta t = 0.0025$ sec at location 9 shown in Fig. 5.13

with 6 contributing modes (Fig. 5.16 presents the mode shapes). The model and measurement error parameters $\sigma_e, \sigma_\epsilon$ and s (see [1] for definition and details) are selected according to the intensities of the acceleration responses (Fig. 5.15). The intensities of the acceleration responses are computed from the finite element model by applying white noise sampled at $\Delta t = 0.0025$ at the input location used in the experimental setup. The model, measurement and prediction error and input parameters used modal expansion method are given in Table 5.5. Small model and measurement errors are considered. The model error is of the order of 1% of the acceleration intensities, while the measurement error is of the order of 0.2% of the acceleration intensities. α is selected to be 10^2 in order to consider large prior uncertainty in the modal coordinates. For the filtering method, the same model and measurement error parameters are used. The process noise and the load model error parameters for filtering are also given in the Table 5.5.

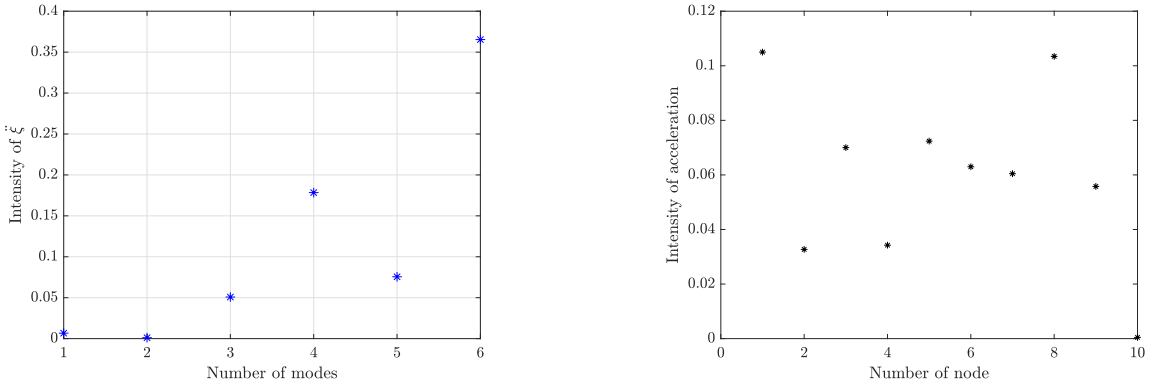

(a) **(b)**

Fig. 5.15. Intensities of (a) $\ddot{\xi}$ modal coordinates and (b) acceleration in x-direction

Table 5.5: Model, measurement and prediction error, input parameter (for ME), process noise (for AKF), and load model error (for AKF) parameters. ϵ_{rms} is the intensity (root mean square) of the nodal acceleration that cover 90% of the selected sensor positions on the blade surface.

Sensor type	$\sigma_e, \sigma_\epsilon$	s	s/ϵ_{rms}	α	σ_x	β
Acceleration	10^{-2}	10^{-4}	2×10^{-3}	10^2	10^{-3}	1

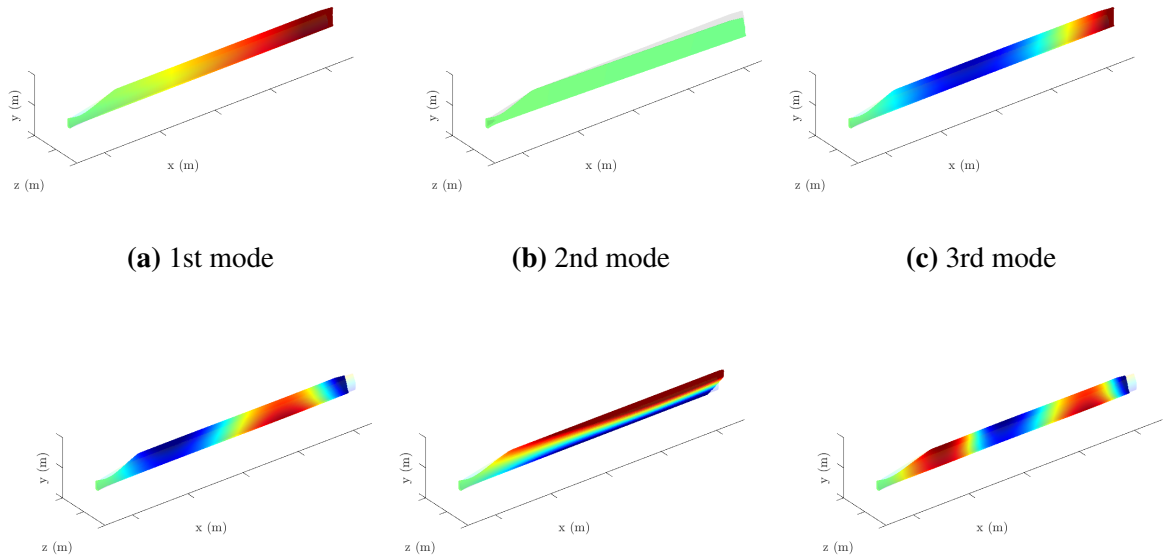

(a) 1st mode **(b)** 2nd mode **(c)** 3rd mode

(d) 4th mode **(e)** 5th mode **(f)** 6th mode

Fig. 5.16. The first six mode shapes of the structure (coloured in the out of plane direction (z-direction)).

5.2.2.1 OSP for acceleration prediction using ME

The modes of the structure excited up to 400 Hz are more than 17. However, when OSP is performed based on the modal expansion technique, there are certain conditions for the methodology to be applied. For informative measurements, the number of sensors should at least be equal to the number of contributing modes. For a number of sensors less than the number of modes, information in the OSP methodology is borrowed from the prior distribution subjectively assigned to the modal parameters. The aforementioned condition between the number of sensors N_0 and the number of modes m has to be taken into account when validation studies using the experimental set up of the helicopter blade with 10 acceleration sensors and white noise input exciting as many as 20 to 30 modes is considered. For validation studies, the number of 10 acceleration sensors in the experimental setup is split into a group of $N_0 = 6$ optimal sensors selected by the methodology as optimal sensor locations and a second group of $10 - N_0$ sensors to be used for validation. This necessitates the use of up to $m = N_0$ modes. Since more than $N_0 = 6$ modes are excited from the white noise input (0-400 Hz frequency content) in the actual experiment, the output measured signals are filtered to keep at most $N_0 = 6$ modes in the signals. Thus, to be able to compare the response prediction results with

the data obtained from the test campaign, a band pass filter is applied to the measured data (almost 7 min duration) to remove the out of band frequencies. A pass band filter of 0.9-35Hz is used to include contribution up to the 6th mode. The original and filtered signals of each sensor are shown in Fig. 5.17. Only the contribution of $m = 6$ modes is taken into account in the OSP methodology.

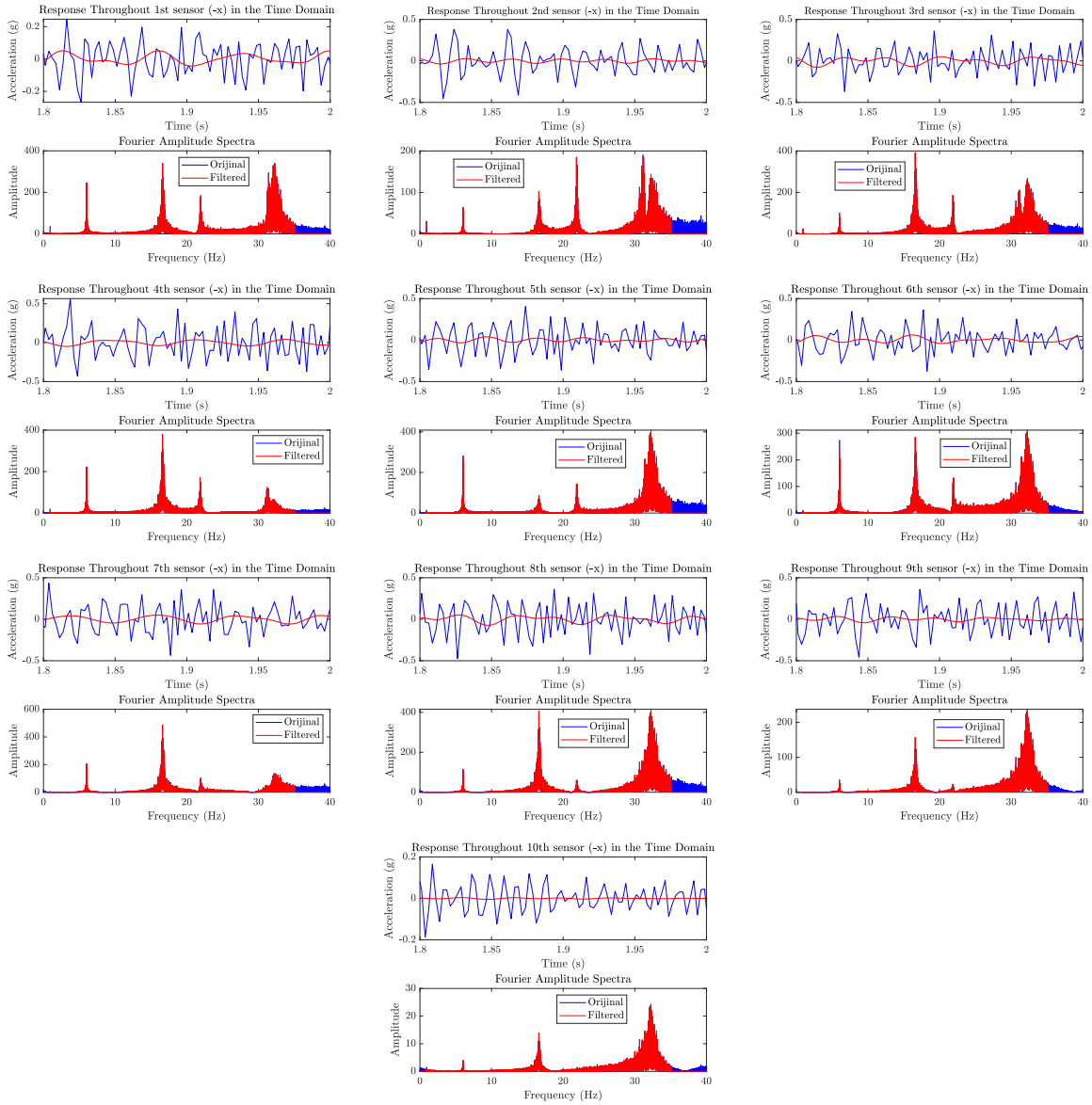

Fig. 5.17. Measured acceleration responses time histories for selected time segments (original and filtered from 0.9 to 35 Hz). Fourier transform of the measured acceleration time history from 0 to 40 Hz (original and filtered from 0.9 to 35 Hz).

The expected information gain (utility) values is calculated by using exhaustive search for 1 to 10 number of sensors (only 10 experiment sensor locations are allowed) and it is presented in Fig. 5.18. In this figure, the maximum utility value U_{max} which can be reached with 10 sensors

is shown as a straight line. As observed from the expected utility values, each additional sensor provides some extra information gain for response prediction of the selected points. However, after $m = 5$ sensors, the extra information gain provided by each additional sensor is negligible. It is also clear that the worst locations of the sensors are also found informative as the difference between the minimum and the maximum utility values is not large. The optimal and the worst positions for the sensors are shown in Fig. 5.19. The best five sensors are well distributed along the blade. The best position for the first sensor is found close to the input location, while the worst sensor position is at the 10th node, which is the one closest to the fixed boundary and has the smallest response in terms of acceleration intensity. As mentioned previously, it is expected that the number of sensors to be greater than or equal to the number of modes in order for the problem to be identifiable and to be able to obtain high information gain values. However, the OSP results show that the contribution of one of the 6 modes (here the 2nd mode) is very small, enabling us to obtain good predictions by using 5 instead of the required number of 6 sensors. Thus, in the following section, 5 optimal sensor positions (found with exhaustive search) are used for validation purposes.

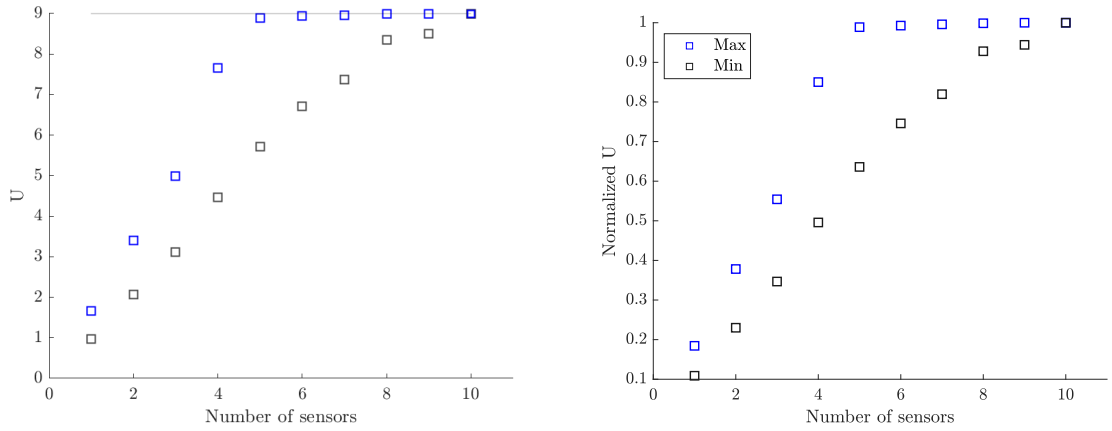

(a) **(b)**

Fig. 5.18. (a) Utility values, (b) normalized utility values. The maximum utility is obtained by using 10 acceleration sensors, placed at the experimental positions, is shown with the grey horizontal line ($U_{max} = 8.99$).

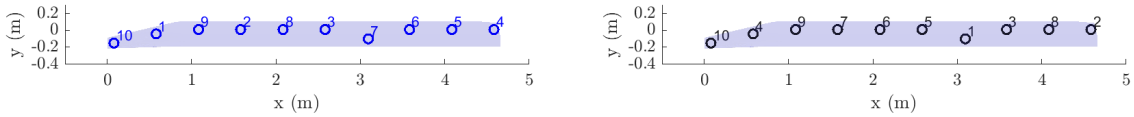

(a) **(b)**

Fig. 5.19. (a) Best and (b) worst sensor positions numbered consecutively from 1 to 10.

For validation purposes, responses at the 10 measured locations are predicted from the modal expansion technique by using the five best sensor locations, the five worst sensor locations, and an arbitrary sensor configuration (among the 10 sensor positions which are selected to be uniformly distributed along the blade). The real filtered measurement data are used to estimate responses in measured and unmeasured locations. RRMS errors between the predictions and the experimental data are presented in Fig. 5.20 for all three sensor configurations according to the node numbers shown in Fig. 5.16. In Fig. 5.21, the relative errors in response predictions are plotted along the blade. 98% of the maximum utility can be gained with five sensors when they are in their best location. The errors at the unmeasured locations vary from 3% at node number 3 to 20% at node number 9. At node number 10, very close to the fixed support, the error is 100%. Comparison of predicted and measured time histories is given for a measured and an unmeasured location in Fig. 5.22. For this figure predictions are obtained using best 5 sensor locations. With the worst sensor locations, 63% of the maximum utility can be gained and the average error in the unmeasured locations is much higher than the one found with the best locations. Additionally, for the arbitrary sensor layout that has a lower utility value than the best layout, the relative error in response predictions in the unmeasured locations is higher than the error caused in the unmeasured locations by the optimal sensor placement.

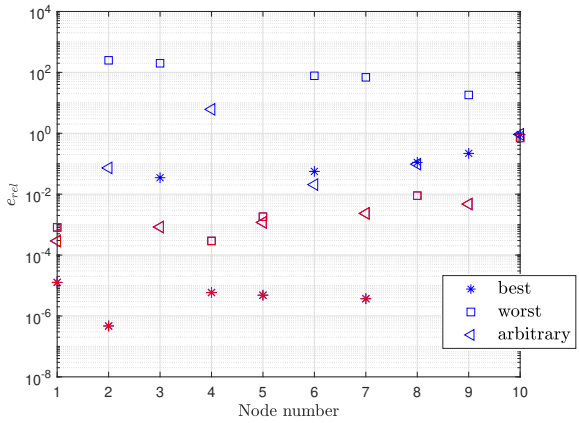

Fig. 5.20. Relative error in response prediction in 10 test locations by using best ($U = 8.83, 98\%$ of U_{max}), worst ($U = 5.63, 63\%$ of U_{max}) and arbitrary ($U = 6.84, 76\%$ of U_{max}) sensor locations. Measured and unmeasured locations are shown in red and blue, respectively.

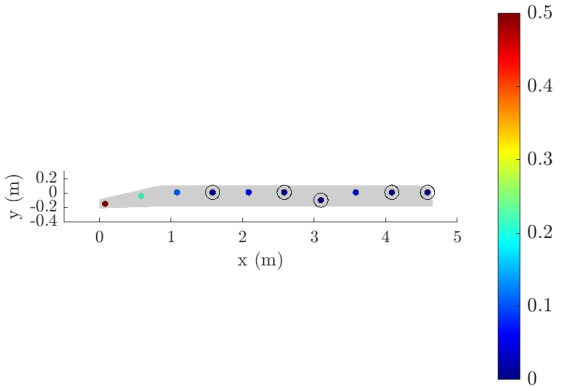

(a) $U = 8.83(98\% \text{ of } U_{max}), e_{avg} = \%13$

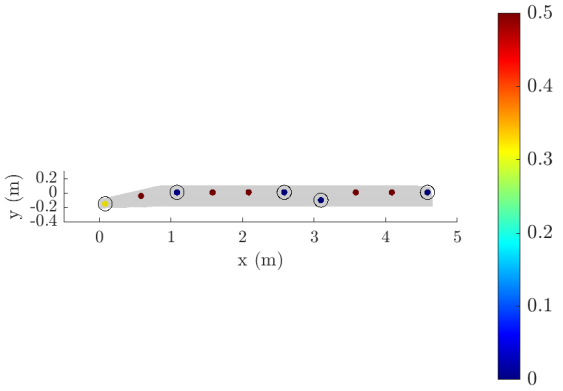

(b) $U = 5.63(63\% \text{ of } U_{max}), e_{avg} = \%6000$

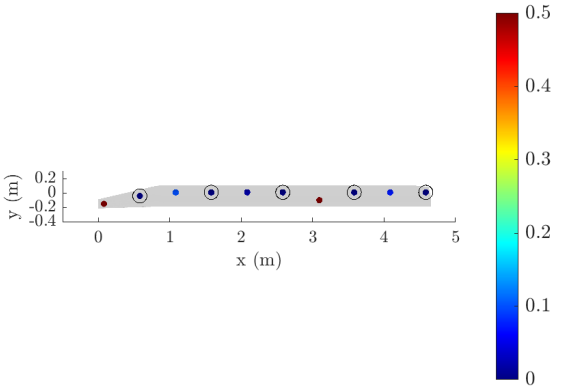

(c) $(U = 6.84(76\% \text{ of } U_{max})), e_{avg} = \%72$

Fig. 5.21. Relative error in response prediction locations using (a) 5 best, (b) 5 worst and (c) 5 arbitrary sensor locations.

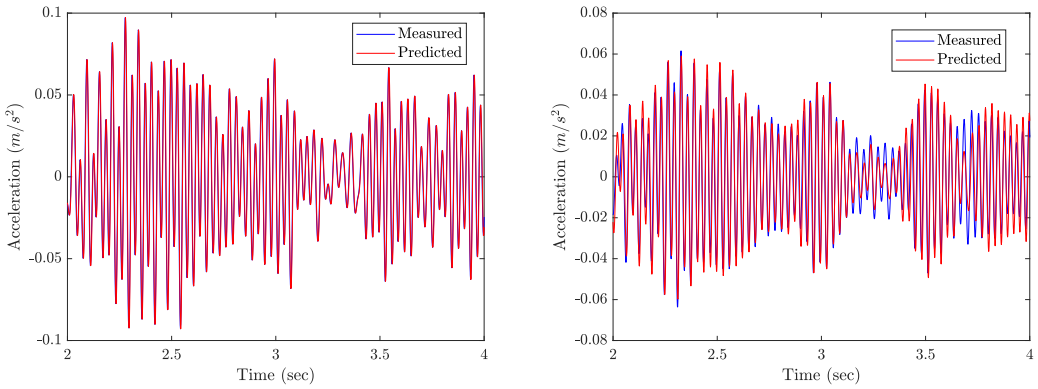

(a) **(b)**

Fig. 5.22. Comparison of measured and predicted time histories (a) at measured location (node number 1), and (b) unmeasured location (node number 9).

5.2.2.2 OSP for acceleration prediction using AKF

Sensor locations are optimized among the 10 experimental location by using AKF. The expected information gain as a function of the number of sensors placed at their optimal locations is presented in Fig. 5.23. In this figure, the maximum utility value U_{max} which can be reached with 10 sensors is shown as a straight line. As observed from the expected utility values, each additional sensor provides some extra information gain for response prediction of the selected points. However, after 4 sensors, the information gain is relatively small. It is also clear that the worst locations of the sensors are also found informative as the difference between the minimum and the maximum utility values is not large. The optimal and the worst positions for the sensors are shown in Fig. 5.24. Similar to the ME results, the best position for the first sensor is found close to the input location, while the worst sensor position is found at the node which is the one closest to the fixed boundary and has the smallest response in terms of acceleration intensity. It should be also noted that the best 5 locations found with the exhaustive search using AKF are the same with the ones found with ME technique. In the following section, 5 best, 5 worst and 5 arbitrary sensors have been used for validation purposes.

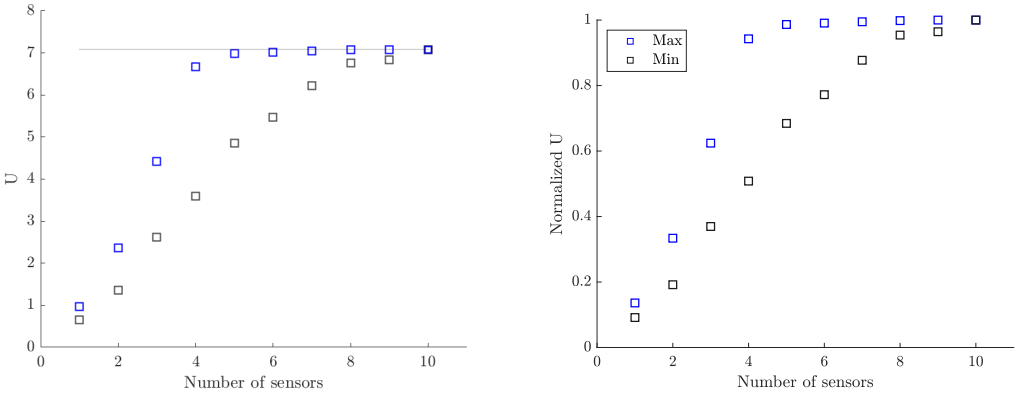

(a) **(b)**

Fig. 5.23. (a) Utility values, (b) normalized utility values. The maximum utility is obtained by using 10 acceleration sensors, placed at the experimental positions, is shown with the grey horizontal line ($U_{max} = 7.08$).

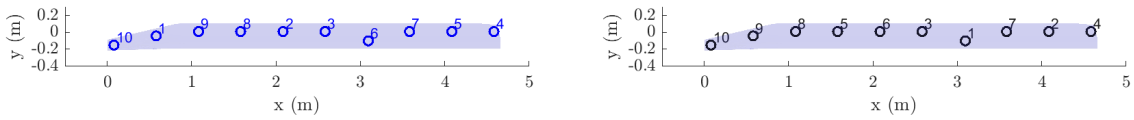

(a) **(b)**

Fig. 5.24. (a) Best and (b) worst sensor positions numbered consecutively from 1 to 10.

To be able to validate OSP results, the responses at the 10 measured locations are predicted using AKF with the best, worst, and an arbitrary sensor configuration (among the 10 sensor positions). Response predictions at 10 prediction points are performed by using the experimental data by assuming that only 5 sensors are available. The average RRMS errors between the predictions and the experimental data are presented in Fig. 5.25 and in Fig. 5.26. According to the results, when the sensors are placed to the five best locations where 98% of the maximum utility can be gained, the errors at the measured locations vary from 15% to 40%. At node number 10, very close to the fixed support with very small acceleration intensity, the error is 100%. With the worst sensor locations, 70% of the maximum utility can be gained and the average RRMS error in the unmeasured locations is much higher than the one found with the best locations. Additionally, for an arbitrary sensor layout, that have a lower utility value than the best layout (86%), the relative error in response predictions is higher than the one obtained by the optimal sensor layout.

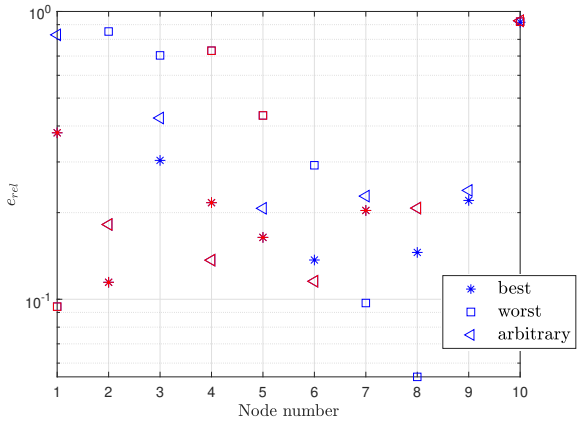

Fig. 5.25. Relative error in response prediction in 10 test locations by using best ($U = 6.99, 99\%$ of U_{max}), worst ($U = 4.85, 68\%$ of U_{max}) and arbitrary ($U = 6.35, 90\%$ of U_{max}) sensor locations. Measured and unmeasured locations are shown in red and blue, respectively.

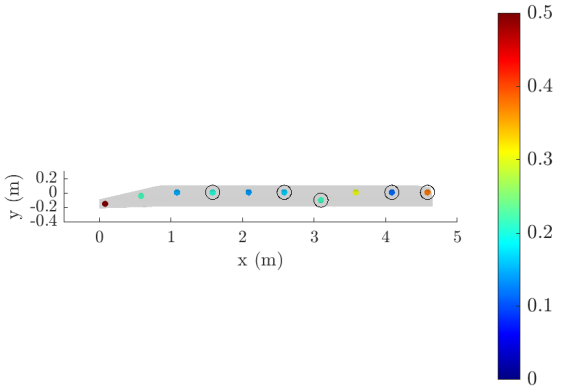

(a) $U = 6.99(99\%$ of $U_{max})$, $e_{avg} = 28\%$

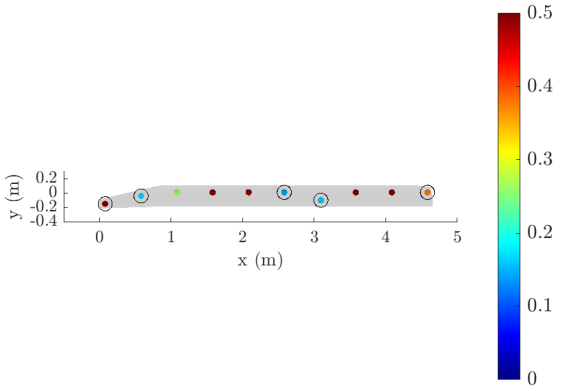

(b) $U = 4.85(68\%$ of $U_{max})$, $e_{avg} = 43\%$

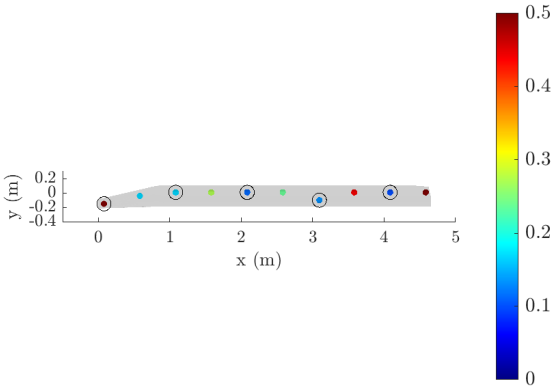

(c) $U = 6.35(90\%$ of $U_{max})$, $e_{avg} = 32\%$

Fig. 5.26. Relative error in response prediction locations using (a) 5 best, (b) 5 worst and (c) 5 arbitrary sensor locations.

5.2.3 Case 2

In case 2, an OSP analysis is performed for response prediction in a larger area on the blade surface involving 150 predicted locations are selected to cover the blade surface as shown in Fig. 5.27. The OSP is performed by exhaustive search for 10 possible sensor locations (the experimental ones. The effectiveness of the best sensor configuration is investigated by using simulated measurements, as there are no experimental data in the selected 150 prediction locations. For the response prediction, simulated acceleration response time histories are generated using a sampling period $\Delta t = 0.0025$ sec and a zero-mean Gaussian white noise sequence with a standard deviation $\sigma_{wn} = 1$. To simulate noise contaminated measurements and thus consider the effect of the measurement error (noise from sensors), independent zero-mean Gaussian white noise sequences with standard deviation equal to 2% of the intensity of the simulated response is added to each simulated acceleration response time history.

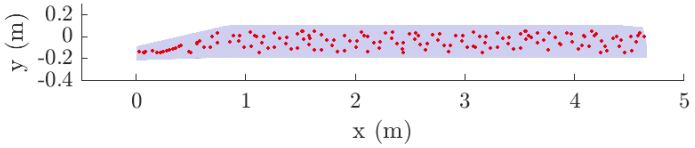

Fig. 5.27. Location of predictions.

5.2.3.1 OSP for acceleration prediction by using ME

OSP results found by ME are presented in Fig. 5.28 and Fig. 5.29 through utility and best and works sensor locations respectively. The expected information gain results given in Fig. 5.28 show that with five sensors, significant information can be captured to estimate reliable responses at the selected 150 prediction locations. It is also observed that the maximum information that can be reached to predict responses by using the 10 experiment locations is lower (slightly lower) than in case 1. According to the optimal and the worst position results, the first optimal positions are sparsely placed along the blade. Similar to the previous case, the worst sensor locations are found close to the fixed boundary.

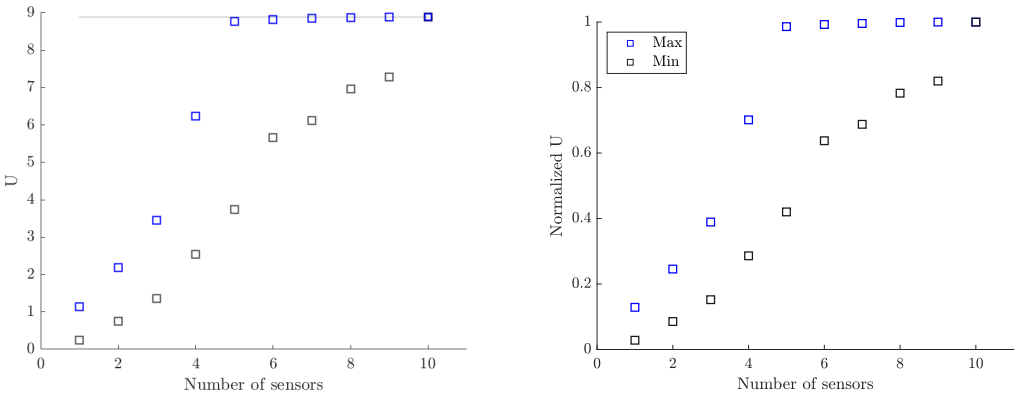

(a) **(b)**

Fig. 5.28. (a) Utility values, (b) normalized utility values. The maximum utility is obtained by using 150 acceleration sensors, placed at the possible sensor positions, is shown with the grey horizontal line ($U_{max} = 8.89$).

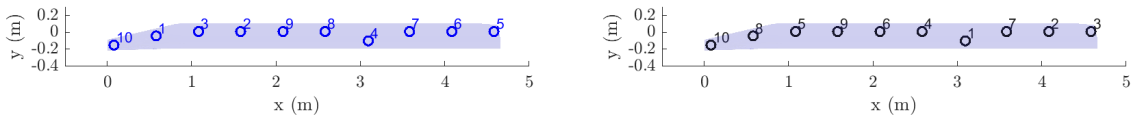

(a) **(b)**

Fig. 5.29. (a) Best and (b) worst sensor positions.

Next, validation results are presented through the RRMS errors between the predictions and the simulated measurements. According to the relative error results presented in Fig. 5.30, 99% of the maximum utility can be gained with five sensors when they are in their best location, and the average error in response prediction is 1.3%. With the worst sensor locations, 42% of the maximum utility can be gained, and the average error is found to be much higher than the one found with the best locations. Additionally, an arbitrary sensor layout (selected among the experiment locations) that has a lower utility value than the best layout (80% of the U_{max}) causes a higher error in the response predictions (the average error is 21%). It should be noted that with 10 experimental sensor locations, very good predictions can be obtained.

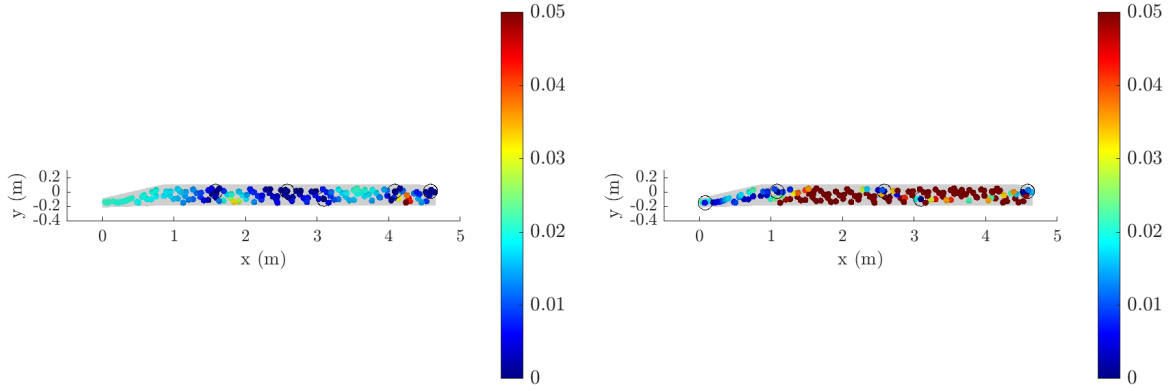

(a) $U = 8.77(99\% \text{ of } U_{max}), e_{avg} = 1.3\%$

(b) $U = 3.74(42\% \text{ of } U_{max}), e_{avg} = 8.8\%$

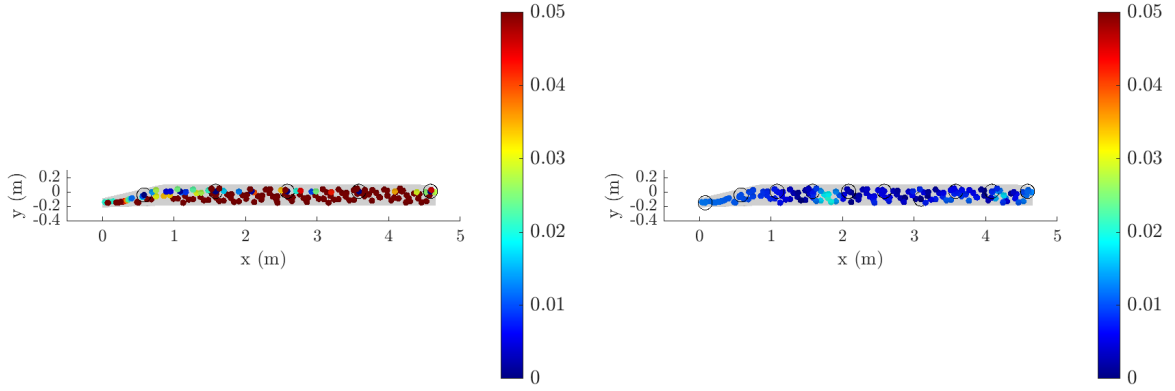

(c) $U = 7.11(80\% \text{ of } U_{max}), e_{avg} = 21\%$

(d) $U = 8.89(99\% \text{ of } U_{max}), e_{avg} = 0.7\%$

Fig. 5.30. Relative error in response prediction locations using (a) 5 best, (b) 5 worst, (c) 5 experiment and (d) 10 experiment locations.

5.2.4 Case 3

In case 3, 150 possible sensor locations and 150 prediction locations are selected to cover the blade surface as shown in Fig. 5.27 to demonstrate the OSP analysis. The existence of a sensor layout which is better than the one used in the experiment is investigated. As in the previous section, the effectiveness of the best sensor configuration is investigated by using simulated measurements, as there are no experimental data in the selected prediction and optimal sensor locations. The intensities of the acceleration response in selected locations are given in Fig. 5.31. Such intensities are simulated using a white noise input.

For this case, optimization is performed by using SSP due to computational cost of exhaustive search for 150 possible sensor locations.

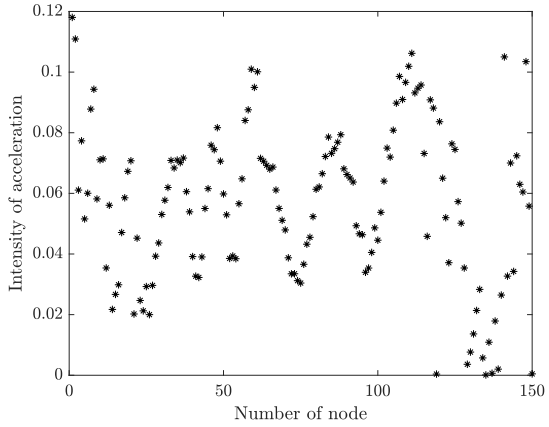

Fig. 5.31. Intensities of acceleration in the x-direction in possible sensor locations (given in Fig. 5.27).

5.2.4.1 OSP for acceleration prediction using ME

OSP results found by ME are presented through utility values in Fig. 5.32 for 1 up to 30 sensors. Best and worst sensor locations are presented in Fig. 5.33 for 1 to 10 sensors.

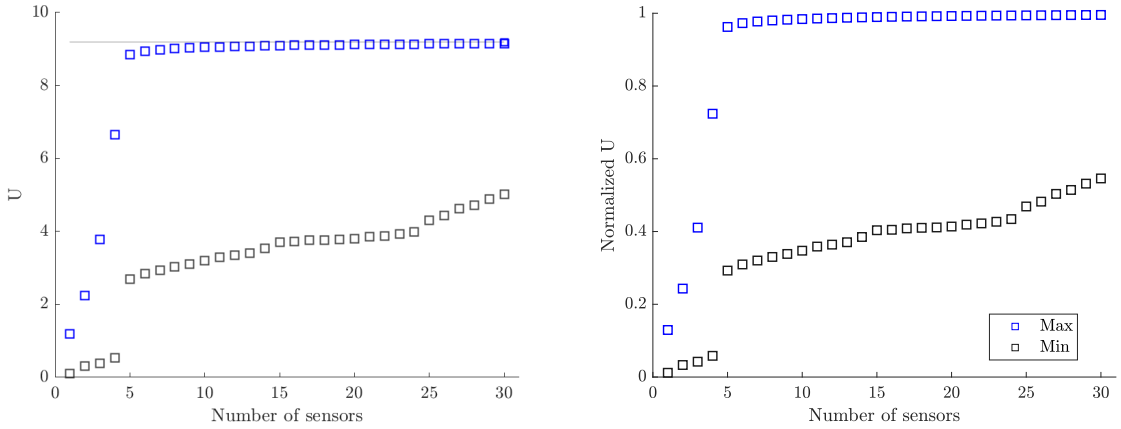

Fig. 5.32. (a) Utility values, (b) normalized utility values up to 30 sensors. The maximum utility is obtained by using 150 acceleration sensors, placed at the possible sensor positions, is shown with the grey horizontal line (U_{max} = 9.19).

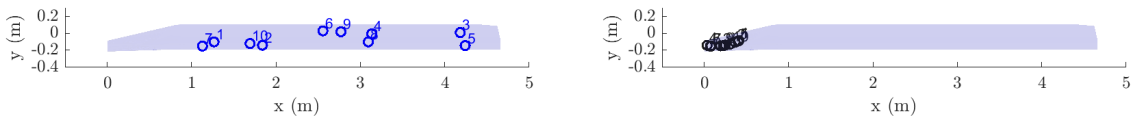

Fig. 5.33. (a) Best and (b) worst sensor positions.

The expected information gain results in Fig. 5.32 show that the optimization of the sensor locations is more effective than the previous cases as the difference between the minimum

and the maximum utility values are high. With five sensors, most of the information can be captured to estimate reliable responses at the selected prediction locations. The 5 optimally located sensors are uniformly distributed along the blade. The 10 sensors are optimally located in clusters, with the clusters relatively well distributed along the blade. The worst locations are found close to the fixed boundary, and it is due to very low intensities and thus high noise to signal ratio. Additionally, the maximum information that can be reached for the case of 150 sensor positions is higher than in case 1 and case 2 involving only 10 sensors. By comparing the maximum information gain in Fig. 5.28 with the maximum information gain in Fig. 5.33, it can be seen that 10 sensors placed at the experimental locations are slightly less informative than the optimal positions found in this case to predict the responses along the blade. This is expected since 150 possible sensor locations give more flexibility to provide a better sensor configuration corresponding to higher information gain than the 10 experimental sensor locations.

For response predictions, measurements have been simulated as described in the previous case. According to the average RRMS results presented in Fig. 5.34, 96% of the maximum utility can be gained with five sensors when they are in their best location, and the average error in response prediction is 0.7%. With the worst sensor locations, 29% of the maximum utility can be gained and the average error that is found to be 12% is higher than the one found with the best locations. An arbitrary sensor layout (with 5 sensors selected among the experiment locations) that has a lower utility value than the best layout will cause a higher error in the response prediction (the average error is 20%). Using 10 sensors locations which are used in the experiment, most of the information can be obtained. However, it is obvious that OSP can provide the same amount of information with fewer sensors.

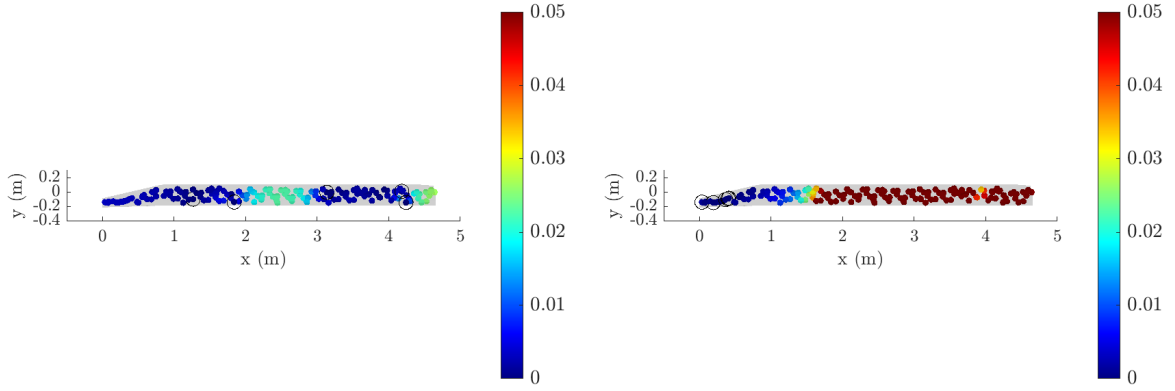

(a) $U = 8.85(96\% \text{ of } U_{max}), e_{avg} = 0.7\%$

(b) $U = 2.69(29\% \text{ of } U_{max}), e_{avg} = 12\%$

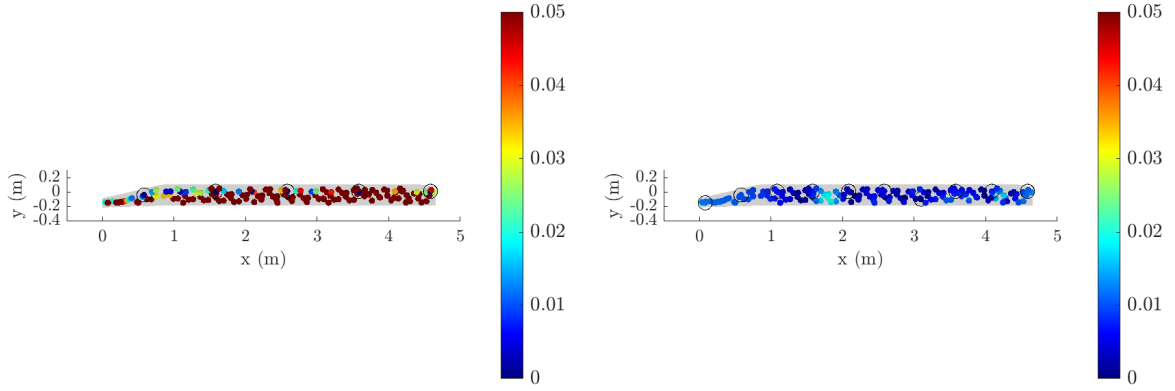

(c) $U = 7.11(77\% \text{ of } U_{max}), e_{avg} = 20\%$

(d) $U = 8.89(97\% \text{ of } U_{max}), e_{avg} = 0.7\%$

Fig. 5.34. Relative error in response prediction locations using (a) 5 best, (b) 5 worst, (c) 5 arbitrary and (d) 10 experiment locations.

5.2.4.2 OSP for acceleration prediction using AKF

OSP results obtained by using AKF technique is presented next. The expected information gain as a function of the number of sensors placed at their optimal locations is presented in Fig. 5.35. In the figure, the maximum utility value U_{max} which can be reached with 150 sensors is shown as a straight line. As observed from the expected utility values, each additional sensor provides some extra information gain for response prediction of the selected 150 points. However, after 4 to 5 sensors, the information gain is relatively small. The optimal and the worst positions for the sensors are shown in Fig. 5.36, and they are well distributed along the blade. The nodes which are close to the fixed boundary are found to be the worst location. Comparing results in Fig. 5.36 and Fig. 5.33, some small differences are identified between the optimal sensor locations promoted by the AKF and ME algorithms.

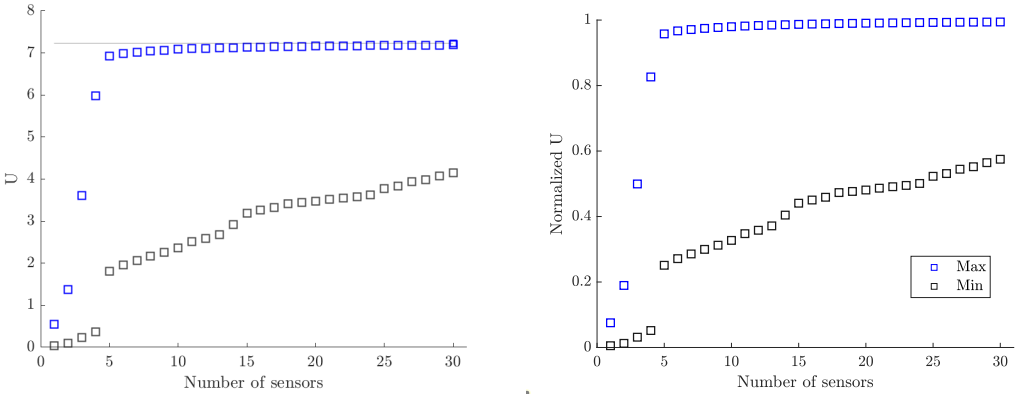

(a) **(b)**

Fig. 5.35. (a) Utility values, (b) normalized utility values up to 30 sensors. The maximum utility is obtained by using 150 acceleration sensors, placed at the possible sensor positions, is shown with the grey horizontal line ($U_{max} = 7.23$).

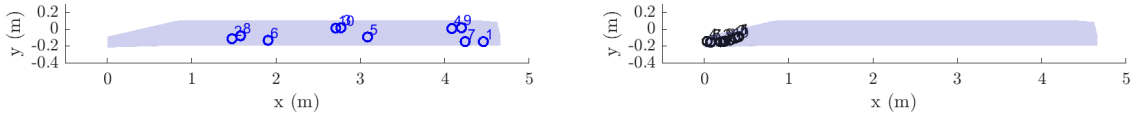

(a) **(b)**

Fig. 5.36. (a) Best 10 and (b) worst 10 sensor locations.

In the following, 5 best, 5 worst and 5 arbitrary sensors have been used for validation purposes. According to the average RRMS errors between the predictions and the simulated data presented in Fig. 5.37, 96% of the maximum utility can be gained with five sensors when they are in their best location, and the average error in response prediction is 1.89%. With the worst sensor locations, 25% of the maximum utility can be gained and the average error that is found to be 3.9% is higher than the one found with the best locations. In Fig. 5.37, locations that are used in the experiment are used to predict responses in 150 locations. With 5 sensors, 85% can be obtained and RRMS error is found 1.68%. with 10 sensors, 96% can be obtained and RRMS error is found as 1.48%.

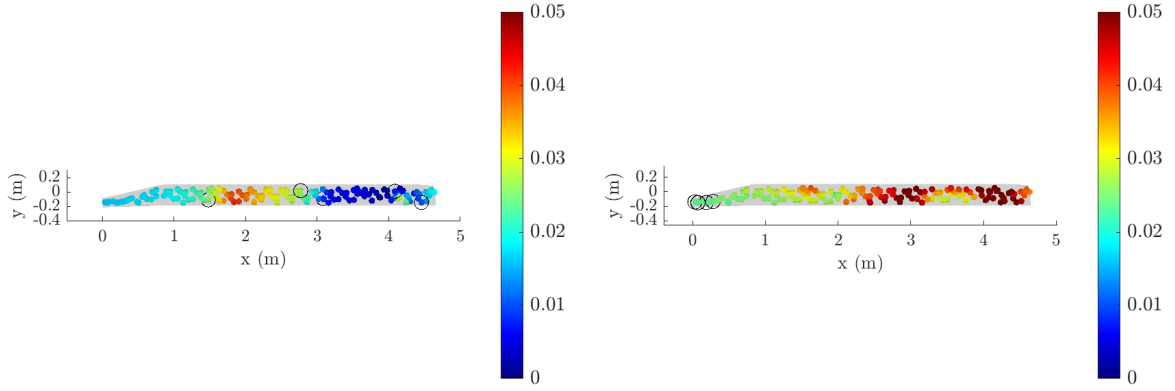

(a) $U = 6.93(96\% \text{ of } U_{max}), e_{avg} = 1.89\%$

(b) $U = 1.82(25\% \text{ of } U_{max}), e_{avg} = 3.9\%$

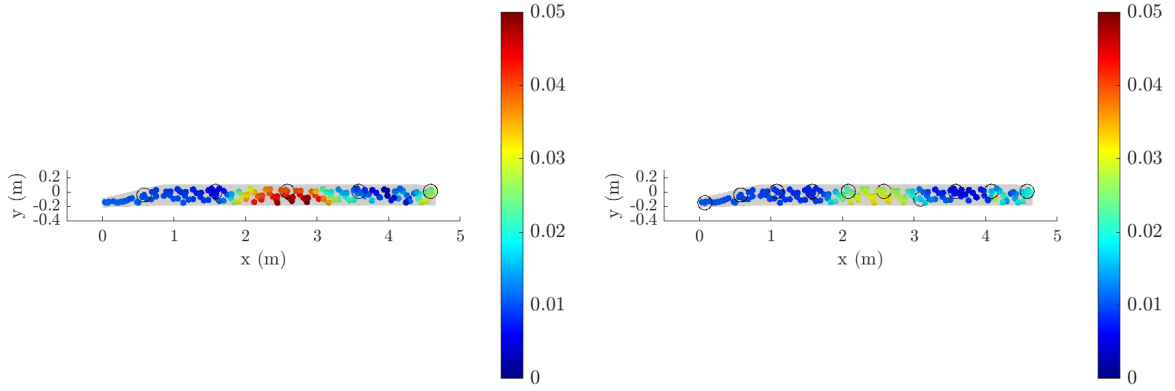

(c) $U = 6.17(85\% \text{ of } U_{max}), e_{avg} = 1.68\%$

(d) $U = 6.97(96\% \text{ of } U_{max}), e_{avg} = 1.48\%$

Fig. 5.37. Relative error in response prediction locations using (a) 5 best, (b) 5 worst, (c) 5 arbitrary sensors and (d) 10 experiment locations.

5.3 Conclusions

In this chapter, the OSP strategies are applied on two full-scale components of engineering structures, both tested at the laboratory. High fidelity complex finite element models with a large number of DOF are used to simulate the dynamics of both components. In these applications, the purpose of OSP is to find the optimal type, number and location of sensors for virtual sensing (response and input reconstruction) using output-only vibration measurements. The two different methods, ME and AKF, developed in Chapters 2 and 3, respectively, were applied and their effectiveness was evaluated.

In the first part, OSP studies are demonstrated by using a wind turbine blade. OSP is performed for reliable strain prediction over the whole surface of the blade. Different combination

of SSP techniques have been used to estimate the optimal solutions in a computationally effective way. The effect of the measurement and model error on OSP is investigated. ME and AKF methods are validated using noise contaminated measurements. OSP for input prediction is also performed and the efficiency of the proposed methods for virtual sensing is demonstrated.

In the second part, the OSP methodology is applied on a helicopter blade, considering 3 different observation and prediction cases. In case 1, available experimental data is used for validation purposes. In the 1st and the 2nd cases, exhaustive search is used to optimize sensor locations, as the possible sensor locations were only 10. For case 1 and 2, the optimal locations of 5 sensors are found to be the same using ME and AKF. Case 3 involves OSP design over a large possible number of sensor locations and is performed using the developed heuristic algorithms. Verification studies performed with real and the simulated measurements demonstrate the applicability and effectiveness of the proposed methodologies. In particular, comparing predictions with measurements obtained from laboratory experiments, it is demonstrated using acceleration measurements at 10 locations along the blade surface that the optimal sensor configuration promoted by the OSP framework outperforms sub-optimal sensor configuration designs.

These studies are important to demonstrate the capabilities of the proposed OSP framework for full-scale components of energy related and industrial structures operating in a highly dynamic and uncertain environment. The proposed framework is applicable and effective to optimize the experimental design for a wide variety of systems that require comprehensive use of limited resources in the experiment due to the high cost of maintenance and inspection.

5.4 References

[1] T. Ercan and C. Papadimitriou. Optimal Sensor Placement for Reliable Virtual Sensing Using Modal Expansion and Information Theory. *Sensors*, 21(10):3400, 2021.

[2] T. Ercan, O. Sedehi, L. S. Katafygiotis, and C. Papadimitriou. Information theoretic-based optimal sensor placement for virtual sensing using augmented kalman filtering, Submitted to MSSP, 2022.

[3] Y. Ou, K. E Tatsis, V. K. Dertimanis, M. D. Spiridonakos, and E. N. Chatzi. Vibration-

based monitoring of a small-scale wind turbine blade under varying climate conditions. part i: An experimental benchmark. *Structural Control and Health Monitoring*, 28(6):e2660, 2021.

[4] K. Tatsis, Y. Ou, V. K. Dertimanis, M. D. Spiridonakos, and E. N. Chatzi. Vibration-based monitoring of a small-scale wind turbine blade under varying climate and operational conditions. part ii: A numerical benchmark. *Structural Control and Health Monitoring*, 28(6):e2734, 2021.

Chapter 6. Conclusions and Future Work

6.1 Concluding Remarks

This dissertation developed novel Bayesian OED methodologies in order to define the most informative and effective test campaigns to improve and validate models and make model-based predictions under modeling and input load uncertainties. The optimal design variables are selected as the ones that maximize the information gain, defined as the KL-div between the prior and posterior distribution of the model parameters or response QoI estimated using Bayesian inference. The presented methodologies are applicable to complex and critical engineering structures, including energy-related structures (e.g. wind turbines and offshore structures), civil infrastructure (e,g. bridges, buildings), aerostructures and industrial structures. The proposed framework gives well-designed sensory systems to monitor structures under operational conditions that provide the most informative data for decision making and maintenance scheduling.

One of the main contributions of this thesis is the development of OSP tools for reliable response reconstruction/virtual sensing by using output-only vibration measurements. Employing the Gaussian nature of the response estimates for linear models of structures, an exact analytical expression of the utility function is formulated in terms of the variance of the responses of the virtually sensed QoI.

Widely used methods for virtual sensing, namely modal expansion and a Kalman-based filtering technique such as AKF, are successfully integrated to the Bayesian OED framework to formulate the utility function in terms of prior and posterior covariances of the prediction errors. Useful properties of the utility function and reasonable choices of the model and prediction error parameters are presented and demonstrated by using the numerical examples. It is shown that the utility depends on the sensor location and the values of nuisance parameters and is independent of the time history of data. OSP based on modal expansion technique provide a reliable design of experiments for reconstructing stress response time histories (by using displacement or strain measurements), useful for predicting fatigue damage accumulation.

Additionally, the AKF based OSP technique for virtual sensing is advantageous as it allows fusing different types of physical sensors and reconstructing, in addition to the responses, the external loads applied to the structures.

Theoretical expressions and demonstrative examples reveal that the choice of the measurement and model/prediction errors and the level of prior uncertainty of the predicted parameters or the QoI affects the OED. Thus, robust solutions to uncertainties in model parameters as well as in model/prediction and measurement errors are more preferable. The sensor placement procedure was extended to consider uncertainties arising from system operational conditions, as well as the large uncertainties related to the interaction of the system or its components with the environment. Monte Carlo or sparse grid methods are needed to compute the utilities that have multidimensional probability integrals over the modeling uncertainties and input variabilities.

The second main contribution of this thesis is the development of an optimal sensor placement framework for model parameter estimation. A Bayesian OED framework for reliable parameter estimation of linear and nonlinear models of structures is presented, accounting for the modelling and input uncertainties. Asymptotic approximations, valid for large number of data, are proposed for estimating the Kullback-Leibler multidimensional probability integrals arising in the utility formulation. The asymptotic approximations provide insightful expressions, with the expected utility expressed in terms of the sensitivities of model responses at the measured locations with respect to the estimated parameters. The optimal sensor configuration maximizes a scalar measure of these response sensitivities which is defined by the determinant of the Fisher information matrix and the inverse of the covariance matrix of the Gaussian prior.

The effects of input uncertainties are comprehensively investigated. To take into account input uncertainties, the utility function is generalized to be the expected information gain over all possible data that would arise under all possible input realizations. In addition to the characteristics of a white noise input, the proposed method can handle uncertainties in the stochastic excitation characteristics such as frequency content and amplitude. Numerical results reveal that the information gain and the optimal locations of sensors are affected by the characteristics of inputs. For parameter estimation problems of nonlinear systems, the optimal excitation frequency is in neighborhood of the lowest resonance frequencies.

The problem of optimizing the locations of actuator(s) and the excitation characteristics (e.g. amplitude and frequency content) was also investigated for reliable parameter estimation. For nonlinear systems the choice of actuating force characteristics to activate the nonlinear

mechanisms and thus enhance the information provided from sensors for the estimation of parameters associated with these nonlinearities is especially important. By using structural systems involving nonlinear behavior modelled with Bouc-Wen type hysteresis, it was shown that information obtained from sensors is increasing with the activated nonlinear features.

Forward and backward heuristic sequential sensor placement algorithms and GA can be used to optimize the design variables involved in OED. However, for complex problems that include large number of possible design variables, combination of FSSP and BSSP and possibly GA provides computationally more efficient solutions with sufficient accuracy. FSSP is the computationally most efficient approach but could suffer from accuracy. For models with large number of possible sensor locations, BSSP could involve high computational cost, but it is significantly more accurate than FSSP. A new modified SSP strategy was proposed to drastically reduce the computational burden of BSSP and provide sufficiently accurate solutions.

The applicability and the efficiency of the proposed OSP framework using output-only vibration measurements was investigated by applying methodologies on realistic and components of structures. Specifically demonstration was performed for the wind turbine blade component of an energy related structure and the for the helicopter blade of an aeroelastic structure. High fidelity complex finite element models were used to model both analysed components. Using simulated measurements contaminated with noise and/or model error and available experimental data, it has been shown that optimal placement of a few sensors significantly improves the accuracy of response and/or input prediction compared to randomly placed sensors.

The OED techniques and optimization schemes proposed in this work provide reliable solutions for the design of the experiments that are set up for parameter estimation and response prediction. Thus, it is important for data-driven safety and performance estimates of systems, and it contributes to the decision making process.

6.2 Future Work

The research presented in this thesis provides several interesting avenues for Bayesian OED in structural dynamics. In future work, the developed OSP framework for response reconstruction under output only vibration measurements can be extended for handling nonlinear models using filtering techniques. Also, the developed Bayesian OED framework for parameter es-

timation can be extended for handling model selection and damage identification problems. Another potential extension of this work is the development of more advance robust techniques. Specifically, robust OED techniques can be used to find sensor configurations that maximize the expected information gain and minimize the variability of the information gain over all possible values of the nuisance parameters. For this, the developed methodologies can be integrated with the multi objective sensor placement algorithms that simultaneously optimize expected utility and minimize the fluctuation of the utility.

In addition, the methodology can be extended to handle issues related to cost of the instrumentation. Such cost depends on the number of sensors used and the location of sensors in the structure. Specifically, for some structures, installation cost for different sensor locations should be considered in the OED due to the fact that some positions are more difficult and thus more costly to access than others. An example includes underwater sensor installation and sensor requirements in offshore structures, which might be significantly more costly than installing sensors on the offshore platform. It might be less costly to gain the same amount of information by using more sensors at accessible locations than using one sensor at an underwater position that is difficult and very costly to access. By augmenting the optimization problem to include cost issues, the proposed methodology can effectively deal with such problem and take into account in the OSP the cost of instrumentation or installation of the monitoring system.

Throughout this thesis, exact formulations or asymptotic approximations of the expected utility functions were developed. For the parameter estimation problem, full sampling techniques available for estimating the multi-dimensional probability integrals involved in information gain measures can also be developed further to account for modelling and input uncertainties. Although the methodologies were developed to address structural dynamics problems, the theoretical developments, uncertainty considerations and optimization algorithms are applicable to other branches of engineering and applied sciences.